Rainfall types over southern West Africa: diagnosis, synoptic environments and representation in satellite retrievals

Zur Erlangung des akademischen Grades eines
DOKTORS DER NATURWISSENSCHAFTEN
von der KIT-Fakultät für Physik des
Karlsruher Instituts für Technologie (KIT)

genehmigte

DISSERTATION

von

M.Sc. Marlon Maranan
aus Aulendorf

Tag der mündlichen Prüfung: 7. Juni 2019

Referent: Prof. Dr. Andreas H. Fink

Korreferent: Prof. Dr. Peter Knippertz

Zusammenfassung

Der südliche Teil Westafrikas (SWA) ist einer der am dichtesten besiedelten Regionen der Erde und hängt stark vom Niederschlag ab, der vom westafrikanischen Monsun (WAM) kontrolliert wird. Eine Reihe von groß angelegten Feldkampagnen, unter anderem begründet durch die große Dürre in der Sahelregion in den 70er und 80er Jahren, führte zu einer beträchtlichen Verbesserung im Verständnis des WAMs und seine Bedeutung für den Niederschlag im Sahel, während SWA weitestgehend vernachlässigt wurde. Die kürzlich in SWA durchgeführte DACCIWA-Kampagne (*Dynamics-Aerosol-Chemistry-Cloud-Interactions in West Africa*) im Jahr 2016 gab jedoch das Ziel aus, über die Untersuchung der Prozesskette beginnend bei bodennahen Emissionen und Aerosolen hin zu ihrem Einfluss auf Wolken, Niederschlag und der WAM-Dynamik die Kenntnis über den WAM zu erweitern. Die vorliegende Arbeit, die innerhalb des DACCIWA-Projektes im Subprojekt "Niederschlagsprozesse" eingebettet ist, behandelt hierbei die Identifikation von Niederschlagssystemen und die Untersuchung ihrer Bedeutung für den Gesamtniederschlag, der typischen Umgebungsbedingungen und ihrer Abbildung in moderner satellitengestützter Niederschlagsmessung über dem SWA. Die Untersuchung letzterer ist motiviert durch die Tatsache, dass Niederschlagsfernerkundung aufgrund des allmählichen Rückgangs von bodengestützten Messungen, u.a. durch Regensammler, immer mehr an Bedeutung gewinnt.

Aus klimatologischer Sicht wird der Gesamtniederschlag über dem SWA größtenteils von intensiven und langlebigen, aber auch relativ selten vorkommender organisierter Konvektion beherrscht, auch *mesoskalige konvektive Systeme* (MCSs) genannt. Jedoch nimmt ihre Bedeutung in Richtung der unmittelbaren Küstenregion ab, in der schwächere und kurzlebigere Konvektion in ihrer Anzahl ansteigen. Alle Typen an Niederschlagssystemen treten typischerweise in Verbindung mit Störungen im Vorticity-Feld in der mittleren Troposphäre auf, von denen manche Wellenstrukturen ähnlich der von sogenannten *African easterly waves* (AEWs) aufweisen. Die Auswirkung dieser Störungen manifestiert sich insbesondere in der Modifikation der vertikalen Windscherung. Hierbei sind organisierte konvektive Systeme im Bereich einer vorauslaufenden antizyklonalen und einer nachfolgenden zyklonalen Anomalie vorzufinden, also in einer Region, in der die Windscherung durch eine stärkere Nordoststströmung in der mittleren Troposphäre und der darunterliegenden südwestlichen Monsunströmung erhöht wird. Im Gegensatz dazu wird konvektive Organisation im Bereich schwächerer Windscherung zwischen einer vorauslaufenden zyklonalen und einer nachfolgenden antizyklonalen Anomalie unterdrückt. In einem weiteren Aspekt gehen allen Niederschlagstypen niedertroposphärische Feuchtekonvergenz voraus, weshalb diese Größe allgemein als Vorhersagegröße für Niederschlag verwendet werden kann.

In einer tiefergehenden Untersuchung werden in dieser Arbeit die Umgebungsbedingungen evaluiert, die zu der Entstehung und der Erhaltung eines langlebigen MCSs führt. Dieses war im SWA vom 10. bis 13. Juni 2016 aktiv. Infolge von tageszeitlicher Aufheizung des Bodens bildete sich das MCS in der semi-ariden Savannenregion im Sudan und entwickelte sich im Verlauf in eine klassische, westafrikanische "Squall line", während sie südwestlich Richtung Nigeria zog. Die Squall line intensivierte und verlangsamte sich nach Ankunft im feuchteren Regime SWAs und initiierte die Entwicklung eines mittel- bis niedertroposphärischen Vortex. All diese Faktoren führten zu einem der höchsten jemals gemessenen 24-stündigen Niederschlag im SWA mit 223.5 mm. Diesem Ereignis ging eine, durch ein lokales und kurzlebiges Hitzetief gesteuerte, starke niedertroposphärische Feuchtekonvergenz voraus, die eine mit extrem viel Feuchte angereicherte Umgebung verursachte und dadurch die Intensivierung des MCSs und die Formierung des Vortex begünstigte. Im Gegensatz zu der trockeneren Savannenzone, wo sich das MCS sehr wahrscheinlich über die selbst erzeugte bodennahe Dichteströmung aufrechterhielt, ist im SWA anzunehmen, dass der Vortex das MCS durch Feuchtekonvergenz und Hebung instabiler Luftmassen stützte. Die Vermutung liegt daher nahe, dass solche mesoskaligen Wirbel im Strömungsfeld generell eine wichtige Rolle für die MCS-Dynamik im SWA spielen können.

Abschließend wird die Leistungsfähigkeit des häufig verwendeten, satellitengestützten Niederschlagsproduktes IMERG (*Integrated Multi-Satellite Retrievals for Global Precipitation Measurement*) hinsichtlich von Niederschlagstypen evaluiert und mit einer Zusammenstellung von DACCIWA-Regensammlern mit hoher zeitlicher Auflösung verglichen. Auf einer monatlichen Skala werden Niederschlagssummen von IMERG sehr gut wiedergegeben, jedoch nimmt die Güte hin zu kleineren Zeitskalen ab. Während die Mehrheit der Niederschlagsereignisse von IMERG erfasst wird, besteht Niederschlag in IMERG zum Teil aus Fehlerkompensationen zwischen unterschiedlichen Niederschlagstypen. Konkret werden schwache und kurzlebige Niederschlagsereignisse hauptsächlich überschätzt, wohingegen die Intensität starker Ereignisse wie der von MCSs größtenteils unterschätzt wird. Weiterhin wird eine relativ hohe Anzahl an *false alarms* festgestellt, die etwa ein Viertel des gesamten Niederschlags in IMERG ausmacht. Eine ergänzende Untersuchung satellitengestützter Daten von Charakteristika an der Wolkenoberkante offenbart ein hohe Anfälligkeit für false alarms in Anwesenheit von dünnen Eiswolken, während Niederschlag aus reinen Flüssigwolken, d.h. warmer Regen, häufig nicht erfasst wird.

Die vorliegende Arbeit leistet einen Beitrag zu einem besseren Verständnis von Niederschlagstypen diverser Natur über dem SWA und von Umgebungsbedingungen, die zu ihrer Entwicklung führen. Dies wurde für SWA auf einer regionalen Skala bisher noch nicht durchgeführt und kann für die regionale Wettervorhersage im SWA auf synoptischen Zeitskalen von großer Bedeutung sein. Insbesondere hebt diese Arbeit die Bedeutung von niedertroposphärischen Wirbeln für die Entwicklung von Starkniederschlagsereignissen hervor, die in dieser Region weder dokumentiert, noch untersucht wurde. Des Weiteren wurden die womöglich regionenspezifischen Stärken und Schwächen eines modernen, satellitengestützten Niederschlagsproduktes beleuchtet, das für zukünftige Niederschlagsstudien mit diesem Produkt im SWA als Referenz dienen kann.

Abstract

Southern West Africa (SWA) is one of the most densely populated regions on earth and highly depends on rainfall that is controlled by the West African monsoon (WAM). Motivated by the major Sahelian drought event in the 1970s and 1980s, among other things, a series of extensive field campaigns led to a substantial improvement in the understanding of the WAM and its implications for rainfall in the Sahel, while the adjacent more humid SWA to the south has remained understudied. However, the recent project *Dynamics-Aerosol-Chemistry-Cloud-Interactions in West Africa* (DACCIWA) targeted SWA and aimed to extend the knowledge of the WAM by investigating the process and feedback chain ranging from surface emissions and aerosols to their influence on clouds, precipitation and WAM dynamics. Being incorporated in the work package "Precipitation processes" of the DACCIWA project, the present work deals with the identification of rainfall types and the evaluation of their importance, typical environmental conditions as well as their representation in space-borne precipitation retrievals over SWA. The latter is done in anticipation of a growing relevance of satellite rainfall products due to a gradual degradation of ground-based facilities for monitoring rainfall in the region.

From a climatological viewpoint, total rainfall over SWA is mainly controlled by intense and long-lived, but relatively rarely occurring organised convection, termed *mesoscale convective systems* (MCSs). However, their overall importance gradually decreases closer to the immediate coastal region, where less-intense and shorter-lived diurnal convective systems become more and more numerous. All rainfall types typically occur in conjunction with midlevel disturbances in the vorticity field, some of which exhibit wave structures reminiscent of so-called *African easterly waves* (AEWs). The major implication of these disturbances is their modification of the strength of the low-level vertical wind shear. Here, organised convection is largely found between a preceding anticyclonic and a succeeding cyclonic anomaly, a region of enhanced wind shear due to stronger midlevel northeasterlies above the prevailing southwesterly monsoon flow. In contrast, convective organisation is suppressed between a preceding cyclonic and a succeeding anticyclonic anomaly, where wind shear is reduced. Furthermore, all rainfall types are preceded by low-level moisture convergence, which can therefore generally be used as a predictor for the occurrence of rainfall events.

In a more detailed manner, the environmental controls leading to the initiation and maintenance of a long-lived MCS, active over SWA between 10–13 June 2016 during the DACCIWA field campaign, is evaluated. As a consequence of diurnal heating, the MCS formed in the semi-arid Savannah zone over Sudan and evolved into a classical, fast-moving West African squall line

while propagating to the southwest towards Nigeria. Entering the more humid regime of SWA, the squall line intensified, decelerated and gave rise to the development of a mid- to low-level vortex, all of which caused one of the highest ever recorded daily rainfall amount over SWA with 223.5 mm. Prior to this event, strong low-level moisture convergence due to the formation of a local heat low created an extremely humid environment, which facilitated the intensification of the MCS and the genesis of the vortex. In contrast to the dry Savannah, where the MCS maintained itself possibly through typical coldpool dynamics, the vortex most likely sustained the MCS over SWA through moisture convergence and lifting of unstable airmasses. It gives rise to the assumption that such vortices are a crucial element of MCS dynamics over SWA.

Finally, a rainfall-type based performance evaluation of the widely used space-borne precipitation product *Integrated Multisatellite Retrievals for Global Precipitation Measurement* (IMERG) is conducted by comparing it against a set of high-resolution rain gauges specifically established for DACCIWA. Rainfall on a monthly scale is well captured by IMERG, but its skill decreases gradually towards sub-daily time scales. While the majority of subdaily rainfall events is detected, IMERG rainfall is partly composed by error compensation tendencies between different rainfall types. Specifically, weak and short rainfall events are almost exclusively overestimated, whereas the intensity of strong rainfall events, such as overpassing MCSs, are largely underestimated. Furthermore, a relatively high number of false alarms are identified, which accounts for around a fourth of total IMERG rainfall. Further inspection of satellite-based information of cloud-top properties revealed a high susceptibility to false alarms and general overestimation tendencies due to the presence of thin ice clouds, while rainfall from purely liquid clouds, i.e. warm rain, is frequently missed by IMERG.

The present work contributes to a more detailed understanding of the different nature of rainfall types over SWA and of the environmental factors that lead to them. This has not yet been performed on a regional scale for SWA and can be of high relevance for numerical weather prediction over the region on synoptic time scales. Specifically the importance of low-tropospheric vortices for the development of extreme rainfall events, which has never been documented nor investigated in this region. Furthermore, the evaluation of a state-of-the-art space-borne rainfall product has identified potentially region-specific strengths and deficiencies that may serve as a reference for future rainfall studies with this product over SWA.

Contents

1. Introduction

Southern West Africa (SWA) roughly comprises the humid region over West Africa south of 9°N and is bounded to the north by the semi-arid Soudan (9–12°N) and the Sahelian regions (12–18°N). Also termed the Guinea Coast region, SWA belongs to the densest populated areas on earth and also to the regions with the fastest growth in terms of population, urbanisation and industrialisation (UN; 2014; Awumbila; 2017). Sustaining economic growth and thus the improvement of life standard and education is expected to impose a substantial demographic challenge in the next several decades to come (UN; 2015). Many of the challenges are related to sufficient energy, drinking water and food supply. Especially the latter is heavily dependent on rainfall due to the prevalence of smallholder farming and rain-fed agriculture in West Africa, where delayed onsets of seasonal rainfall, flash floods, larger-scale seasonal inundations and longer-term droughts can have large socio-economic impacts.

The climate of SWA and West Africa in general is closely linked to the West African Monsoon (WAM) circulation, apart from the Indian and East Asian monsoon one of three major monsoon systems on earth. Exhibiting a pronounced spatiotemporal variability (Diatta and Fink; 2014), the WAM has exposed the strong vulnerability of the population to changes in the rainfall characteristics on interannual to interdecadal time scales. Particularly the Sahelian drought that commenced by the end of the 1960s and peaked in the early to mid-1980s gained substantial medial attention and has led to a long history of comprehensive studies addressing this issue (e.g. Lamb and Peppler; 1992; Nicholson et al.; 1998; L'hote et al.; 2002; Lebel and Ali; 2009; Nicholson et al.; 2012). Nicholson (2005) showed that rainfall during this dry period reached just 60% of the magnitude compared to the 1950s and 1960s, which are considered as a wetter-than-normal period. There has been some debate whether the recent decades have left the dry period (e.g. Elagib and Elhag; 2011; Sanogo et al.; 2015). That is not least due to the occurrence of a series of wet monsoon seasons in the last decade, one of which was the season of 2007 that affected almost the entire sub-Saharan belt from Senegal to Kenya and an overall 1.5 million people due to floods and inundations (WHO; 2007; Paeth et al.; 2011). On a global scale, a number of studies on multi-decadal global trends in a warming world have emphasised a changing character of rainfall in recent decades. Specifically the frequency and intensity of extreme precipitation have largely increased, even in regions with decreasing annual rainfall totals (e.g. Easterling et al.; 2000; Alexander et al.; 2006; Trenberth et al.; 2007; Donat et al.; 2013). However, West Africa is poorly sampled in these works, largely as a consequence of data paucity, which is a general problem in the region (e.g. Panthou et al.; 2014).

Understanding these multi-timescale rainfall variabilities requires an understanding of the dynamics of the West African monsoon (WAM) and their implications to rainfall. Our current knowledge of the WAM and rain-bearing cloud systems is based on early eye observation as well as a series of extensive field projects over different regions in West Africa. As one of the first studies, the pioneering work of Hamilton et al. (1945) about the meteorology of Nigeria documented the existence of so-called *disturbance lines* as spatially extended convective storms and further defined the "four weather zones" for West Africa that outlined basic dynamic components of vertical structure of the WAM. Ground-breaking for West African meteorology was the major international field project *Global Atmospheric research Program Atlantic Tropical Experiment* (GATE, Kuettner and Parker; 1976; Polavarapu and Austin; 1979) in 1974 held in the eastern tropical Atlantic, which drafted the basic structure and physical mechanisms of the disturbance lines - today known as *squall lines* (Houze and Betts; 1981). They were later substantiated by results from the *Convection Profonde Tropicale 1981* campaign in the West African Soudan region (COPT81, Sommeria and Testud; 1984). Furthermore, through GATE, the occurrence of *mesoscale convective systems* (MCSs), the generic term for spatially extended, highly organised convection like squall lines (Glickman and Zenk; 2000), were associated with the existence of wave disturbances propagating along a midlevel easterly jetstream (e.g. Payne and McGarry; 1977; Fortune; 1980), commonly termed as African easterly waves (AEWs, Burpee; 1974; Reed et al.; 1977) and African easterly jet (AEJ, e.g. Burpee; 1972), respectively. Based on these findings and motivated, among other things, by the large socio-economic crisis of the 1980s in the Sahel, the two scientific programmes *JET2000* (Thorncroft et al.; 2003) and the *African Monsoon Multidisciplinary Analysis* (Redelsperger et al.; 2006; Lebel et al.; 2010) realised a multi-spatiotemporal scale investigation of the WAM and its components aiming to improve the skill of general circulation models (GCMs), which have been known to poorly represent rainfall on a diurnal and interannual timescale. Specifically, the role of diurnal as well as seasonal fluctuations in the magnitude of the AEJ, the so-called Saharan heat low (SHL) and turbulence in the convective boundary layer associated with the SHL were found to be decisive factors for the onset of seasonal rainfall and the formation of MCSs in the Sahel through controlling the meridional and vertical moisture transport (e.g. Parker et al.; 2005a; Flamant et al.; 2007; Lavaysse et al.; 2009). Together with advancements in satellite meteorology, it is today widely accepted that MCSs are the single most important rain-bearing systems for the Soudano-Sahelian region, whose contribution to total rainfall can be as high as 90% (Mathon and Laurent; 2001; Mathon et al.; 2002; Fink et al.; 2006; Laing et al.; 2008).

As much as has been learned about the atmospheric dynamics and rainfall characteristics over the Soudano-Sahelian region, less is known for the denser populated SWA. Difficulties in short-term rainfall forecasts in numerical weather models (Vogel et al.; 2018) as well as long-term rainfall projections for SWA in global climate models (Christensen et al.; 2013) are arguably linked in part to a misrepresentation of the widespread low- to midlevel cloudiness (Knippertz et al.; 2011; Hannak et al.; 2017) owing to the moister environment over SWA, which can alter the diurnal cycle of convection (Schuster et al.; 2013). Building on the legacy of AMMA and to extend the perspective of the WAM for the scientifically underrepresented SWA, the *Dynamics-*

Aerosol-Chemistry-Cloud-Interactions in West Africa (DACCIWA) project from 2013 to 2018 (Knippertz et al.; 2015; Flamant et al.; 2018) investigated the process and feedback chain from surface emissions (burning and traffic, for instance) to aerosols, clouds, precipitation, radiation and ultimately the regional WAM circulation. The present work is part of the DACCIWA project within the framework of work package *WP6: Precipitative processes*, which, among other things, aimed to evaluate the composition of rainfall systems that contribute to regional rainfall, and to provide rainfall measurements from a set of new high-resolution rain gauges in order to support the validations of GCMs as well as spaceborne precipitation measurements.

A long-term monitoring of the climate variable "rainfall" from space is of particular importance for West Africa due to the gradual degradation of ground-based observational instrumentations (Flamant et al.; 2018). Thus, this becomes crucial for the identification of interannual rainfall variability over the region. The emergence of geostationary satellites in the early 1980s, which now provide images of clouds on several spectral channels, and further technological progress in the rainfall retrieval from radars and microwave imagers culminated in the launch of the American-Japanese joint project *Tropical Rainfall Measuring Mission* (TRMM, 1998–2014) (Kummerow et al.; 1998) and the successor *Global Precipitation Measurement* (GPM) in 2014 (Hou et al.; 2014), providing global rainfall data of unprecedented spatiotemporal resolution. However, for TRMM, although results from Nicholson et al. (2003) have suggested a good agreement of monthly-to-seasonal rainfall estimates over West Africa, other studies have noticed biases depending on different cloud characteristics from different rainfall types (e.g. Tompkins and Adebiyi; 2012; Petković and Kummerow; 2017). How the more advanced GPM satellites perform over the region, even on shorter time scales than on a monthly basis, has yet to be evaluated. However, the aforementioned rain gauge network within DACCIWA provides an ideal test bed to realise this.

2. Aims and structure of the work

With the present work, three questions are addressed. These are:

1. Which rainfall types constitute the total rainfall over SWA, what are their lifetime characteristics and under which conditions do they typically develop from a climatological standpoint?

2. What environmental factors specifically control the development of MCSs over SWA?

3. How do state-of-the-art spaceborne rainfall measurements perform over SWA under the presence of different clouds and rainfall systems?

Regarding the first point, the moist environment over SWA implies a variety of types apart from MCSs, the most important convective system for the semi-arid Soudano-Sahelian region (see chapter 1. However, their relative importance has never been quantified for SWA on a regional level. This is mainly realised by exploiting data from the aforementioned TRMM project, whose satellite carried, among other things, a precipitation radar during the 16-year mission. Ground-based observations with rain gauges would have required both a high-temporal resolution as well as a widespread and dense network to be representative for SWA. A facility of this size and ability does not exist over the region. How the analysis is executed is described in detail in the beginning of chapter 4.

For the second point, the development and atmospheric conditions around a series of intense convective systems involving a long-lived MCS are investigated, which caused one of the highest ever recorded daily rainfall amounts over SWA on 12 June 2016 during the period of the DAC-CIWA field campaign. An exceptional aspect of this case was the fact that the MCS traversed the different environments of the semi-arid Savannah zone and the humid SWA. Thus, it enables an evaluation of how MCSs evolve in such opposing regimes, complementing earlier studies on MCSs performed in the Soudano-Sahelian region (e.g. Schrage et al.; 2006). A combination of DACCIWA field data, satellite cloud and rainfall measurements as well as global reanalysis data of atmospheric variables are synthesised for this case study. Again, a description of data and methodology precedes the analysis in chapter 5.

Finally, in large part due to the high spatiotemporal resolution of its products, the aforementioned GPM mission that builds on the success of the TRMM project (Houze et al.; 2015) is expected to become one of the widely used spaceborne precipitation datasets for precipitation studies in the tropics and sub-tropics, and in particular West Africa. As such, the existence of a

set of minutely recording rain gauges specifically established for the DACCIWA project allows a direct comparison of GPM rainfall estimates from space and the surface-based rainfall at sub-daily time scales, which further allows to evaluate GPM based on different rainfall types. Complementary to this, a satellite-based cloud dataset is implemented into the analysis in order to relate the behaviour of the rainfall retrieval of GPM to certain cloud characteristics of the rainfall types (chapter 6.

Before the analyses are presented, chapter 3 provides an overview of the physical background of convection and a description of the WAM, in which rainfall systems over SWA are embedded. The latter also introduces key mechanisms for the occurrence of convection over the region as well as earlier studies that have dealt specifically with rainfall characteristics over SWA.

3. Theory and fundamentals

Although the initiation, modulation and life cycle of convective systems may differ distinctively over West Africa compared to other regions in the world, as seen in this chapter, the physical principles are the same. Therefore, it is feasible to present the physical understanding of convection and types of convective systems first, before a description of the West African Monsoon, the dominating atmospheric circulation over West Africa in which convective processes are embedded, is given. A major part of the current understanding of convective systems in general and West African meteorology is based on the two major field experiments GATE and AMMA. Key findings have been synthesised in books, such as *Mesoscale Meteorology in Midlatitudes* by Markowski and Richardson (2011) and *Mesoscale Meteorology in Midlatitudes* by Parker (2017a). The present chapter has been inspired in large parts by both books. Direct references will be given particularly at used images.

3.1 Requisites for convection

3.1.1 Initiation

The formation and further development of deep convection is commonly forecasted and analysed using a thermodynamical diagram such as the Skew-T-log-p diagram as shown in Figure 3.1. This diagram shows the atmospheric state in the (approximately) vertical column at a point on earth based on the profiles of the ambient (virtual) temperature (right black curve) and the dewpoint (left black curve) obtained by radiosonde profiling. The potential for convective processes with respect to the atmospheric state is estimated by the application of the so-called parcel theory, which describes an idealised rising air parcel (green curve) while neglecting interaction with the environment, such as mixing of air through entrainment and detrainment. Therefore, in absence of thermodynamic phase changes like condensation or freezing, the air parcel follows the curves of constant potential temperature (isentropes or dry adiabats) while moving in the vertical. The dry adiabats are represented as solid and slightly curved grey lines skewed towards the left. Once the air within the parcel is saturated, which occurs due to adiabatic cooling in the case of a lifted air parcel from the surface, condensation sets in. This point is identified by searching for the intersection between the dry adiabat of the air parcel (bottom section of the green curve) and the line of constant mixing ratio (dotted grey lines skewed to the right) beginning from the surface value of the dewpoint profile. In case of a forced ascent of an air parcel, this intersection point

is termed lifting condensation level (LCL). Upon further ascent, the air parcel cools at a slower rate due to the release of latent heat (curved section of the green line) and now follows the moist adiabats (dashed grey lines), which asymptotically approximates the dry adiabats at higher levels because of the gradual drying of the air parcel.
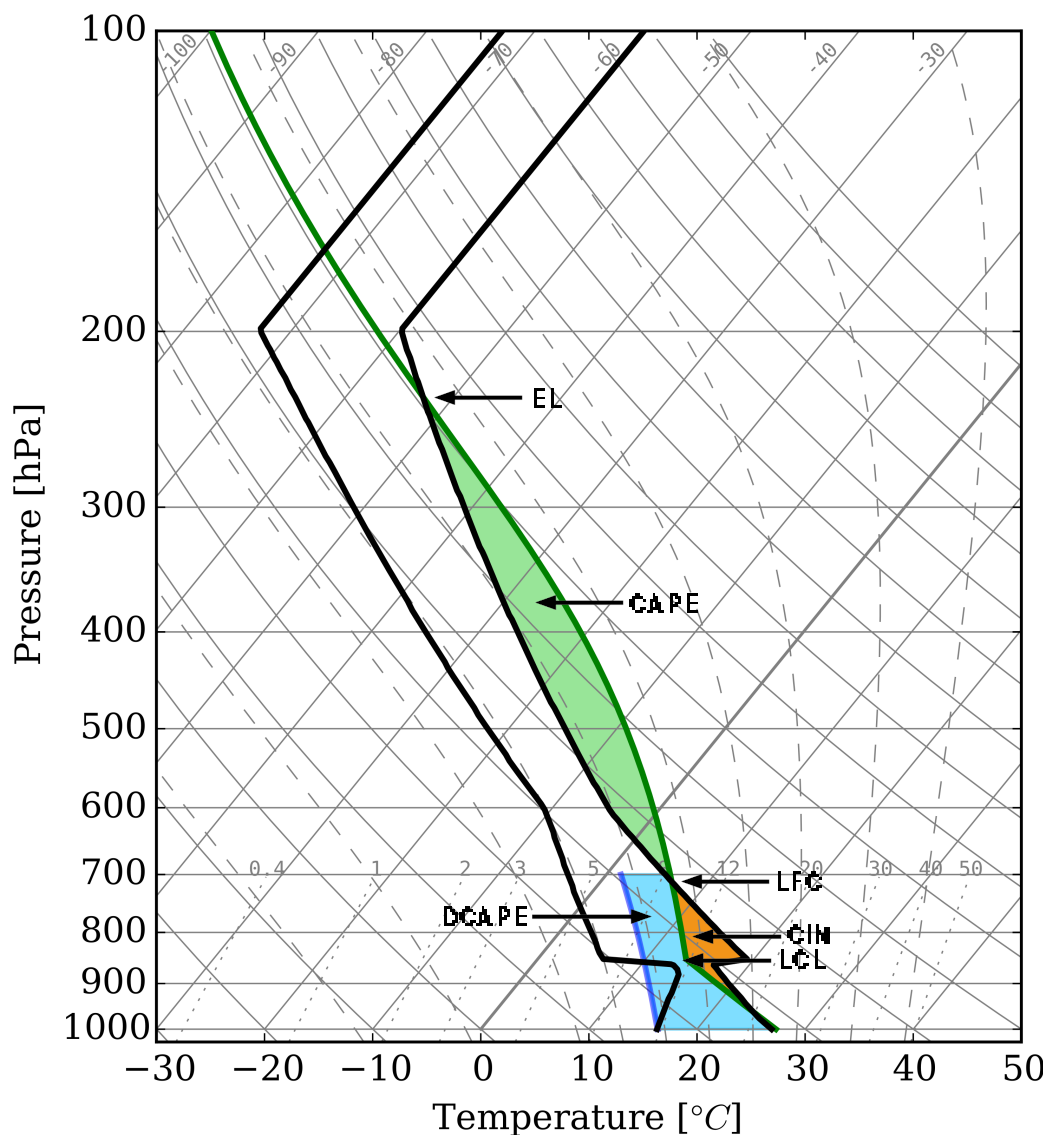
Figure 3.1: Idealised vertical profiles of (virtual) temperature (right black curve) and dewpoint (left black curve) as well as the path of an idealised ascending (green curve) air parcel from the surface following the parcel theory. The blue curve is a moist-adiabatically descending air parcel to illustrate DCAPE (blue shaded area, see section 3.1.2). The green and orange shaded areas denote CAPE and CIN, respectively. Other significant points along the parcel path are given as well. The temperature profile is an amended version of the profile defined in Weisman and Klemp (1982).

The upward acceleration of an air parcel can be approximated by the buoyancy force B. Neglecting the effects of hydrometeors such as rain drops, which acts as a drag force, B can be

approximated as:

$$B \approx g \left(\frac{T_{v_p} - T_{v_{env}}}{T_{v_{env}}} \right) \tag{3.1}$$

where g is the gravitational acceleration, T_{v_p} and $T_{v_{env}}$ are the virtual temperatures of the air parcel and the environment, respectively. The virtual temperature, defined as $T_v \approx T(1 + 0.61q)$ with q as specific humidity (ratio between water vapour mass and mass of humid air in a unit volume), accounts for the lowering of air density due to the water vapour included in the air. It is the temperature a completely dry air parcel would attain, if it had the same (lower) density than water vapour-laden air. Thus, water vapour increases buoyancy. An integrated measure of the buoyancy force in a vertical column is the convective available potential energy defined as:

$$\text{CAPE} = \int_{\text{LFC}}^{\text{EL}} B \, dz \quad \approx \quad g \int_{\text{LFC}}^{\text{EL}} \left(\frac{T_{v_p} - T_{v_{env}}}{T_{v_{env}}} \right) dz \tag{3.2}$$

where the integrands LFC and EL denote the "level of free convection" and "equilibrium level". The LFC is the intersection point between the temperature profile of the air parcel and the ambient temperature profile, from where the air parcel is warmer than the environment. EL, in turn, is where the air parcel becomes colder than the environment again and commonly designates the estimated top of the convective cloud. In Figure 3.1, CAPE is estimated by the green-shaded area that is enclosed by the ambient virtual temperature profile and the ascending air parcel following the moist adiabats as a consequence of latent heating. CAPE is related to the kinetic energy of an air parcel that is obtained by the excess of buoyancy over the entire vertical column and is a necessary but insufficient requirement for deep convection.

In a well-mixed, neutrally stratified convective boundary layer, where the ambient near-surface temperature profile closely follows dry adiabats, the LFC is often equal to the LCL. Particularly if the surface is strongly heated, convective systems can be initiated by lifting air parcels through turbulence or along sloped terrain to the LCL/LFC, from where is rises freely without inhibition, provided a strong inversion aloft is absent. However, in many cases, convective inhibition (CIN) is present, which suppresses a premature development of convective systems and which is often necessary for the occurrence of strong convective systems. CIN is basically defined as the integrated potential energy of negative buoyancy in the lower troposphere, which is calculated from the surface to the LFC:

$$\text{CIN} = - \int_0^{\text{LFC}} B \, dz \quad \approx \quad -g \int_0^{\text{LFC}} \left(\frac{T_{v_p} - T_{v_{env}}}{T_{v_{env}}} \right) dz \tag{3.3}$$

In Fig. 3.1, the area of CIN is denoted by the orange area.

As mentioned, CAPE is an insufficient condition for the initiation of convective systems and requires the consideration of CIN as well. Both can be modulated significantly in space and time, e.g. by diurnal heating through insolation. However, while CAPE is usually present over West Africa owing in particular to the warm lower troposphere, it is often the estimation of the strength and the timing of the break-down of CIN that imposes a general challenge in forecasting

potential initiation regions. Figure 3.2 sketches three mechanisms of how CIN can be reduced or removed if a temperature inversion is capping the boundary layer underneath (Markowski and Richardson; 2011). The first mechanism involves large-scale lifting of the tropospheric column (Figure 3.2a). As indicated by the blue section of the ambient temperature profile, the inversion is shifted to higher levels, which leads to an almost unimpeded moist-adiabatic ascent of the air parcel (dashed line) once LFC is reached. The second possibility refers to a moistening of the boundary layer, which shifts the dewpoint profile closer to that of the environmental temperature (Figure 3.2b). As a consequence, the LFC is reached earlier at a lower altitude and enables the parcel to stay warmer than the inversion layer (blue dashed line). Finally, CIN can be overcome by warming the boundary layer, where the inversion effectively vanishes and which creates the well-mixed, convective boundary layer mentioned above.
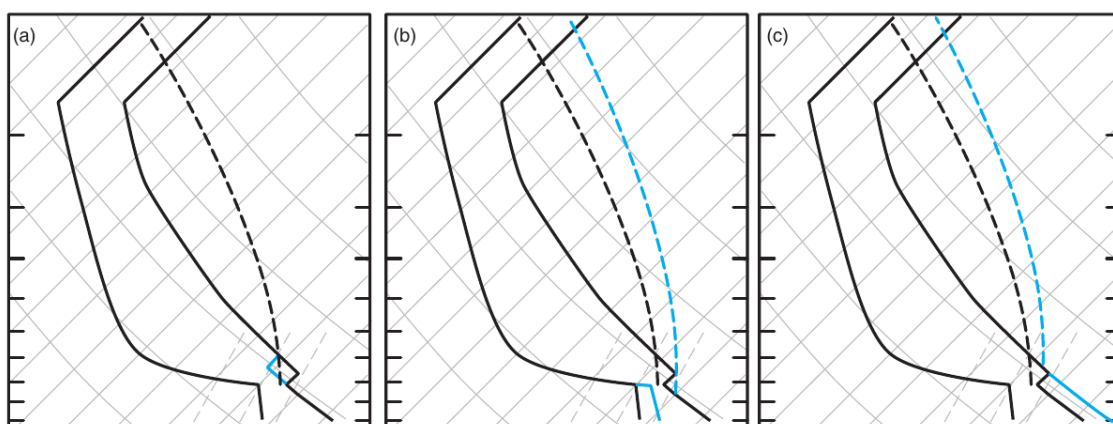
Figure 3.2: Three schematic mechanisms leading to a reduction of CIN: (a) large-scale rising motion, (b) low-level moistening (e.g., moisture advection), and (c) low-level warming (e.g., insolation). In (a)–(c), the isotherms and isentropes are solid gray lines, the constant mixing ratio lines are gray dashed lines, the sounding and trajectory taken by an air parcel lifted from the surface are solid and dashed black curves, respectively, and the modified sounding and parcel trajectory are blue solid and dashed curves, respectively. Note that (b) and (c) are also accompanied by increases in CAPE. From Markowski and Richardson (2011), Chapter 7, Figure 7.9, Copyright (c) 2010, John Wiley & Sons, Ltd.

Particularly the second and third mechanisms in Figure 3.2 are of general importance over SWA. As will be seen in section 3.3, SWA is largely influenced by the southwesterly monsoon flow that constantly supplies moisture to the region. However, especially in such an environment, processes to locally accumulate moisture may be of larger importance than the mere availability itself. Therefore, moisture convergence is commonly used as a forecasting tool to locate favourable regions for convective initiation (Banacos and Schultz; 2005; Birch et al.; 2014). Moisture convergence is written as

$$-\nabla \cdot (q\boldsymbol{v}_h) = -q\nabla \cdot \boldsymbol{v}_h - \boldsymbol{v}_h \cdot \nabla q \qquad (3.4)$$

where $\boldsymbol{v}_h$ refers to the horizontal wind field and the right-hand side of the equation to the contribution of moisture convergence through moisture advection and the convergence of the horizontal

wind field within a given moisture distribution. The importance of moisture convergence, however, lies not only in the increase of q at the surface but the increase of moisture in the entire boundary layer. By combining the local change of specific humidity as well as the formulation for the incompressible mass continuity linked with q, respectively:

$$\frac{\partial q}{\partial t} = -\boldsymbol{v}_h \cdot \nabla q - C + E, \tag{3.5}$$

$$q\frac{\partial w}{\partial z} = -q\nabla \cdot \boldsymbol{v}_h \tag{3.6}$$

it becomes clear that only the advection term of the moisture convergence modulates the local q-field, aside from the moisture sink and sources C and E through condensation and evaporation, respectively, while the convergence of the wind field is fully balanced by the vertical motion term. Therefore, the latter provides a deeper moist boundary layer. The implication of this is that a more humid boundary layer decreases the entrainment of dry air into an air parcel ascending to its LCL and LFC, which can be of particular importance in the dry regions of West Africa towards the Sahel. As mentioned, the parcel theory neglects such exchange processes with the environment. In reality, strong entrainment can be an inhibiting factor for the establishment of a stable updraught within a growing convective cloud. Since the majority of water vapour is found in the lower troposphere (Holton and Hakim; 2012), a simple measure for its total availability in an atmospheric column is provided by the precipitable water (PW). According to the American Meteorological Society (AMS) glossary (Glickman and Zenk; 2000), PW bounded in a layer between p_1 and p_2 is given by:

$$\text{PW} = \frac{1}{\rho g} \int_{p_1}^{p_2} r(p)\, dp \tag{3.7}$$

where r is the mixing ratio, i.e. the ratio between the mass of the water vapour and the mass of dry air in a unit volume, ρ the density of water. The unit is mm. Over West Africa, PW, among other things, is used to estimate the depth of the northward penetration of the moist southwesterly monsoon flow, marked by the so-called intertropical front or discontinuity (ITF/ITD, see section 3.3).

3.1.2 Vertical wind shear and organisation of convection

Once a convective cloud has formed, its further evolution still depends on some parameters discussed above, such as the distribution of CAPE and moisture. However, vertical wind shear is considered as a major factor in the development of certain storm types. In operational forecasting, the term "vertical wind shear" is commonly used for the vector difference between two layers (unit in ms^{-1}), specifically between 600 and 925 hPa over West Africa (e.g. Laing et al.; 2008). While 600 hPa is roughly the height of the African easterly jet (AEJ), the 925 hPa is usually located just above the planetary boundary layer. A description of the WAM elements will be provided in section 3.3. A schematic spectrum of the storm types as a function of the magnitude of the vertical wind shear is presented in Figure 3.3. Single convective cells are typical for

low-sheared environments, while multi-cellular convection or even so-called supercells are found under stronger-sheared conditions. It shall be noted that the formation of supercells occur under significant influence of the Coriolis force. In low-latitude regions such as SWA, the Coriolis parameter (e.g. at 10°N) is smaller by a factor of four compared to regions in midlatitudes at 45°N. Therefore, supercells occur far less frequent over West Africa in general, if at all (Lafore et al.; 2017c), and are not discussed in detail here. However, vortices in the wind field are still observed over West Africa (section 3.3) and is of particular importance in chapter 5.
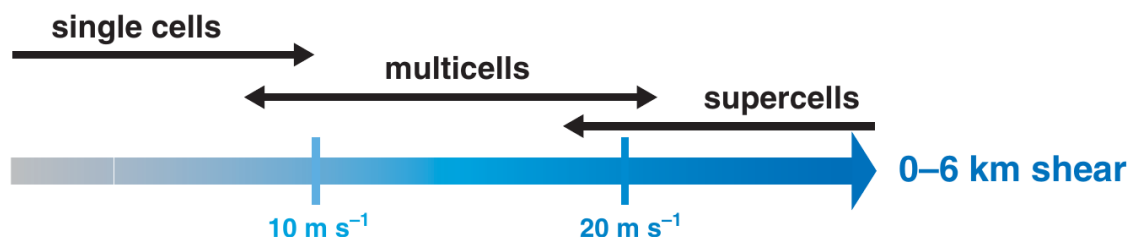

Figure 3.3: Schematic spectrum of storm types as a function of (0–6 km) vertical wind shear. From Markowski and Richardson (2011), Chapter 8, Figure 8.5, Copyright (c) 2010, John Wiley & Sons, Ltd.

The role of vertical wind shear for convective elements is initially focused on its influence on the tilting of the convective updraught. The life cycle of a single-cell convective system under low-sheared conditions is shown Figure 3.4. Once the LFC is reached, the convective cloud grows upwards under the consumption of CAPE during the "cumulus stage" (Figure 3.4a). Upon further growth, the formation of rain-sized hydrometeors begins. Its efficiency is particularly high in the glaciated part of the convective system, where ice particles increase in size by virtue of water vapour deposition. Once heavy enough, the hydrometeors fall through large parts of the updraught in the absence of strong wind shear. This designates the "mature stage" of a single cell (Figure 3.4b). While forming an anvil at the height of the tropopause, a part of the precipitation evaporates in the presence of dry mid- and low levels, which manifests in a downdraught spreading horizontally as a density current once the surface is reached. Once it begins to cut the supply of unstable air for the updraught, the dissipation stage commences (Figure 3.4c). Thus, a low-sheared environment promotes short-lived rainfall events, where a typical lifetime of such single-cell convection lies in the order of 30–60 minutes.

On a further note, the strength of the downdraught is related to the amount of momentum and negative buoyancy that is available for the density current, also termed "cold pool". As will be seen later, the cold pool is a fundamental element for the maintenance of highly organised convective systems. Since midlevel dryness plays a major role through evaporation of rainfall, a measure called downdraught CAPE (DCAPE) is often utilised to estimate the potential strength of the downdraught and coldpool. DCAPE is similarly formulated as CAPE (equation 3.2), but quantifies the potential energy due to negative buoyancy from a defined base height downward to the surface. In Figure 3.1, the 700 hPa-based DCAPE is denoted as a blue area.

Stronger vertical wind shear increases the probability of multi-cellular convection. While ver-
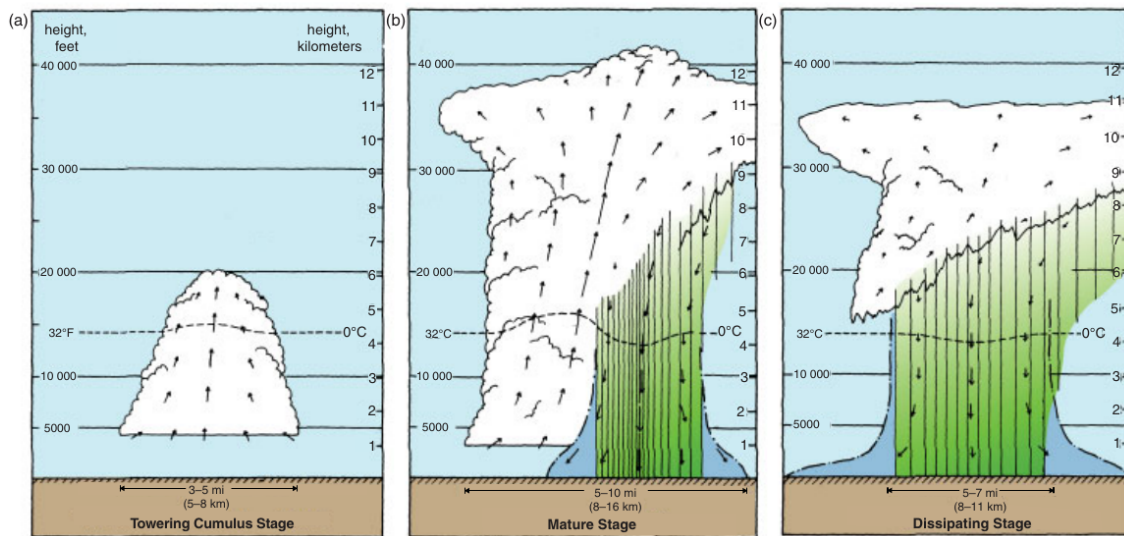
Figure 3.4: Three development stages of a single cell: (a) towering cumulus stage, (b) mature stage and (c) dissipating stage. The arrows denote the vertical motions. The region of precipitation is denoted in green, while the blue shade indicate density current through evaporative processes. From Markowski and Richardson (2011), Chapter 8, Figure 8.8, Copyright (c) 2010, John Wiley & Sons, Ltd.

tical wind shear increases the tilt of the updraught, leading to a more distinct separation from the downdraught region, its importance for convective organisation is rather reflected in a more efficient lifting of airmasses on the downshear side of a coldpool. This ideally leads to a succession of newly generated convective cells, each being promoted by the cold pool of the previous system. Such a situation is illustrated in Figure 3.5, showing convective cells in different stages of their respective lifetimes. The arrow under the "S" on the left side of the figure denotes the direction of the shear vector, i.e. the downshear side. Here, a typical wind field in this case, considering the left and right side of the image as west and east, respectively, would be stronger westerlies with height, as denoted by the wind profile on the far left side (stacked black arrows). The enhanced promotion of new convection on the downshear side compared to the upshear side of the coldpool can be understood by considering the interaction between coldpool and the ambient shear through their generated horizontal vortices (white and purple circular arrows). The coldpool on the downshear side produces horizontal vorticity that is of opposite direction (here anti-clockwise) to the imprinted clockwise vorticity field by the wind shear, which leads to a net flux of horizontal vorticity of zero. Thus, the cancelling effect of the vortices lead to an enhanced upward directed lifting of buoyant airmasses at front of the undercutting coldpool, whereas the equally directed vortices on the upshear side would result in a strongly slanted lifting with a decreased chance for air parcels to reach the LCL/LFC.

Although strong wind shear is considered to be favourable for the longevity of convection by virtue of a separated up- and downdraught, it is also apparent that a too strongly tilted convective cloud exposes itself to stronger entrainment and thus weakens its further development. In fact, as presented later, it is also believed that strong wind shear in conjunction with coldpool interactions
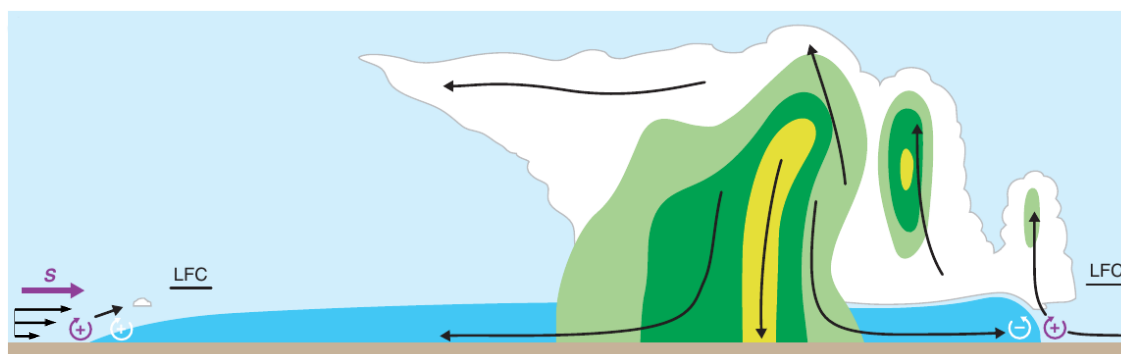
Figure 3.5: Mechanism of lifting by the coldpool on the upshear and downshear side in a moderate-shear environment. The shear is westerly (see purple shear vector "S" and wind profile in the bottom left corner). Rain and hail are schematically indicated by the green and yellow shading, the convective clouds are white. Evaporatively cooled outflow is shaded dark blue. Some select storm-relative streamlines are shown as black arrows. The LFC is also indicated. The sense of the horizontal vorticity induced by the coldpool is indicated with white circular arrows, while the purple circular arrows denote the horizontal vorticity from the ambient vertical wind shear. From Markowski and Richardson (2011), Chapter 8, Figure 8.12b, Copyright (c) 2010, John Wiley & Sons, Ltd.

rather promotes a more upright updraught that opposes the tilting.

3.2 Mesoscale convective systems

As mentioned in the introduction, a mesoscale convective system (MCS) is the overarching term for highly organised convective clusters that underwent upscale growth with a horizontal scale in order of 100 km in at least one direction (Glickman and Zenk; 2000). As for the relatively dry Soudan and Sahelian region of West Africa, they represent the most important source of rainfall during the peak monsoon season in July and August (e.g. Mathon and Laurent; 2001; Mathon et al.; 2002; Fink et al.; 2006). A prominent sub-category of MCSs are so-called squall lines, which are fast-moving and self-sustaining MCSs typically featuring a distinct convective line. Because of their relatively high fraction among occurring MCSs in the Sahel (Fink and Reiner; 2003), the structure and proposed maintenance of squall lines are presented in the following.

3.2.1 Structure of an idealised squall line

A widely accepted conceptual model of a mature squall line from Houze Jr et al. (1989) is illustrated in Figure 3.6. This model represents the leading-convective and trailing-stratiform type of squall lines, where the shear vector is directed orthogonally to the idealised convective line. Other types of squall lines include the so-called leading-stratiform as well as parallel-stratiform squall-lines, which can occur under different directional orientations of the wind shear in the vertical. In the following, only the trailing-stratiform type is discussed. It can be roughly partitioned into three parts (Lafore et al.; 2017c): (1) the leading convective line, represented as dark-shaded areas denoting high values of radar rainfall reflectivity, (2) the trailing and widespread stratiform region

featuring a slanted ascending front-to-rear flow, and (3) the region underneath the stratiform region including a descending rear inflow (Smull and Houze Jr; 1987) and the undercutting coldpool, the latter of which is induced by the convective downdraught. The translation of a squall line can be understood by the superposition of the motion of the cloud cluster steered by the ambient mean wind field as well as the successive generation of new convective cells in the convective region. The latter basically follows the principle of the formation of multi-cellular convection described in the previous section. Thus, the arrows presented in Figure 3.6 denote the motion relative to the squall line with the downshear side to the right.
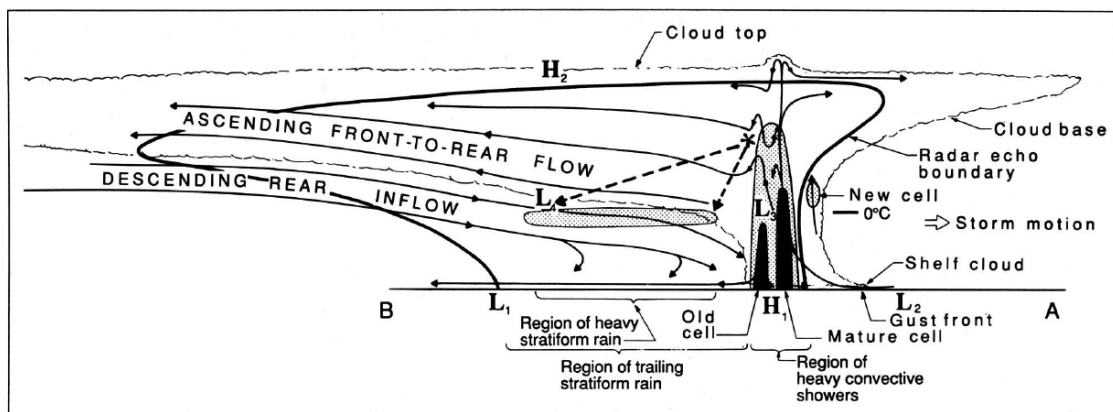
Figure 3.6: Conceptual model of a squall line with a trailing stratiform area viewed in a vertical cross section oriented perpendicular to the convective line (i.e. parallel to its motion). More details in the text. From Houze Jr et al. (1989), Figure 1, Copyright (c) American Meteorological Society.

In principle, a squall line is penetrated by airmasses from front to rear. As the air parcel is lifted by the leading edge of the coldpool to its LFC, strong latent heating sets in and manifests in pronounced upward motion within the convective line and heavy convective precipitation. The mid-level low-pressure perturbation ("L_3") is largely a result of strong positive buoyancy within the updraught. Because of the storm motion, the air parcels leave the convective updraught and release the remaining latent heat in the trailing stratiform region, which is reflected by a slow, slantwise ascent as well as the formation of another midlevel region of low pressure ("L_4"). The region underneath is typically accompanied by weak-to-moderate stratiform rainfall, which can last several hours (e.g. Fink et al.; 2006). The rear inflow descends parallel to the slanted anvil of the trailing stratiform region and is induced by the aforementioned mesoscale low pressure systems L_3 and L_4. Since both L_3 and L_4 are largely of hydrostatic origin, i.e. a consequence of vertical buoyancy gradients due to latent heating, the rear inflow increases in magnitude with higher CAPE, which can then become a "rear inflow jet". The implication of the rear inflow over West Africa is that it is often an accelerated branch of the AEJ, which in turn is partly fed by the return flow of the dry convection region over the Saharan heat low (SHL, see section 3.3). Thus, the rear inflow can become very dry and enhances cooling through more efficient evaporation of the stratiform rainfall, which can support the convective coldpool as well as the maintenance of the squall line. Again, DCAPE can be used to estimate the coldpool strength. Squall line

maintenance is briefly discussed in the following subsection.

3.2.2   Maintenance of a squall line

A popular but also debated mechanism for squall line maintenance is known as the "RKW theory" presented in Rotunno et al. (1988), named after Richard Rotunno, Joseph B. Klemp and Morris L. Weisman. The RKW theory postulates a relationship between longevity of a squall line and the updraught tilt of systems generated along the gust front of the coldpool as a function of the strength of both coldpool and ambient vertical wind shear. As discussed for multi-cellular convection in Figure 3.5, an enhanced upright updraught is reached when the net flux of horizontal vorticity, i.e. a cancelling of the vortices produced by the shear and coldpool, is zero. The more upright updraught decreases the influence of entrainment of dry air into the cloud. According to the RKW theory, a direct upward lifting over the depth of the troposphere is reached if the velocity of the coldpool c and the integrated tropospheric vertical wind shear $\Delta u + \Delta u_{deep}$ is equal, where Δu and Δu_{deep} are the low-level shear and the shear above the depth of the coldpool, respectively. Figure 3.7 presents four scenarios of different configurations for c and Δu, Δu_{deep} and the resulting upward motion. Given a stronger coldpool than low-level vertical wind shear with no upper-level shear (Figure 3.7a), the updraught will be tilted to the downshear side above the depth of the coldpool because of an overall overcompensation by the coldpool induced circulation. A balanced state between the coldpool and $\Delta u + \Delta u_{deep}$ (Figure 3.7b) results in a more upright but not entirely vertical updraught. While the coldpool overcompensates low-level shear like in the first scenario, the shear above the coldpool prevents a deflection of the updraught to the downshear side. The third case in Figure 3.7c is considered as the ideal scenario by the RKW theory, where the low-level shear balances the coldpool induced circulation to create a vertical updraught that is not further influenced by wind shear aloft. The final scenario in Figure 3.7d depicts the result of the previous case with upper-level windshear, which leads to a downshear deflection under the condition of a equally oriented horizontal vorticity as the coldpool generated one.

As presented in the next section, the second scenario is commonly found over West Africa with the AEJ in the midlevels and the southwesterly monsoon flow in lower levels. Together with relatively dry conditions in the Sahelian region, conducive conditions for squall line formation and maintenance is found. As mentioned earlier in chapter 2, one of the questions that the present work want to address is how such organised convection evolves over SWA, which is a different regime compared to the Sahel in particular due to its much moister environment.

3.3   The West African Monsoon

3.3.1   General structure

The West African Monsoon (WAM) is the dominant atmospheric circulation and the main driver for rainfall over West Africa. Unlike the textbook notion of a monsoon circulation, which is largely based on the climatological structure of the Hadley cell, the WAM is characterised by a complex interplay between low-level flow of different origins, moist and dry convection, and jet
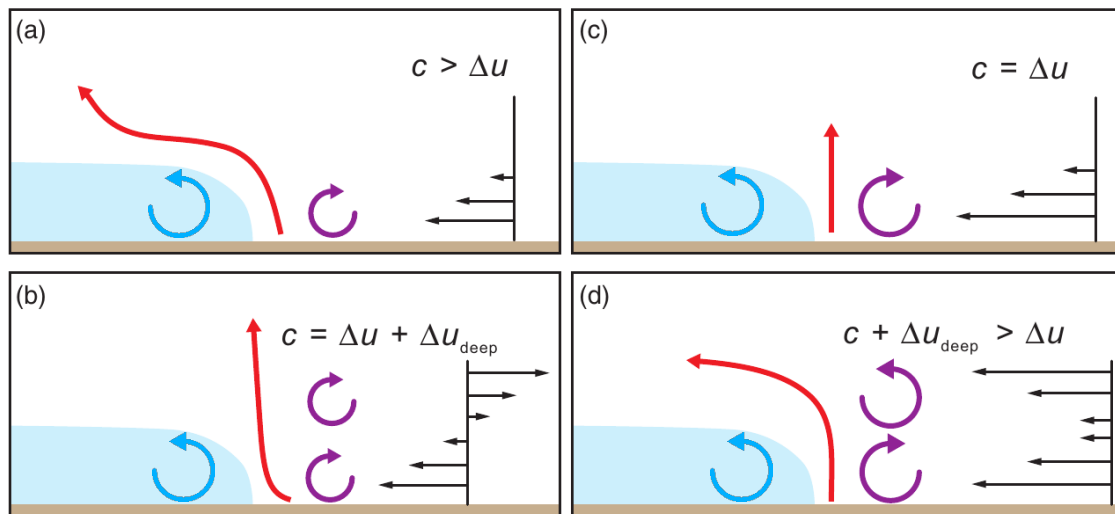
Figure 3.7: The effect on the lifting of air parcels (red arrows) at the front of a coldpool (blue shaded area) for four configurations of deep layer shear (Δu_{deep}) and low-level shear (Δu). The respective vertical wind profiles are shown on the right side of the panels. The sense of horizontal vorticity generated by the coldpool (ambient shear profile) is indicated by purple (blue) circular arrows. From Markowski and Richardson (2011), Chapter 9, amended version of Figure 9.21, Copyright (c) 2010, John Wiley & Sons, Ltd.

streams at different tropospheric levels. However, following the origin of the term "monsoon", i.e. a seasonal change of the main wind direction, the WAM features a distinct seasonality. From a plan perspective, the structure of the WAM during boreal winter (January) and boreal summer (July) is summarised in Figure 3.8. The blue streamlines denote the flow in the lower troposphere. The other components are listed in the legend. During boreal winter (Figure 3.8a), which marks the main dry period during the WAM season, the general low-level circulation is controlled by the high pressure systems over the southern Atlantic, Azores and Libya as well as a zonal but largely unstructured low pressure "channel" due to maximum surface heating extending from central Africa to parts of West Africa. The southerly flow towards the low pressure region is related to the southern Atlantic high pressure system and turns from a southeasterly to a southwesterly flow once it crosses the equator. This southwesterly flow is commonly known as the "monsoon flow", which is the main source of moisture for West Africa. The monsoon flow is countered from the north by northeasterlies, which are termed the "Harmattan". The Harmattan largely originates from Sahelian and Saharan region and is characterised as a dry airmass with low static stability. The zonally oriented convergence region where both monsoon flow and Harmattan meet is called the intertropical discontinuity (ITD). The ITD is marked by a strong gradient in both temperature and dewpoint or PW and often delineates the northern boundary where rainfall events occur. A common misconception is that the ITD and the intertropical convergence zone (ITCZ) are used interchangeably (Nicholson; 2009b). The latter is often used to refer to the region of maximum rainfall, maximum cloudiness or surface wind convergence (Nicholson; 2013). In fact, the region of maximum rainfall, in the case of boreal winter, lies offshore the West African coast over the Gulf of Guinea (dashed blue line), while the ITD is found onshore close to the West African

coastline around 8°N. A closer relationship between surface wind convergence and rainfall max-ima is found over the oceans, where environmental conditions a more homogeneously distributed. Since the ITD stays onshore even during the main dry period of the WAM, the immediate coastal region of SWA remains under the influence of the monsoon flow throughout the year. The green arrow-tagged line between the ITD and the region of maximum rainfall is the African easterly jet (AEJ), commonly found between 600–700 hPa. It is a response to the baroclinicity imposed by the north-south oriented temperature gradient between the hot Sahara and the cooler Atlantic and follows the thermal wind relation as an easterly wind maximum (Thorncroft and Blackburn; 1999).

Towards boreal summer (Figure 3.8b), strong surface heating over the Sahara leads to the establishment of the shallow, thermally induced Saharan heat low (SHL) or West African heat low to make a distinction to its counterpart in the eastern Sahara (Lavaysse et al.; 2009). The increase of the meridional pressure gradient results in a deeper penetration of the monsoon flow into the continent, leading to the moistening of virtually entire SWA. The ITD, which bulges on the eastern flank of the SHL, shifts northward to around 20°N. The region of maximum rainfall is now located between 8–10°N, while the AEJ lies further north around 15°N. The brown arrow-tagged lines found at around 6°N marks the so-called Tropical easterly jet (TEJ) maximised in the upper levels around 200 hPa. Similar to the AEJ, it originates from a north-south oriented temperature gradient, but between the hot Tibetan plateau and the cooler Indian Ocean. The heating of the Tibetan plateau leads to the formation of a strong upper-level anticyclone, where the TEJ is driven on its southern flank. Thus, the TEJ can be regarded as a link between the WAM and the south Asian (or Indian) monsoon circulation. The strength of TEJ has been linked to modulations in the strength of the WAM rainfall, e.g. a stronger TEJ with wet WAM seasons in the Sahel (e.g. Grist and Nicholson; 2001), on an interannual timescale. Finally, the pink-coloured contours denote the presence of so-called African easterly waves (AEW) featuring a southern and a northern branch. AEWs are known to modulate rainfall and rainfall systems on synoptic time scales and are discussed in a later section.

A meridional cross section through the WAM circulation is presented in Figure 3.9. An early and thus more simplified concept was first introduced in the pioneering work by Hamilton et al. (1945) and has remained a basic model for the understanding of the WAM ever since. A major element of this concept involves the definition of four different zones (Zone A–D) along the north-south transect through the WAM (i.e. right to left in Figure 3.9), which is part of the following description. Note that the situation during boreal summer in July is depicted. As already seen in Figure 3.8b, the low-level monsoon flow penetrates West Africa northward up to the ITD, where it overturns and moves back southward at roughly 700 hPa. The ITD also marks the northern border of the so-called monsoon layer (pink shaded area), whose depth is a measure for the thickness of the moist layer of West Africa (Lafore et al.; 2017b). North of the ITD is Zone A, characterised by highest temperatures (black solid curve) and lowest dewpoints (orange curve, typically <14–15°C) and the location of the SHL (see dashed black line). Within the SHL, dry convection, i.e. ascent of buoyant air without condensation due to dryness, takes place and is capped by the descending branch of the WAM circulation aloft (here, the descending branch of the northern Hadley cell).
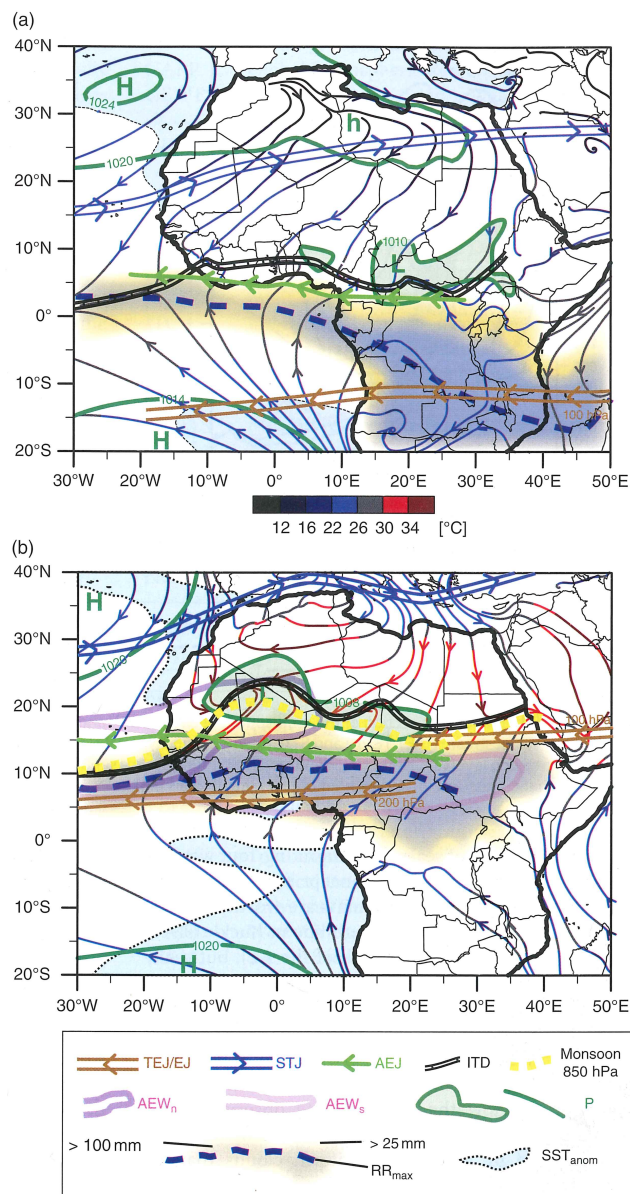
Figure 3.8: Schematic illustration of atmospheric and oceanic features determining the weather and climate of West Africa in a) January and b) July. Shown are the positions of the ITD, the monsoon trough, upper-level air streams (AEJ, TEJ/EJ (Easterly Jet), and STJ), surface winds coloured according to the 2 m air temperature (see colour bar), the tropical rain belt with the maximum axes of rainfall ($RR_{textmax}$), northerly and southerly AEW vortices propagation zones (AEWn and AEWs, respectively), areas with relatively cold sea surface temperatures ($SST_{textanom}$), and example pressure lines marking the Azores ("H"), Libyan ("h") and Saint Helena ("H") Highs and the heat low ("L"). From Parker (2017a), Chapter 1, Figure 1.33, Copyright (c) 2017, John Wiley and Sons Ltd.

As indicated by the streamlines, the divergent region at the top of the SHL partly feeds the AEJ at around 600 hPa. The AEJ is incorporated in Zone B and C. The former is located north of the AEJ core with occasional, but overall rare developments of convective systems because it is capped by dry midlevels. Zone B, in turn, is south of the AEJ core and the region of highest

rainfall amounts (see rainfall distribution in the bottom panel). It also incorporates the main ascending branch of the WAM circulation, which simply reflects the zone of highest convective activity (see grey-shaded clouds). The TEJ core in the upper levels slopes down southwards and is generally found at the southern end of Zone C. Also apparent from Figure 3.8b, the rainfall maximum in Figure 3.9 lies between the axes of the TEJ and AEJ. While the former is believed to act mainly through upper-level divergence and thus enhancing convective activity (e.g. Nicholson and Grist; 2003), the latter is associated with AEWs. The southernmost zone D is characterised by the deepest monsoon layer, indicating the largest availability of moisture in the vertical column. This zone possesses a more maritime character with an overall more stable atmosphere, resulting in less frequent deep convection. During July, SWA is located within this zone and experiences a decrease in monthly rainfall, which is known as the "little dry season" (e.g. Vollmert et al.; 2003).

3.3.2   Seasonal evolution of rainfall and environmental conditions over West Africa

From a seasonal perspective, the rainband of the WAM generally follows the region of maximum near-surface moist static energy (i.e. highest equivalent potential temperature θ_e) and features a northward migration from the Atlantic towards the Sahelian region roughly from February to August (Figure 3.10). However, during this period, the rainband varies in strength and in the velocity of the northward shift. The start of the rainy season over the SWA or the Guinea Coast region ("GC" in Figure 3.10) is around March to April and is delayed accordingly farther north in the Soudan and Sahelian region to approximately May and June, respectively. SWA experiences its first rainfall maximum in May and June, associated with the strengthening of the peak of the rainband over the ocean that already sets in in April. Sultan and Janicot (2003) described the stage around maximum rainfall at the Guinea Coast as the "monsoon preonset" for the Soudano-Sahelian region, which is characterised by the arrival of the ITD, and thus an increase in moisture availability, to 15°N. In June, the rainfall peak of the rainband features a distinct "jump" from the Guinea coastline at around 4°N to the Soudan region at roughly 10°N. This is commonly referred to as the "monsoon onset" (e.g. Sultan and Janicot; 2003; Gu and Adler; 2004; Hagos and Cook; 2007; Fitzpatrick et al.; 2015), which leads to a relatively dry period over SWA from July and August known as the little dry season, as mentioned above. The reasons for the sudden northward migration are still debated and are possibly, among other things, related to a rapid northward displacement of the SHL deep into the Sahara leading to a more inland pentration of moist air (Ramel et al.; 2006; Sultan and Janicot; 2003). The rainband starts again to retreat southwards from the Soudan and Sahelian region during September. Its second overpass over SWA marks the region's secondary seasonal rainfall peak, generally lasting from September to October. Thus, SWA experiences a two rainy seasons, which manifests in a bimodal seasonal rainfall profile, whereas that of the Soudano-Sahelian region exhibits a unimodal seasonal distribution. The earlier rainfall peak over SWA is usually considered as the "primary" rainy season, not only because because of the relative strength of the WAM rainband around this time but also because of its slower northward propagation (and thus longer rainy period) compared to the speed during the southward retreat (Fink et al.; 2017).
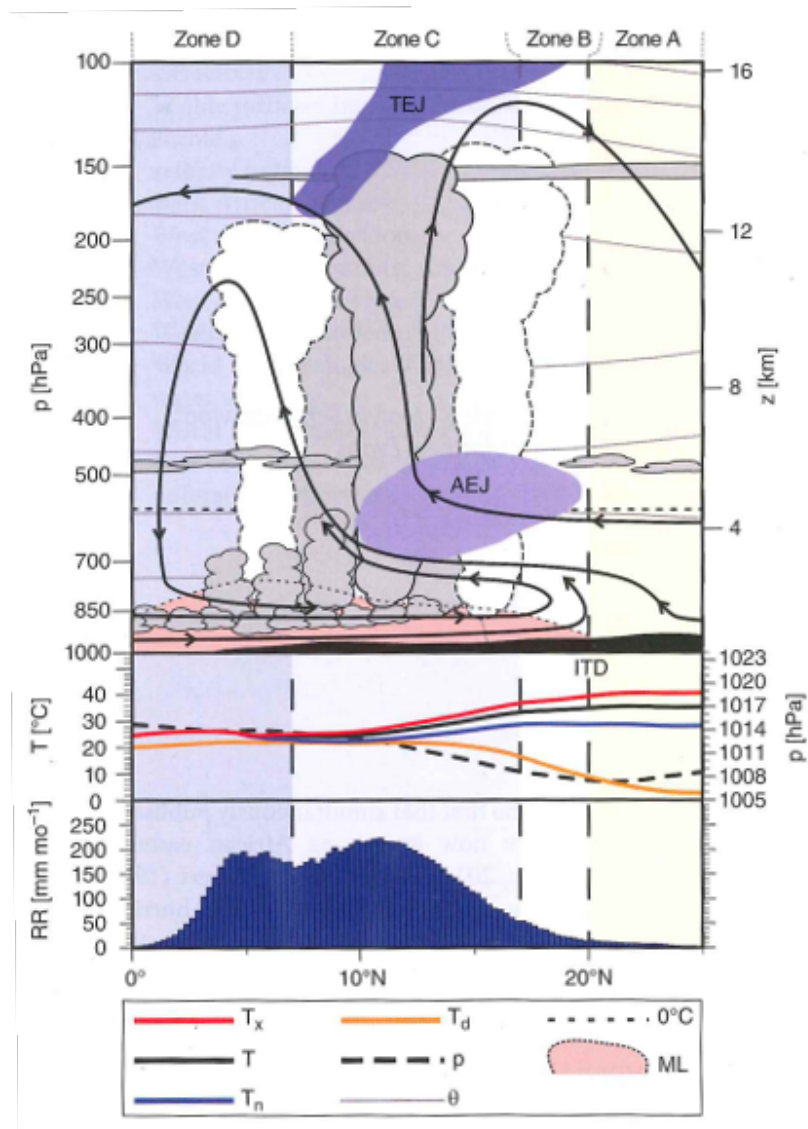
Figure 3.9: Schematic cross-section of the atmosphere between 10°W and 10°E in July and illustration of the weather zones A-D of the West African monsoon. Shown are the positions of the ITD, upper-level jet streams (AEJ, TEJ), the monsoon layer (ML) (as defined by westerly, i.e. positive zonal winds), streamlines, clouds, the freezing level (0°C isotherm), isentropes (θ), minimum (T_n), maximum (T_x) and mean (T) and dew point temperatures (T_d), atmospheric pressures (p), and mean monthly rainfall totals (RR). From Parker (2017a), Chapter 1, Figure 1.1, Copyright (c) 2017, John Wiley and Sons Ltd.

From the standpoint of moisture flux in conjunction with large-scale controls, Thorncroft et al. (2011) recently drafted an extended view of the environmental conditions associated with rainfall over SWA during the poleward migration of the rainband (Figure 3.11). Their concept largely focuses on the development of the sea surface temperature (SST) over the Atlantic and the influence of the continental heat low, which, during the peak monsoon in July and August, reflects the SHL. Thorncroft et al. (2011) defined four phases, during which the SSTs and the heat low change their characteristics that lead to different patterns in moisture flux convergence. The "oceanic phase"
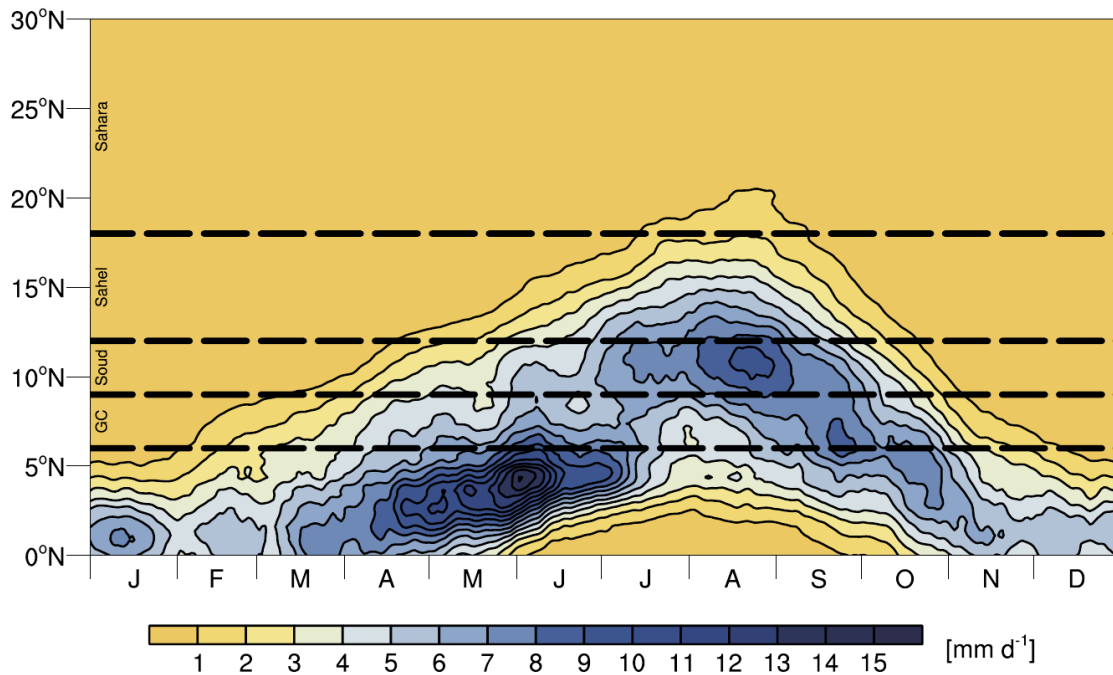
Figure 3.10: Hovmoeller diagram of the 15-day running mean of daily precipitation, averaged between 10°W and 10°E. Source: Tropical Rainfall Measuring Mission (TRMM) 3B42 Version 7, 1998–2012. From Parker (2017a), Chapter 1, Figure 1.4b, Copyright (c) 2017, John Wiley and Sons Ltd.

ranges from November to mid-April (Figure 3.11a) and is characterised by warm SSTs (>28°C) and a heat low over land located around 10°N. While the location of the main rainband is associated with the region of highest θ_e as well as strongest moisture flux convergence (MFC) over the ocean around 1°N (see solid black contours), the heat low over land induces a shallow meridional circulation with further MFC regions at the bottom of the upward branch (i.e. the ITD region) and in the region of the rainband (blue shaded clouds) at midlevels. As the first rainy season over SWA progresses, the "coastal phase" (mid-April to June) features both the development of the so-called Atlantic cold tongue (ACT) and a northward migration and strengthening of the heat low (Figure 3.11b). The latter supports the establishment of the ACT, which in turn results in an enhancement of the monsoon flow due to higher meridional pressure gradients. In combination, the rainband shifts polewards to 4°N close to the Guinea coastline, where, due to frictional deceleration of the monsoon flow from ocean to land, MFC increases. As mentioned before, this stage represents the wettest period over SWA (monsoon preonset). It is believed by Thorncroft et al. (2011) that this pronounced MFC at the coast may be an important factor for the slow poleward migration of the rainband. At the same time, the more pronounced northern position of the heat low, now developing into the SHL, accordingly shifts the MFC patterns of the oceanic phase farther inland, improving the conditions for rainfall there. However, the midlevel MFC region at 700 hPa (solid red circle) has moved to the poleward side of the rainband, which is suggested to be important for the monsoon onset by deepening of the moist layer. The short "transitional phase" in the first half of July features a temporary weak rainfall period and marks the beginning of the monsoon

onset (Figures 3.11c and 3.10). The SSTs at the coast decrease due to upwelling of cold water, potentially due to enhanced ocean surface stress by the monsoon flow (Vollmert et al.; 2003). While the shallow meridional circulation associated with the SHL retains the MFC structure at a progressively more northern position, a secondary MFC region at 850 hPa (green solid circle) was observed by the authors at around 10°N, which ultimately becomes the new latitudinal position of the rainband and the final setting during the "Sahelian phase" (mid-July to September, Figure 3.11d).

3.3.3 African easterly waves and their role for rainfall

The dynamical aspects of the WAM and their influence on the seasonal and sub-seasonal variability of rainfall are complex and still of great debate, which is, for instance, reflected in ongoing challenges forecasting of rainfall at these time scales (e.g. Thiaw and Kumar; 2015). On synoptic time scales, wave disturbances along the AEJ known as African easterly waves (AEWs) have been observed to be associated with the occurrence of MCSs and fast-moving squall lines particularly in the Sahelian region (Payne and McGarry; 1977; Fortune; 1980; Rowell and Milford; 1993; Fink and Reiner; 2003; Gu et al.; 2004; Janiga and Thorncroft; 2016, e.g.). With a common wavelength of 2000–4000 km and a translation velocity of around 8 m s^{-1} (Reed et al.; 1977; Laing et al.; 2008), they re-appear with a periodicity of 3–5 days over a given region in West Africa. This subsection provides a brief description of their structure and implication for rainfall.

Prerequisites for the initiation of AEWs are instability criteria at the AEJ that must be fulfilled for disturbances to develop. Following the theorem of Charney and Stern (1962) for barotropic and baroclinic instability, exponential growth of disturbances for an inviscid, adiabatic flow is possible once, among other things, the meridional gradient of the potential vorticity PV, defined for a purely zonal flow as (Burpee; 1972)

$$PV = \left(-\frac{\partial u}{\partial y} + f \right) g \, \frac{\partial \theta}{\partial p} \tag{3.8}$$

changes sign anywhere in the domain of the AEJ. Its compliance with the AEJ can be visualised by using a sketch by Parker et al. (2005b), which shows a meridional cross section of the ambient conditions around the AEJ as well as typical locations of higher convective activity (Figure 3.12). First, the structure of the AEJ by featuring a jet core already implies a change in sign of the meridional gradient of the absolute vorticity (first term on the right-hand side of 3.8) both on the cyclonic (equatorward) and anticyclonic (poleward) shear side of the AEJ. The static stability in turn (second term on the right-hand side of 3.8) steadily decreases poleward, evident by decreased number of isentropes in the vertical towards the Sahara (solid lines in Figure 3.12). In combination, a meridional PV reversal is mostly found south of the AEJ. Furthermore, deep convection and in particular organised MCSs, which are usually favoured south of the AEJ with the region of highest θ_e, increase the positive PV anomaly equatorward of the AEJ (e.g. Thorncroft et al.; 2003). However, convection is occasionally also found on the poleward side of the AEJ. Here, through boundary layer moistening, the undercutting monsoon flow can reduce CIN, which
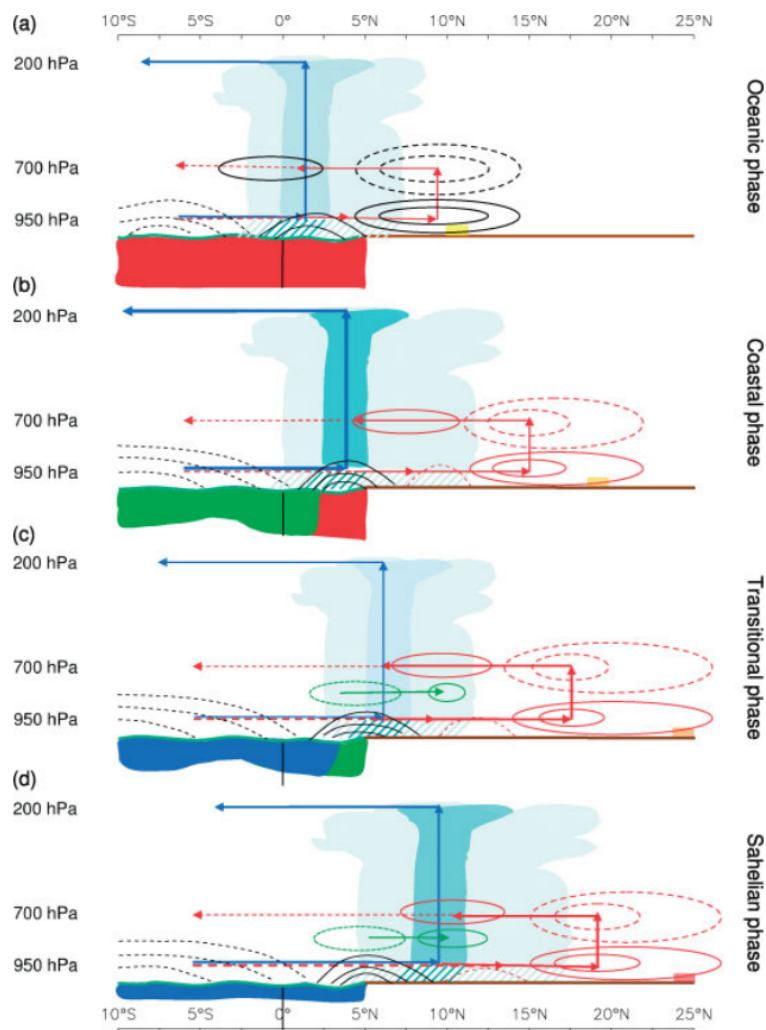
Figure 3.11: Schematic showing the four key phases of the annual cycle of the West African monsoon. Included for each phase are the following: the location of the main rain band (indicated by clouds and rainfall with peak values highlighted by darker shaded clouds and rainfall), the location of the Saharan heat-low (indicated by yellow, orange and red shading at the surface poleward of the rain band, with increased redness indicating increased intensity). Atlantic ocean temperature and associated mixed-layer depth (with decreased temperatures indicated by the red-to-green-to-blue transition). Moisture flux convergence maxima and minima (solid contours indicate moisture flux convergence and dashed contours indicate moisture flux divergence), and the deep and shallow meridional circulations (blue and red lines with arrows); dashed lines suggest some uncertainty about the extent to which the return flow of the shallow meridional circulation penetrates the latitude of the main rain band or not. The moisture flux convergence quadrupole structure is highlighted by red contours and the dipole at 850 hPa structure is highlighted by green contours. From Thorncroft et al. (2011), Figure 12, Copyright (c) 2011, Royal Meteorological Society.

is generated by the dry midlevels above (see Figure 3.2b).

The generation of AEWs has been observed to occur in conjunction with convective activity over the eastern Sahel at topographic features such as the Darfur Mountains (Berry and Thorn-
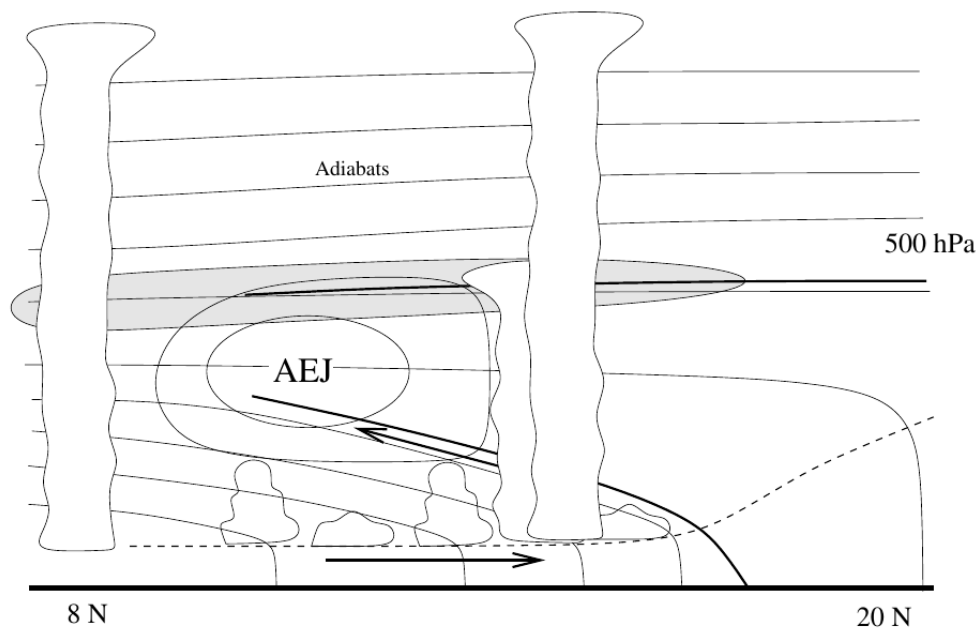
Figure 3.12: A schematic diagram of the thermodynamic structure on a latitude-height section through the African easterly jet system. Adiabatic "Saharan Air Layer" (SAL) boundaries are denoted by bold lines and the top of the monsoon layer by a dashed line. A shallow layer of intermittent altocumulus and stratocumulus (grey shading) occurs at the top of the SAL, with increasing amounts and depth towards the south. The meridional circulation marked is that of the 28 August 2000 observations, and is expected to vary diurnally and synoptically. From Parker et al. (2005b), Figure 10, Copyright (c) 2005, Royal Meteorological Society.

croft; 2005) and the Ethiopian Highlands (Mekonnen et al.; 2006), which coincides with a common entrance region of the AEJ (Leroux and Hall; 2009). The susceptibility of AEW triggering in this area of the AEJ has further been emphasised in a modelling study by Hall et al. (2006). In advanced stages, the AEW can intensify through conversion of energy through barotropic (i.e. horizontal shear instability) as well as baroclinic processes (i.e. thermal advections), which is often further accompanied by energy from convection, as seen by the high fraction of AEW-convection couples in Fink and Reiner (2003). Although highly variable in its structure, a typical AEW was drafted by Cornforth et al. (2017) shown in Figure 3.13 as a consensus of many observational and modelling studies. The sketch also illustrates its role in modulating environmental conditions for convective activity.

The upper panel in Figure 3.13 shows the AEW structure (blue streamlines) at the AEJ level (600–700 hPa), centred on the AEW trough, while the middle and bottom panels present the wave structure and its influence at successively lower levels at 850 hPa and the near-surface layer, respectively. At 850 hPa, the presence of an AEW is often reflected in a closed vortex ("C") on the equatorward shear side of the AEJ, which is in many cases accompanied by a corresponding vortex on the poleward side. Some studies detected such vortex couples while propagating westward alongside AEWs (e.g. Fink and Reiner; 2003; Chen; 2006; Zawislak and Zipser; 2010) and have been found to form a distinct northern (i.e. roughly 15–20°N) and a southern band of tracks (i.e.
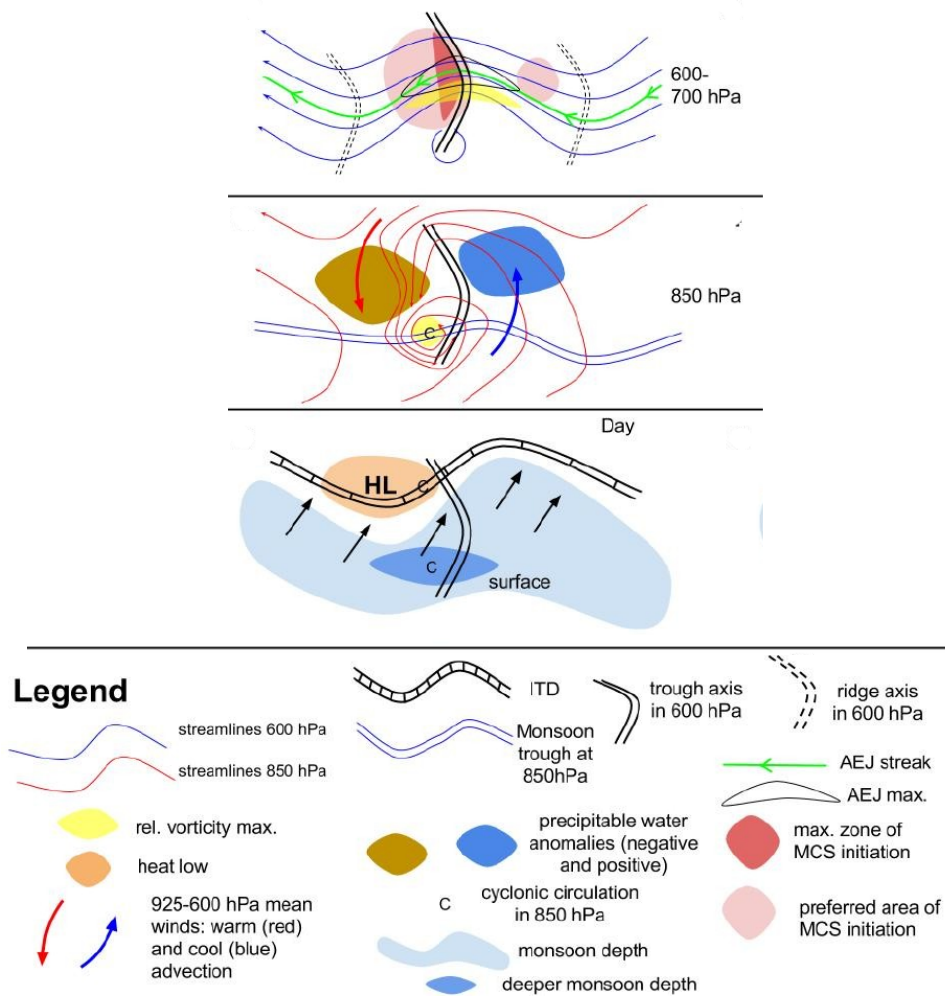
Figure 3.13: Schematic of the various observable elements of an "typical" AEW (see legend), as far as this exists, and likely relationships between these. The upper panel shows the situation at the level of the AEJ (600–700 hPa), the middle panel in 850 hPa and the bottom panel close to the surface. From Parker (2017a), Chapter 2, amended version of Figure 2.10, Copyright (c) 2017, John Wiley and Sons Ltd.

approximately 5–10°N) over West Africa (Fink and Reiner; 2003). The baroclinic nature of the AEW manifests in the displacement of this 850 hPa vortex center to the west of AEW trough axis at 600 hPa, implying an eastward tilt of the trough axis with height and thus a westward propagation of the AEW, following the concept of baroclinic waves (e.g. Holton and Hakim; 2012). Over the entire depth, this configuration leads to the advection of moist and cool air from the south at the eastern (upstream) flank of the trough and, accordingly, dry and warm airmasses from the north on the western (downstream) side (see patches for PW anomalies in the middle panel), also seen in the respective curvature of the ITD (bottom panel). This low-level northward surge of moist air in the northeastern part of the trough usually act to increase CAPE and lower CIN (see Figure 3.2b), making this region more susceptible for convective activity. In fact, two preferential areas for MCS initiation exist along the AEW, the first as just mentioned and the second being slightly west of the AEW trough axis (top panel).

The relationship of AEWs and rainfall is complex and can vary significantly from case to case. However, it is well documented that a large fraction of AEWs embed convection (e.g. Burpee; 1974; Reed et al.; 1977; Tetzlaff and Peters; 1988; Schrage et al.; 2006) and even promote fast-moving squall lines. For West Africa, Fink and Reiner (2003) found that an overall 42% of all squall lines were AEW-driven. Furthermore, they identified differences in their position within the AEW between the aforementioned southern and northern track. While squall lines in the southern track tended to be located in the region of the northeasterlies ahead of the AEW trough, they were found both ahead and behind in the northern track, as indicated in Figure 3.13, which shows similiarities to findings in Gu et al. (2004) and Kiladis et al. (2006). However, due to the low propagation speed of AEWs (around 8 m s^{-1}) compared to that of the AEJ (Thorncroft and Blackburn; 1999, around 12.5 m s^{-1},), squall lines were also observed to cross the AEW trough during their lifetimes from east to west and intensify, potentially due to higher vertical wind shear in the region of the northeasterlies west of the trough (e.g. Fink et al.; 2006).

Overall, being in the region of the southern AEW track, SWA experiences highest AEW activity in the period around May and June as well as September and October. However, owing to the much moister regime compared to the Sahel, a variety of rainfall systems, apart from highly organised convection, are known to influence SWA. The following subsection provides a brief summary of Guinea Coast rainfall and of earlier studies that quantified rainfall from different rainfall types specifically for SWA.

3.3.4 Guinea Coast rainfall

As seen in Figure 3.8, part of SWA remains south of the ITD under the influence of the moist southwesterly monsoon flow throughout the year and generally experiences a longer rainy season compared to the Soudano-Sahelian region farther north. This becomes evident in the mean annual rainfall distribution in Figure 3.14, where SWA is within the 700 mm isohyet (i.e. line of equal mean precipitation). While a distinct meridional gradient is found in the Soudano-Sahelian region north of 11°N, zonal variations over SWA are more pronounced, not least at the immediate coastline. Total rainfall is enhanced in regions where the coastline is orientated more perpendicular to the monsoon flow, partly supported by orographic features like the Guinea Highlands in the far west. The visible strip of lower rainfall east of the 0° meridian is known as the "Dahomey Gap", which is assumed to be related to, among other things, the seasonal coastal cold-water upwelling prior to the monsoon onset (Vollmert et al.; 2003).

Few studies have dealt with the question of how rainfall is composed over SWA. Because of their vigorous nature, early works focused on so-called disturbance lines, which today can be classified as squall lines. While Hamilton et al. (1945) featured a detailed dynamical description of these disturbance lines over Nigeria, Eldridge (1957), as one of the first for SWA, quantified the contribution of disturbance lines to monthly rainfall over Ghana and described their seasonal occurrence shown in Figure 3.15 for four stations in different climatic areas. Here, Eldridge (1957) used the definition of disturbance lines following Hamilton et al. (1945) as west-southwestward moving thunderstorms accompanied by strong wind gusts (typically 30–40 miles per hour, i.e.
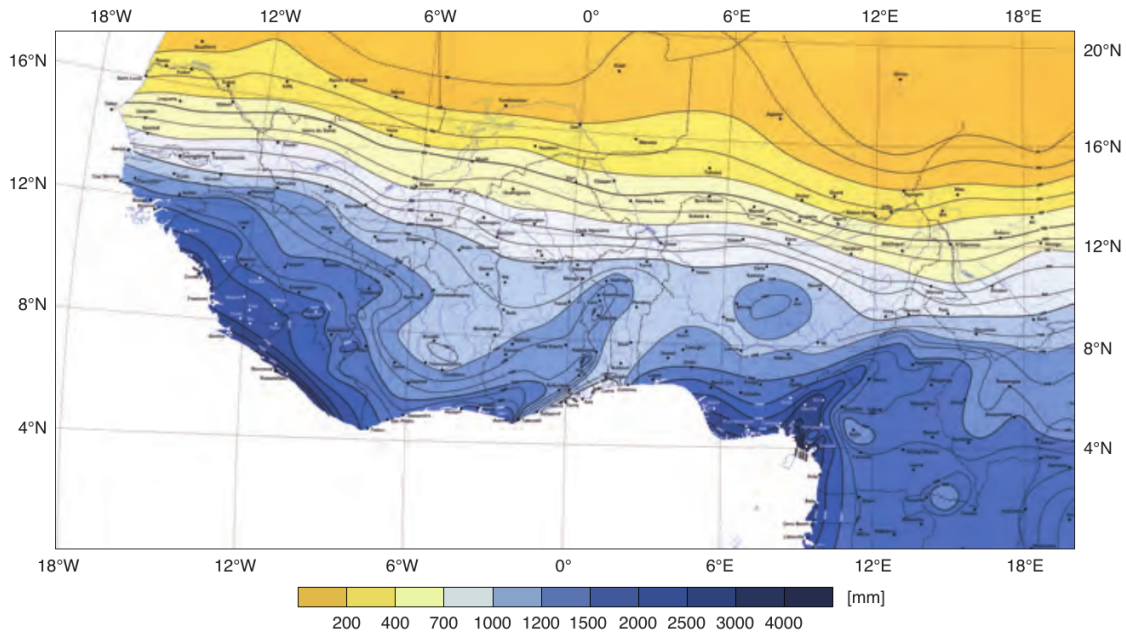
Figure 3.14: Mean annual precipitation for the period 1951–1989. The isohyets are based on 890 rainfall stations (Source: Institut de Recherche pour le Développement (IRD)). From Parker (2017a), Chapter 1, Figure 1.3, Copyright (c) 2017, John Wiley and Sons Ltd.

roughly 13–20 ms^{-1}) upon arrival. Evidently, the coastal stations Accra and Axim feature a bimodal seasonal cycle with a stronger primary rainy season, similar to Kumasi farther inland but with rather equally strong rainy periods. Eldridge (1957) noted an occurrence of disturbance lines mainly during the two Guinea Coast rainy seasons and their absence during the little dry season. Novrongo, located in the Soudan region and featuring a unimodal cycle, was reported to mainly receive its rainfall from disturbance lines.

Subsequent studies further specified the different rainfall types, their contribution to total rainfall and the respective environmental conditions, however, for different regions in SWA (Table 3.1). Fink et al. (2006) distinguished between fast-moving squall lines and slower moving but organised MCSs, which were observed in a strongly (weakly) sheared environment with dry (moist)

Table 3.1: Rainfall contribution of different rainfall types (in percent) over different regions based on the indicated studies. The regions are indicated in parentheses below the source. Note that for Acheampong (1982), the average percentages over the set of Ghanaian stations are given. In Fink et al. (2006), the type of some rainfall events remained unclear and are not listed here.

	Acheampong (1982) (Ghanaian Coast)	Omotosho (1985) (Nigeria)			Fink et al. (2006) (Central Benin)
		4°N	9.5°N	12.5°N	
Squall lines / MCS	17.8	21.3	51.6	69.9	82
Local thunderstorm	32.7	50.9	39.8	26.5	5
Monsoon/vortex	49.5	28.2	26.5	3.9	9
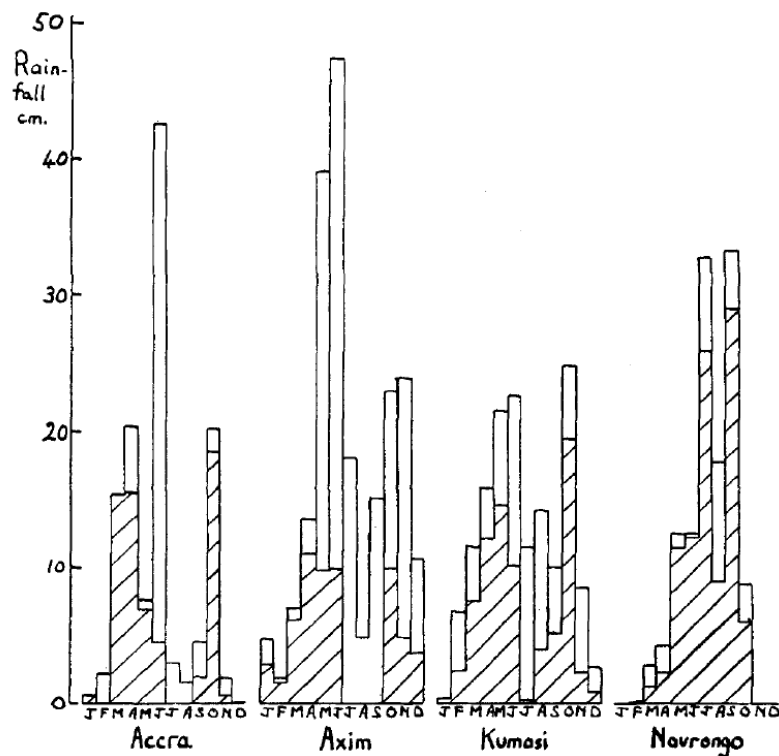
Figure 3.15: Total monthly rainfall in 1955 for Accra (5.5°N, 0°W), Axim (5°N, 2.5°W), Kumasi (7°N, 2°W) and Navrongo (11°N, 1°W). The rainfall amount due to disturbance lines is the hatched area. From Eldridge (1957), Figure 8.

midlevels, respectively. Apart from these organised systems, a general consensus has also been the importance of non-MCS rainfall types. Local thunderstorms were described as short-lived, stationary convective phenomena with a lifetime of 1–2 hours (Kamara; 1986) as a consequence of diurnal heating (Omotosho; 1985). They most likely represent the single cell type in Figure 3.4 and have been found to strongly contribute to rainfall over regions close to the coastline. A rather undefined type of rainfall are monsoon rains, described as widespread, continuous and mostly non-thundery (Kamara; 1986; Acheampong; 1982) in a moist low-CAPE and low-CIN environment. Because of the similarities in the rainfall patterns and the presence of cyclonic signatures at midlevels, Fink et al. (2006) also termed them "vortex rainfall". Despite their, to some extent, significant contribution to total rainfall, not much is known of how exactly they are controlled and, furthermore, how the corresponding midlevel vortices usually form Fink et al. (2006).

Because of increased moisture availability in the environment compared to the drier Soudan and Sahelian regions, so-called warm clouds, i.e. clouds purely in the liquid phase, are found in abundance over SWA particularly after the monsoon onset (Stein et al.; 2011; Schrage and Fink; 2012; Schuster et al.; 2013; van der Linden et al.; 2015). Not until recently has the question been tackled of how frequent "warm rain" occurs over SWA, which may originate from, among other things, shallow convective showers (Schumacher and Houze; 2003; Liu and Zipser; 2009). Here, during episodes of warm rain clouds, Young et al. (2018) found an enhanced warm rain probability during the little dry season in August and generally in the vicinity of the coast, which

suggest some importance for the local rainfall budget. However, since this analysis was purely based on satellite retrievals, a complementary view on warm rain is addressed in the present work.

4. Satellite-based climatology of rainfall types and their relationship to environmental conditions over SWA

4.1 Preface

With some minor adjustments in the text, the following chapter is fully based on the article "Rainfall types over southern West Africa: Objective identification, climatology and synoptic environment" by Marlon Maranan, Andreas H. Fink and Peter Knippertz, first published on 15 July 2018 by the Quarterly Journal of the Royal Meteorological Society in Volume 144, Issue 714 (doi: 10.1002/qj.3345. Copyright ©2018, John Wiley & Sons. This article is available under the terms of the Creative Commons Attribution License (CC BY).

Within the environmental setting over SWA described in the previous chapter, a climatology of rainfall types is compiled using the TRMM precipitation radar (TRMM-PR), which was active for 17 years. It allowed a three-dimensional scanning and subsequent characterization of convective cloud elements (Awaka et al.; 1997; Iguchi et al.; 2000) and has been widely used to investigate the variable nature of convection in the tropical belt (Houze et al.; 2007; Romatschke et al.; 2010; Romatschke and Houze; 2010; Zuluaga and Houze; 2013; Houze et al.; 2015; Zuluaga and Houze; 2015). A caveat of TRMM-PR is its sampling, which is based on instantaneous overpasses over a given region. Thus, the lifetime of convective systems could not be monitored. To bridge this gap, TRMM-PR data are combined with geostationary, infrared (IR) cloud data from Meteosat, where clouds are continuously observed in time. Furthermore, using global reanalysis data from the European Centre for Medium-range Weather Forecasts (ECMWF), composite cross-sections of meteorological fields are used to determine the environmental conditions around the occurrence of rainfall types.

4.2 Data sources and processing

4.2.1 TRMM Precipitation Radar products

The TRMM-PR aboard the TRMM satellite orbited the earth at an altitude of 402.5 km (350 km before August 2001) scanning with a swath width of 247 km (215 km) with a surface horizontal resolution of 5 km (4.3 km) at the earth's surface (Kummerow et al.; 1998; Kawanishi et al.; 2000). The resolution in the vertical is 250 m with the highest layer at 19.75 km. Convective systems are investigated using the level-2 (i.e. orbital) products 2A25 and 2A23 (V7) from the TRMM-PR (Iguchi et al.; 2000) for the period from 1998 to 2013. Data from 2014 were discarded due to shut down preparations during the same year (Houze et al.; 2015). The 2A25 dataset contains the three-dimensional, attenuation-corrected radar reflectivities and rain-rate profiles (Heymsfield et al.; 2000), while the 2A23 dataset provides information about the rainfall type (convective, stratiform, other). These two products were used for the classification of rainfall systems (see section 4.3). The radar swath intersected the wider study area displayed in Figure 4.1 on four to six occasions per day at no specific location and time of day. Thus, the TRMM-PR dataset does not provide continuous observations in space and time, but provides random instantaneous values from different stages in the lifecycles of convective systems. The instantaneous rainfall rates in the 2A25 product are given in mm/h and all statistics are inferred as if the "lifetime" of all rainfall elements is one hour.

For a more convenient comparison with the other datasets described in this section, the data were re-gridded from their native non-cartesian geolocation onto a 0.05°×0.05° spaced latitude-longitude grid based on the procedure described in Houze et al. (2007). Furthermore, while retaining the vertical resolution, a correction of the vertical geolocation was performed. Since the same coordinates are stored at all height bins along the radar beam, a horizontal offset is introduced that gets larger with higher elevation. By removing this offset a correction of radar echo structures is performed as well.

4.2.2 Meteosat SEVIRI Infrared imagery

Convective cloud features were tracked using the IR dataset (Channel 9 at approximately 10.8 μm) of the Spinning Enhanced Visible and Infrared Imager (SEVIRI) on the Meteosat satellite operated by the European Organisation for the Exploitation of Meteorological Satellites (EU-METSAT). Before applying the actual tracking procedure (see section 4.3), the native radiance datasets were first converted into brightness temperature fields by using the approach presented in Tjemkes (2005). The dataset comes on an irregular horizontal grid with a spacing of 3 km at the sub-satellite point on a 15 minute basis, allowing for an assessment of the history of the convective systems before and after the TRMM overpasses. To ensure comparability, the fields were interpolated onto the same grid as the TRMM-PR data. However, since it is known that convective systems originating as far east as 30°E can influence West Africa (e.g. Laing et al.; 2008), the data and tracking were extended eastward to this longitude. While the TRMM-based rainfall classification was performed for the whole year between 1998 and 2013, IR-based system
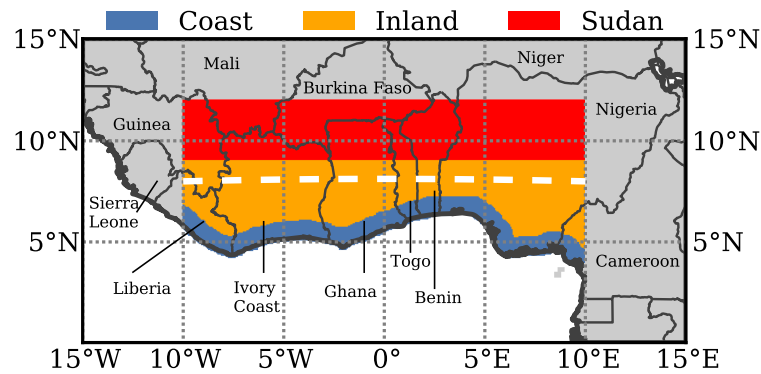
Figure 4.1: Definition of the subregions used in section 4.5: The "Coast" in blue which encompasses all pixels within a 100 km distance from the coastline, the "Inland region" as far north as 9°N in orange and the "Soudan region" in red from 9°N to 12°N. All regions are zonally bounded between 10°W and 10°E. The dashed white line at 8°N denotes the latitude which was taken to construct the time-height cross sections shown Figure 4.7. From Maranan et al. (2018), Figure 1, Copyright ©2018, John Wiley & Sons Ltd.

tracking was only performed during the major rainy seasons between April and October and only for the SEVIRI 2004–2013 period.

4.2.3   Global reanalysis data

Three-dimensional, six-hourly ECMWF Interim reanalysis (ERA-Interim) fields (Dee et al.; 2011) on a 0.75° grid are used to investigate the environmental conditions around rainfall events. All available pressure levels from 1000 to 100 hPa were considered. In a further step, long-term mean fields were created to enable an analysis of anomalies. Here, the reference period is 1998–2013 in accordance with the TRMM-PR period.

4.3   Methods

4.3.1   TRMM-PR based classification of rainfall types

Rainfall systems in the TRMM-PR data are classified based on the method described in Houze et al. (2007, 2015), who applied structure-based thresholds on the three-dimensional radar echoes. Here two additional categories of convective systems are also considered (MOD and STR, see below). These were omitted by other authors because of their relatively low contribution to total rainfall in the entire tropics and subtropics (Houze et al.; 2015) but over SWA they turn out to be of some relevance.

As in Houze et al. (2015), rainfall elements are identified by filtering areas of at least two neighbouring pixels with a radar signal. As this study focuses on convective systems over land, a stricter threshold of 40 dBZ is applied (Houze et al.; 2007; Romatschke and Houze; 2010;

Houze et al.; 2015). The existence and the structure of 40 dBZ cores within the contiguous, three-dimensional echo volumes of convection determines the category the rainfall system falls into. The following categories are considered for further analyses.

- Isolated shallow echo (ISE) is the only pure warm-rain category. Signals from this shallow convective type are included in the 2A23 product and indicate isolated systems with an echo top of at least 1 km below the climatological freezing level (4.5 km) (Schumacher and Houze; 2003).

- Moderate convection (MOD) is used for convective volumes whose cores do not exceed a reflectivity of 40 dBZ and that are not ISEs. MODs are introduced here as one of the two additional categories to extend the analysis to weaker convection.

- If a 40 dBZ core is found in the convective volume, it is classified as strong convection (STR) at first. This remains as long as the definitions of the subsequent categories are not fulfilled. STR is the second category that is added in this study.

- A deep convective core (DCC) is identified if a 40 dBZ core exceeds the altitude threshold of 10 km above mean sea level.

- Wide Convective Cores (WCC) are rainfall systems where the horizontal extent of ground-projected 40 dBZ cores reach at least 1000 km^2. Zuluaga and Houze (2015) attribute systems with such extensive convective areas to larger convective complexes with a high degree of organisation. It should be noted that a height criterion is not applied here, meaning that DCCs and WCCs do not coincide.

- If the height criterion for DCCs and the area criterion for WCCs are fulfilled at the same time, the system is assigned to a new category called deep and wide convective core (DWC). As such, DWCs are treated here as a discrete rainfall category and are therefore no subsets of either DCCs or WCCs.

- Convective elements with a horizontal stratiform echo of at least 50,000 km^2 are called broad stratiform regions (BSR). Here, the 40 dBZ criterion is not a necessary condition since such large, contiguous stratiform regions are most likely linked to mature MCSs (Houze; 2004) that emanated from the categories above.

Although all categories are disjunct, successive TRMM overpasses may sample the same convective system during different stages and thus belonging to different categories. However, given that on average every radar pixel is sampled once every about three days (see section 4.4), this only applies to few long-lived and/or fast moving systems.

4.3.2   Tracking of convective clouds with SEVIRI data

A slightly modified version of the tracking routine introduced in Schröder et al. (2009) was applied which, in essence, is a combination of the methods of Williams and Houze Jr (1987) and

Mathon and Laurent (2001). Cloud pixels in the brightness temperature fields were first identified by applying a threshold of 233 K and then connected using an eight-pixel neighbour algorithm, resulting in contiguous cold cloud areas. This temperature threshold has been widely used in order to delineate cloud areas in tropical regions with potential rainfall (Arkin; 1979; Mathon and Laurent; 2001; Fink et al.; 2006).

As in Schröder et al. (2009), a minimum threshold of 900 km^2 for clouds ($\approx$ 36 pixels in the interpolated SEVIRI data at nadir) is chosen to track smaller, non-MCS type systems while maintaining robustness in tracking. The actual tracking method contains an area overlap approach. The assignment of clouds in two successive IR images at t_0 and t_1 is determined by a forward ($t_0 \rightarrow t_1$) and backward ($t_1 \rightarrow t_0$) similarity analysis of area overlap, horizontal translation of the center of mass and the difference in cloud size as described in Schröder et al. (2009). However, an assignment between a cloud pair is only possible, if an area overlap of at least 50% in either forward or backward analysis is reached. Visual inspection of tracks from slow and faster-moving cases over SWA showed that the assignment of clouds with this overlap threshold and a size cut-off of 900 km^2 are overall plausible, as long as successive images on a 15-minute basis are used. The definition of split and merger events are adopted from Mathon and Laurent (2001). Here, the most similar cloud at t_1 receives the same label as the parent cloud at t_0, whereas the other system undergoes a so called "split generation" or "merger end".

4.4 Rainfall climatology from TRMM-PR

In this section, the spatial rainfall climatologies over SWA based on the instantaneous 2A25 rainfall rates is examined first to assess possible impacts of the sampling. For this purpose, the spatial distribution of the mean annual rain rate and the diurnal harmonic phase of rainfall over SWA based on the TRMM-PR 2A25 product are presented in Figure 4.2. Here, the mean rain rate at a pixel was first calculated as the average rain rate of all overpasses (originally in mm h^{-1}) and then served as a basis for an annual estimate. A given pixel over SWA was scanned over 2000 times by the TRMM-PR during the mission period, equivalent to one overpass every three days statistically. It can be seen that the pixel-to-pixel variability of rainfall rate based on TRMM-PR is quite high (Figure 4.2a). This has two primary reasons: (a) The randomness in overpasses and time of day, and (b) a more detailed representation of smaller-scale, more intense convective parts of the rainfall systems by TRMM-PR, which can leave isolated footprints of higher rainfall amounts. However, the overall rainfall distribution in TRMM-PR over SWA exhibits spatial structures well-known from the literature, also seen in Figure 3.14 of chapter 3.

Despite the highly variable pattern in the TRMM-PR rainfall field, the spatial distribution of its mean phase of the diurnal harmonic reveals some coherent signals (Figure 4.2b). The most striking feature is the difference in the diurnal peak of rainfall over land and sea. Over the ocean close to the coastline, convection is most active during the night and early morning. The mean phase shifts to after sunrise towards open waters, especially over the convectively active Bight of Bonny (3°N, 8°E) (see also Negri et al.; 1994). Over land near the coast, the phase of most active rainfall is from noon to early afternoon. Apparently, the land-sea-breeze circulation is the driving
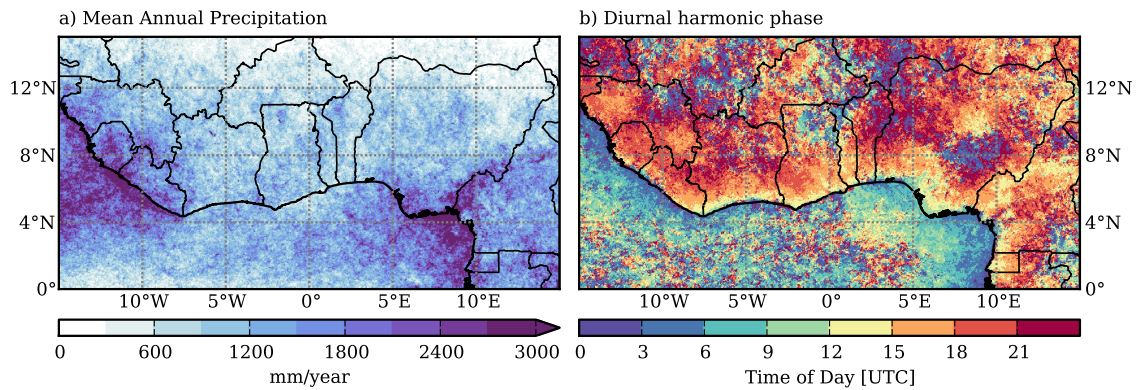
Figure 4.2: TRMM-PR based rainfall maps over SWA. (a) The mean annual precipitation and (b)
the phase of the diurnal harmonic based on >2000 overpasses over a given pixel during the period
1998–2013. For (a), the accumulated rainfall rate in the TRMM 2A25 product was divided by
the number of TRMM-PR overpasses for each pixel and then used for an annual estimate. The
diurnal phase was computed through discrete Fourier transformation. UTC roughly corresponds
to local time. From Maranan et al. (2018), Figure 2, Copyright ©2018, John Wiley & Sons Ltd.

force for rainfall here, but rainfall systems may also migrate northwards (Parker et al.; 2017b).
This is in accordance with findings in Yang and Slingo (2001), He et al. (2015) and Derrien and
Le Gléau (2005), where a strong meridional phase shift in time of cold cloud and rainfall patterns
at the coast is evident. The diurnal phase shifts gradually towards late afternoon and eventually
early evening hours farther inland. Farther north at some distance from the coast, coherence be-
comes less pronounced, which reflects a higher spatial variability of the diurnal cycle. While this
is suggested to be a consequence of a sampling issue to first order, variations in lifetime and trans-
lation speeds of MCSs as well as the gradual northward decrease of annual rainfall might further
contribute to the higher spatial variability of the diurnal phase. Overall, the described patterns
are similar to those presented in Janiga and Thorncroft (2014), who investigated the period July–
September during 1998–2012. This indicates that these three peak rainy season months alone
contribute substantially to the diurnal variation over SWA.

For the upcoming analyses in section 4.5, the SWA domain from 10°W to 10°E was subdivided
into three regions (Figure 4.1).

- The Coast region, representing the 100 km wide strip of land along the coastline;

- The Inland region, bounded to the south by the Coast region and extending northwards up
  to 9°N;

- The Soudan region, the northernmost subregion of SWA from 9°N to 12°N.

The decision to separate the coastal strip from the Inland region is related to the fact that the
former is influenced by land-sea breeze convection as suggested by the morning peak in rainfall
(Figure 4.2b). The Soudanian zone is defined with reference to Fink et al. (2006, 2017) and is
regarded as the transition region between the more humid Guinea coast region to the south and
the drier Sahel to the north.

The annual cycle of TRMM-PR rainfall in each of the subregions is shown in Figure 4.3a. The profiles emphasise the progressive meridional change in seasonal rainfall based on the seasonal migration of the rainbelt (see Figure 3.10). The Coast region exhibits a bimodal cycle with a clear primary rainy season peaking in June and a secondary maximum in September and October during the southward retreat of the rainbelt. This bimodal configuration is also seen for the Inland region where, however, the monthly accumulated rainfall during the southward retreat of the rainbelt in September is somewhat higher than earlier in the year. Over both the Coast and Inland regions, the monthly rainfall decreases from June to July and a local minimum is found in August, marking the little dry season (e.g. Nicholson; 1981; Le Barbé et al.; 2002; Vollmert et al.; 2003). In contrast, the Soudan region is characterised by an unimodal profile that peaks in August. This is generally consistent with annual profiles of raingauge-based data (Judex and Thamm; 2008; Dezfuli et al.; 2017; Fink et al.; 2017) in the respective regions. Compared to the TRMM product *3B42* (Figure 4.3b), where data from TRMM-PR, the TRMM microwave imager (TMI), IR rainfall estimates and ground-based rain gauges are combined for a three-hourly, spatially gridded but two-dimensional best estimate of rainfall, the monthly rainfall totals are considerably lower. Again, this is the result of the discontinuous sampling of TRMM-PR in space and time. Nonetheless, the fundamental differences between the subregions with respect to the annual cycle are reasonably captured by TRMM-PR, with the exception that a clear bimodal configuration is absent for the Inland region in TRMM 3B42.
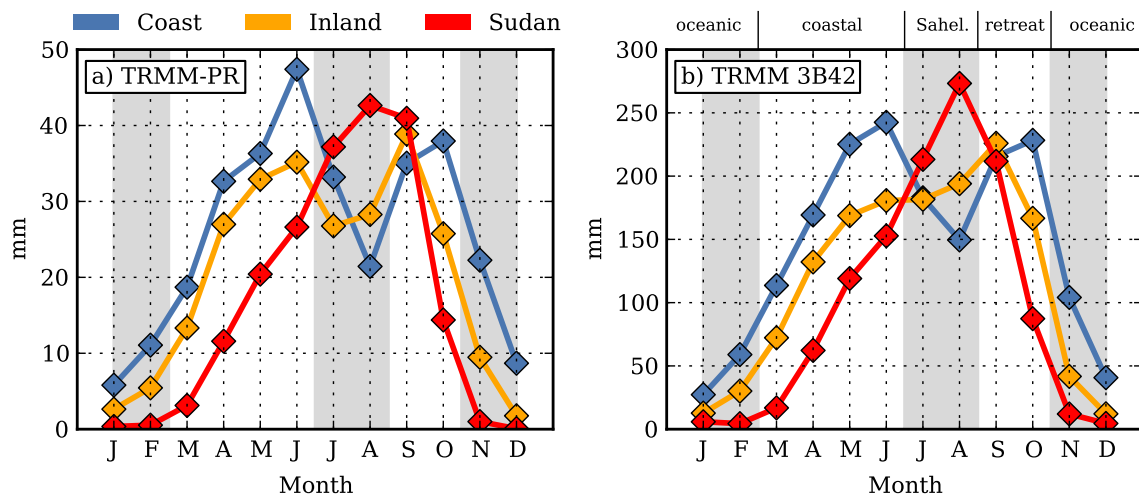
Figure 4.3: Region-averaged annual profiles of accumulated rainfall (a) for TRMM-PR and (b) for TRMM 3B42. The shadings denote different phases of the rainy season over SWA (after Thorncroft et al. (2011) with small amendments): The oceanic phase from November to February, the coastal phase from March to June, the Sahelian phase from July to August and the retreat phase from September to October (also indicated at the top of the panel (b)). Note the different scales of the ordinate between (a) and (b). For TRMM 3B42, the entire continuous 3-hourly record from 1998–2013 was used to compile the profiles in (b) whereas (a) is based on >2000 overpasses over a given pixel. From Maranan et al. (2018), Figure 3, Copyright ©2018, John Wiley & Sons Ltd.

To provide a better orientation for the remainder of the chapter, different phases of the West African rainy season are considered. Hereafter, the months November to February are labeled as

oceanic phase, March to June as coastal phase, July to August as Sahelian phase and September to October as retreat phase, indicated as alternating shading in Figure 4.3. This discrimination is a slightly amended version of the definitions made in Thorncroft et al. (2011), who relate the different phases to the position of maximum moisture flux convergence and thus the position of the rainfall belt (see section 3.3.2). The beginning of the Sahelian phase is also termed *monsoon onset* by many authors (e.g. Sultan and Janicot; 2003; Parker et al.; 2005a; Thorncroft et al.; 2011; Fitzpatrick et al.; 2015).

4.5 Spatiotemporal climatologies of rainfall types

4.5.1 Number and rainfall contribution

The contribution to the total number of events and the amount of rainfall of all categories defined in section 4.3 across the regions are presented in Figure 4.4a. As can be inferred from the diamond markers, 89% (Soudan region) to 92% (Coast) of all identified convective elements are ISEs, MODs or STRs. The relative number of ISEs at the Coast is about 18% higher than in the Soudan region. Being typical for the ocean (Schumacher and Houze; 2003; Houze et al.; 2015), it indicates the more maritime environment of the coastal region that is enhanced through land-sea-breeze interactions. The occurrence frequency of deep and wide categories is fairly uniform across SWA, where WCCs account for around 7% of all systems. In contrast to its numbers, WCCs alone dominate the contribution to total rainfall and produce almost half in any region. Combined with contributions from DWCs and BSRs this contribution increases to 56% at the Coast region and to 71% in the Soudan region. As they represent the MCS-type elements, the latter fraction is comparable with findings in Fink et al. (2006), who attributed around 82% of annual rainfall in central Benin to organised convection (see 3.3.4). Analysing the 2A23 product of TRMM-PR, it is interesting to note that around 36% of the produced rainfall by WCCs, DWCs and BSRs together are of stratiform nature (stratiform rainfall fractions are denoted as black framed bars in Figure 4.4a) and even over 50% when considering BSRs alone. This stresses the overall importance of stratiform rainfall of mature MCSs not least since this portion of the convective cloud may take several hours to overpass a region (Fink et al.; 2006; Dezfuli et al.; 2017). The difference in rainfall production of WCCs, DWCs and BSRs between the Coast and the Soudan region is mainly balanced by the contribution of STRs with 37% in the Coast region down to 21% over the Soudan region. This category, representing smaller-sized and only moderately deep convective cores, is the most frequent category across SWA and their preponderance in the coastal stripe suggests their association with afternoon land-sea breeze convection. Despite their high frequency, ISEs and MODs together contribute only 3%–7% to total rainfall.

The ratio between the integrated surface rainfall and the number of occurrences is shown in Figure 4.4b which is a simple measure to compare the rainfall production per event across the categories. It is normalised based on the lowest value, which for ISEs is in the Soudan region. As expected, BSRs produce the largest integrated rainfall amount per event among the different rainfall classes in all regions. Compared to ISEs their ratios are almost three orders of magnitude
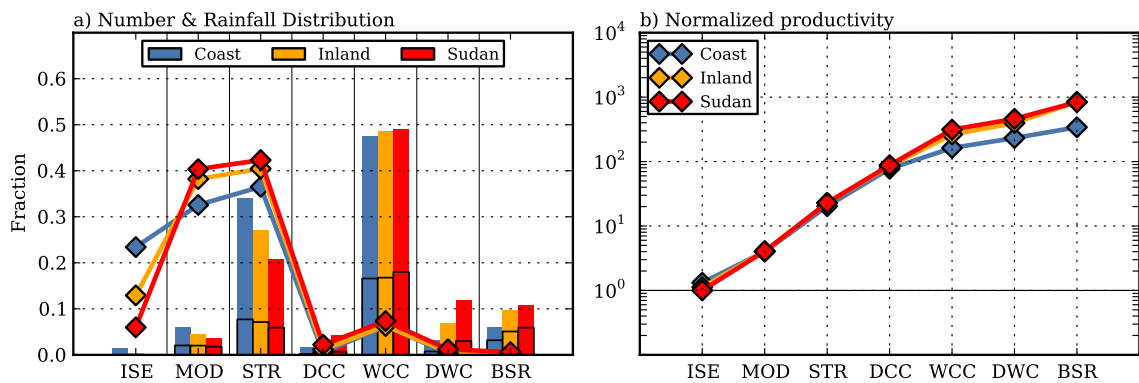
Figure 4.4: Occurrence frequency, rainfall contribution, and rainfall productivity per type. (a) Fractional contribution of each rainfall category in each subregion to the number of events (lines) and rainfall amount (bars). The black framed bars indicate the fraction of stratiform rainfall. (b) Normalised rainfall amount of each rainfall category in each subregion relative to the mean rainfall amount of ISEs in the Soudan region, which is the lowest of all values. The measure indicates the factor of how much more integrated rainfall is produced by any other rainfall category in any region compared to ISEs in the Soudan region. From Maranan et al. (2018), Figure 4, Copyright ©2018, John Wiley & Sons Ltd.

higher over the Inland and Soudan regions. In other words, one BSR produces the same amount of rainfall as 10^3 ISEs. It is apparent that rainfall productivity increases with horizontal growth of convective systems but also with depth. Although DCCs contribute only up to 4% to total rainfall in SWA (Figure 4.4a), their instantaneous rainfall amount reaches already 10% of the of that of BSRs. The productivity of WCC, DWC and BSR over the Coast region is reduced compared to the other regions but this does not necessarily indicate a lower intensity. Due to the smaller north–south extent of the Coast region there is a limitation for how much a mature convective system can contribute to the total rainfall amount.

4.5.2 Diurnal and Seasonal Cycles

The occurrence of the different rainfall types exhibits a distinct annual cycle. Figure 4.5 shows region-dependent seasonal cycles of the occurrence frequency of the rainfall categories with respect to their total number in each region. The following patterns are worth noting:

- ISEs are predominantly a phenomenon during the Sahelian phase, peaking in August in all regions (Figure 4.5a). The sharpness of the annual cycles grows from south to north and a jump from 5% to 20% from June to July is visible for the Inland and Soudan regions, which marks the sudden northward progression of the WAM. A jump of this magnitude is not seen for the Coast, where the profile exhibits a gradual rise and decline before and after August, respectively.

- For MODs and STRs (Figures 4.5b,c) a weakly bimodal distribution in the Coast region transforms into a single-peak mode in the Soudan region. This is similar to the mean annual cycle in Figure 4.3. Over the Soudan region, two increases can be identified. The number

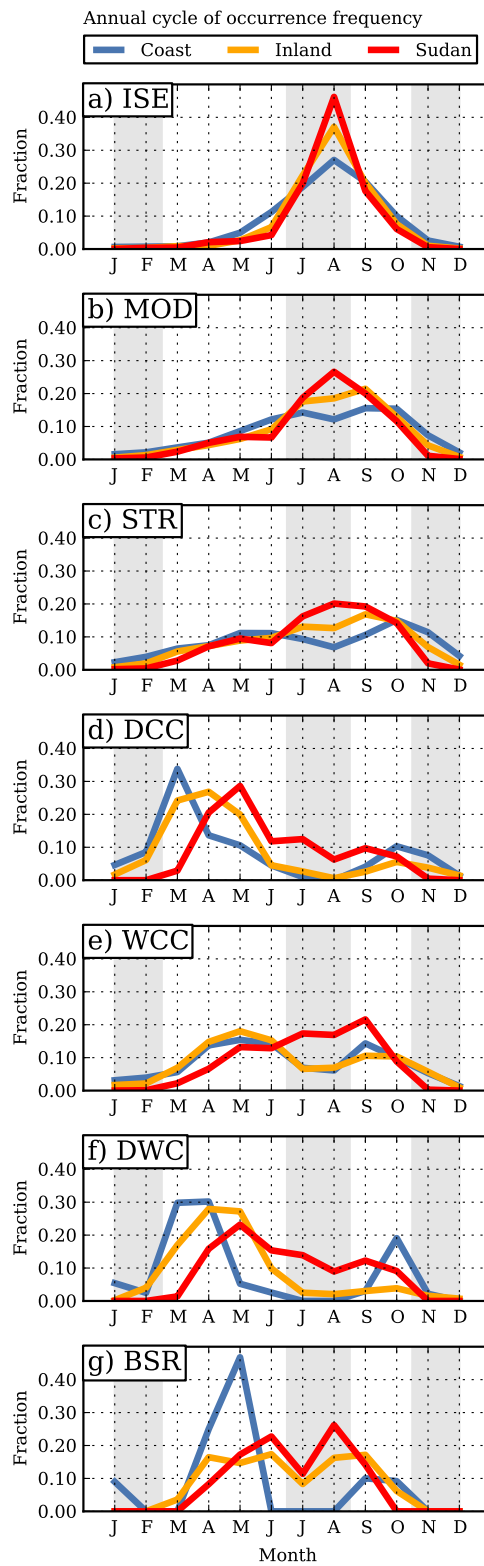Figure 4.5: Mean annual cycle of the fractional occurrence for each rainfall category in each subregion. The shadings again denote different phases of the rainy season over SWA (see Figure 4.3). From Maranan et al. (2018), Figure 5, Copyright ©2018, John Wiley & Sons Ltd.

of identified systems first increases during the coastal phase and then plateaus in June, followed by a sudden jump at the beginning of the Sahelian phase. The first increase may be related to the passage of the Intertropical discontinuity (ITD, see Figure 3.8), which eventually leads to an overall moister environment. Like for ISEs, the second increase is clearly linked to the sudden northward shift of the WAM rainbelt.

- Convective systems that grow very deep (DCCs, DWCs) occur predominantly during the coastal phase (Figures 4.5d,f). The northward progression of maximum occurrence during the early rainy season is clearly visible. Apparently, one to two months are needed to create favourable environmental conditions for deep systems between the Coast and the Soudanian zone. Into the Sahelian phase, deep systems vanish almost completely over the Coast and Inland regions and re-appear during the retreat phase, but are then less numerous. The numbers in the Soudan region are gradually decreasing towards the beginning of the oceanic phase in November.

- For WCCs, the bimodal cycles for the Coast and Inland regions show a strong similarity both in peak positions (May and September) and magnitude (Figure 4.5e). Unlike for deep systems, the conditions for larger organised convection appear to be uniform over a wider region throughout the year. In the Soudan region, the growth in numbers is faster during the coastal phase but peaks in September. Interestingly, this peak coincides with the secondary peaks over both Coast and Inland.

- The profile for BSRs is bimodal in all regions due to a drop in July (Figure 4.5g). While the Coast region exhibits a marked primary peak during the coastal phase, the magnitude of the peaks over the Inland and Soudan regions are similar. During the late Sahelian and retreat phases the occurrence frequency peaks progressively later going southward.

Figure 4.6 depicts the diurnal cycle of the number distribution including the location of the maxima based on harmonic analysis (denoted as dashed vertical lines). In general, the more intense and organised convective systems are, the more they are shifted into nighttime. While MODs, STRs and DCCs typically occur in the afternoon and early evening, WCCs and BSRs appear in the late evening and past midnight, respectively. On average, this reflects the lifetime of fully developed MCSs that are initiated in the afternoon, organise in the evening when conditions are favourable and survive during the night owing to their self-sustaining abilities (cf. 3.2.2). This was found in a similar fashion by earlier studies of e.g. Mathon and Laurent (2001), Fink and Reiner (2003), Laing et al. (2008) and Zuluaga and Houze (2015), who investigated the occurrence of different convective systems for the Sahel. The self-sustainment and thus longer lifetime of WCCs and BSRs is also reflected in their flat diurnal profiles, indicating that these systems are less bound to the diurnal cycle once they have formed. While the distributions over the Inland and Soudan regions are quite similar, convective systems in the Coast region develop around two hours earlier with ISEs predominantly appearing even before noon. The latter may explain the enhanced pre-noon rainfall probability that was found at the Beninese coast based on rain gauge recordings (Fink et al.; 2008). Similarly, using continuous geostationary-based
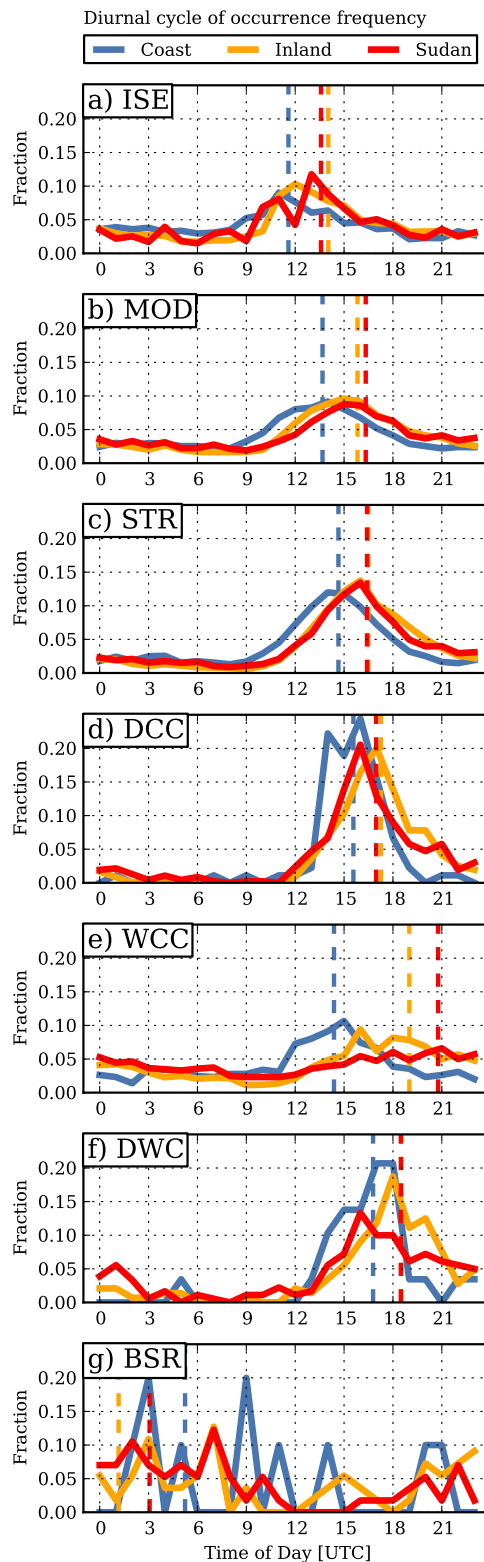
Figure 4.6: As Figure 4.5 but for mean diurnal cycles. The vertical dashed lines denote the phase of the diurnal harmonic for each curve, i.e. the time of maximum occurrence, calculated through discrete Fourier transformation. From Maranan et al. (2018), Figure 6, Copyright ©2018, John Wiley & Sons Ltd.

cloud property retrievals from SEVIRI, Young et al. (2018) found the highest frequency of warm rain along the coastline around midday. At the Coast, the frequency of WCCs already peaks in the early afternoon, which is partly caused by coastal convection forming a contiguous line with strong radar echoes (not shown). The land-sea-breeze circulation likely acts as an trigger for convective systems to overcome convective inhibition and to develop earlier during the day than in the regions farther north.

4.6 Environmental conditions around rainfall events

In this section, the environmental conditions in which the convective systems grow and propagate are described. This is preceded by a brief discussion of the mean annual cycle of factors known to be related to the degree of convective organisation.

4.6.1 Mean seasonal cycle

To investigate the (thermo-) dynamic factors leading to rainfall events, the underlying conditions from a seasonal perspective is addressed first. A zonally averaged annual cycle of the vertical profiles of relative vorticity and horizontal wind based on ERA-Interim data is shown in Figure 4.7 as a time-height diagram. The zonal average was taken from 10°W to 10°E at 8°N (see white dashed line in Figure 4.1) and thus represents the Inland region. Early in the year, the transition from the oceanic to the coastal phase is roughly marked by the change from weak northeasterlies to the southwesterly monsoon flow at lower levels (Figure 4.7a) with the meridional component (black contours) staying above 2 m s^{-1} until the end of the Sahelian phase. During the latter, the monsoon flow gains more westerly momentum (see vectors at low-levels during July and August) and also extends to higher levels. In the mid-troposphere around 650 hPa, the occurrence of the AEJ is denoted with red contours (i.e. zonal wind < -8 m s^{-1}) during the coastal and the retreat phase. During the Sahelian phase, the AEJ moves out of the domain and is located at around 15°N. This seasonal north-south meandering of the AEJ is accompanied by a change of sign in the mean field of relative vorticity, owing to the change from the anticyclonic to the cyclonic shear side and back. The first AEJ passage also marks the period of highest 600-925 hPa vertical wind shear with over 15 m s^{-1} in mid-June. Vertical wind shear is considered to be a key factor for the organisation of shear-perpendicular convective elements (e.g. Sultan and Janicot; 2003; Nicholls and Mohr; 2010; Taylor et al.; 2017, see also section 3.2.2). It decreases during the Sahelian phase down to around 8.5 m s^{-1} and slightly regains strength during the second passage of the AEJ in the retreat phase (up to 10 m s^{-1}). Strong easterlies are also found in the upper troposphere related to the Tropical Easterly Jet (TEJ), which peaks during the Sahelian phase.

The change of the low-level flow is also evident in the divergence and humidity fields (Figure 4.7b). During the oceanic phase convergence prevails in the layer up to 900 hPa with corresponding divergent motions aloft. It marks the period of the shallow meridional overturning in the region of the ITD at the surface and the anticyclonic shear side of the AEJ aloft (Nolan et al.; 2007; Zhang et al.; 2008). With the onset of the monsoonal southwesterlies, the specific hu-
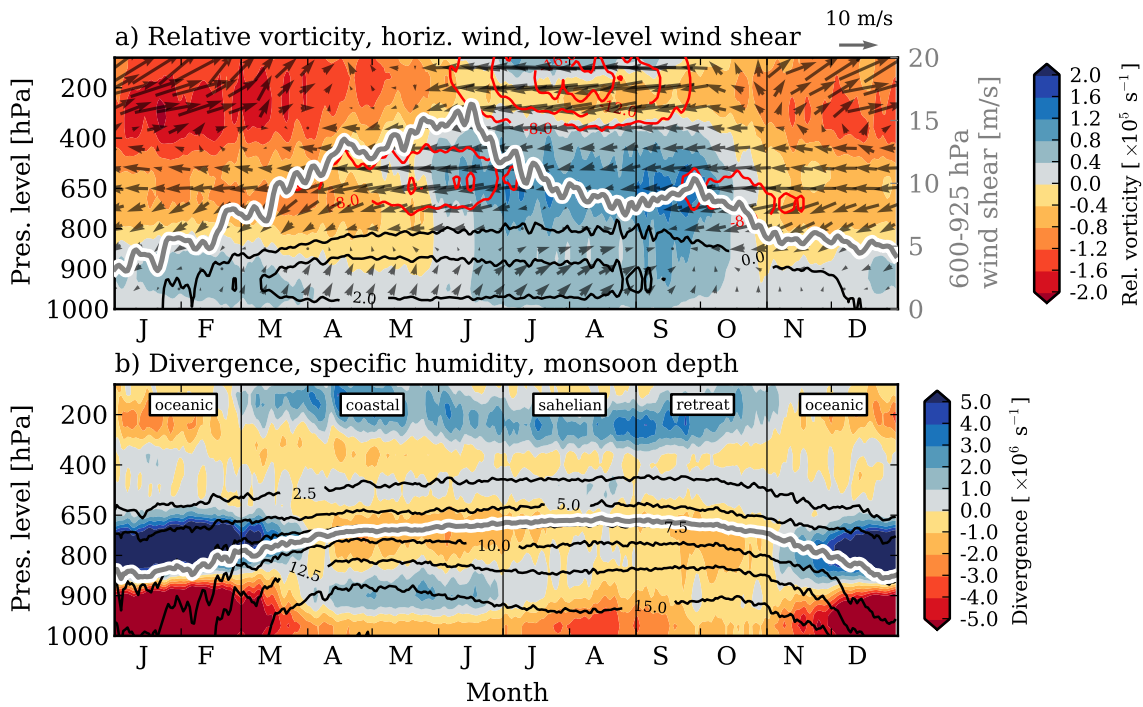
Figure 4.7: Climatologies of seasonally-varying environmental conditions. (a) Annual cycle of the vertical profile of relative vorticity (colour-shaded), speed and direction of the horizontal wind (arrows) and the 600-925 hPa wind shear (grey curve, in m s^{-1}). The red contours denote strong easterlies (lower than -8 m s^{-1}) with an interval of 4 m s^{-1}. The black contours highlight a well-established southerly monsoon flow with an interval of 2 m s^{-1} in the layer up to 700 hPa. (b) Annual cycles of the vertical profile of divergence (colour-shaded), the specific humidity (black contours, interval: 2.5 g kg^{-1}) and the monsoon layer depth (grey curve). The latter is calculated after Lafore et al. (2017b). All quantities are based on ERA-Interim data averaged from 1998–2013 as a 10°W–10°E zonal mean at 8°N (see white dashed line in Figure 4.1). The thin vertical black lines denote the transition between the phases of the rainy season (see Figure 4.3), which are labelled in (b). From Maranan et al. (2018), Figure 7, Copyright ©2018, John Wiley & Sons Ltd.

midity at low levels rises quickly to over 15 g kg^{-1}. It decreases during the Sahelian phase and briefly rises in the retreat phase. During the period of higher specific humidity between March and October divergent flow is also found at the 200 hPa level in accordance with the onset of a higher frequency of deep convection (see Figure 4.5). The seasonal variations in specific humidity decrease with height. The development of the monsoon layer (grey curve), a thermodynamic measure for the depth of humid air in the monsoon (Lafore et al.; 2017b) based on precipitable water (PW), shows a rather gradual increase in height towards the Sahelian phase and a decrease in the retreat phase. The curve roughly follows the 7.5 g kg^{-1} isoline of specific humidity.

4.6.2 Results for TRMM-PR based rainfall types

The local development of the environmental conditions in a 4-day window around the rainfall events is analyzed in Figures 4.8 and 4.9 based on anomalies from six-hourly mean profiles of ERA-Interim. These mean profiles are based on the 1998–2013 period. For the calculation of the

anomalies, all profiles in the 4-day window were taken from the closest ERA-Interim gridpoint to the position of the convective system in TRMM-PR and were eventually subtracted from the respective mean profiles. Note that the positions of the rainfall systems were determined by their center of gravity, which means that the leading portion of the rainfall area may have arrived earlier at a gridpoint, specifically for larger systems such as BSRs. For the purpose of a condensed analysis, Figures 4.8 and 4.9 show composites over all subregions combined. In essence, the structures of the anomaly fields are mostly comparable between the subregions but their magnitudes differ. References to figures in the Appendix are given where necessary.
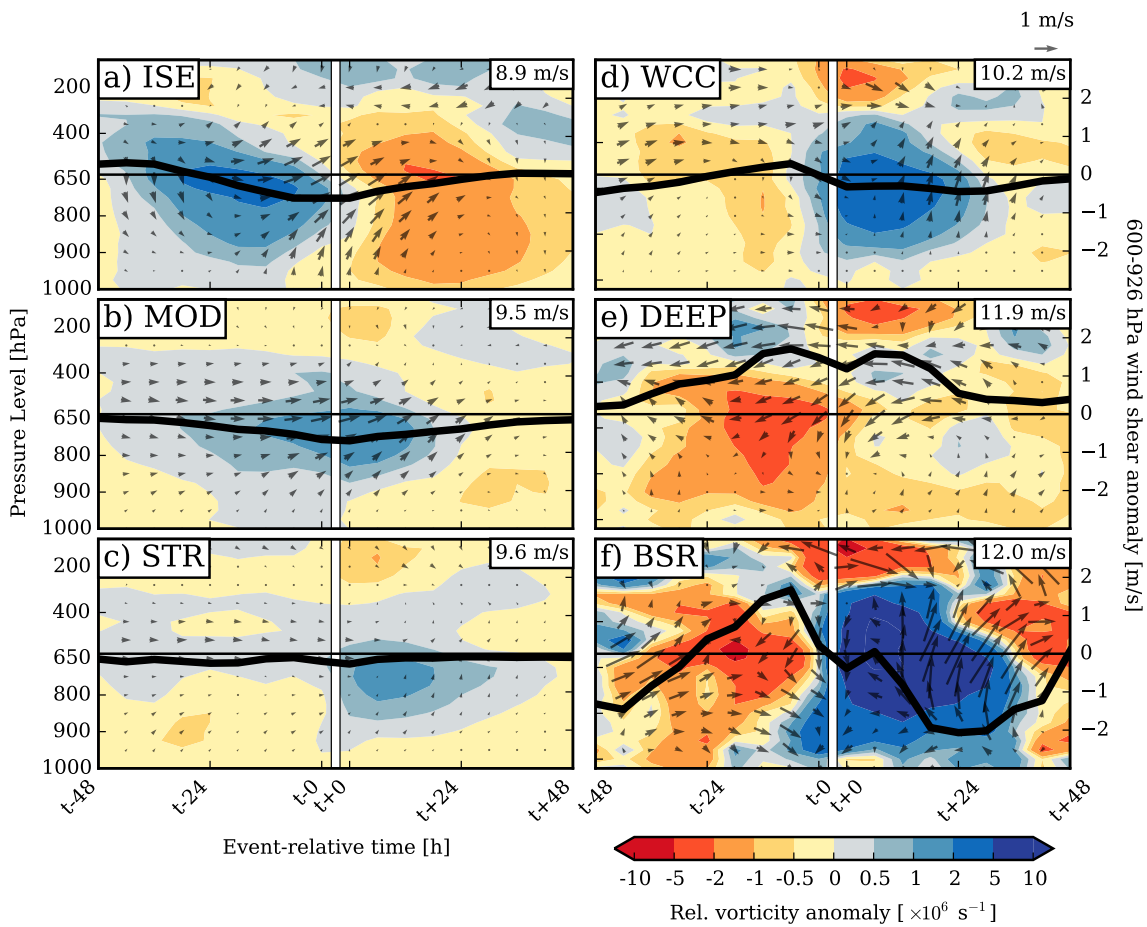
Figure 4.8: Composited time-height ERA-Interim profiles of the anomalies of relative vorticity (colour-shaded) and of horizontal wind in speed and direction (arrows) in a ±48 hours timeframe around the passage of a convective system belonging to a given rainfall category (vertical white line) at the respective gridpoints. t±0 represent the closest timesteps before and after the onset of the event, respectively. The anomalies were determined by subtracting the values at the actual event from its respective 1998–2013 mean. Additionally, numbers denoting the mean background absolute wind shear for the rainfall types is given in the top right corner of the respective figure frames. The thick black curves denote the anomaly of the 600–925 hPa vertical wind shear [in m s^{-1}]. The thin horizontal black line is the zero line for the wind shear anomaly. Information from DCC and DWC are combined to "DEEP". From Maranan et al. (2018), Figure 8, Copyright ©2018, John Wiley & Sons Ltd.

Figure 4.8 shows the evolution of the anomaly fields of relative vorticity, the anomaly of the

horizontal wind expressed as arrows and the anomaly 600-925 hPa wind shear denoted as black curves. Additionally, the climatological background values of low-level wind shear determined by the mean fields described above are indicated in the top right corners. For this analysis, information from the deep core categories DCC and DWC are combined to "DEEP", as no substantial differences were found between them with respect to the anomaly fields. It is evident that rainfall events over SWA generally occur in connection with midlevel vorticity disturbances. ISEs and MODs develop under distinct westerly to southwesterly wind anomalies at midlevels (Figures 4.8a,b). They appear to be linked with a cyclonic anomaly that acts to reduce the lower tropospheric wind shear. Note that the respective background low-level wind shear is already lowest among all categories (8.9 and 9.5 m s^{-1}, respectively), which suggest that less intense convection favourably occur in a weakly sheared environment. In the case of ISEs, such a regime is established in between a deep dipole configuration of a preceding cyclonic and a succeeding anticyclonic anomaly. One can assume that this and the wave-like pattern of the wind anomalies reflect the passage of a mid-tropospheric wave, most likely but not exclusively an AEW. ISEs develop predominantly on the eastern flank of the wave trough. Such a dipole configuration is absent in the case of MODs which predominatly develop during the passage of a single cyclonic disturbance. This regime may occur on the southern flank of the cyclonic anomaly where the usually prevailing midtropospheric easterlies are weakened the most. However, the effect of reduced low-level wind shear decreases towards the region ahead of the cyclonic anomaly and enables the occurrence of more intense rainfall systems, as can be inferred from the profile of STRs where anomalies in the horizontal flow are weak (Figure 4.8c). Organised convection (WCCs, BSRs; Figures 4.8d,f) occurs ahead of a cyclonic and behind an anticyclonic vorticity anomaly. Westerly wind anomalies at midlevels prior to the event are suppressed and turn to southerly directions. The influence of this vorticity dipole on the vertical wind shear is clearest for BSRs (Figure 4.8f), where the passage of the anticyclonic (cyclonic) vortex strongly enhances (reduces) shear. That said, BSRs develop predominantly during periods with a large background shear (12 m s^{-1}). In the case of DEEP (Figures 4.8e), anticyclonic signals at midlevels precede the event, accompanied by northeasterly anomalies and thus increased low-level vertical wind shear. However, the structure of a cyclonic anomaly is less pronounced. This profile is in stark contrast to those of MODs and STRs (Figures 4.8b,c).

The distinct dipole structure of the anomaly field of relative vorticity around BSR events is typical for the Soudan region but becomes less pronounced towards the Coast region (see Figures A.1–A.3). In fact, BSRs in near coastal areas tend to occur closer to the center of the cyclonic disturbance while the vorticity dipole vanishes at the same time. In a similar although less striking fashion, the occurrence of ISEs is drawn towards the cyclonic center over the Soudan region. These distinctive differences of the environmental conditions for convective systems on the opposite side of the intensity spectrum indicate where favourable conditions for organised convection are created by midlevel disturbances in different regimes.

In Figure 4.9, controlling factors for rainfall at lower levels are analyzed through the anomaly fields of divergence (shaded), the moisture field (contoured) as well as the anomaly in PW (black curve). The background values of PW are presented in the top right corners. Note that some
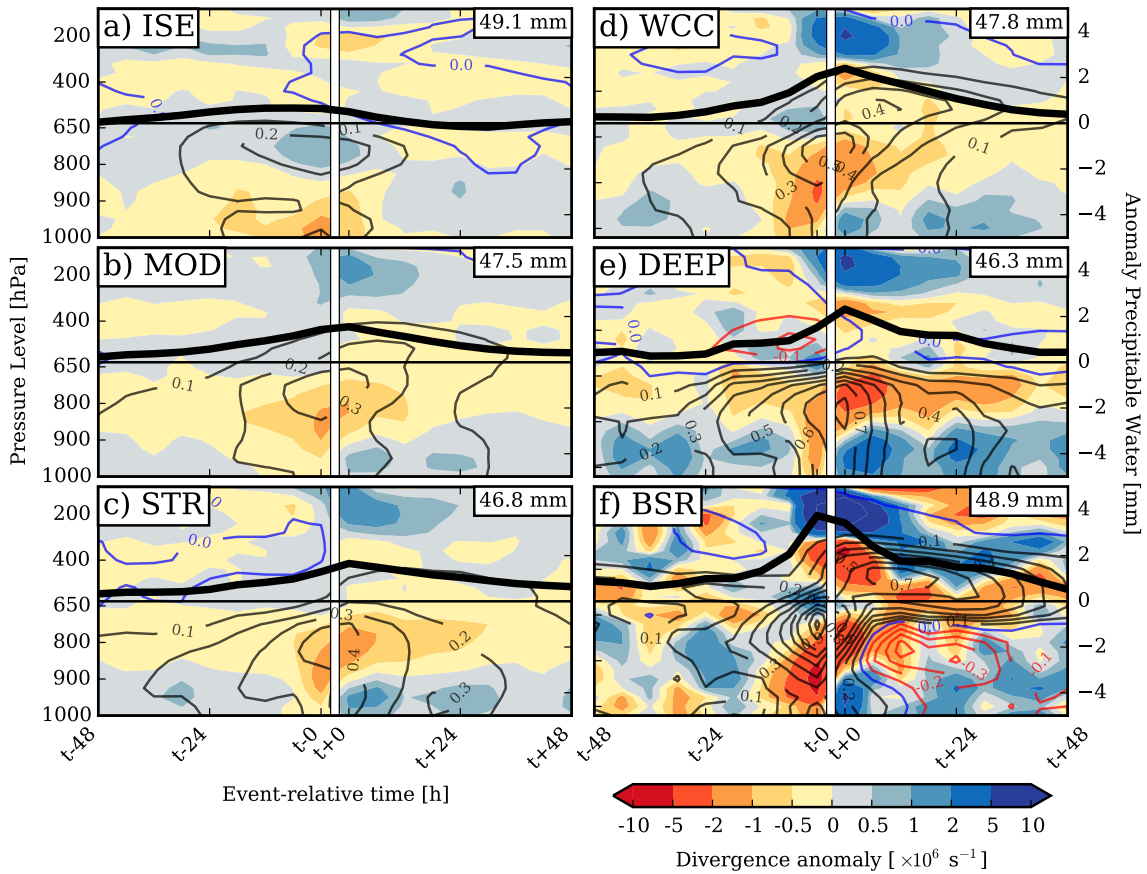
Figure 4.9: As in Figure 4.8 but for the anomalies of divergence (colour-shaded), of specific humidity (contours) and of Precipitable Water (PW, thick black curve). For the specific humidity, positive values are highlighted as black and negative values as red contours in a $0.1\,\mathrm{g\,kg^{-1}}$ interval. The blue contour denotes the zero line. The mean background PW for the rainfall types is given in the top right corner of the respective figure frames. Information from DCC and DWC are combined to "DEEP". From Maranan et al. (2018), Figure 9, Copyright ©2018, John Wiley & Sons Ltd.

uncertainties with respect to these three quantities have to be taken into account; since the evolution of both mass and moisture budgets is governed, amongst other things, by precipitation (e.g. Berrisford et al.; 2011), the representation of the respective fields depends on the ability of ERA-Interim to resolve the rainfall systems. Nonetheless, coherent signals of low-level convergence just ahead of the passage of any rainfall category prevail and coincide with an increase of both positive specific humidity and PW anomaly, all strongest in the case of BSRs (Figure 4.9f). This indicates that local moisture convergence plays a substantial role for the establishment of organised convection. However, from the perspective of absolute values, PW is not a suitable predictor for rainfall types. For instance, the environment around low-intense ISE events (Figure 4.9a) exhibit the highest background value of PW among all categories (49.1 mm). Therefore, for the more humid SWA, it can be assumed that a redistribution of existing moisture through low-level convergence/divergence has a higher impact on the evolution or occurrence of certain rainfall types than the mere availability of moisture itself. Finally, it shall be noted that ERA-Interim

is able to capture large convective systems, such as a BSR. After its passage, a vertical dipole structure in the anomaly field of specific humidity is found with drying in the lower troposphere and a layer of ongoing moistening aloft (Figure 4.9f). This is the widespread trailing stratiform region of the BSRs. The overall structure is in accordance with the radiosonde profile of what was termed *organised convective systems* (OCS) in Fink et al. (2006), i.e. most likely squall lines, which exhibits a drying (moistening) of the low (mid to upper) levels.

Figure 4.10: Cumulative distribution function of (a) CAPE, (b) CIN and (c) 700 hPa DCAPE in J kg^{-1} for each rainfall category. The respective value ranges were divided in 50 bins, resulting in an interval of 100 J kg^{-1} for CAPE, 5 J kg^{-1} for CIN and 20 J kg^{-1} for DCAPE. I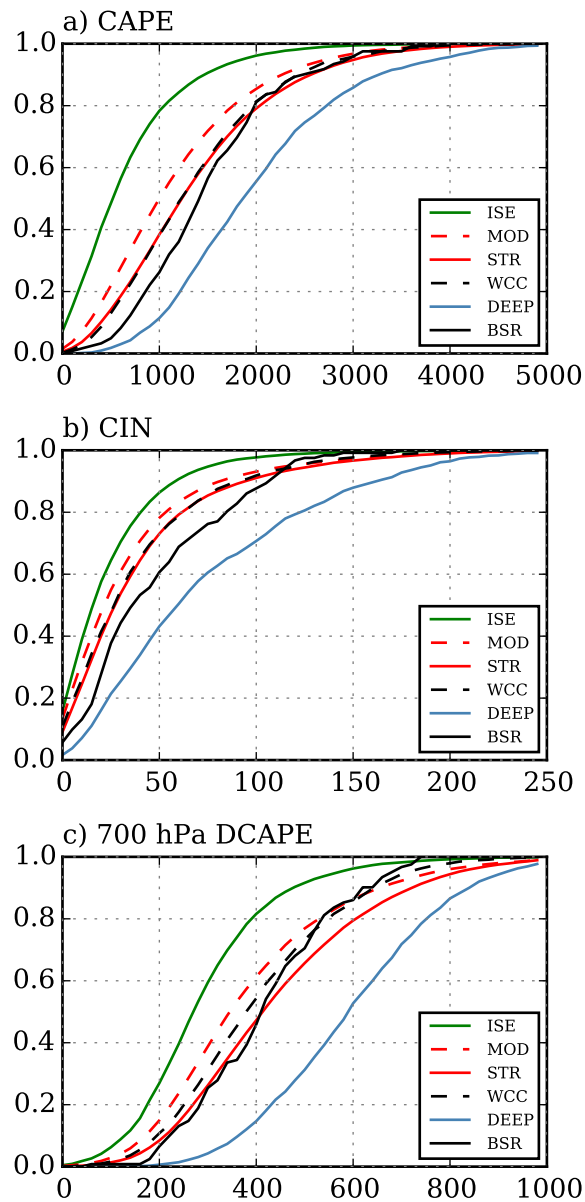nformation from DCC and DWC are combined to "DEEP". From Maranan et al. (2018), Figure 10, Copyright ©2018, John Wiley & Sons Ltd.

It shall be stressed here that the environmental conditions shown in Figures 4.8 and 4.9 are bulk means. In fact, pre-storm conditions for all rainfall categories exhibit large variations specifically with respect to the magnitudes of vertical wind shear (cf. Nicholls and Mohr; 2010) and low-level convergence, which are masked out in the composites. Figure A.4 in the Appendix shows the broad range of values for the magnitude of vertical wind shear and low-level convergence before the occurrence of MCS-type rainfall systems. In a similar fashion, the thermodynamical controls prior to the rainfall event show strongly varying values as indicated in Figure 4.10 which shows the cumulative distribution function of the (lowest 100 hPa based) CAPE, CIN and 700 hPa based DCAPE (see chapter 3) averaged over the 24-h period before the onset of the events. As mentioned earlier, DCAPE quantifies the potential acceleration of an air parcel cooled by evaporation when it descends pseudo-adiabatically towards the surface. Thus, it can serve as an estimator for the strength of a coldpool and the potential degree of self-sustainment of an MCS. It shall be stressed that the purpose of comparing ERA-Interim derived convective indices is to highlight differences in the thermodynamic fields among the rainfall categories. Since these indices are generally influenced by model numerics and parameterisations in analysis products (Molini et al.; 2011), the focus here is more on comparison between rainfall categories and less on absolute values. All three thermodynamical variables are lognormally distributed which reflects the highly variable conditions under which the rainfall categories of different degrees of organisation occur. However, with respect to the overall representation of the curves, three distinct groups can be identified: First, ISEs stand out exhibiting the lowest median values in CIN (-20 J kg^{-1}), CAPE (618 J kg^{-1}) and DCAPE values (-290 J kg^{-1}). Such low CAPE and CIN conditions are known to be prevailing over the ocean (Riemann-Campe et al.; 2009). As such, ISEs form in a moisture-laden troposphere (see background value of PW in Figure 4.9a), which explains the maximum frequency in the Sahelian phase in all regions. As seen in Figure 4.8 it is established through deep southwesterly anomalies before the event. The second group contains MODs, STRs, WCCs and BSRs. The group median values are -29 J kg^{-1} for CIN, 1222 J kg^{-1} for CAPE and -398 J kg^{-1} for DCAPE. The fact that this group includes categories of varying intensities and degree of organisation insinuates that the magnitude of the thermodynamic variables are of lesser importance for the higher organised categories WCC and BSR, particularly if coldpool dynamics start dominating the initiation process of new convective cells. This is also evident in Fink et al. (2006) where no clear relationship between rainfall type and the magnitude of radiosonde derived convective indices before the rainfall event was evident. The third group is formed by DEEP (DCCs + DWCs) that exhibit the highest median CIN, CAPE and DCAPE values (CIN: -64 J kg^{-1}, CAPE: 1962 J kg^{-1}, DCAPE: -610 J kg^{-1}). As DEEP are predominantly phenomena during the coastal phase, this reflects the conditions during that stage of the WAM season. Composite vertical profiles from ERA-Interim of temperature and dewpoint temperature reveal that higher DCAPE is caused by the presence of drier air at midlevels (cf. Figures 4.9d and 4.9f), while the higher values of CIN and CAPE are due to drier and warmer low levels, respectively (not shown). Therefore, moisture convergence is crucial as it acts to lower CIN (not shown) while high CAPE explains the deep nature of DCCs and DWCs.

4.7   Link between TRMM-PR and IR-based rainfall types

Since TRMM-PR provides only snapshots, no further information about the lifecycle of the observed convective systems can be extracted. Up to this point, all rainfall systems in the TRMM-PR have the same "lifetime", i.e. one hour, and thus, do not develop from or into one of the other categories. The advantage of IR imagery is its ability to continuously observe cloud features and their development with high spatial and temporal resolutions. Thus, this section attempts to shed light on the question how the categories defined on the basis of TRMM-PR are related to existent IR-based classifications of convective systems by earlier studies.

An overview is given in Figure 4.11a, which shows a two-dimensional histogram of convective systems with respect to the mean storm velocity and lifetime. Here, only those systems were included that intersected the domain from 4°N–12°N and 10°W–10°E and that underwent a clean lifecycle of at least 1h, i.e. no splitters or mergers by definition (see section 4.3). First, the IR-based classification of Lafore et al. (2017c) is applied. The sample is split into four classes: C1 are short-lived (i.e. <9h of lifetime) and slow systems (i.e. <10 m s^{-1}) and C2 are long-lived and slow. Accordingly, C3 are short-lived but fast moving convection while C4 are fast, long-lived systems. It becomes evident that the majority of convective systems over SWA exhibit a rather short lifetime. Around 94% belong to the short-lived classes C1+C3. However the storm velocities are quite variable and can reach up to 20 m s^{-1}. Overall, the average velocity is around 8.2 m s^{-1}. As the lifetime of convective systems increases, there is a clear lower and upper limit for the storm velocity at which such systems propagate. For systems with a lifetime >24 h, there are very few systems propagating slower and faster than 5 and 15 m s^{-1}, respectively. The latter value is comparable to highly organised systems in the Soudan and Sahelian region, where systems move at an average speed of 12 to 13.5 m s^{-1} (Mathon and Laurent; 2001; Fink et al.; 2006), in some cases even faster than 15 m s^{-1} (Schrage et al.; 2006). Considering the classes of long-lived systems (C2+C4), an average speed of 9 m s^{-1} and 10.3 m s^{-1} is found for those with a lifetime of >24 h. From Figure 4.11b, which shows the mean lifetime-spanning minimum brightness temperature (Tb$_{min}$) of the cloud top for each bin, a relationship between lifetime and Tb$_{min}$ becomes evident. Cloud top temperatures of very long-lived systems (>24h) can drop lower than 190 K, while the average temperatures gradually increase for shorter lifetimes. Systems within C1 and C3 rarely exhibit Tb$_{min}$ lower than 200 K on average. These long-lived systems typically originate in the proximity of elevated terrain and are found in higher numbers during the coastal and retreat phases of the WAM (not shown).

Table 4.1 summarises the assignment of the TRMM-PR rainfall categories to the aforementioned IR-based classification. Being warm cloud systems by definition (i.e. cloud top temperatures above freezing), ISEs are excluded from this analysis as such clouds were not tracked. In addition, some systems of the other categories were not incorporated in the analysis for two reasons: First, splitters and mergers are not considered. The percentage of convective systems that were omitted for this reason is denoted as "Split and/or merge" in Table 4.1. A relatively high fraction (>30%) of WCCs, DWCs and BSRs originate from split and/or end their lifecycle by merging with another convective system. This fraction is lower for the less intense categories
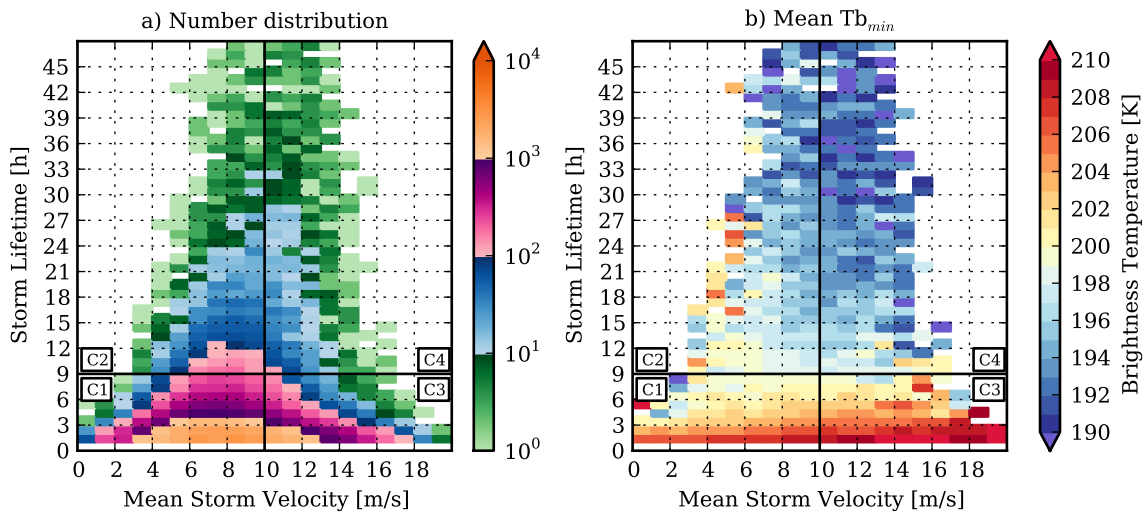
Figure 4.11: 2D-histograms of (a) the number of convective systems in relation to their mean translation speed (abscissa, in m s^{-1}) and their lifetime (ordinate, in hours) and (b) the minimum brightness temperature (Tb$_{min}$) of the cloud-top averaged over the whole lifetime for each bin. Convective elements were detected through the tracking routine described in section 4.3 that was applied on the IR dataset of SEVIRI for the period 2004–2013. Note that convective systems originating from a split or ending up as a merger are not included to avoid contamination of the distribution with respect to lifetime. Furthermore, only convective systems with a lifetime >1h are presented. Only the first 48 hours of lifetime are displayed. The convective systems are classified in four groups after Lafore et al. (2017c): short-lived (i.e. <9h of lifetime) and slow systems (i.e. <10 m s^{-1}) as C1, long-lived and slow systems as C2, short-lived and fast systems as C3 and fast, long-lived systems as C4. From Maranan et al. (2018), Figure 11, Copyright ©2018, John Wiley & Sons Ltd.

MOD and STR. Second, some systems are unassigned, as they fail to match at least one of the thresholds for area (900 km^2) and temperature (233 K) of the tracking routine (denoted as "no label" in Table 4.1). This applies to 63% of MODs and 79% of STRs.

As expected, BSRs are purely long-lived systems (i.e. a lifetime > 9h) and tend to be faster than 10 m s^{-1} (C4=69.2% compared to C2=30.8%). Longevity is also emphasised for the wide classes WCC (C2+C4=66.8%) and DWC (C2+C4=84.4%). The fact that the majority of BSRs and DWCs belong to the faster category reflects their typical environment with high vertical wind shear (see Figure 4.8). For shear-perpendicular linear systems, such as squall lines, high vertical wind shear is known to be crucial for the generation of new cells on the downshear side of the systems (e.g. Rotunno et al.; 1988) and effectively leads to a higher translation speed. Note that this does not hold for shear-parallel systems and/or non-linear systems (e.g. Nicholls and Mohr; 2010) which might be represented by the slower category C2. From Table 4.1, the mean velocity of MCS-like categories ranges from 9.3 to 10.6 m s^{-1}. STRs and DCCs are predominantly slow systems (C1+C2 is 66.4% and 68.9%, respectively) whereas, interestingly, 63.4% of MODs are assigned to long-lived convection. However, it can be assumed that the fraction of MODs contributing to the short-lived classes C1 and C3 is higher than indicated. As mentioned above, a high percentage of the sample drops out of analysis also due to the temperature restriction of the tracking routine.

Table 4.1: Assignment of TRMM-based rainfall categories to IR-based categories C1–C4, as defined by Lafore et al. (2017c) (for details see text and Fig 4.11). "Sample size" denote the number of convective systems that are available from 2004-2013 from the TRMM-PR dataset. "no label" indicates the percentage of "Sample size" that was missed by the tracking routine due to unmatched temperature and/or area size thresholds. "Split and/or merge" indicates the percentage of "Sample size" that is omitted because it originates from a split and/or ended as a merger, both of which is not considered for Figure 4.11. From Maranan et al. (2018), Table 1, Copyright ©2018, John Wiley & Sons Ltd.

TRMM-PR category	C1	C2	C3	C4
BSR	0.0%	30.8%	0.0%	69.2%
DWC	12.2%	35.6%	2.6%	49.6%
WCC	24.3%	38.3%	7.8%	29.6%
DCC	40.7%	28.7%	10.8%	19.8%
STR	43.3%	24.3%	13.2%	19.2%
MOD	29.5%	34.3%	7.2%	29.0%

TRMM-PR category	Sample size	no label	Split and/or merge	Avg. speed [m/s]
BSR	65	0%	38%	10.6
DWC	158	0%	31%	9.9
WCC	1538	3%	36%	9.3
DCC	376	6%	21%	8.6
STR	12640	63%	12%	8.8
MOD	14314	79%	7%	9.1

The fact that short-lived systems exhibit the warmest cloud tops (Figure 4.11b) suggests that a larger fraction of unassigned MODs may fall into either of the categories C1 or C3. This likely holds for STRs, too.

In a further analysis, the IR classification introduced in Mathon et al. (2002) and Fink et al. (2006) is applied. The authors define cloud features with a contiguous area of at least 5000 km^2 and a temperature of ≤233 K as MCSs. Furthermore, OCSs (organised convective systems) are identified if the cloud exhibit a contiguous area of ≤213 K exceeding 5000 km^2 for at least three subsequent hours. Additionally, systems must propagate at an average speed of ≥10 m s^{-1}. The occurrence frequency of MCSs as a function of mean speed and storm lifetime is shown in Figure 4.12a. Here, the frequency is determined as the number of storms that fulfil the MCS criterion for at least one time step (i.e. 15 minutes) divided by the total number of identified convective systems per bin (see Figure 4.11a). The MCS occurrence frequency depends on storm lifetime but already reaches a percentage of >90% at six hours. Around 98% of all systems with a lifetime longer than six hours are MCSs. In contrast, OCSs are less frequent (Figure 4.12b), primarily since a mean velocity of at least 10 m s^{-1} is a necessary condition for an OCS as mentioned above. However, of all systems that exceed 10 m s^{-1} and live longer than six hours, only around 66% reach the stage of an OCS. The 90% mark is reached around a storm lifetime of 14 hours. Around this value, there is a slight tendency for more OCSs with faster propagation. This supports the suggestion that a strongly sheared environment, which is assumed to be associated with faster propagation

of convective clouds (e.g. Fink et al.; 2006), favour the development of highly organised systems (Schrage et al.; 2006).
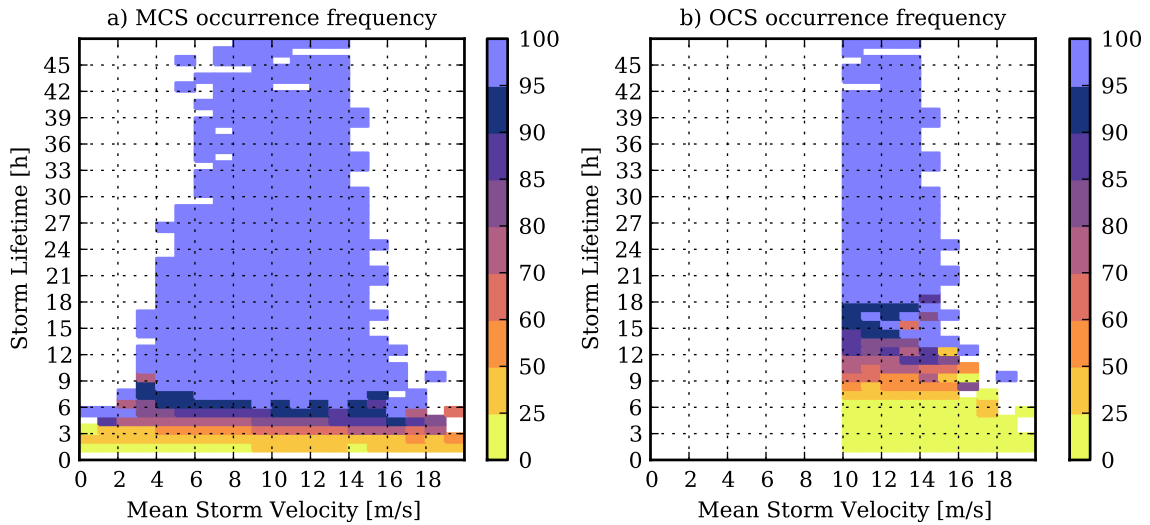
Figure 4.12: 2D-histograms for (a) the occurrence frequency of MCSs and (b) the occurrence frequency of OCSs per bin expressed in percent. The definition of MCSs and OCSs follows Mathon and Laurent (2001) and Fink et al. (2006). For each bin, the frequency was calculated by the number of MCS/OCS divided by the total number of convective systems of the respective bin (see Figure 4.11a). From Maranan et al. (2018), Figure 12, Copyright ©2018, John Wiley & Sons Ltd.

In Table 4.2, the fraction of the TRMM-PR categories fulfilling the definition of MCSs and OCSs is presented. Generally, the fraction of systems that become MCSs at one point during their lifetime is high. Not surprisingly, all the BSRs and DWCs reach the MCS stage. The fraction is lowest for STRs at 80.7%. The fact that MODs exhibit a higher value than STRs may again be a reflection of the sampling issue for MODs that became evident in Table 4.1. The percentage of systems becoming an OCS is substantially smaller than that for MCS for every TRMM-PR category. Again, BSRs and DWCs exhibit the highest fraction with 68.2 and 52.2%, respectively. For WCCs the fraction already drops to 30.2%. The major limiting factor in this context is the velocity threshold of 10 m s^{-1} for OCSs, which is only exceeded by BSRs on average (Table 4.1). Nonetheless, for WCCs, a bit less than a third of all MCSs become OCSs (31.4%). This MCS-to-OCS conversion rate is lowest for DCCs and STRs at 23.1% and 25.1%, respectively.

4.8   Summary and discussion

In a novel approach, datasets from the TRMM-PR, ECMWF reanalysis and Meteosat to explore the rainfall characteristics over SWA from a climatological perspective. The results have shown that the majority of rainfall over SWA is provided by MCS-type rainfall systems with extensive convective and stratiform regions, although they are considerably outnumbered by smaller and less-intense rainfall types. There is a latitudinal dependence with the relative contribution of MCSs to total rainfall decreasing southward (71% in the Soudan region to 56% at the coast), while

Table 4.2: Assignment of TRMM-based rainfall categories to the IR-based categories MCS and
OCS as defined in Mathon and Laurent (2001) and Fink et al. (2006). "MCS-to-OCS conversion"
indicates the percentage of MCSs that eventually reached the stage of an OCS. From Maranan
et al. (2018), Table 2, Copyright ©2018, John Wiley & Sons Ltd.

TRMM-PR category	MCS	OCS	MCS-to-OCS conversion
BSR	100%	68.2%	68.2%
DWC	100%	52.2%	52.2%
WCC	96.1%	30.2%	31.4%
DCC	93.7%	21.6%	23.1%
STR	80.7%	20.2%	25.1%
MOD	90.7%	28.9%	31.9%

the contribution of weaker convective systems increases. Typically, these less-intense rainfall
systems are phenomena which occur predominantly in the afternoon, whereas the MCS types
organise later in the evening and mature in the night. The general implication of these findings
is that the frequency of MCSs crucially determines the magnitude of annual rainfall. However,
their importance is progressively reduced towards the moister coastal region where non-organised,
diurnal convection becomes more and more significant.

The different character of rainfall at the immediate coastline compared to the regions farther
inland was highlighted as well. Not only is the fractional occurrence of shallow, pure warm-rain
events highest at the coast, but the initiation of isolated diurnal convection as well as intense con-
vective lines parallel to the coast is also shifted forward in time by around two hours to midday
and early afternoon. In a consistent manner, long-term rainfall measurements across Benin for
the period 1962–1990 have shown highest rainfall probability in the morning hours at coastal
stations (Fink et al.; 2008). The rainfall probability then swiftly shifts to the late afternoon at
inland stations. Therefore, coastal rainfall on a diurnal timescale is likely dominated by the ef-
fects of land-sea-breeze interactions, promoting both typical oceanic phenomena such as shallow,
warm-rain clouds through the establishment of a more maritime environment and intense coastal
convection through sea-breeze convergence. The general importance of warm-rain events to total
rainfall over SWA is difficult to discern. Contrary to their high numbers at the coast, the results
indicate that the importance of these shallow warm-rain events with respect to total rainfall is
quite low (2%). However, with respect to their definition in this chapter, they only comprise
the isolated, convective elements below freezing-level (Schumacher and Houze; 2003). In fact,
warm-rain processes are not only constrained to e.g. stand-alone, isolated clouds (Liu and Zipser;
2009) nor to environments with temperatures above $0°C$ (i.e. supercooled clouds, e.g. Huffman
and Norman Jr; 1988). In chapter 6, ground-based rainfall measurements are used in combination
with satellite-based cloud data to obtain a refined quantification of warm rain.

In composited vertical profiles derived from ERA-Interim fields, the (thermo-) dynamic condi-
tions and their evolution around the time of occurrence of each rainfall type were presented. The
typical environmental conditions for each rainfall type defined in this chapter are summarised in
Table 4.3. On that note, it shall be stressed again that the composites presented in Figures 4.8

and 4.9 conceal strong variations in the environmental controls under which the various range of rainfall categories develop over SWA. In principle, rainfall events are accompanied by midlevel vorticity anomalies that have a direct impact at least on the low-level (i.e. 600–925 hPa) wind shear. The passage of a cyclonic (anticyclonic) disturbance coincides with decreased (increased) wind shear due to southwesterly (northeasterly) anomalies at midlevels. These two regimes promote rainfall types on opposite sides of the intensity spectrum. A higher degree of convective organisation is found in situations of enhanced shear, leading to the occurrence of MCS-type rainfall systems, particularly fast-moving squall lines as found in Schrage et al. (2006). In contrast, less intense convective systems typically occur in areas of suppressed wind shear under the influence of a single cyclonic disturbance. Particularly deep westerly anomalies are typically accompanied by weak but long-lasting rainfall, termed as "vortex-type rainfall" by Fink et al. (2006) and Schrage et al. (2006). Furthermore, the modulation of vertical wind shear was found to be particularly pronounced during the passage of an AEW or similar wave disturbances. The most (least) intense rainfall types (i.e. MCSs with a developed convective and stratiform region and isolated shallow echoes, respectively) are typically located in the region west (east) of the wave trough, i.e. the regime of highest (lowest) low-level wind shear. This is in line with a recent study by Janiga and Thorncroft (2016) who found more intense systems in the area of AEW maximum northerlies ("N" or AEW phase 2, west of the wave trough) and a larger amount of weak systems in the region of maximum southerlies ("S" or AEW phase 6, east of the wave trough).

However, the location of mature MCSs (i.e. BSRs) within the wave signature and the structure of the wave itself is region dependent (see Figures A.1–A.3). While the aforementioned dipole structure of vorticity is typical for the Soudan region, it becomes less pronounced in near coastal areas. Furthermore, mature MCSs tend to occur closer to the center of the cyclonic disturbance. Interestingly, the opposite is true for non-organised shallow convection whose occurrence is drawn closer to the cyclonic disturbance over the Soudan region. This latitudinal region dependence for favourable conditions of organised convection in coastal and continental regimes over West Africa has already been mentioned in early studies (e.g. Asplided et al.; 1976; Duvel; 1990) and also draws comparisons to the oceanic-continental regimes described in Janiga and Thorncroft (2016).

Unlike vertical wind shear, the results suggest that thermodynamic conditions (measured by CAPE, CIN and 700 hPa DCAPE) are of small importance for the horizontal growth of convective systems, but rather indicate the potential of their initial vertical development. In a similar fashion, Fink et al. (2006) found no substantial relationship between the magnitude of CAPE and CIN and the degree of convective organisation which may be attributed to the lower dependence of coldpool dynamics of higher organised systems on the thermodynamical condition to initiate new convective cells and thus to increase lifetime. However, CAPE, CIN and DCAPE tend to be highest for systems with intense deep convective cores (DCC and DWC, later combined to "DEEP"). Furthermore, as they are predominantly found early in the WAM season (March to May), the high values are likely to reflect the typical environmental conditions during this period, comparable to a regime described in Vizy and Cook (2018) and also Parker et al. (2005b). The latter is depicted in Figure 3.12. The poleward flank of the AEJ, where SWA is situated early in the year, is characterised by a moist low-level monsoon layer overlain by dry air of high po-

tential temperature that may in some cases originate from the Sahara region through shallow dry convection (see also Sultan and Janicot (2003) and Figure 3.9). Within the dry mid-levels, there is often a near dry adiabatic lapse rate that can create a layer of high conditional instability and may favour the development of these deep convective cores once latent heat is released within the clouds. On the other hand, the mid-levels equatorward of the AEJ are more stable and moister and prevail particularly in the peak monsoon season in July and August (termed Sahelian phase in this chapter) over SWA, during which the occurrence of these deep core systems decreases and that of non-organised, shallow warm-rain system is promoted. The relatively large differences of CAPE and DCAPE values between the deep core categories and shallow convection may reflect these contrasting mid-level regimes.

Low-level convergence and a subsequent increase of low-level moisture prior to the rainfall event is a common feature among all rainfall types. It is strongest in the case of mature MCSs whose convective and stratiform structures appear to be well captured by ERA-Interim. This specifically leads to a lowering of CIN (not shown) and higher PW, the latter being more a consequence of the system passage. This is consistent with the presumption of Dezfuli et al. (2017) that low-level convergence is a necessary condition for convection over West Africa. However, for the more humid SWA, the results suggest that the absolute value of PW is not a suitable predictor for the different rainfall types, since the background PW is high. Similarly, Nicholls and Mohr (2010) showed that PW does not yield significant results for the prediction of the intensity of convective systems over West Africa, not even in the drier regions. The convergent motions and the associated increase of PW rather determine where convection in general is more likely to occur.

Comparisons with IR-based classifications of convective systems of Lafore et al. (2017c) (C1–C4 classifcation) and Mathon et al. (2002) and Fink et al. (2006) (MCS-OCS classification) were performed by overlaying IR SEVIRI images onto the TRMM-PR snapshots. IR-based track information was used in the process to assign the TRMM-PR categories to classes defined by the above-referenced studies. This sequential approach was motivated by the fact that TRMM-PR does not provide continuous observations of rainfall and thus no information about the lifecycle of convective systems. The degree of horizontal growth of a convective system is an indicator for the length of its lifetime. While mature MCSs (i.e. BSRs) are almost exclusively long-lived systems (i.e. >9h), less intense rainfall types are predominantly short-lived, diurnal phenomena. Furthermore, the majority of these BSRs (almost 70%) are fast-moving systems as well (i.e. a mean velocity of ≥ 10 m s^{-1}). This is part of the definition of the C4 class in Lafore et al. (2017c) and of OCSs in Mathon et al. (2002) and Fink et al. (2006), which is assumed to represent West African squall lines. Yet, the three MSCs-like systems are slower than in the Sahel, a finding consistent with Fink et al. (2006) and Lafore et al. (2017c), and tend to occur predominately during the early part of the first coastal rainy season. As the environment around BSR events show indications of AEWs, this can be considered as a testimony of the relevance of wave disturbances to the existence of squall lines (e.g. Fink and Reiner; 2003). However, not every AEW is accompanied by a BSR nor do BSRs solely develop under the presence of AEWs. It is further complicated by the fact that mid-level wave disturbances in SWA can be of non-AEW type (Knippertz et al.;

Table 4.3: Qualitative summary of the (thermo-) dynamical conditions during the passage of the TRMM-PR based rainfall categories, sorted by their rainfall production after Figure 4.4b from low to high. The AEW phases were taken from e.g. Reed et al. (1977) and Janiga and Thorncroft (2016). A differentiation was made between the AEW phases for the Coast region, the Inland region and the Soudan region, based on Figures A.1–A.3 in the Appendix. From Maranan et al. (2018), Table 3, Copyright ©2018, John Wiley & Sons Ltd.

No.	Category	Windshear	CAPE	CIN	DCAPE	Possible AEW phase (Coast/Inland/Soudan region)
1	ISE	Low	Low	Low	Low	7/6/5
2	MOD	Low	Medium	Medium	Medium	–
3	STR	Medium	Medium	Medium	Medium	–
4	DCC	High	High	High	High	–
5	WCC	Medium	Medium	Medium	Medium	3/2/2
6	DWC	High	High	High	High	–
7	BSR	High	Medium	Medium	Medium	4/3/2

2017). Moreover, less intense rainfall systems, which typically occur in the absence of AEWs, can sometimes exhibit long lifetimes. This demonstrates that the understanding of the relationship between wave disturbances and rainfall systems can still be further improved.

5. Case study of an extreme MCS event on 10–13 June 2016 during the DACCIWA field campaign

5.1 Preface

With modifications in text and figures, the following chapter has been published on 11 June 2019 as a research article by the Monthly Weather Review of the American Meteorological Society with the title "Interactions between convection and a moist vortex associated with an extreme rainfall event over southern West Africa", authored by Marlon Maranan, Andreas H. Fink, Peter Knippertz, Sabastine D. Francis, Aristide B. Akpo, Gbenga Jegede and Charles Yorke (doi: `10.1175/MWR-D-18-0396.1`; ©American Meteorological Society. Used with permission.)

The previous chapter has shown that organised convection account for the majority of rainfall over SWA despite their relatively low frequency. Therefore, MCSs remain a vital source for the hydrological budget in this region. However, due to their strength, rainfall associated with MCSs can also be extreme. Despite the impacts that extreme rainfall can have over West Africa as mentioned in the introduction, there is a dearth of studies investigating their dynamic controls. Because of its impactful nature causing a record-breaking daily rainfall amount of 263 mm, the Ouagadougou case in 2009 in the Soudano-Sahelian region of Burkina Faso was strongly covered in recent studies (Galvin; 2010; Lafore et al.; 2017a; Engel et al.; 2017). From a dynamical perspective, the event was caused by the "breaking" of the arguably strongest AEW in the 1974–2014 period and a subsequent formation of an intense mid- to low-tropospheric vortex, which led to excessive precipitable water (PW) and a slow-down of the movement of an associated MCS.

In a not less extreme fashion, a series of intense convective systems caused one of the highest ever recorded daily rainfall amounts in the Guinea Coast region at the southern Nigerian station Abakaliki during the DACCIWA campaign on 12 June 2016 (223.5 mm) and more than 100 mm at coastal stations farther west on the following day. In anticipation of the following sections, it involved a long-lived MCS that formed in western Sudan over the Darfur Mountains and eventually crossed almost the entire Guinea Coast in a span of around three days. This MCS traversed the different ambient conditions of the dry Savannah and the moister Guinea Coast region, dur-

ing which fundamentally different interactions between the MCS and the environment took place that caused its longevity. Several in-situ measurements from the DACCIWA campaign as well as space-borne observations and the new reanalysis cycle ERA5 of the European Centre for Medium-Range Weather Forecasts (ECMWF) are synthesised in order to investigate the (thermo-)dynamic controls that led to the extreme nature of this rainfall case. It serves as an example of how rainfall is brought to SWA.

5.2   Data sources and methods

5.2.1   Global reanalysis data

A major part of this study is based on the fifth generation of the ECMWF reanalysis ERA5 (Hersbach and Dee; 2016), successor of ERA-Interim (ERA-I, Dee et al.; 2011). ERA5 is provided on an hourly basis and has a native horizontal resolution of 0.28125° (approximately 31 km). For the sake of convenience, the atmospheric fields were interpolated onto a 0.3° grid. By the time this chapter was compiled, ERA5 was available only from 2000–2018, but will eventually be extended back to the beginning of ERA-I in 1979. Thus, ERA-I was used for the analysis of long-term periods. The fields are confined to the domain of study illustrated in Figure 5.1. The thermodynamic metrics convective available potential energy (CAPE), convective inhibition (CIN) as well as downdraft CAPE (DCAPE) were estimated from the reanalysis using vertical profiles based on 137 model levels in the ERA5 dataset. If not noted otherwise, the mixed-layer CAPE concept over the lowest 100 hPa was applied to determine the theoretical path of an air parcel. DCAPE quantifies the maximum kinetic energy a hypothetical air parcel could gain as it descends along a pseudoadiabat due to evaporative cooling (Gilmore and Wicker; 1998) and can therefore serve as an estimator for the strength of a convective coldpool. The initial height for the calculation of DCAPE was set to 650 hPa, where typically the lowest values of equivalent potential temperature in the midlevels were identified in this case study (not shown). Furthermore, the temperature profiles were virtual-temperature corrected to account for the additional buoyancy caused by humidity (Doswell III and Rasmussen; 1994). Precipitation in ERA5 is only available in the forecast, provided twice per day at 0600 and 1800 UTC. Precipitation timeseries were compiled by using the forecast beginning at hour 6 (i.e. 1200 UTC in the 0600 UTC forecast, for instance) up to the point where hour 6 is reached in the new forecast (i.e. 0000 UTC in the 1800 UTC forecast accordingly) to leave some time for spin-up. Thus, the precipitation timeseries of ERA5 consists of a series of forecasts.

5.2.2   Cloud datasets

Equally to the previous chapter, IR satellite data from the SEVIRI as well as the tracking algorithm were used to monitor the life cycles of the convective systems that are involved in this study. The translation velocity of a convective system was obtained by calculating the spatial shift of the "center of mass" for the 233 K cloud top envelope divided by the temporal resolution of 15 minutes. Due to the existence of splits and mergers (e.g. Mathon and Laurent; 2001) the
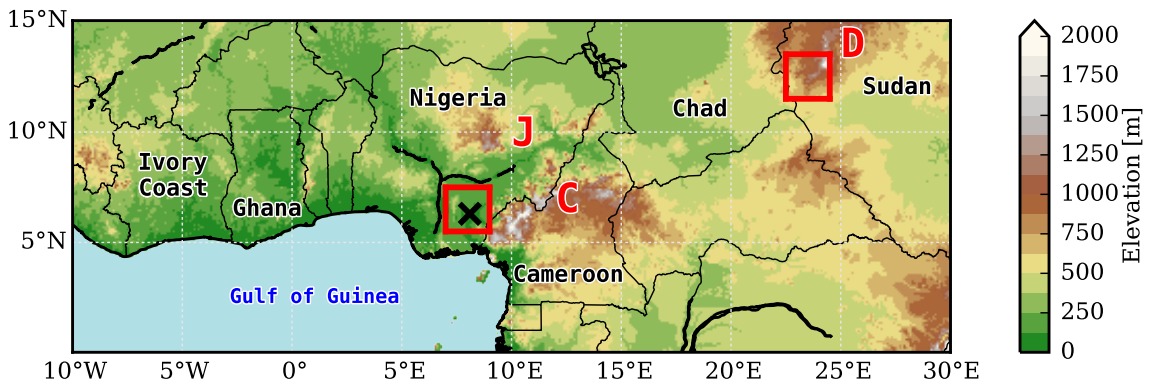
Figure 5.1: Map showing Central and West Africa. Shading denotes the terrain elevation as provided by the Global Land One-km Base Elevation Project (GLOBE) (Hastings et al.; 1999). Countries mentioned in the text are indicated. Red capital letters denote the Darfur Mountains (D), Jos Plateau (J) and the Cameroon Highlands (C). The red boxes denote the area where spatial averages are performed in sections 5.4 and 5.5. The black x-mark indicates the location of the rain gauge station Abakaliki. From Maranan et al. (2019), ©American Meteorological Society. Used with permission.

translation velocity can attain unphysical values at some timesteps. Those were omitted in the analysis. Furthermore, a two-hour running mean was applied for smoothing purposes.

An analysis of the upper-tropospheric wind field was performed using atmospheric motion vectors from EUMETSAT, which have been made available for a wide range of spectral channels on an hourly basis. The analysis is restricted to the water vapour channel 5 with a centre-wavelength of 6.2 μm for two reasons: First, the mid- and lower troposphere are usually opaque over the tropical regions in the water vapour channels due to high moisture availability. Therefore, mostly upper-level wind information remain. Secondly, the corresponding upper-level divergence product of EUMETSAT has currently been computed for channel 5 only (EUMETSAT; 2015).

Aside from the continuously measuring SEVIRI instrument, the analysis makes use of spaceborne passive microwave (MW) radiometer datasets from the five-channel Microwave Humidity Sounder (MHS) and from the six-channel Sounder for Probing Vertical Profiles of Humidity (SAPHIR) of the satellite mission Megha-Tropiques. The MHS is currently deployed onboard the American weather satellites NOAA-18 and NOAA-19 as well as the European MetOp-A and MetOp-B on a sun-synchronous orbit at nominal altitudes of around 870 km and 820 km, respectively (Arriaga; 2000; Bonsignori; 2007). It provides information on 90 cross-track pixels per scan line with a footprint diameter of 16 km at nadir over a swath width of roughly 1920 km. For reasons described in Redl et al. (2015), only the 157-GHz channel is used for the analysis. SAPHIR operates with six channels near the 183.31-GHz water vapour absorption line at a nominal altitude of 867 km (Desbois et al.; 2007). Like the MHS, SAPHIR scans with a cross-track viewing geometry, but at a resolution of 10 km at nadir over a swath width of approximately 1705 km. The 183.31 ±11 GHz channel corresponds to the observation of the 250-100 hPa layer (Subrahmanyam and Kumar; 2013) and was therefore chosen to obtain cloud top information.

5.2.3   Rainfall and weather observation

The spaceborne rainfall mission Global Precipitation Measurement (GPM) went fully operational in early 2014 and replaced its successful predecessor Tropical Rainfall Measuring Mission (TRMM) (Simpson et al.; 1996; Kummerow et al.; 1998, 2000). The spatial coverage of the gridded rainfall product Level 3 Integrated Multi-Satellite Retrievals for GPM (IMERG, Version 5), which will be described in more detail in chapter 6, extends from the tropical belt well into the midlatitudes up to 60° of either hemisphere and updates rainfall estimates every 30 minutes at a spatial resolution of 0.1° (Hou et al.; 2014). IMERG is a blended product that consists of MW estimates as well as MW-calibrated IR estimates, if MW information is absent. Regional rainfall biases are then corrected by the incorporation of monthly rain gauge data. A step-by-step description of the algorithm is given in Huffman et al. (2015). Alongside IMERG, this study uses information from over 350 rain gauge stations, distributed over the Guinea Coast region comprising 10°W – 10°E and 4°N – 8°N. First observations at some stations date back to the year 1888 (for June–July 2016, see Fink and Njeri; 2018). However, the overall spatiotemporal coverage is highly variable and depends on both station and country (not shown).

Reports on weather conditions were taken from selected stations, namely Abidjan (Ivory Coast, WMO-number: 65578) and Axim (Ghana, 65465). Both the FM-12 (SYNOP) and FM-15 (METAR) report formats are available for Abidjan, only FM-12 is present for Axim. The report formats are described in WMO (2009) in more detail. Additionally, vertical wind profiles from radiosonde launches at the airports of Cotonou (Benin, 65344), Abuja (Nigeria, 65125) and Enugu (Nigeria, 65257) were used to investigate pre-storm conditions (Maranan and Fink; 2016). Note that radiosonde data of Abuja and Enugu are not disseminated operationally through the Global Telecommunication System (GTS) and are therefore not assimilated in reanalysis data such as ERA5.

5.2.4   Pressure tendency and vorticity equation

The pressure tendency equation (PTE) has been applied in earlier studies to investigate the intensification of cyclones in the tropics (Kong; 2006) and extratropics (Fink et al.; 2012), but also for the analysis of synoptic-scale dynamics in tropical West Africa (Knippertz and Fink; 2008). The analysis follows PTE description of Fink et al. (2012):

$$\frac{\partial p_{sfc}}{\partial t} = \rho_{sfc} \frac{\partial \phi_{p_2}}{\partial t} \qquad\qquad (D\phi)$$

$$+ \rho_{sfc} R_d \int_{sfc}^{p_2} \frac{\partial T_v}{\partial t} \ d\ln p \qquad\qquad (ITT)$$

$$+ g\,(E - P) \qquad\qquad (EP)$$

$$+ RES_{PTE} \qquad\qquad (5.1)$$

where p_{sfc} is the surface pressure, ρ_{sfc} the air density at surface level, R_d the gas constant of dry air, T_v the virtual temperature, g the acceleration of gravity. The upper boundary p_2 was chosen to be 100 hPa. The four terms on the right-hand side (rhs) that affect the pressure tendency (Dp) are

the temporal change in upper-boundary geopotential ($D\phi$), the vertically integrated temperature tendency (*ITT*), the net mass change due to precipitation P and evaporation E (*EP*) and a residual term due to spatiotemporal interpolation and discretisation (RES_{PTE}). Note that Dp can be calculated directly from the temporal change of the mean sea level pressure (MSLP) in the surface dataset of ERA5.

The *ITT* term, in turn, can be expanded as:

$$ITT = \rho_{sfc} R_d \int_{sfc}^{p2} -\boldsymbol{v}_h \cdot \nabla_p T_v \; d\ln p \qquad (TADV)$$

$$+ \rho_{sfc} R_d \int_{sfc}^{p2} \left(\frac{R_d T_v}{c_p p} - \frac{\partial T_v}{\partial p} \right) \omega \; d\ln p \qquad (VMT)$$

$$+ \rho_{sfc} R_d \int_{sfc}^{p2} \frac{T_v \dot{Q}}{c_p T} \; d\ln p \qquad (DIAB)$$

$$+ RES_{ITT} \qquad\qquad\qquad\qquad (5.2)$$

where $\boldsymbol{v}_h$ and ω are the horizontal and vertical wind components, respectively, c_p is the specific heat capacity for isobaric processes, T the air temperature, p the air pressure and $\dot{Q}$ the diabatic heating rate. The surface pressure can be modified due to horizontal temperature advection (*TADV*), vertical motion and therefore adiabatic heating/cooling of air (*VMT*), diabatic processes such as latent heat release due to condensation (*DIAB*) and spatiotemporal discretisation errors (RES_{ITT}). Refer to Knippertz and Fink (2008) and the Supplementary Material of Fink et al. (2012) for the derivations of the PTE and *ITT* as well as a detailed explanation of the terms.

The vorticity equation (VTE) can be obtained by first applying the time derivative to the vertical component of the curl of the three-dimensional wind field. After incorporating the momentum equations, the local change of the relative vorticity ζ in isobaric coordinates can be expressed as (see e.g. Holton and Hakim; 2012):

$$\frac{\partial \zeta}{\partial t} = \underbrace{-\boldsymbol{v}_h \cdot \nabla \eta}_{HADV} \underbrace{- \omega \frac{\partial \zeta}{\partial p}}_{VADV} \underbrace{- \eta \nabla \cdot \boldsymbol{v}_h}_{DIV} + \underbrace{\boldsymbol{k} \cdot \left(\frac{\partial \boldsymbol{v}_h}{\partial p} \times \nabla \omega \right)}_{TILT} \qquad (5.3)$$

where f and $\eta = \zeta + f$ are the planetary and absolute vorticities, respectively, $\boldsymbol{k}$ is the vertical unit vector and the other variables are as in eqs. 5.1 and 5.2. The first and second term on the rhs of eq. 5.3 is the horizontal (*HADV*) and vertical advection (*VADV*) of absolute vorticity, respectively. The third term describes the change of vorticity through divergence (*DIV*). It is sometimes also called "stretching term", since mass continuity implies $\partial_x u + \partial_y v = -\partial_z w$, with ∂_x being the derivative in x-direction (y, z accordingly). For a divergent (convergent) flow, vorticity decreases (increases) in time. Finally, the fourth term represents changes in ζ due to an inhomogeneous vertical motion field and is also called tilting term (*TILT*). If horizontally aligned vortex tubes are present, differential vertical motion fields can act to tilt the tubes to the vertical and thus change existent ζ. These situations typically occur in environments with strong low-level wind shear alongside strong updraughts associated with convective systems. It is well known that *TILT* is vital for the development of extreme convective phenomena, such as supercells in the midlatitudes

(see chapter 3).

Both tendency equations for surface pressure and vorticity were calculated using the hourly analysis and forecast fields of ERA5. In principle, the procedure of Fink et al. (2012) is applied, but for hourly changes, that is, between t_{-1h} and t_0, and generally for a 2°×2° box (see also Figure 5.1). Furthermore, Fink et al. (2012) were not able to directly calculate *DIAB*, since diabatic heating rates were not available in ERA-I. However, they do exist in ERA5 in the forecast dataset and are therefore used for the analysis.

5.3 Overview of the extreme rainfall event

5.3.1 MCS evolution

On 12 June 2016, the weather station in Abakaliki in the southeastern part of Nigeria reported 223.5 mm in 24 hours, one of the highest daily rainfall sums ever recorded in Nigeria. Reports of high rainfall accumulations followed on 13 June at the coastal stations Axim (Ghana) with 114.8 mm and Abidjan (Ivory Coast) with 106.2 mm. The analysis of the IR-based tracking reveal that these successive rainfall events were caused by a long-lived MCS (Figure 5.2a). It formed in the afternoon of 10 June at the Darfur Mountains in western Sudan from where it grew rapidly, and quickly moved towards the southwest at an approximate peak translation velocity of 18.3 ms^{-1}. This is at the upper end of the typical range of 10-20 ms^{-1} for squall lines in northern tropical Africa (Desbois et al.; 1988; Mathon and Laurent; 2001; Fink and Reiner; 2003; Fink et al.; 2006; Schrage et al.; 2006; Laing et al.; 2008). Arriving over Nigeria in the late evening of 11 June, the MCS suddenly intensified, characterized not only by colder minimum cloud top temperatures below 190 K, but also by an overall increased area, particularly extending farther to the north (Figure 5.2a). The latter is indicated by the northward shift of the MCS track. Note that such abrupt changes in the direction of tracks are somewhat unphysical and, in this case, a consequence of a merging convective cell at the northern edge of the MCS. During 12 June, the MCS reached the northern Gulf of Guinea and moved farther west along the Guinea Coast. The minimum cloud top temperature quickly rose as soon as the MCS moved over open water, indicating a shallower cloud system. Furthermore, the translation velocity of the MCS decreased down to 11.2 ms^{-1}. By early 13 June, another turn in the track is visible over Ivory Coast (Figure 5.2a). As seen later in section 5.6, it is associated with the development of new convective cells in the wake of the decaying MCS. These convective systems, which particularly cause the high rainfall amount at Abidjan, eventually merge and intensify while moving westward. Thus, although Figure 5.2a implies one single MCS throughout, it shall be emphasised that the new convective cells continue the storm track towards the eastern Atlantic.

From the perspective of MW images of the MHS and SAPHIR (see section 5.2), Figure 5.2b shows six key stages of the development of the MCS. During its southwestward shift, the MCS evolves from a small convective cluster of two main cores at the beginning of the lifetime (snapshot 1, see textbox in Figure 5.2b for dates and times) to a moderately (snapshot 2) and eventually highly organised and well-defined squall line (snapshot 3) with a typical leading convective line
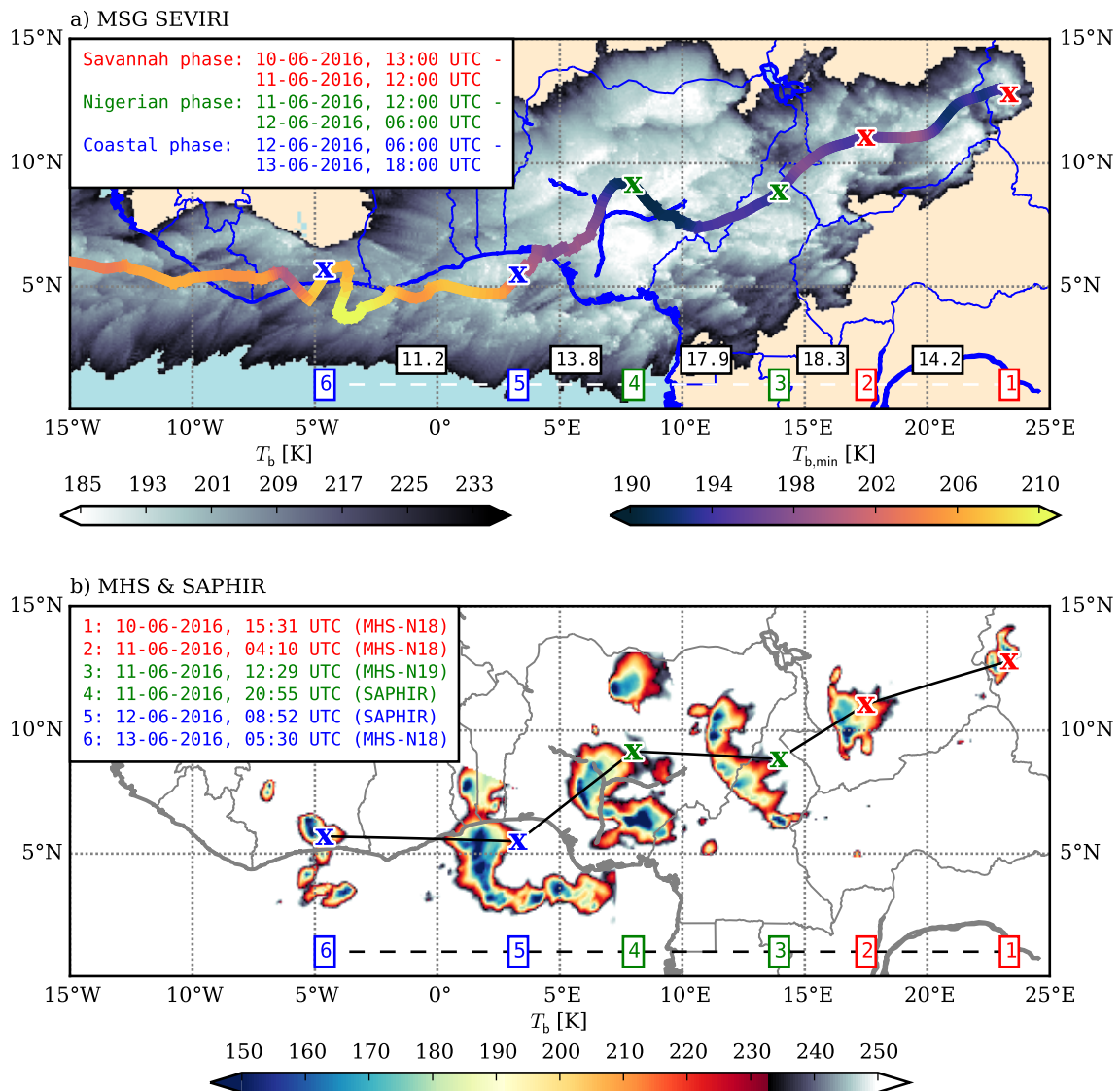
Figure 5.2: Composites of the cloud characteristics of the MCS. (a) The grayscale shading denotes the spatial extent of the MCS. The track of the weighted center of mass of the MCS is shown as a thick line, where the colours indicate the minimum SEVIRI IR brightness temperature of the MCS $T_{b,min}$ at the respective timesteps. The coloured markers along the track refer to the coloured numbers at the bottom, which in turn correspond to snapshots of the MCS as seen in (b). The marker colours refer to the textbox, where the different phases of the MCS are named (see the respective sections for more details). The values between the snapshot numbers indicate the zonal translation velocity of the MCS between the respective snapshots. (b) Snapshots from MW channels of MHS and SAPHIR of key stages in the MCSs' lifetime, which are numbered at the bottom like in (a). Note that different MW frequencies are used between MHS and SAPHIR (see section 5.2). The textbox indicates the day and time of overpass, coloured according to the MCS phases. From Maranan et al. (2019), ©American Meteorological Society. Used with permission.

and signals of pronounced scattering by ice particles (i.e. low T_b). As it intensifies over Nigeria, the MCS deforms and features three intense cores (snapshot 4). The main core crosses central Nigeria and mainly dictates the pace of the entire cloud cluster, although at an overall slower

speed than in previous stages (see Figure 5.2a). The second core is located directly to the southeast of the main core over the Abakaliki region. This core exhibits particularly low brightness temperatures (T_b <150 K), suggesting the presence of more ice particles at the cloud top and thus a more efficient rainfall production. The third convective core forms independently and crosses the northern part of Nigeria before merging with the MCS between stages 4 and 5. Cloud signatures from the three cores, which indicate their respective paths, are already visible in Figure 5.2a. While the main and northern cores clearly take a southwestward path, the core over the Abakaliki region has a slow-moving character. In more detail, successive IR cloud images around 11 June, 2000 UTC (see Figure A.5 in the appendix), show the convergence of several convective cells within the MCS over the Abakaliki region, which ultimately form the intense core at snapshot 4. At snapshot 5, the MCS has moved over the ocean and features a pronounced tail at the southern flank (Figure 5.2b). The latter, however, is not the remainder of the Abakaliki core, but rather a consequence of dynamical characteristics described in section 5.6. Interestingly, unlike the IR T_b in Figure 5.2a, the T_b in the MW channel in Figure 5.2b indicate that the MCS has retained its strength between snapshots 4 and 5. Eventually, snapshot 6 illustrates both the fragments of the decaying MCS to the south as well as a new convective core at the northern edge, which leads to the above-mentioned unphysical loop in the track. Again, this development is discussed in more detail in section 5.6.

5.3.2 Climatological context

The second half of the MCS period, referring henceforth to 10–13 June (feature B in Knippertz et al.; 2017), marked the wettest spell of the entire DACCIWA period at the Guinea Coast with a peak zonal rainfall rate of around 2 mm h^{-1} in the 8°W–8°E band (Knippertz et al.; 2017). A substantial portion of this rainfall can be attributed to the MCS itself. Figure 5.3a shows the accumulated rainfall during the passage of the 233 K envelope of the MCS and the 24-hour rainfall sum as estimated by IMERG and as measured by affected rain gauge stations, respectively. Note that the overpass falls within two reporting periods at some stations, that is, including the change of the measurement day at 0600 UTC (at 0900 for Ghana). The higher value out of the two days is taken in this case. Along the path of the MCS, several convective rainfall bands are visible. This can be seen particularly well east of 10°E with three distinct cores forming the MCS as a squall line. The two cores propagating through central and northern Nigeria, as mentioned before, are evident as well. Probably the most striking feature is the high rainfall accumulation in southeastern Nigeria over the Abakaliki region, which peaks at over 200 mm in IMERG, consistent with the associated station value of 223.5 mm (diamond marker). Considering the substantially lower daily rainfall totals at surrounding rain gauge stations, it becomes apparent how localised the extreme event was. Along the Guinea Coast region west of 5°E, the rainfall amounts as estimated by IMERG agree reasonably well with the rain gauge network. Stations close to the West African shore line appear to be affected mostly by the northernmost convective core of the MCS. The main core is most active offshore and exhibits an intensity comparable with the Abakaliki event, but did not substantially affect the onshore regions.
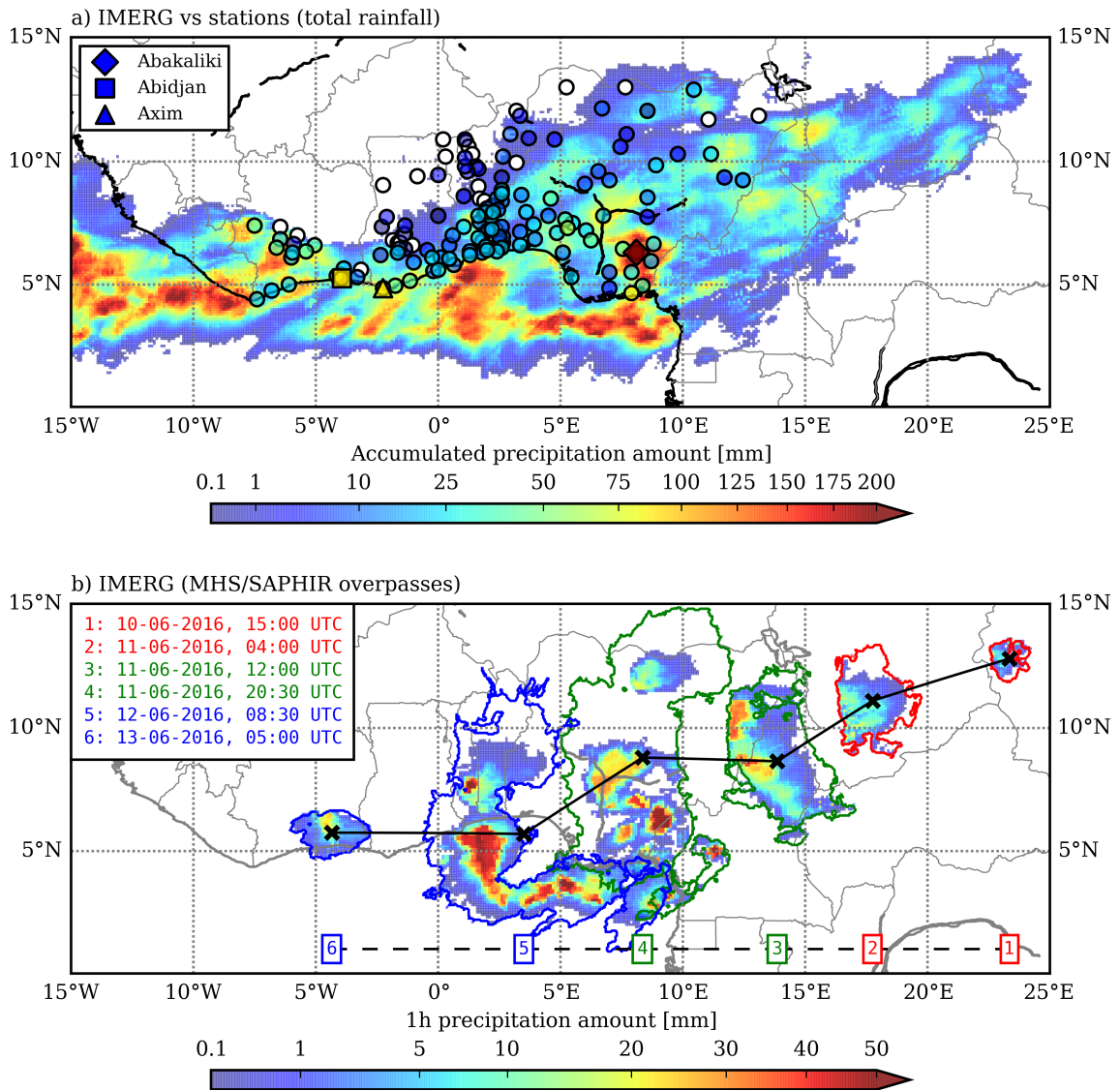
Figure 5.3: Precipitation composites. (a) Colour shading denotes the IMERG estimated total rainfall produced within the 233 K envelope of the MCS (see Figure 5.2a). The coloured dots show the daily rainfall amount at various stations over West Africa at the day of the MCS overpass. Note that daily rainfall in Ghana is operationally accumulated from 0900–0900 UTC, otherwise regularly from 0600–0600 UTC. From Maranan et al. (2019), ©American Meteorological Society. Used with permission. (b) One-hour accumulated IMERG rainfall estimates during the overpasses of MHS and SAPHIR (see Figure 5.2b) starting from the time indicated in the legend. The contours outline the 233 K isotherm of the MCS, coloured according to the MCS phase as in Figure 5.2.

Hourly rainfall accumulations at the time of the passage of MHS and SAPHIR are presented in Figure 5.3b. Compared to the MW field in Figure 5.2b, high precipitation rates are generally found where MW T_b is low, which reflects the pronounced relationship between rainfall estimates from IMERG and MW data due to the calibration towards MW retrievals (see section 5.2). In contrast, a more flawed relationship to IR becomes evident, particularly at snapshot 4, where IMERG precipitation is absent in large parts within the 213 K envelope of the MCS. The deficiencies of

IR-based rainfall retrievals compared to MW is well known (e.g. Kidd and Levizzani; 2011). In essence, many of the features described in Figure 5.2b are also visible in Figure 5.3b.

In the context of the climatology of daily rainfall, the value measured in Abakaliki (223.5 mm) is extraordinary in its rainfall regime. For Figure 5.4, daily non-zero rainfall values for the month of June from long-term rainfall datasets (see section 5.2) were assembled for three regions (Figure 5.4a), namely southwestern coast (SW-Coast, 69 stations) with Axim and Abidjan included, southern Nigeria (S-Nigeria, 21 stations) where Abakaliki is located, and the Guinea Coast region (GC region, 352 stations), enclosing both SW-Coast and S-Nigeria and extending up to 8°N. The cumulative distribution function (CDF) of non-zero precipitation days in June is presented for these three regions in Figure 5.4b, binned every 1 mm. As expected, daily rainfall values are approximately exponentially distributed across the GC region in general and exhibit median values around 10 mm. The obvious difference is that the CDF of SW-Coast is shifted to higher values compared to S-Nigeria. The 99th percentile at SW-Coast is 144.5 mm and higher by over 43 mm than that of S-Nigeria (101.1 mm over S-Nigeria, 107.4 mm over GC region). Although S-Nigeria belongs to the wettest places of the GC region (Fink et al.; 2017), it indicates that daily precipitation is not as extreme as, for instance, over SW-Coast. However, note that this result is based on the rainfall dataset described in section 5.2, which is far from continuous (see example in Figure A.6 in the appendix). While the rainfall amounts at Axim (114.8 mm) and Abidjan (106.2 mm) are clearly lower than their region-wide 99th percentile, Abakaliki surpasses the 99th percentile of S-Nigeria by over 122 mm, which emphasises the exceptionality of this rainfall event. Further evidence is given in Figure 5.4c, where the cumulative daily precipitation amount of June 2016 at Abakaliki is compared with the June climatology of S-Nigeria. Until the passage of the MCS (blue line section), rainfall was below the regional average, but still within one standard deviation (1σ). The MCS caused the curve to increase beyond $+2\sigma$ and is the major reason that June 2016 at Abakaliki ended up as an above-average month. Both Axim and Abidjan (Figures 5.4d and 5.4e) are located in the climatologically wetter part of SW-Coast (Fink et al.; 2017), indicated by their respective long-term June mean, which is generally just below the $+1\sigma$ line of SW-Coast. For 2016, Axim experienced a relatively normal June, whereas Abidjan was anomalously dry and even below its own -1σ line. However, the MCS period was the wettest spell in June 2016 in Abidjan. June rainfall at the three stations in 2016 generally ceased after 23 June, shortly after the monsoon onset on 22 June (Knippertz et al.; 2017).

5.4   The Savannah phase (SP)

In the following, an in-depth analysis of the local- and regional-scale environmental conditions leading to the unusual development of the MCS is provided. For this purpose, the MCS period is subdivided into three phases (see also the textbox in Figure 5.2a). The first phase, "Savannah phase", refers to the period from formation until the arrival of the MCS in Nigeria as a squall line (10 June, 1300 UTC – 11 June, 1200 UTC) (section 5.4). The following "Nigerian phase" addresses the intensification phase of the MCS over Nigeria (11 June, 1200 UTC – 12 June, 0600 UTC) (section 5.5). The last phase, termed the "Coastal phase" (12 June, 0600 UTC – 13 June,
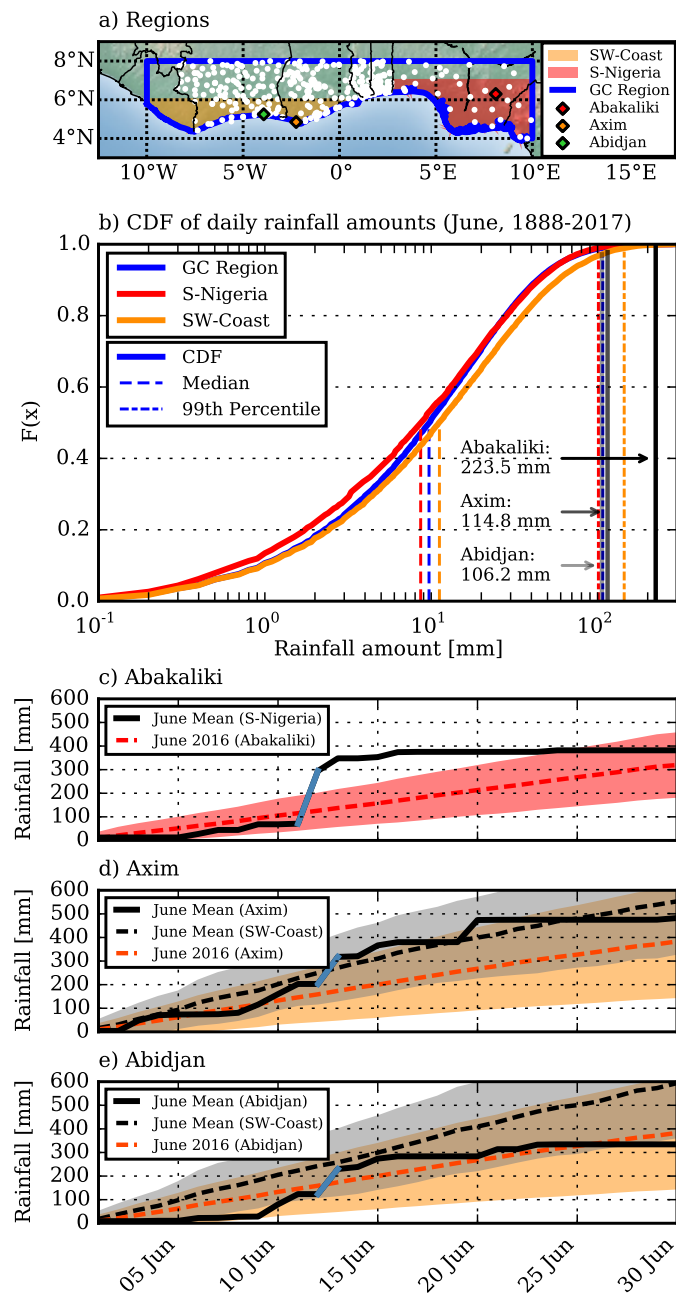
Figure 5.4: Climatological context for the rainfall at Abakaliki on 12 June, and at Axim and Abidjan on 13 June 2016. (a) Spatial distribution of stations used to create the statistics in (b). The Guniea Coast region (GC region) is outlined in blue, the orange and red shadings indicate the southwestern coast region (SW-Coast) and southern Nigeria (S-Nigeria), respectively. The white dots denote the position of rain gauge stations. (b) Cumulative distribution function (CDF) of non-zero daily rainfall values in June during the 1888–2017 period for the three aforementioned regions. The median, 99th percentile and the rainfall values at Abakaliki, Axim and Abidjan are indicated with dashed, dotted and gray shaded vertical lines, respectively. (c)-(e) Cumulative rainfall at the stations Abakaliki, Axim and Abidjan during June 2016. The blue line section denotes the daily rainfall at the day of MCS overpass. The dashed black and coloured lines denote the mean cumulative June rainfall at the station and the surrounding region, respectively. The colour shadings indicate the area within one standard deviation of the mean cumulative rainfall. Note that, apart from few fragments in other years, only 2016 was available for Abakaliki. Therefore, no climatology could be calculated for this station.

1800 UTC), discusses the evolution of the MCS during its westward migration along the Guinea Coast, particularly the aforementioned regeneration stage over Ivory Coast (section 5.6).

5.4.1   Regional-scale setting and initiation

The regional-scale dynamical setting during the occurrence of this long-lived MCS is described in the DACCIWA overview paper by Knippertz et al. (2017). Briefly summarised, the MCS period was characterised by the presence of a pronounced Atlantic cold tongue (ACT) and an intense phase of Saharan heat low (SHL), which is usually favourable for Sahelian rainfall owing to a stronger monsoon flow (Nicholson; 2009a, see also section 3.3.2). The SHL was located anomalously far north with associated low-level southerwesterlies penetrating deep into the eastern Sahel. This development may have aided the initiation of the MCS over western Sudan with sufficient moisture prior to its formation. Furthermore, upwelling of cold water at the coast and thus the tendency of suppressed coastal convective activity did not occur until 18 June, meaning that the SST during the MCS period remained around the long-term average of 28°C. Finally, the AEJ started to gradually migrate northward. It was located over southern Chad on 7 June, creating a zone of strong low-level wind shear over the region. The role of vertical wind shear on the intensification of convective systems was covered in section 3.1.2.

Within this the above-mentioned conditions, the MCS formed on 10 June around 1400 UTC over the Darfur Mountains in western Sudan. Elevated terrain is known to facilitate the initiation of convective systems by virtue of increased heating and associated deepening of the planetary boundary layer (e.g. Whiteman; 2000). Earlier studies already pointed out the importance of the Darfur Mountains as a source region for Sahelian MCSs (Tetzlaff and Peters; 1988; Laing et al.; 2008). Mohr and Thorncroft (2006) found a particularly strong relationship between intense convective systems and the elevated terrain of the Darfur Mountains in August. They argued that a high-CAPE and high-shear environment, the latter associated with the northward migration of the AEJ into the region, generally favours the development of intense systems in the vicinity of high terrain. In Figure 5.5, the (thermo-) dynamical conditions as well as precipitation between 36 hours before and after the time of initiation (black vertical line) are presented. The variables were averaged over a 2°×2° box at the western side of the Darfur Mountains (easternmost red box in Figure 5.1). Both CAPE and CIN exhibit a distinct diurnal cycle within the 72-hour window (Figure 5.5a), which emphasises the role of insolation for the build-up of the convective boundary layer in this region. Furthermore, there are clear signals of diurnal rainfall as well in both IMERG and ERA5 (Figure 5.5b), favoured by the simultaneous increase and breakdown of CAPE and CIN, respectively, during daytime. Note again that precipitation was taken from the forecast data of ERA5. Precipitation is used to assess the capability of ERA5 to reproduce the observed (thermo-) dynamical conditions. A good agreement with IMERG suggests high confidence in the representation of the environmental conditions in ERA5. Around the rainfall episodes, a slight increase of PW to a value of around 40 mm is visible (Figure 5.5b). This is by no means extreme and is 7 mm less than the 1979–2016-based 99th percentile of 47 mm within ERA-I. The recurrent weak rise in PW is controlled by the column-integrated convergence of moisture

flux (MFC, Figure 5.5c), which is strongest just ahead of the peak rainfall in ERA5. MFC has been widely used in forecasting convective initiation (see chapter 3) and can mostly be attributed to convergent motions in the lower troposphere (Banacos and Schultz; 2005; Birch et al.; 2014). Since these episodes coincide with diurnal minima of MSLP prior to MCS formation (not shown), they are most likely thermally driven. The magnitude of the vector difference between the 600 and 925 hPa layer, a common proxy for low-level wind shear (LLWS hereafter) over West Africa (e.g. Laing et al.; 2008), also shows a diurnal cycle and is almost in phase with CAPE just before the initiation of the MCS. This situation fits the high-CAPE, high-shear environment concept of Mohr and Thorncroft (2006). Overall, the results suggest that low-level controls within the diurnal cycle played a major role in the MCS initiation.
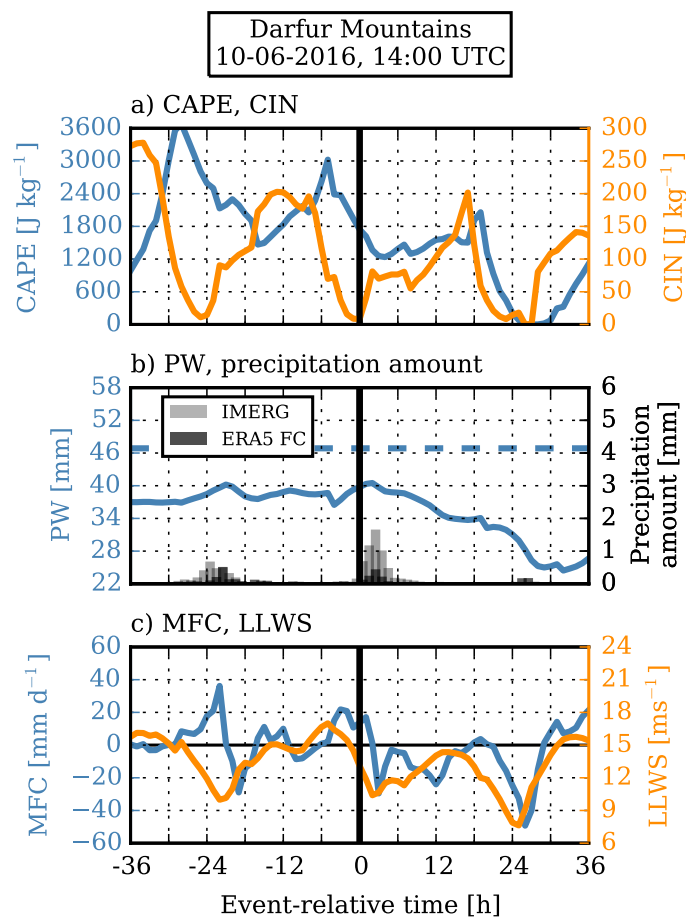
Figure 5.5: Environmental conditions averaged over the 2°×2° box over the Darfur Mountains (see Figure 5.1) in a ±36 hour window centered around the passage of the MCS (black vertical line) on 10 June 2016, 1400 UTC. Shown metrics are (a) CAPE and CIN, (b) precipitable water (PW) and hourly rainfall from IMERG (light gray bars) and ERA5 forecast (dark gray bars), (c) column-integrated moisture flux convergence (MFC) and 600–925 hPa low-level vertical wind shear (LLWS). Amended figure from Maranan et al. (2019), ©American Meteorological Society. Used with permission.

5.4.2   The squall line stage

A key factor for the development of the MCS into a highly organised system is its subsequent migration towards the southwest. The conditions along the MCS's path from snapshot 1 to 3 (see Figure 5.2b) are illustrated in Figure 5.6a. Here, the variables were calculated for a moving $2°\times2°$ box, always two hours before the arrival of the MCS to analyse pre-storm conditions. Along the path, CAPE, LLWS and PW gradually increase compared to the initial point. The first visible increase of PW, which potentially increases CAPE due to higher low-level moisture, is a direct consequence of the southward migration into a moister regime, as indicated by the associated rise of the 99th percentile within ERA-I (dashed black line). At the same time, CIN increases as well. Processes to overcome it may include lifting at the downshear side of the coldpool (see section 3.2.2), which is not directly resolved in ERA5. However, DCAPE exhibiting around 900 J kg^{-1} along the track indicate conducive conditions for the generation of an efficient coldpool due to midlevel dryness. The evolution into a squall line between snapshot 2 and 3 coincides with additional increases in CAPE, PW and LLWS (Figure 5.6a). The latter was already mentioned in the large-scale analysis in Knippertz et al. (2017) and can be explained by a synoptic-scale disturbance in the mean flow. Figure 5.6b shows the 600-950 hPa mass-weighted flow ($V_{600-950}$ hereafter, cf. Lafore et al.; 2017a) as well as the magnitude of the LLWS shortly after snapshot 2 (June 11, 0500 UTC). At that time, the MCS is located slightly ahead of the axis of a wave trough, within a region of pronounced northeasterlies. Over West Africa, $V_{600-950}$ is usually strongly influenced by the AEJ layer, which imposes a distinct easterly component onto it. It can be concluded that the northeasterly flow also dictated the direction of the MCS's path during SP. Considering the time of day, the higher magnitude of LLWS between snapshot 2 and 3 is most probably a product of the combination of the northeasterlies and the southwesterly nocturnal low-level jet (NLLJ), the latter a well-known phenomenon during the West African rainy season (e.g. Parker et al.; 2005b; Lothon et al.; 2008; Knippertz et al.; 2011; Schrage and Fink; 2012). The NLLJ is typically strongest in the 950–900 hPa layer and accounts for most of the northward moisture transport over West Africa (Parker et al.; 2005b). For the present MCS case, there is some evidence that the NLLJ is further enhanced by being channeled northeastward in the Benue valley between the orographic features of the Jos Plateau and Cameroon Highlands (see Figure 5.1 for geographical reference), leading also to an increase in low-level specific humidity in the area ahead of the MCS over southern Chad and northern Cameroon (not shown). Local concentration of moisture in this area is then obtained by a strengthening of MFC, which leads to the aforementioned second increase of PW up to the 99th percentile in ERA-I towards snapshot 3 (Figure 5.6a). Furthermore, the increase of LLWS between snapshot 2 and 3 (Figure 5.6a) coincides with an increase in translation speed of the MCS (Figure 5.2a), indicating the typical propagation behaviour of squall lines within front-to-rear system-relative winds dominated by LLWS (Figure 3.6).
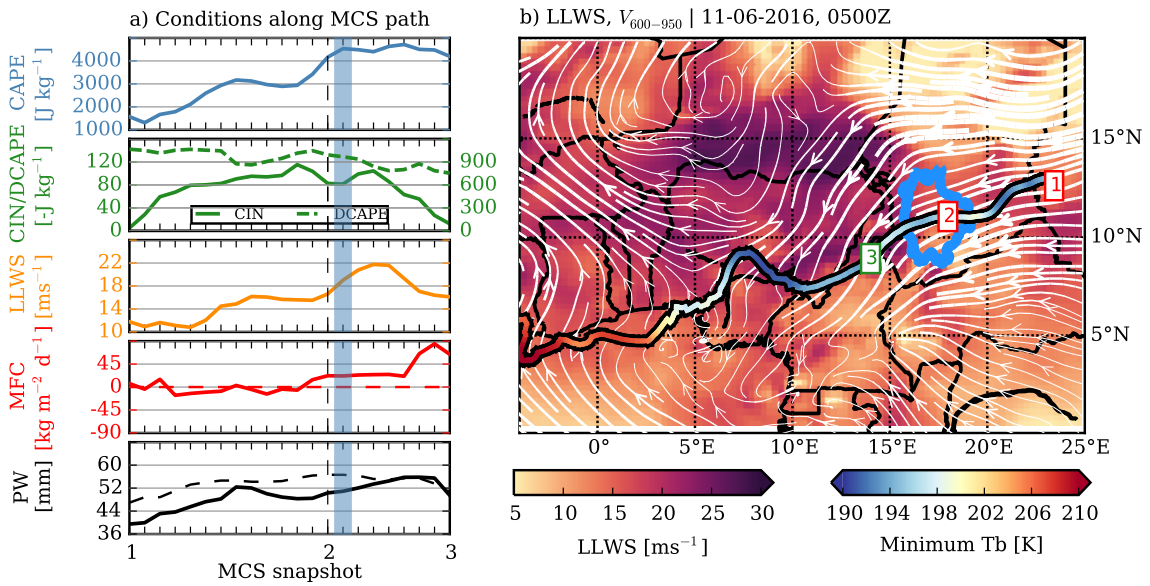
Figure 5.6: (a) Environmental conditions along the MCS track between MCS snapshot 1 and 3 (see Figure 5.2). The values indicate the situation two hours before arrival of the MCS. The dashed lines for MFC and PW denote the zero line and the ERA-I 99th percentile, respectively. (b) LLWS (colour shaded) and the 600–950 hPa mass-weighted flow (white streamlines) along the MCS track. The colours on the track line denote the minimum IR brightness temperature at the respective timesteps. The blue contour indicates the spatial extent of the 213 K cloud area of the MCS on 11 June 2016, 0500 UTC. The coloured numbers show the locations of the MCS snapshots 1–3 on the track. Amended figure from Maranan et al. (2019), ©American Meteorological Society. Used with permission.

5.5 The Nigerian phase (NP)

The MCS entered the NP during the afternoon of 11 June as a fast-moving squall line. Earlier case studies of MCSs over tropical West Africa indicated that high local accumulation of rainfall were primarily a consequence of a slow MCS passage or even passages of multiple convective systems (Schrage et al.; 2006; Engel et al.; 2017). Together with Figure 5.3a, Figure 5.2b already hinted at the development of an intense slow-moving convective cell over the Abakaliki region that formed through converging convective cores within the MCS (Figure A.5). But which factors caused this development?

5.5.1 Intensification of the MCS

Similar to Figure 5.5, an analysis of the dynamical and thermodynamical metrics around the passage of the MCS (11 June, 1800 UTC) is performed in Figure 5.7, but for a 2°×2° over the Abakaliki region (see Figure 5.1). Distinct changes in the regime between southern Nigeria and the area over the Darfur Mountains are evident from the diurnal evolution of CAPE and CIN (Figure 5.7a, cf. Figure 5.5a). Diurnal oscillations are largely absent over the Abakaliki region. While CAPE is generally high (>3000 J kg^{-1}), a low-CIN environment is found, owing, among other factors, to warm and quite unstable low levels (not shown). The most striking feature is the

sharp increase in CAPE together with an almost complete removal of CIN that sets in around eight hours before the passage. However, no rainfall is detected within the box in IMERG or ERA5 forecasts until 2 hours before the passage of the MCS core (Figure 5.7b). The rainfall distributions of the datasets differ distinctly in peak intensity and duration, which suggest difficulties for the ECMWF model to predict this extreme event. Just before the passage, PW experiences a pronounced rise and clearly surpasses the 99th percentile of ERA-I in the process. As indicated in Figure 5.7c, this is associated with an extreme MFC that peaks at over 140 mm day^{-1}, followed by an even stronger maximum 12 hours later. This double peak is reflected in a similar double peak in precipitation in the ERA5 forecast. The first strong peak in MFC is related to a notable decrease of the mean sea level pressure (MSLP) by 6 hPa. This is twice as strong as the long-term mean variation of MSLP in the tropics associated with the diurnal and semidiurnal atmospheric tides (Dai and Wang; 1999; Le Blancq; 2011).
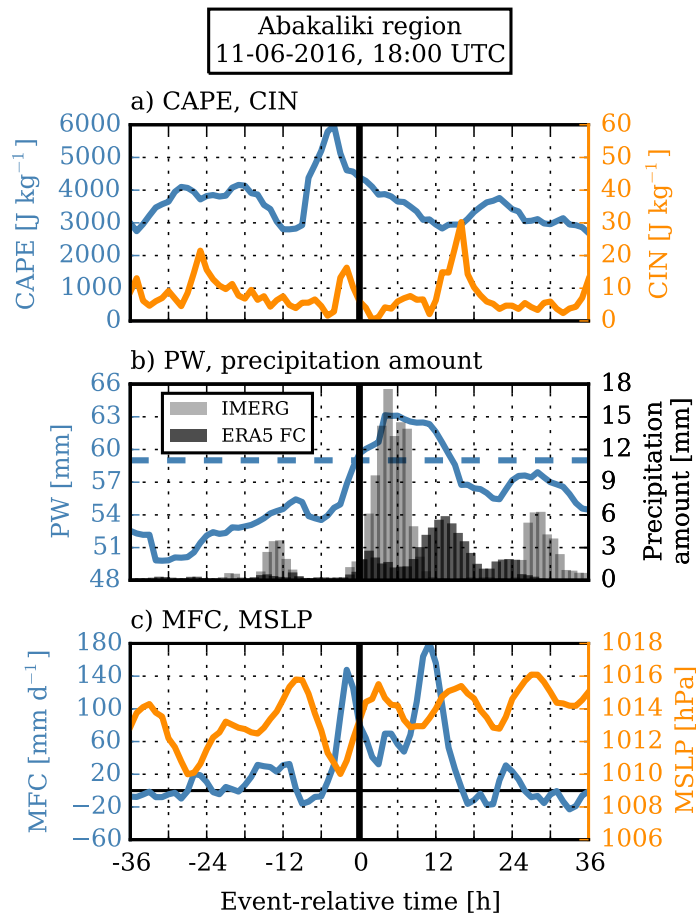
Figure 5.7: Same as Figure 5.5, but for the Abakaliki box (see Figure 5.1) centered around the start of the MCS passage on 11 June, 1800 UTC. Mean sea level pressure (MSLP) is shown instead of LLWS in (c). Amended figure from Maranan et al. (2019), ©American Meteorological Society. Used with permission.

Although the decrease of MSLP just before the MCS passage is distinctively stronger than usual, above-normal pressure fluctuations at the beginning of the analysis period in Figure 5.7c, for instance, have not produced a comparable increase of MFC. The MSLP field at the time of the

minimum in Figure 5.8a (11 June, 1500 UTC) reveals that a local MSLP minimum is present in the Abakaliki region. Consequently, the low-level flow, represented by streamlines at 925 hPa, is directed towards this MSLP minimum. Clear evidence of the existence of this pressure low from actual wind measurements is illustrated in Figure 5.8b. Vertical wind profiles from radiosonde launches on 11 June, 1200 UTC at the surrounding stations Cotonou, Abuja and Enugu (see section 5.2) are plotted in a hodograph. The wind profile at Enugu (purple curve), the closest station to Abakaliki (see map section), exhibits a cyclonic rotation at low levels before turning into strong northeasterlies above around 700 hPa. The latter might indicate the upper boundary of the low pressure area. At Cotonou (green curve), which is almost exactly to the west of Abakaliki, the wind profile is nearly zonal at all levels up to 600 hPa. Westerlies prevail at low-levels and easterlies above 800 hPa. Low-level southwesterlies were present at Abuja (blue curve) to the north of Abakaliki before the flow again turned easterly at higher levels.
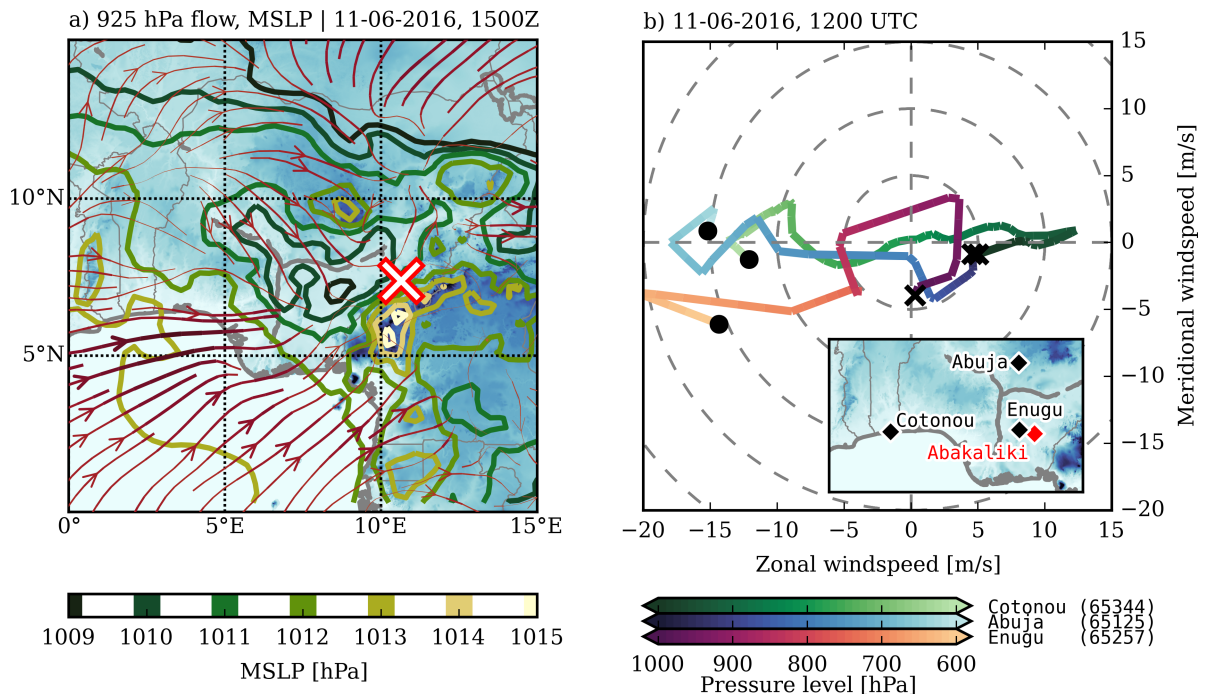
Figure 5.8: (a) Mean sea level pressure field (coloured contours) and 925 hPa flow (streamlines) on 11 June 2016, 1500 UTC. The marker denotes the location of the MCS's center of mass. The terrain height is shaded in blue, with higher elevation being darker (see Figure 5.1 for more details). (b) Hodographs deduced from radiosonde wind data at Cotonou, Abuja and Enugu on 11 June 2016, 1200 UTC. Black cross markers indicate the lowest, black dots the highest altitude. The hodographs are cut at 600 hPa. The map on the lower right shows the location of the radiosonde sites and Abakaliki. Amended figure from Maranan et al. (2019), ©American Meteorological Society. Used with permission.

To investigate the causes behind the formation of the low, the PTE (see eq. 5.1) was applied on the same box over the Abakaliki region as for Figure 5.7. Figure 5.9a shows the timeseries of the magnitude of the PTE components over the course of 11 June. It shall be noted here that components, which were calculated with the reanalysis or forecast dataset of ERA5, are

denoted with (A) or (F) in the legends. Figure 5.9a focuses on the reanalysis. The time of MSLP minimum (1500 UTC) is denoted by the green vertical shading. The evolution of the pressure tendency at the surface Dp (solid black line) is characterised by a semidiurnal fluctuation with a net pressure fall starting at 0900 UTC that eventually leads to the MSLP minimum. The pressure fall is mainly controlled by ITT, which is sometimes compensated and sometimes supported by $D\phi$. Contributions from EP are negligible and tend to coincide with higher RES_{PTE}. This means that the PTE is already reasonably closed by $D\phi$ and ITT alone. Part of the decrease of MSLP may be attributed to atmospheric tides, where the diurnal (red curve) and semidiurnal pressure tendency (blue curve) exhibit negative values after 1200 UTC. However, their influence on the formation of the pressure minimum itself is difficult to assess since atmospheric tides act on the large-scale (not shown, cf. Dai and Wang; 1999).

Further inspection of the components of the ITT term (see equation 5.2) is performed in Figure 5.9b. Since forecasts contain the temperature tendencies due to parameterisations, the forecast version of the ITT (ITT_F) is evaluated here, which also reproduces the episode of pressure fall (dashed black curve in Figure 5.9a). Here, the radiation part of $DIAB$ can be calculated explicitly for shortwave ($DIAB_{SW}$) and longwave radiation $DIAB_{LW}$, respectively. Thus, the remainder of $DIAB$ can be attributed to temperature changes due to latent and sensible surface heat fluxes and friction and is termed $DIAB_{dyn}$ hereafter. We find two characteristics that do not change much over time. First, $DIAB_{LW}$ is always positive around a value of 0.4 hPa h^{-1} and can be attributed to the cooling effect of terrestrial longwave radiation. Second, the influence of $TADV$ is small, which is not surprising considering the rather small spatiotemporal variations in the temperature field in tropical environments. $DIAB_{dyn}$ usually counteracts VMT, particularly during the MCS passage from 1800 UTC onwards. The positive VMT, associated with strong lifting inside the MCS and thus adiabatic cooling, is largely balanced by latent heat release within $DIAB_{dyn}$. However, during the period of pressure fall, both are mostly negative with $DIAB_{dyn}$ exhibiting rather small values. Moreover, the negative pressure tendency is further enhanced by $DIAB_{SW}$. Solar radiation ($DIAB_{SW}$) appears to warm the tropospheric column immediately after sunrise at 0600 UTC and is the strongest contributor to the pressure fall with a peak tendency of -0.8 hPa h^{-1}.

This development may be explained by analysing the upper-level dynamics. The upper-tropospheric divergence and wind fields derived from cloud motion vectors for 11 June, 1345 UTC, approximately an hour before the MSLP minimum, is presented in Figure 5.10a and b, respectively. In general, convective systems are a source of upper-level divergence (Figure 5.10a, black contours), while cloud-free regions are usually associated with upper-level convergence (white contours). The latter is present over large parts of central and southern Nigeria at the afore-mentioned timestep. The location of the developing pressure minimum in ERA5 (red diamond marker) was embedded in this region of low cloud cover. Based on the spatial distribution of divergent motions, the region of upper-level convergence was created by surrounding convection to the north and south and by the approaching squall line to the east. Furthermore, the upper-level wind field in Figure 5.10b indicates enhanced wind speeds of over 40 kn (orange shading) to the west of the MCS within the easterly flow. This is most likely related to the strong outflow of the MCS, further enhancing the easterly flow related to the TEJ. It shall be stressed, however, that
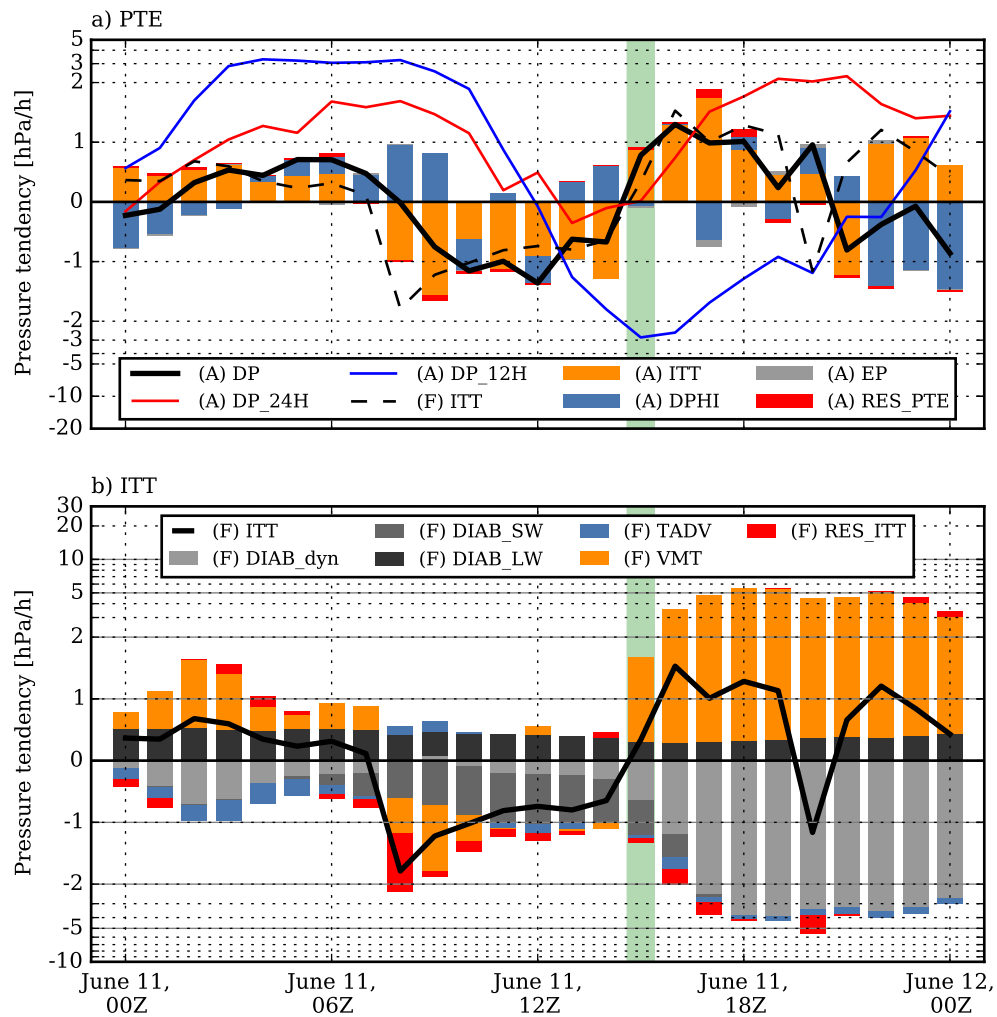
Figure 5.9: (a) Hourly contribution of the PTE components (bars) to changes in MSLP from the ERA5 reanalysis (A) and forecast (F). The black solid line denotes the net hourly change of MSLP. The blue and the red curve indicate the 12-hour and 24-hour pressure changes, respectively. The black dashed line shows the ITT of the forecast. The green shading marks the time of the MSLP minimum, also indicated in (b). (b) Hourly contribution of the ITT components (bars) to changes in MSLP. The black solid line denotes the net hourly contribution of ITT. Only the ERA5 forecast (F) is used here. Amended figure from Maranan et al. (2019), ©American Meteorological Society. Used with permission.

the area of convergence over central Nigeria is less pronounced than that over other regions with little cloud cover (e.g. at 5°W, 10°N in Figure 5.10a). So the question remains if it would have been present at all were it not for the approaching intense squall line and its outflow. Combining these findings with Figure 5.9b, the MSLP minimum likely formed during a period of low cloud cover due to subsidence (i.e. negative VMT) from upper-level convergence, which in turn allowed insolation to further warm the tropospheric column (negative $DIAB_{SW}$). The net subsidence assumably prevented strong convection to form prematurely despite the simultaneous build-up of CAPE and removal of CIN around this timestep, as mentioned earlier (cf. Figure 5.7a).

As indicated by Figure 5.7c, MFC strongly increased shortly after the formation of the pressure
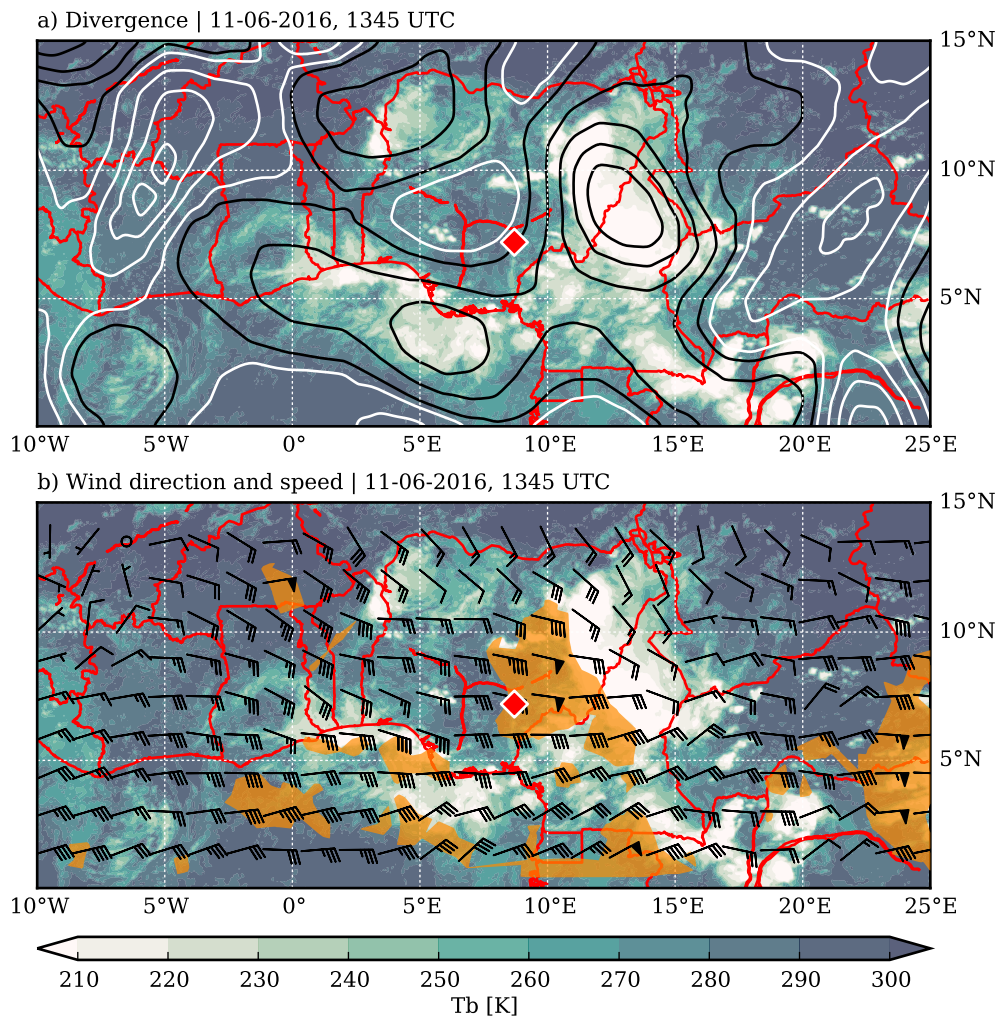
Figure 5.10: Upper-level motion fields on 11 June 2016, 1345 UTC, derived from the SEVIRI 6.2 μm water vapour channel (channel 5). (a) Divergence (black contours) and convergence (white contours) are plotted over the IR brightness temperature field T_b. The contours start at $\pm 0.25 \times 10^{-5}$ s^{-1} incremented by $\pm 10^{-5}$ s^{-1}. The red marker denotes the location of the MSLP minimum in Figure 5.8a. (b) Upper-level wind field (barbs) together with areas of >40 knots (orange shadings). Amended figure from Maranan et al. (2019), ©American Meteorological Society. Used with permission.

low and established an extremely moist environment, favourable low-level conditions for further intensification of the approaching squall line. Interestingly, according to the vertically integrated moisture flux at the time of MSLP minimum (11 June, 1500 UTC) (vectors in Figure 5.11a), the Abakaliki region is fueled with moisture effectively from the direction of the MCS in the northeast. The direction of the moisture flux vectors agrees well with the direction of 700–950 hPa mass-weighted flow ($V_{700-950}$, blue streamlines). As this has also been used to display wave disturbances (cf. Lafore et al.; 2017a), it suggests that the moisture inflow into the Abakaliki region is strongly influenced by the northeasterly regime of the synoptic-scale wave trough. Furthermore, channelling effects caused by the orographic features of the Jos Plateau and the Cameroon Highlands might have supported the pronounced increase of both MFC (red contours) and PW

along the Benue valley and, finally, the Abakaliki region.
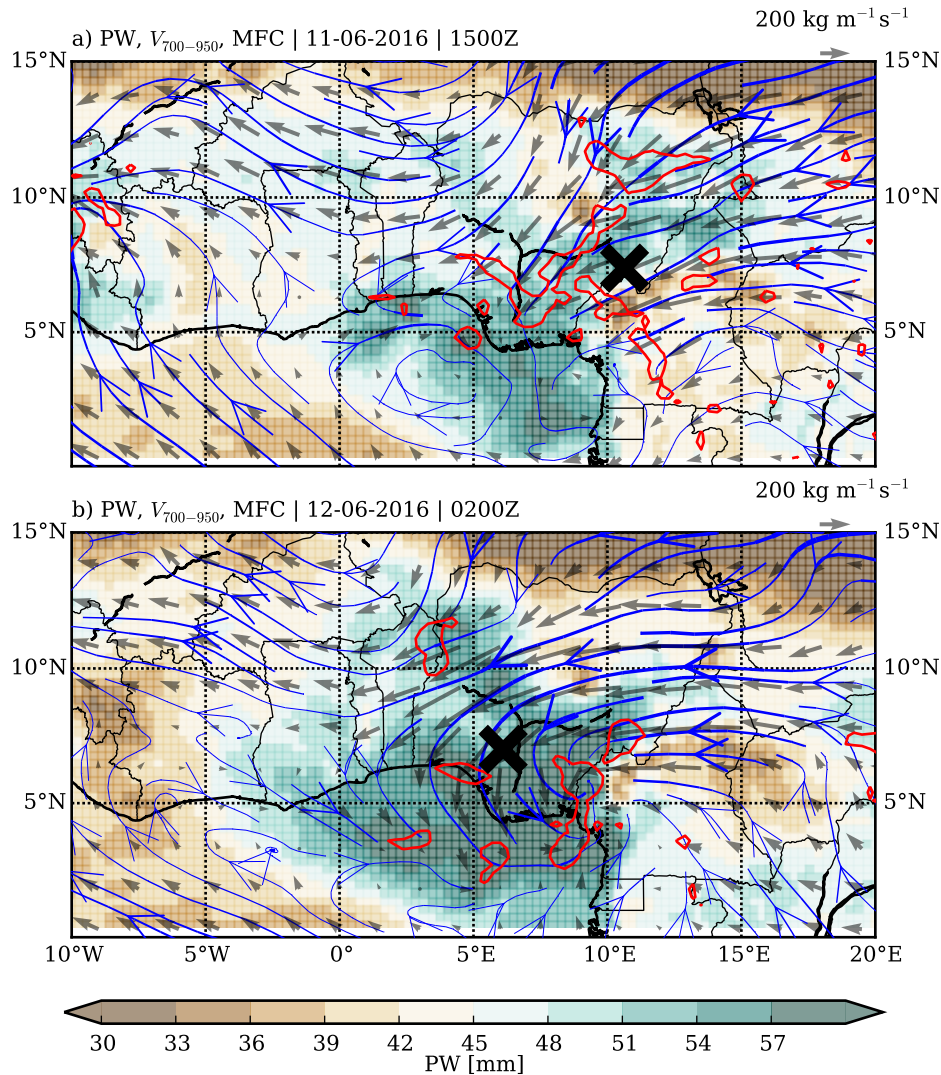
Figure 5.11: Precipitable water (PW, color shaded), moisture flux (vectors), 700–950 hPa mass-weighted flow (blue streamlines) and moisture flux convergence (MFC, red contours) are shown for (a) 11 June, 1500 UTC, and (b) 12 June, 0200 UTC. The contours for MFC outline areas with values >100 mm day^{-1}. From Maranan et al. (2019), ©American Meteorological Society. Used with permission.

5.5.2 Moist vortex

The low pressure system over the Abakaliki region, which extends vertically to around 700 hPa (see Figure 5.8b), likely supported the convergence of convective cells within the MCS (Figure A.5) during its passage and led to its local intensification. Furthermore, this development most probably triggered a substantial deformation in the low-level flow. Figure 5.11b shows the PW, moisture flux and $V_{700-950}$ during the passage of the MCS (12 June, 0200 UTC). $V_{700-950}$ indicates the formation of a cyclonic vortex with its center being located over the Abakaliki region. This vortex itself manifests already several hours earlier, i.e. around 2200 UTC on 11 June (not

shown), and coincides with the development of the intense convective core at snapshot 4 in Figure 5.2b. The moisture flux creates a region of high MFC around the vortex center in southeastern Nigeria (Figure 5.11b). PW is further increased and eventually "trapped" within the vortex. Possible orographic effects due to forced ascent at the Cameroon Highlands might have supported the intensification process. This development shows some similarities to the extreme rainfall event in Ouagadougou in 2009, where a strong vortex linked with an intense MCS was formed as well (Lafore et al.; 2017a; Engel et al.; 2017).

To evaluate possible mechanisms behind the vortex formation, the VTE was applied on the $2°\times2°$ box over the Abakaliki region during the observed passage of the MCS (11 June, 1800 UTC – 12 June, 0600 UTC). We stress that by using a global reanalysis dataset, the VTE will not capture the effects of small-scale vorticity sources and sinks, i.e. eddy fluxes (cf., Sui and Yanai; 1986; Davis and Galarneau Jr; 2009), and is one reason why the VTE is not entirely closed. Given the size of the MCS and its clear representation in ERA5 (e.g., Figure 5.9), emphasis is put onto the resolved mesoscale response. The upper row of Figure 5.12 shows vertical profiles of relative vorticity ζ (solid black lines), divergence δ (darkgray dashed lines), and vertical velocity w (lightgray dashed-dotted lines) at four different timesteps. The ζ-profiles indicate upward development of the cyclonic flow with a subsequent strengthening and deepening. On 12 June, 0200 UTC, the vortex is fully visible in the mass-weighted flow (Figure 5.11) and closed streamlines are found up to 700 hPa (not shown). At this time, cyclonic vorticity reaches up to 300 hPa (Figure 5.12c) and is further enhanced by 12 June, 0600 UTC (Figure 5.12d). As a consequence of the heat low, the low-level flow is already convergent early on (Figure 5.12a) and also deepens throughout the MCS passage as the vortex forms. Divergence, in turn, is mainly found at upper levels resulting from the convective outflow, accompanied by an enhanced mesoscale vertical velocity up to around 0.4 ms^{-1} at 300 hPa (Figure 5.12d). Figure 5.12e–h illustrate the contributions of the VTE components to the net change in relative vorticity $D\zeta$ (black line) at the respective timesteps. In principle, the maxima of positive $D\zeta$ exhibit a gradual upward migration, leading to the deep layer of positive ζ. It coincides with an upward development of the horizontal vorticity advection (*HADV*), which is primarily steered by the synoptic-scale wave disturbance. Thus, the time-displaced passage of the trough axis, leading to the *HADV* maxima at subsequently higher altitudes, reflects the baroclinic nature of the wave. While *HADV* initially contributes to the deepening of the positive ζ-layer (Figure 5.12g), it is fully balanced by the divergence term (*DIV*) at all levels towards the end of the MCS passage (Figure 5.12h). In general, anticorrelated VTE components (*HADV-DIV*, *VADV-TILT*) appear to be a typical feature, once the vortex is created, comparable to studies that investigate mesoscale convective vortices in midlatitudes (e.g., Knievel and Johnson; 2003). At low levels, *HADV* reacts to the column stretching produced by *DIV*. The latter starts to strengthen on 12 June, 0200 UTC, in the 800–900 hPa layer (Figure 5.12g) and deepens up to 500 hPa at 0600 UTC (Figure 5.12h). With the vortex center in the box, any inflow results in a negative tendency of *HADV*. The vertical vorticity advection *VADV* generally cancels *TILT* at low levels, but outweighs it in the layer above 600 hPa (Figure 5.12h). Thus, *VADV* strongly contributes to the positive $D\zeta$ in this layer. Overall, the development of the vortex appears to be a result of the strong latent heat release within the intensified MCS, leading to col-

umn stretching in the lower and pronounced vertical vorticity transport in the upper troposphere, respectively.
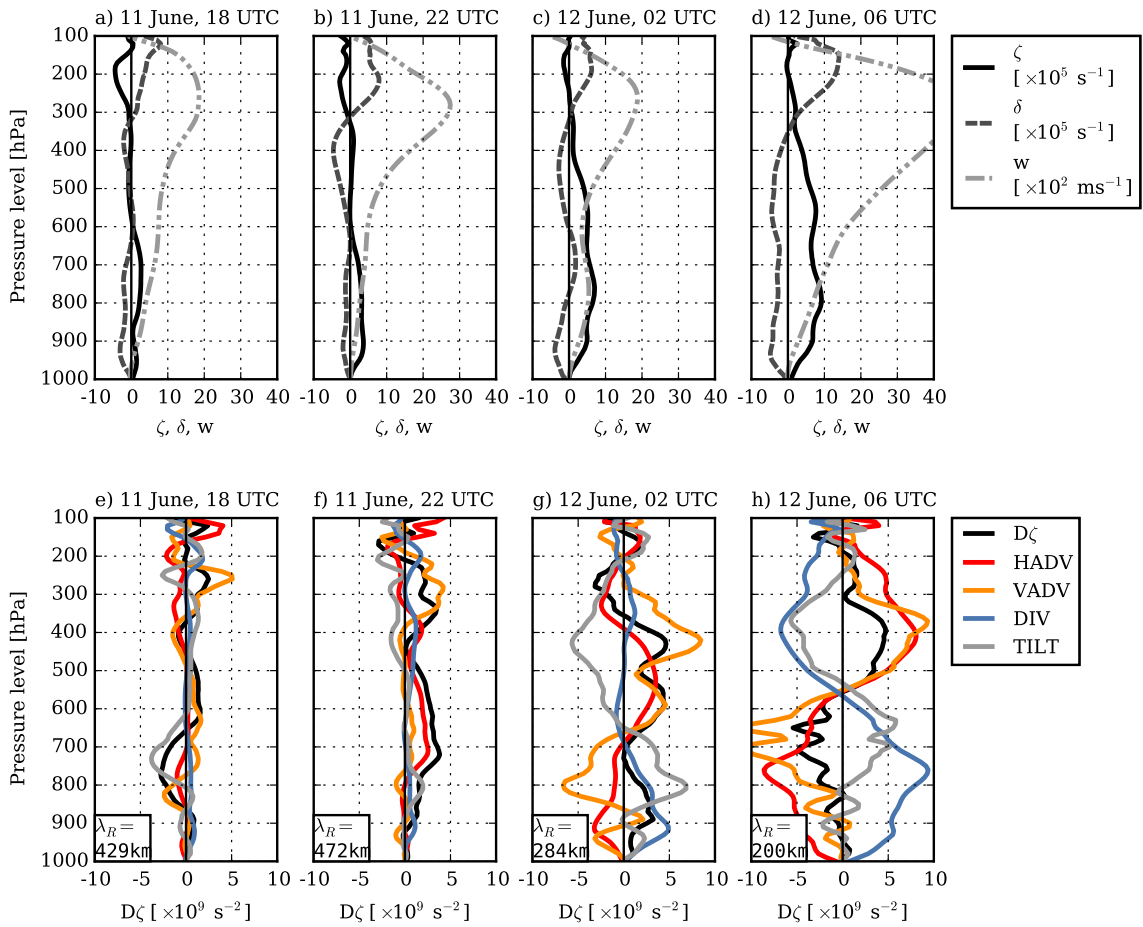
Figure 5.12: (a) Vertical profiles of relative vorticity ζ, divergence δ and vertical velocity w averaged over the Abakaliki box (see Figure 5.1) for four timesteps during the MCS passage (11 June 1800 UTC – 12 June, 0600 UTC). (b) Hourly contribution of VTE components to the change in relative vorticity (Dζ, black line) at the same timesteps as in (a). The values in the lower left corner indicate the Rossby radius of deformation. From Maranan et al. (2019), ©American Meteorological Society. Used with permission.

The importance of the MCS to the vortex formation is further emphasized when considering the geometrical size of the MCS compared to the Rossby radius of deformation λ_R, defined as

$$\lambda_R = \frac{NH}{(\zeta + f)^{1/2} (2VR^{-1} + f)^{1/2}} \tag{5.4}$$

where N is the Brunt-Väisälä frequency, H is the scale height of the circulation (i.e. the vortex), V is the tangential wind speed and R is the radius of curvature. In a saturated environment, as almost fulfilled in the current case, changes in buoyancy due to latent heat release are taken into account by replacing N with N_m, as defined in Durran and Klemp (1982). Since λ_R depends inversely on f, the time the atmosphere requires to balance the introduced disturbance is higher in the tropics than in midlatitudes for a given basic state. Using the approximate depth of the

vortex, i.e. 700 hPa or H =3 km, an estimated curvature radius of 200 km (cf. Figure 5.11b) and box-averaged values for ζ, f and V, eq. 5.4 yield values for λ_R as indicated in Figures 5.12e-h. Throughout the MCS passage and the development of the vortex, λ_R is drastically reduced by a few hundreds of kilometres down to 200 km on 12 June, 0600 UTC. The implication of this λ_R reduction is that the required horizontal length scale of a convective system to develop a state of quasi-horizontal balanced flow, i.e. the formation of a vortex, is decreased as well. Thus, judging from the geometrical size of the MCS, it has become "dynamically large" (e.g Ooyama; 1982; Cotton et al.; 1989). In the present case, the lowering of λ_R is realised by virtue of decreasing the moist static stability (i.e. lower N_m, not shown) and gradually increasing the background relative vorticity through MCS dynamics and the synoptic-scale wave over the depth of the vortex (Figures 5.12a-d). The subsequent MCS-vortex interaction becomes a distinct feature of the CP.

5.6   The Coastal phase (CP)

5.6.1   MCS-vortex couple

Over the course of 12 June, the MCS reached the Gulf of Guinea and moved in a more zonal direction westward along the Guinea Coast (Figure 5.2a). Figure 5.13 shows a Hovmöller diagram for the 3°–7°N averaged and 600–950 hPa mass-weighted meridional wind (coloured), the zonal wind greater than 1 ms^{-1} (green contours) and the relative vorticity greater than 2×10^{-5} s^{-1} (black contours) to highlight the vortex center. The formation of the vortex over the Abakaliki region (around 7°–9°E) is evident from the pronounced dipole in meridional wind as well as the strong signal in positive relative vorticity. The MCS at snapshot 5 (indicated with "5" in Figure 5.13) is located in the periphery of the vortex to its west within northerly and westerly flow. The latter is reflected by the distinct curvature in the shape of the MCS with a trailing southern flank (Figure 5.2b). However, it becomes apparent that the MCS is accompanied by a secondary vortex towards snapshot 6, which separates from the western flank of the main vortex (not shown) and eventually attains a zonal translation speed similar to the MCS of around -11.4 ms^{-1}. The MCS remains ahead, i.e. west of both vortex centers, at all times. Interestingly, the main vortex moves westward at a substantially slower zonal speed of around -5.5 ms^{-1}. It remains strong throughout 12 June and then dissipates in the early morning of 13 June.

It is unclear why this secondary vortex develops out of the main vortex and becomes the feature that accompanies the MCS. Some indications can be inferred from the upper-level divergence field (Figure A.7 in the appendix), where two regions of pronounced divergence over the Gulf of Guinea exist around this period. When compared to EUMETSAT atmospheric motion fields (Figure A.8), which are assimilated in the ECMWF system (Salonen and Borman; 2016), one divergence region is related to the upper-level outflow of the MCS. While the location of the secondary vortex center closely corresponds to this region, the main vortex is linked to the other divergence branch, which is not directly obvious from observation. The dynamic causes of the separation of the vortices are hard to determine with potentially some issues related to the physics of the ECMWF model.
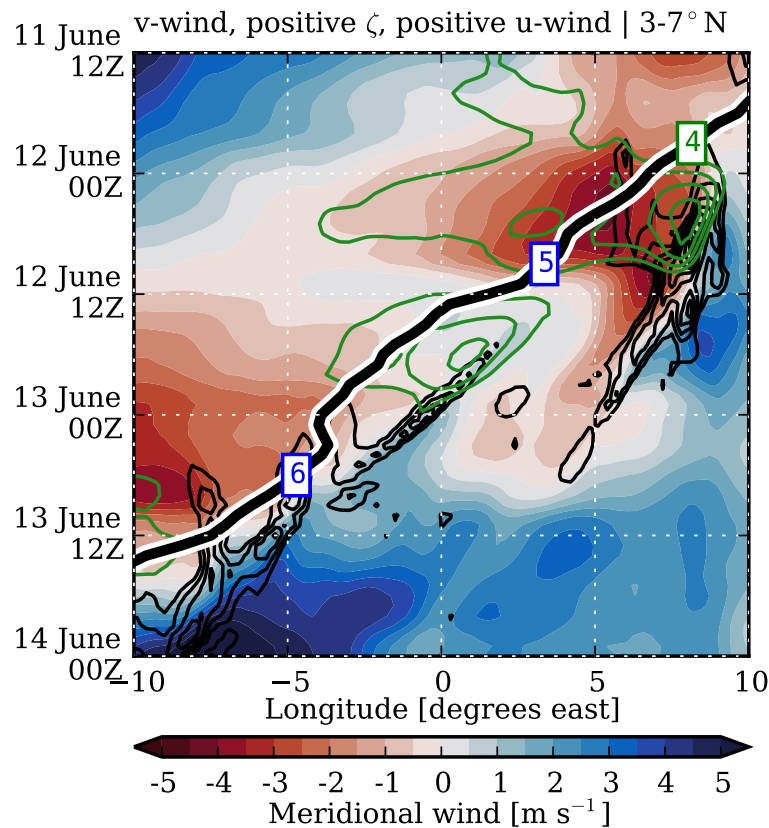
Figure 5.13: Hovmöller diagram of meridional wind (colour shaded), positive relative vorticity (black contours) and positive zonal wind (green contours) from 11 June, 1200 UTC – 14 June, 0000 UTC averaged in the 3°–7°N band and over the 600–950 hPa layer. The black contours start at 2×10^{-5} s^{-1} incremented by 10^{-5} s^{-1}, the green contours at 1 ms^{-1} incremented by 1 ms^{-1}. The numbers on the MCS track correspond to the MCS snapshots shown in Figure 5.2. From Maranan et al. (2019), ©American Meteorological Society. Used with permission.

Similar to Figure 5.6, the environmental conditions along the MCS track during the CP are illustrated in Figure 5.14. As in Figure 5.13, it reflects the conditions ahead of the vortex core. As soon as the MCS moves over the ocean around snapshot 5, CAPE sharply decreases owing to an overall more stably stratified troposphere. DCAPE exhibits a similar behaviour and can be explained by moister midlevels as well as a cooler lower troposphere. PW remains extreme at around 60 mm throughout the CP, which matches the 99th percentile of ERA-I. Together with a pronounced MFC and low convective inhibition, the vortex appears to be capable of sustaining a very moist environment that helps the MCS to live on. Because of less conducive conditions for the generation of a strong coldpool as indicated by low DCAPE, MCS maintenance in this low-CIN and near-saturated environment at the Guinea Coast differs fundamentally from the coldpool-driven squall line in the drier savannah region during SP. While pronounced LLWS, in conjuction with dry midlevels, is a likely key factor for MCS maintenance during SP (see also section 5.4), its role during CP is not clear. Note that the propagation speed of the MCS along the Guinea Coast, as indicated in Figure 5.2a, is distinctively lower than the magnitude of LLWS (cf. Figure 5.14), which underlines the MCS-vortex interaction. A brief discussion on this topic is given in
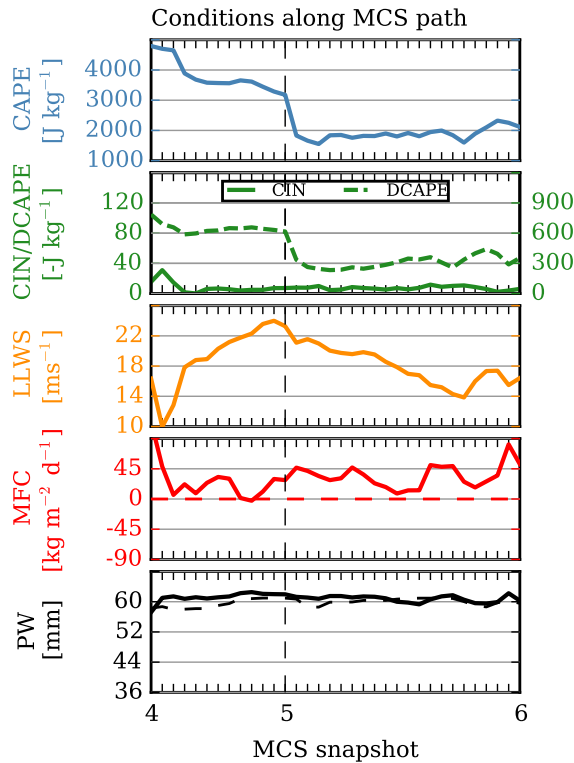
section 5.7.

Figure 5.14: Same as Figure 5.6, but between MCS snapshot 4 and 6 (see Figure 5.2). Amended figure from Maranan et al. (2019), ©American Meteorological Society. Used with permission.

5.6.2 MCS regeneration

The rainfall amounts measured at the stations in Axim and Abidjan associated with the MCS are of similar magnitude (Figure 5.4). However, the evolution of rainfall accumulation differ between both stations and can be attributed to a regeneration process of the MCS over the coast of Ghana and Ivory Coast, which also causes the unphysical loop in the MCS track (Figure 5.2). A summary of space-borne IR observations from SEVIRI and weather station reports between 12 June, 0600 UTC, and 13 June, 0600, is presented in Figure 5.15. Refer to section 5.2 for additional information about the respective datasets. The MCS reaches Axim around the midday of 12 June (Figures 5.15a) and eventually affects both station by 1800 UTC (Figure 5.15b). During the night, the MCS begins to dissolve over the ocean (Figures 5.15c). However, two initially separated convective cells (TS1 and TS2) form in the wake of the MCS. While Axim is influenced by the periphery of TS2, Abidjan is hit by the merger of TS1 and TS2 (TS1/2 in Figure 5.15d). The three-hourly SYNOP report at Axim (AXM) and both SYNOP and half-hourly METAR reports at Abidjan (ABJ-S, ABJ-M) give some indication about the evolution of rainfall events (Figure 5.15e). At Axim, first rainfall (RA) is reported at 1500 UTC on 12 June, which turns into a thunderstorm (TSRA) three hours later. This thunderstorm, i.e. the MCS, lasts at least until 13 June, 0000 UTC, and causes a total of 99 mm up to that point. Until 13 June, 0600 UTC, the

rainfall amount increases by an additional 16 mm to a total of 115 mm, which is caused by TS1/2. TS1/2 is not thundery over Axim, since only its edge passes over the station (Figure 5.15c). Over the course of the 24-hour period, Abidjan is hit by three different convective systems, all of which are thunderstorms. The first event occurs before noon of 12 June, independent of the MCS. From the IR image in Figure 5.15a, this system is hardly detectable. Given the time of day and the prevailing southwesterlies, land-sea-breeze effects could have played a role in the formation of this short-lived thunderstorm. It causes 2 mm at the SYNOP station according to the report on 12 June, 1200 UTC. MCS rainfall over Abidjan occurs in a span of 5.5 hours and arrives at around 1530 UTC. Cloud top temperatures in Figure 5.15b suggest that Abidjan is hardly influenced by the more intense part of the MCS farther to the southeast. Indeed, only an additional 1.7 mm is reported for the period between 12 June, 1200 UTC, and 13 June, 0000 UTC. The majority of rainfall over Abidjan is produced by TS1/2 after midnight when continuous rainfall is reported for five hours. 3.5 hours thereof are "heavy thunderstorm rainfall" (+TSRA). Eventually, TS1/2 accounts for over 100 mm within six hours until 13 June, 0600 UTC. It goes on to become the convective cell that continues the MCS track after snapshot 6 (see Figure 5.2a,b).
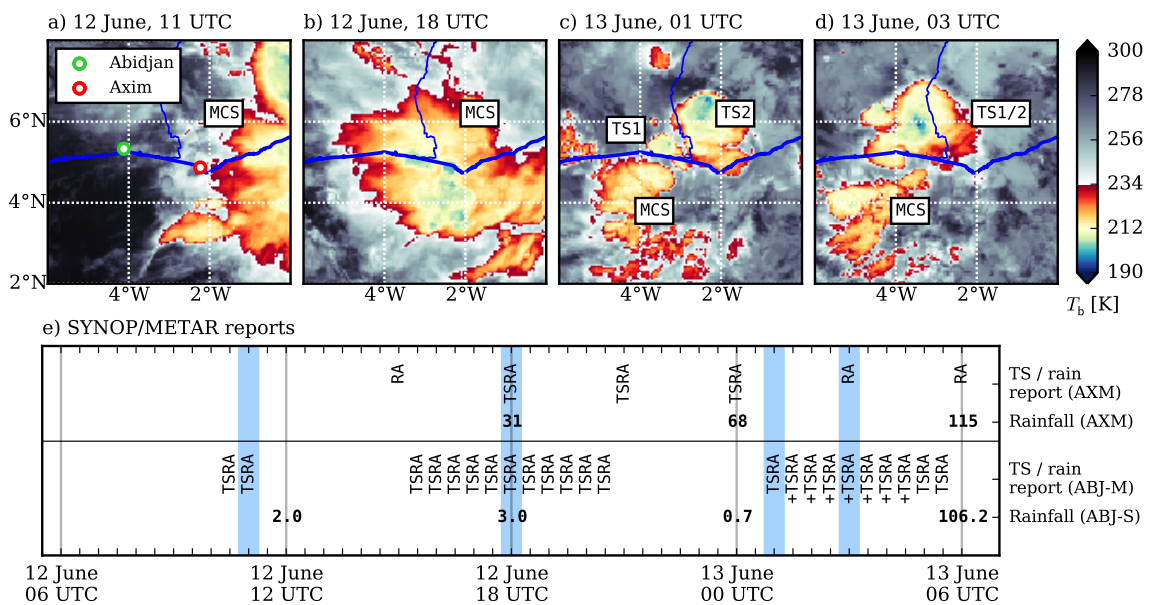
Figure 5.15: Weather observations during the MCS passage at Axim and Abidjan. (a)-(d) SEVIRI IR brightness temperature fields at timesteps indicated in the respective title. Coloured is the area of 233 K or less. (e) Three-hourly SYNOP report at Axim (AXM) and both SYNOP and half-hourly METAR reports at Abidjan (ABJ-S and ABJ-M, respectively), with respect to present weather and rainfall amount. The following rainfall reference periods apply to the synoptic times: 0000 UTC: previous 6h; 0600 UTC: previous 24h; 1200 UTC: previous 6h; 1800 UTC: previous 12h. The blue shadings refer to the snapshot times in (a)-(d).

The question arises of how the thunderstorms TS1 and TS2 were able to form in the wake of the MCS, also considering that this happenes during the night. Upon further inspection of ERA5 reanalyses (not shown), strong MFC behind the MCS prevails associated with the trailing vortex. Additionally, the MFC signature is aligned parallel to the coastline as a consequence of converging

moisture flux vectors coming from the southeast over the ocean and northeast over land. This may indicate in some way sea-breeze-like interactions with supported lifting of buoyant airmasses due to an abrupt change in surface stress.

5.7   Summary and discussion

This chapter investigated (thermo-) dynamic controls of an extreme rainfall event along the Guinea Coast during the DACCIWA field campaign (feature B in Knippertz et al.; 2017), which caused one of the highest ever daily rainfall accumulations in southern Nigeria. The 223.5 mm at the station Abakaliki on 12 June 2016 by far exceeded the 99th percentile based on multi-decadal rain gauge series from 21 southern Nigerian stations. Despite this exceptional event, the total rainfall of June 2016 at Abakaliki ended up within 1σ of climatological values in southern Nigeria. More than 100 mm of rain was reported on the following day on at the coastal stations Axim and Abidjan in Ghana and Ivory Coast, respectively, each exhibiting even a drier-than-normal month.

The high rainfall amounts were caused by an intense, long-lived MCS, which crossed almost the entire Guinea Coast region, and new convective cells in the wake of the decaying MCS around Ivory Coast. Three stages of the MCSs' lifecycle were analysed using a combination DACCIWA measurements, satellite observations and ERA5 reanlysis data. The salient developments and dynamic features, which are summarised in Fig. 5.16, are:

- The Savannah phase (SP, 10 June, 1300 UTC – 11 June, 1200 UTC) was characterised by the development of a classical West African squall line. After being initiated over the Darfur Mountains due to diurnal heating, the MCS quickly moved southwestward over southern Chad towards Nigeria, steered by northeasterlies within a mid- to lower-tropospheric wave trough. Pronounced LLWS between these northeasterlies and the undercutting southwesterly NLLJ as well as dry midlevels suggest conducive conditions for coldpool formation, which supported the upscale growth of the MCS into a squall line (Fig. 5.16f, left). Furthermore, increasing CAPE and PW values were detected along the southwestward MCS track.

- The Nigerian phase (NP, 11 June, 1200 UTC – 12 June, 0600 UTC) culminated in a strong intensification of the squall line and the formation of a moist vortex over the Abakaliki region. The intensification was promoted by an extremely moist lower troposphere (box-averaged total PW > 99th percentile), which was established by strong MFC (peak at 140 mm d^{-1}) prior to the arrival of the squall line. Both the development of a short-lived local heat low and the advection of additional moisture along the wave disturbance are proposed to be responsible for this extreme MFC. The heat low formed mainly as a consequence of MCS-forced subsidence and further column warming due to insolation according to the PTE (see also Fig. 5.16f, middle). As indicated by the VTE, the intensification of the MCS in this moist environment led to a substantial production of cyclonic vorticity in the column above the heat low due to vortex stretching and vertical vorticity advection. The passage of the midlevel wave disturbance further deepened the layer of cyclonic vorticity. Moreover,

the gradual decrease of the Rossby radius of deformation to around 200 km suggests that the spatial extent of the MCS was large enough to enable the mid- to low-tropospheric moist vortex to form, which in turn was capable of both trapping moisture and slowing down the propagation of the MCS. The latter supported the extreme rainfall accumulation over Abakaliki.

- During the Coastal phase (CP, 12 June, 0600 UTC – 13 June, 1800 UTC), a secondary vortex separated from the western flank of the main vortex. Subsequently, the MCS was closely linked to this accompanying secondary vortex, both of which travelled at a similar propagation speed along the Guinea Coast. Since lower DCAPE values during CP compared to SP indicate less favourable conditions for an efficient development of a convective coldpool, it is suggested that high PW and constant MFC associated with the secondary vortex ensured the continuation of the MCS in an overall low-CIN environment. The formation of new convective cells in the wake of the dissipating MCS and in the range of the secondary vortex particularly caused the high rainfall amount in Abidjan and continued the storm track towards the Atlantic.

A vortex formation due to an MCS passage and the subsequent coupling between vortex and MCS has hardly been documented in detail yet for the Guinea Coast region. A substantial amount of work on this topic has been dedicated to the midlatitudes (e.g. Cotton et al.; 1989; Knievel and Johnson; 2003; Galarneau Jr et al.; 2009), where more conducive conditions for the development of midlevel mesoscale convective vortices prevail than in the tropics, owing to the higher background planetary vorticity. This is a major element of the concept of the Rossby radius of deformation λ_R, which quantifies the required horizontal length scale of a disturbance capable of establishing a geostrophically quasi-balanced circulation. As discussed in section 5.5.2, λ_R was significantly lowered by virtue of the reduction of lower-tropospheric moist static stability and the increase of background relative vorticity during the MCS passage. The latter was supported by latent-heat-release driven column stretching and vertical vorticity advection as well as the synoptic-scale wave disturbance. It suggests that the juxtaposition of these processes enabled the MCS to become "dynamically large" at some point, that is larger than λ_R, which in turn allowed the MCS to efficiently transmit energy from latent heat release into the background flow. In principle, Cotton et al. (1989) already pointed out that larger modifications to the inertial stability around MCSs in tropical regions is primarily subject to the areal extent of an MCS and/or the presence of substantial rotation within it. The present case outlined the dimensions under which a quasi-balanced vortex is able to form in a low latitude region such as the humid Guinea Coast.

Although novel for the Guinea Coast, at least two cases of vortex generations are documented for the Sahelian and Soudanian bands farther north, which show some parallels to the dynamical characteristics over the Abakaliki region. First, the high-impact rainfall event around Ouagadougou 2009 in the Sudanian zone was caused by the passage of two successive convective cells within a moist vortex, the latter of which developed from a "breaking" AEW (Galvin; 2010; Lafore et al.; 2017a; Engel et al.; 2017). Together with their slow-moving behaviour, the dynamical and thermodynamical controls associated with these vortices, such as trapped moisture
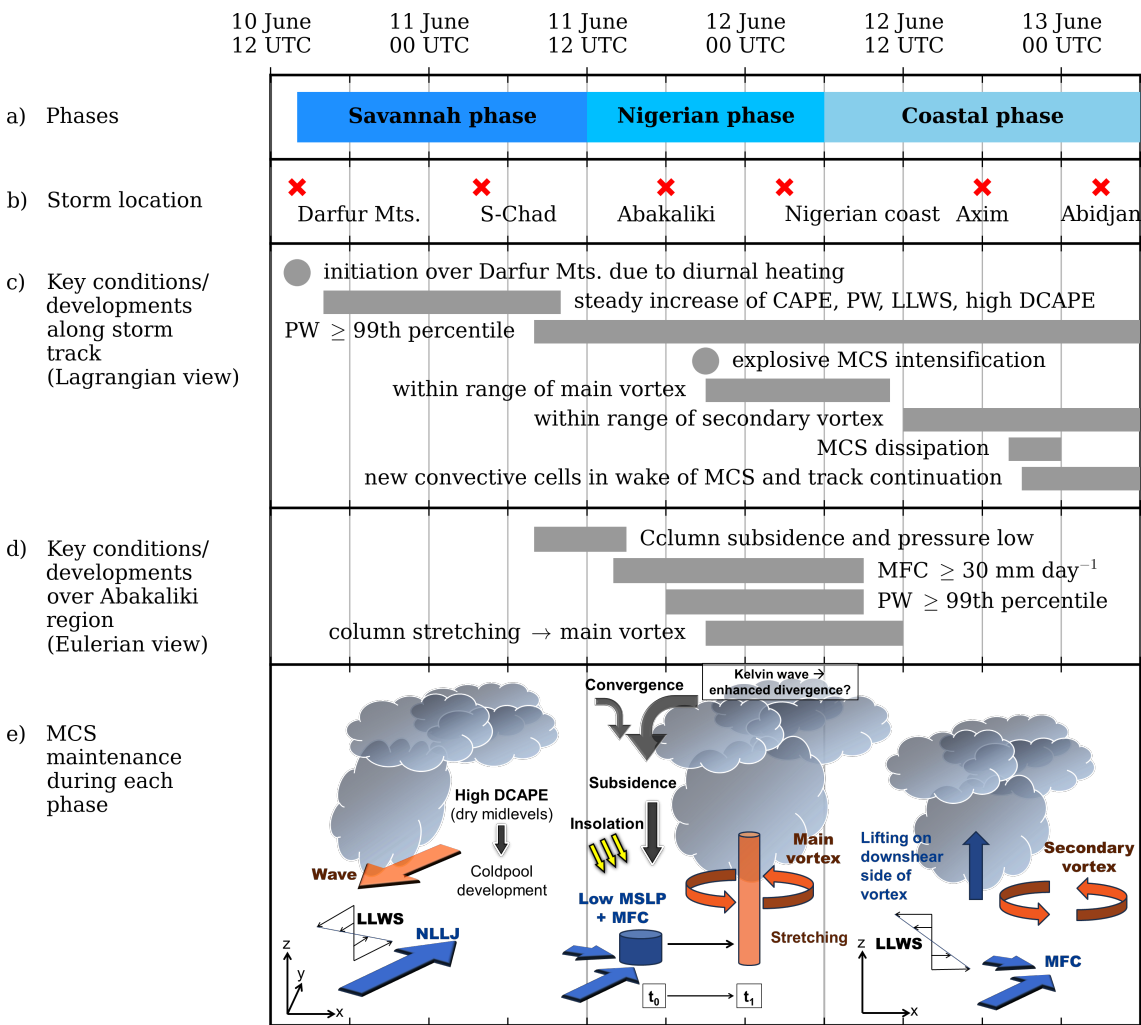
Figure 5.16: Schematic summary of the evolution of the extreme rainfall event in a timeline encompassing 10 June 2016, 1200 UTC, and 13 June 2016, 0600 UTC, and containing (a) the three phases of MCS development discussed in this chapter, (b) the location of the storm, (c)-(d) key conditions and developments along the storm track and over the Abakaliki region, respectively, and (e) proposed mechanisms for MCS maintenance during the different phases with more details in section 5.7. In (c)-(d), the gray bars denote the length of the periods. From Maranan et al. (2019), ©American Meteorological Society. Used with permission.

and high MFC, appear to be favourable ingredients for local rainfall amounts beyond 200 mm, irrespective of the climatic zone within West Africa. However, judging by the generally high moisture availability, the development of these conditions in the Guinea Coast region may not require the high intensity of the vortex as in the Ougadougou case, which was significantly stronger. In the second case, Schwendike and Jones (2010) investigated the dynamic controls leading to the precursor of hurricane Helene in 2006, which was influenced by strong vortex stretching due to the superposition of a low-level cyclonic circulation and a midlevel AEW anomaly. Although mostly driven by the MCS in the present case, vortex stretching also occurred with a pre-existing low-level depression (Fig. 5.16f, middle) and was further supported by the passage of the wave disturbance at midlevels. The succession of these dynamic characteristics for the vortex develop-

ment are similar to the present case.

For the subsequent MCS maintenance in the moist Guinea Coast region, the (secondary) vortex likely played a major role. Such midlevel vortices are generally known to be favourable for prolonged rainfall (Fink et al.; 2006) due to prevailing widespread low-level convergence (e.g. Acheampong; 1982; Buckle; 1996), which was also true in the present case. However, since cases of vortices coupling with MCSs at the Guinea Coast have rarely been reported, if at all, there is no established theory for MCS maintenance in this region. For the present study, the exact mechanisms also remain uncertain. In the absence of favourable conditions for coldpool generation, which is more typical for the drier Savannah and Sahelian region (cf. Fig. 5.16f, left), strong MFC within an extremely moist environment associated with the vortex (PW > 99th percentile along the MCS track) is a likely key ingredient. Although at times stronger during CP compared to SP, the role of LLWS, in turn, for MCS maintenance and propagation is not clear. In their theory about long-lived MCSs, Raymond and Jiang (1990) postulated a mechanism of forced ascent that includes the presence of two ingredients: a positive potential vorticity (PV) anomaly, i.e. the vortex, and ambient shear in the lower troposphere. In principle, as vortex-relative flow follow isentropic surfaces under the assumption of adiabatic processes, lifting is promoted both underneath and on the downshear side of the PV anomaly. If easterly shear is assumed, like in the present case, strongest ascent would therefore occur effectively to the west of the PV anomaly (Fig. 5.16f, right). Since highest convective activity associated with the MCS is located to the west of the vortex during the entire CP (Fig. 5.13), this would fit the theory. The MCS can be maintained as long as moisture and unstable airmasses are supplied and lifted (Markowski and Richardson; 2011), which may explain why the MCS was tied so closely to the vortex, as indicated by their respective propagation velocities. However, this mechanism remains speculative because of the highly non-idealised setting.

6. Ground-based identification of rainfall systems and validation of GPM IMERG

6.1 Overview of IMERG

Due to a dedicated evaluation of its performance in this section, a more detailed description of the production of the Integrated Multi-Satellite Retrievals for Global Precipitation Measurement (IMERG, Version 5), which was already used in chapter 5, is now given. The base satellite of Global Precipitation Measurement (GPM), the so-called GPM Core Observatory (GPM-CO), deploys two precipitation radars, operating at 35.5 GHz (Ka-band) and 13.6 GHz (Ku-Band), as well as a passive microwave (PMW) radiometer, the GPM Microwave Imager (GMI), whose 13 channels range from 10–183 GHz (Kojima et al.; 2012; Draper et al.; 2015; Grecu et al.; 2016). The basic principle behind this instrumentation set-up is twofold. First, GMI rainfall measurements are calibrated using physically more direct rainfall estimates from the precipitation radars; and second, look-up tables are created, which store PMW-based rainfall estimates for given cloud characteristics over given regions (e.g. Andronache; 2018). The latter is then used to calibrate a constellation of several partner PMW sensors, such as from Megha-Tropique (see chapter 5), via a Bayesian approach, which assigns the most likely rainfall values consistent with both observations and climatology or a priori estimates (Grecu et al.; 2016). This network of PMW sensors enables a revisiting time of 1–2 hours at a given pixel. Within IMERG, infrared (IR) based rainfall estimates from almost continuously measuring geostationary satellites are added into the database, which are calibrated against PMW values as well. This provides an almost global, half-hourly precipitation dataset with a spatial resolution of 0.1° (Hou et al.; 2014).

In a further step, rainfall information from a gridded, ground-based rain gauge dataset compiled by the Global Precipitation Climatology Centre (GPCC) (Huffman et al.; 2015) are used to perform regional calibrations of the purely satellite-based rainfall estimations, which, however, is naturally confined to land areas. The satellite information are nudged towards the rain gauge data on a monthly basis. Here, the monthly dataset is composed simply by summation of all half-hourly data fields. A preliminary gauge-adjusted monthly satellite estimate is then combined with the original gridded rain gauge information via inverse-error-variance weighting (Huffman;

1997), which yields the combined and optimised satellite-gauge (SG) dataset. The workflow of the IMERG algorithm can be found in Huffman et al. (2015). The final post-processing step applies a rescaling of the raw, satellite-only half-hourly dataset to ensure consistency with the monthly rainfall product. Here, it is multiplied by the ratio of the monthly SG and satellite-only dataset. Both the monthly and half-hourly gauge-calibrated rainfall datasets are part of the "final run" product of IMERG, which is generally used in the following analysis (stored as "precipitationCal" in the half-hourly data). The non-gauge-calibrated version, termed "precipitationUncal", is provided in the final run dataset as well.

6.2   Other datasets and methods

6.2.1   Rain gauge dataset

The establishment of the DACCIWA rain gauge (RG hereafter) network began in June 2015 and went fully operational in December of the same year. A total of 17 RGs were placed within a radius of 80 km around the city of Kumasi, Ghana, roughly 200 km inland (Figure 6.2). Considering the spatial partitioning of SWA for the satellite-based rainfall analysis (Figure 4.1), the RGs are located at the southern end of the Inland region. Figure 6.2 shows the spatial distribution of the RGs as of November 2018, which exhibits a distinct north-south and west-east transect. By that, it was ensured to capture the movement of convective systems, particularly of westward propagating MCSs (e.g. Laing et al.; 2008). In July 2017, the RG station Owabi (marked in red) was relocated to the Kumasi airport (RG13_Airport) due to maintenance issues in a dust- and insect-laden environment.

The RG instrumentation consists of a rainfall collector, a solar panel and a logger box. The latter controls the electricity through a solar regulator that recharges a built-in battery and switches between battery and solar panel mode, depending on which provides a higher voltage output. Therefore, the RG instrumentation forms a stand-alone system, which keeps monitoring rainfall throughout the day and night. The rainfall collector operates on the principle that rain water falling into the collector is funnelled through a hole, which leads to the formation of drops of the same diameter. Here, one drop is equal to 0.01 mm rainfall. The passage of a drop is registered by an infrared sensor within the collector and causes an electric signal, which is sent back to the logger box. Here, the temporal resolution of data recording is one minute. The upper bound of measurable rainfall rate is approximately 300 mm hr^{-1}. At this rate, the water load is too high and causes a stream of water rather than single drops.

For the present study, RG data from 2016 and 2017 are evaluated. Figure 6.3 illustrates the availability of RG data in this period at every RG station as well as daily rainfall values after quality control. The quality control was performed on daily rainfall and consisted of two main steps. First, a manual removal of obvious erroneous periods, such as unrealistic values or long periods of failed recordings, was performed by comparison with neighbouring RGs. The basic idea behind this very first step was the assessment of coherence among the RGs. Second, where possible, individual RGs were compared with collocated RGs from the Ghana Meteorological
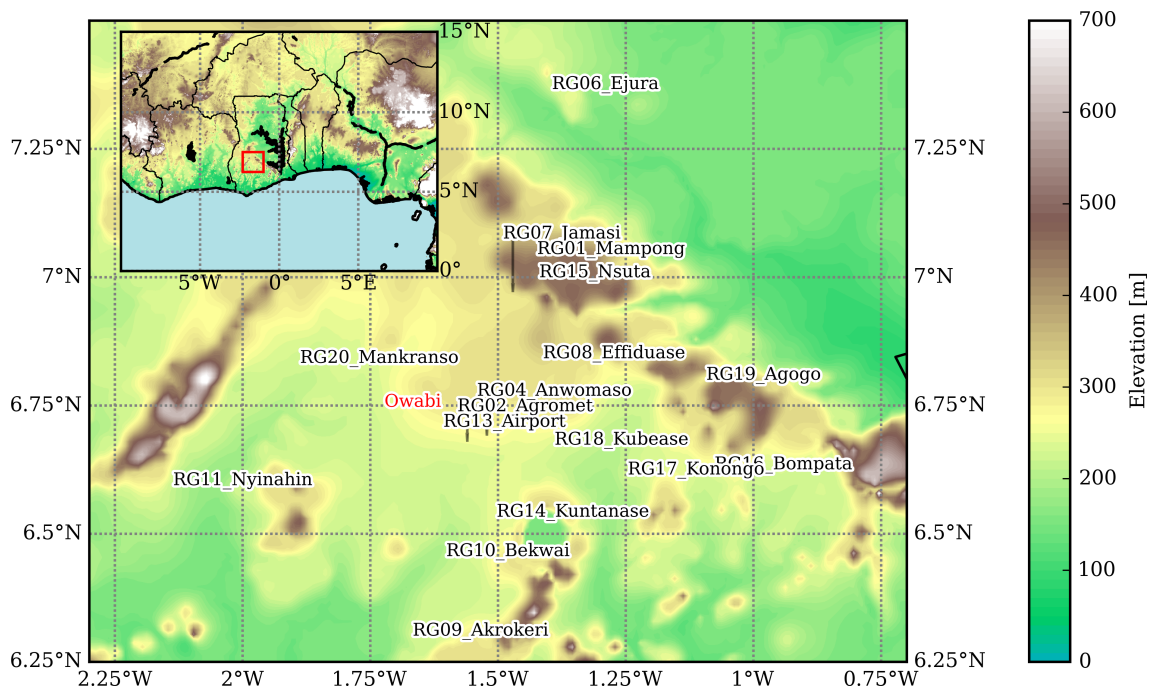
Figure 6.1: Spatial distribution of the rain gauges (black labeling) in the Ashanti region of Ghana as of November 2018 (see red box in the map inset in the upper left corner). The station Owabi (labeled in red) was relocated to the Kumasi airport (RG13_Airport) in June 2017. The terrain elevation is colour-shaded.

(a) Enclosed rain gauge instrumentation. The solar panel sits on top of a small scaffolding that holds the data logger.

(b) Close-up of a rain collector showing the funnel and a thin-wired filter in the middle.

Figure 6.2: Rain gauge instrumentation on a school yard in Konongo (RG17), illustrating the three main components, i.e. solar panel, data logger and rain collector.

Agency (GMET) using rainfall accumulation curves. Days within the RGs that causes a strong deviation to GMET were removed. In Figure 6.3, periods of missing data are particularly visible between September 2016 and May 2017, where rainfall data were temporarily obtained from only seven RGs. Note that the period of zero rainfall in the beginning of 2016 comprises the main dry season over SWA (see Figure 4.3).

Figure 6.3: Availability of data between January 2016 and December 2017 for each of the 17 RGs. The coloured lines denote the daily accumulated rainfall from 0000 UTC – 2400 UTC. The labels on the right axis indicate the fractional data availability in the aforementioned period. Missing or excluded data are blank spaced areas.
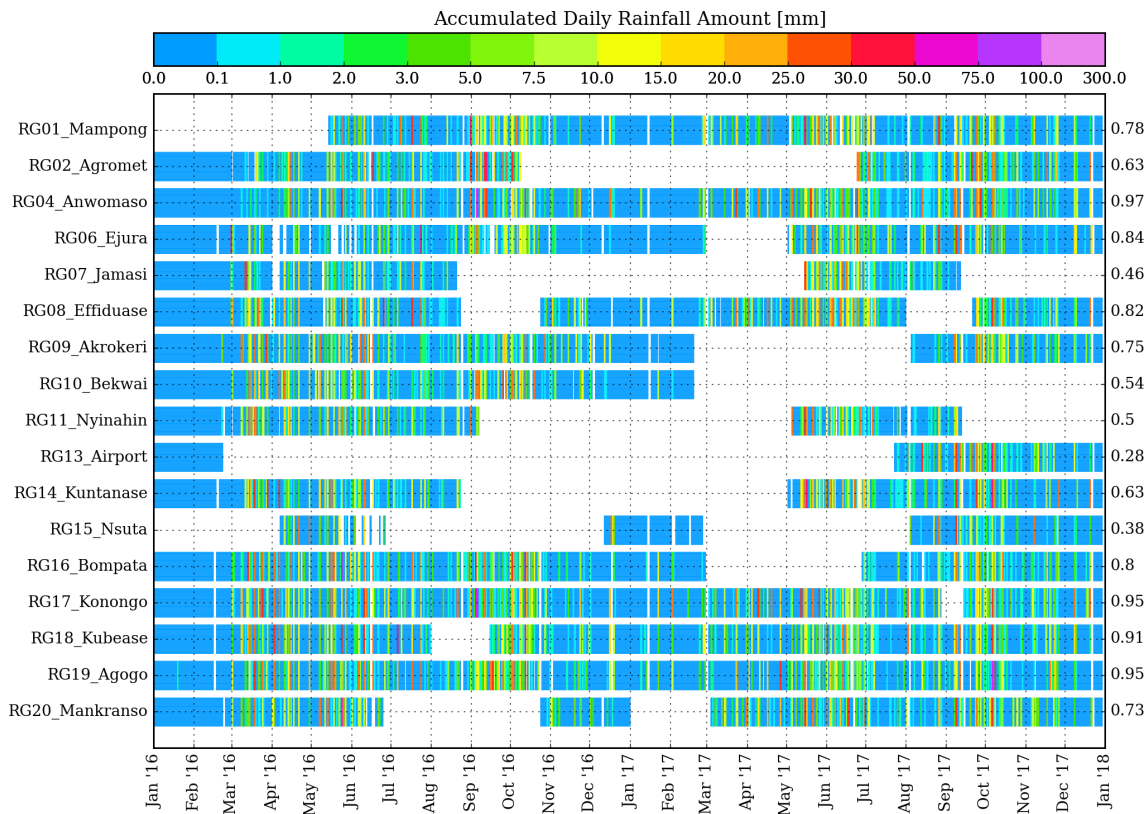
6.2.2   Cloud property dataset using SEVIRI edition 2 (CLAAS-2)

The CLAAS-2 dataset (Stengel et al.; 2014; Benas et al.; 2017) is compiled by the Satellite Application Facility on Climate Monitoring (CM SAF) and specifically contains cloud-top information derived from multiple spectral channels of SEVIRI at the same native spatial grid and temporal resolution (see chapter 4 for more information about SEVIRI). Here, the thermodynamic cloud phase (CPH), cloud top pressure (CTP) and temperature (CTT), and cloud optical thickness (COT) are used. The retrieval of the cloud properties follows the cloud physical properties (CPP) scheme described in Roebeling et al. (2008) and consists of two main parts. First, the CPH is determined through several threshold tests on observed and simulated IR brightness temperature fields, which ultimately yields a flag ("liquid" or "ice") for every cloudy pixel. In the second step, observed reflectances at the visible and near-IR wavelengths 0.6 and 1.6 μm, respectively, are compared with simulated reflectances in look-up tables to retrieve COT as well as the cloud particle effective radius for both liquid and ice pixels. In the same manner as for IMERG, the closest gridpoint to the respective RG positions are considered in the analysis.

6.2.3   Identification of rainfall events within the RG dataset

Convective systems crossing the domain of the RG network may be detected by multiple RGs if they are sufficiently large. To minimise redundancy in the number of rainfall events, such cases must therefore be assigned as the same event in the RG datasets. For this purpose, a method largely based on that of Upton (2002) is used, which applies a cross-correlation-regression algorithm that allows the identification of coherent rainfall events as well as their translation direction and velocity. The RG data were pre-processed by eliminating minutely rainfall of less than 0.02 mm or if the rainfall event lasted for less than five minutes. Particularly one-minute rainfall spikes have occurred for unknown reasons even under dry conditions and are therefore discarded.

For the event identification, a "dry period" was defined at first, which is a period with at least 15 minutes of zero rainfall in all available RGs. This dry period already separates different rainy spells. The RG data were then aggregated to a 30-minute centered moving average to reduce the noise in the cross-correlation curve. Here, the correlation for a given timeshift l is defined as

$$r_{ij}(l) = \frac{\sum_i \sum_j d_i(t) d_j(t+l)}{\sqrt{\sum_i d_i^2(t) \sum_j d_j^2(t+l)}} \tag{6.1}$$

where $d_i(t)$ is the difference between the rainfall measurement $R_i(t)$ and the mean rainfall value of the event $\bar{R}_i$ at RG station i at time t, and $d_j(t+l)$ the corresponding difference at station j at time $t+l$. Instead of setting a fixed threshold for the correlation in order to eliminate questionable RGs, the coherence within the entire correlation matrix was examined. In principle, questionable RGs will yield a much lower mean correlation value compared to the mean correlation value of the matrix. If the absolute value of this difference exceed the variance of the matrix by a factor of three, the respective RG measurement is discarded (see Upton (2002) for a more detailed explanation). The idea behind this approach instead of using a fixed threshold is that the variance of the correlation values can be relatively large, particularly in convective situations, where rainfall profiles may vary significantly from station to station. A fixed threshold would lead to a higher rate of elimination. However, to further minimise erratic assignments, an additional condition is introduced where stations that register rainfall must be located within 40 km of each other. This ensured that small and independent convective systems passing over distant stations around the same time were not considered as one single event. The distance threshold is somewhat arbitrary but was chosen based on the spatial distribution of the stations. Finally, with a set of stations and their respective time lags l_{ij} to each other, a least squares planar regression is applied following the equation

$$l_{ij} = \alpha x_{ij} + \beta y_{ij} \tag{6.2}$$

where x_{ij} and y_{ij} are the zonal and meridional distance of station i and j, respectively. An

Table 6.1: Definition of six rainfall types based on the event duration and the mean rainfall intensity, similar to the approach of Dezfuli et al. (2017).

	Duration [min]	Intensity [mm h^{-1}]
Weak short rainfall (WSR)	5–80	<10
Strong short rainfall (SSR)	5–80	$10 \leq RR < 30$
Intense short rainfall (ISR)	5–80	≥ 30
Weak long rainfall (WLR)	≥80	<10
Strong long rainfall (SLR)	≥80	$10 \leq RR < 30$
Intense long rainfall (ILR)	≥80	≥ 30

estimation of the velocity $|v|$ and direction of storm movement φ is given by

$$|v| = \sqrt{\alpha^2 + \beta^2} \qquad (6.3)$$

$$\sin(\varphi) = \alpha \quad \text{and} \quad \cos(\varphi) = \beta, \qquad (6.4)$$

respectively. It should be noted that both velocity and direction were calculated only if four or more stations registered rainfall, in order to obtain more robust values.

6.2.4   Definition of rainfall types

Having used the identification algorithm, rainfall types were defined by following an extended approach of Dezfuli et al. (2017) based on the maximum event duration and the corresponding maximum mean rainfall rate (Table 6.1). With respect to the duration, an 80 minute threshold was set to distinguish "short rainfall (SR)" from "long rainfall (LR)". Two thresholds were applied with respect to the mean rainfall rate (10 mm h^{-1} and 30 mm h^{-1}) leading to "weak (W)", "strong (S)" and "intense (I)" events. The larger threshold was not used in Dezfuli et al. (2017) but was taken here to allow a more distinct characterisation of the rainfall types. Everything combined yields six classes. In the following, "weak and short rainfall" for instance is abbreviated "WSR", while "strong and long rainfall" is termed "SLR". The aforementioned emphasis on "maximum" duration and mean rainfall rate implies that if a station records only little rainfall from an event identified overall as an SLR, for instance, this rainfall amount will be counted in favour of SLR despite being, say, a WSR event individually.

6.2.5   The 2×2 contingency table and skill measures

IMERG will largely be evaluated using the 2x2 contingency table (Table 6.2), which is a common tool for model as well as non-probabilistic forecast verification (e.g. Doswell III et al.; 1990). Four cases (a)-(d) can occur: (a) hit, (b) missed event, (c) false alarm and (d) correct negative. A hit is identified if both the RG and IMERG register rainfall above 0.1 mm. This threshold applies for all evaluated timescales in the upcoming analysis. Missed events are detected in event that rainfall is registered within the RG, but is absent in IMERG. False alarms are defined the other

Table 6.2: 2×2 contingency table for the pairs of RG and IMERG rainfall observations.

	RG yes	RG no
IMERG yes	Hit (a)	False alarm (c)
IMERG no	Missed event (b)	Correct negative (d)

way round. If rainfall is zero in both data, a correct negative occurs.

From here, some scalar attributes are used to describe the behaviour of IMERG, which are the bias ratio *BIAS*, the false alarm ratio *FAR*, and the probability of detection *POD*:

$$BIAS = \frac{a+b}{a+c} \quad , \quad FAR = \frac{b}{a+b} \quad , \quad POD = \frac{a}{a+c} \tag{6.5}$$

A bias ratio of *BIAS* = 1 indicates an unbiased observation by IMERG, meaning that the same number of rainfall events in IMERG and RG are observed. Depending on the number of false alarms and missed events, rainfall events are over- and under-observed if *BIAS* > 1 and *BIAS* < 1, respectively. *FAR* indicates the number of false alarms made by IMERG relative to all of its observed rainfall events. Here, the best outcome is *FAR* = 0, the worst *FAR* = 1. *POD* in turn is the ratio of all hits made by IMERG and the total number rainfall events within RG. It ranges from 0 to 1 with *POD* = 1 being the best result.

Finally, a relative accuracy measure commonly known as the Heidke Skill Score (HSS) (Heidke; 1926) is applied as well, which takes the form

$$HSS = \frac{2(ad-bc)}{(a+c)(c+d)+(a+b)(b+d)} \tag{6.6}$$

The *HSS* evaluates the accuracy of IMERG compared to the accuracy attained by purely random chance. A value of *HSS* = 1 indicates maximum skill, a value of *HSS* = 0 means no skill. Technically, the *HSS* can become negative, which would imply a lower skill of IMERG than random observations.

6.3 Analysis of rainfall types in the RG network

6.3.1 Number and rainfall contribution

During 2016 and 2017, a total of 4797 rainfall events were identified within the RG data. Figure 6.4 shows the distribution of rainfall events with respect to the event duration and both mean rainfall rate (Figure 6.4a) and maximum accumulated rainfall (Figure 6.4b) during the event. A distinct division of the six rainfall types is visible in Figure 6.4a since exactly these parameters were thresholded for the rainfall type definition. In general, the number of events decrease with higher intensity and duration as expected. Here, WSRs dominate the fractional number of events and account for more than half of all events (%n=51.4%). Together with the stronger SR types, 90% of all events are of SR type. This number resembles the occurrence frequency of weakly

organised systems identified with satellite data of TRMM-PR in chapter 4. It suggests that the majority of these weak TRMM-PR-based rainfall systems are short-lived. While SR types occur far more frequently than LR, they contribute only around 40% to total rainfall (see %RR in Figure 6.4). Again, the TRMM-PR-based rainfall types exhibit a similar characteristic, where less-intense convection contributes between 29% and 44% of the total rainfall despite being more numerous (cf. Figure 4.4). Following Figure 4.4, the relative strength of the rainfall types can be better visualised by calculating the ratio between the fractional rainfall %RR and occurrence frequency %n for the six rainfall types (termed %nRR in Figure 6.4a), normalised with respect to WSRs (%nRR of WSRs is 1). Averaged per event, ILRs produce 110 times more rainfall than WSRs. Even though being in the same intensity interval, still 14 times more rainfall is registered for WLRs due to their longer duration (>80 min by definition). Comparing the most intense types, ILRs account for over six times more rainfall per event than ISRs. It shows that the event duration is a major factor for local rainfall accumulation. The duration is, among other things, a function of the size of the rainfall system, which was particularly emphasised in the Abakaliki case study in chapter 5.
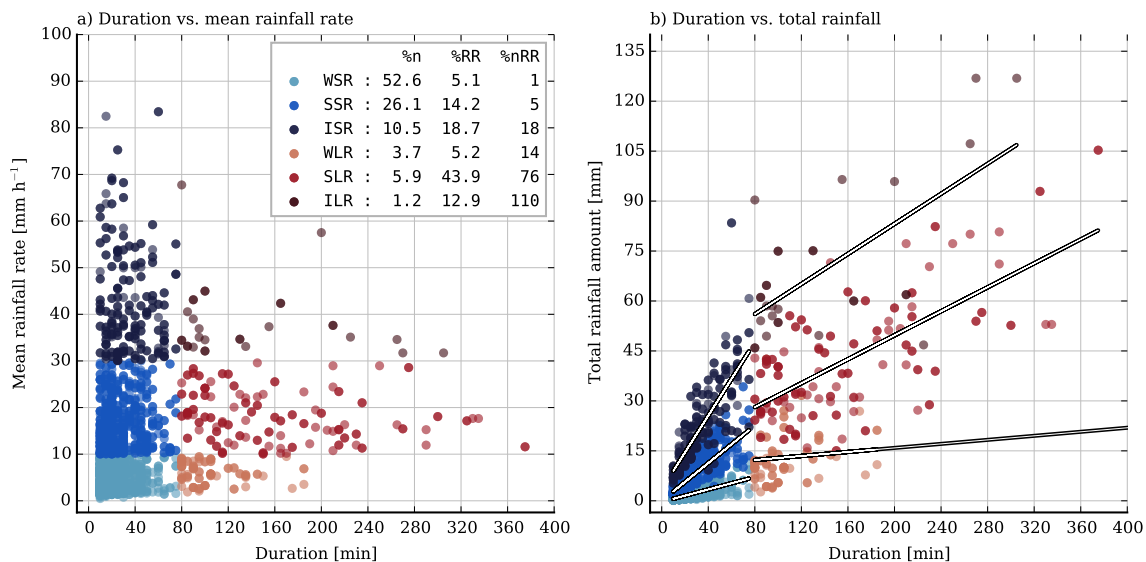
Figure 6.4: Scatter plots showing all identified rainfall events with respect to (a) the event duration and the mean rainfall rate, and (b) the duration and accumulated rainfall amount during the event. Generally, short rainfall types (SRs) and long rainfall types (LRs) are plotted in different shades of blue and red, respectively. In the legend in (a), the rainfall types defined in section 6.2 are listed as well as their fractional occurrence (%n), the fractional rainfall contribution (%RR) and the WSR-normalised ratio between %RR and %n (%nRR, it is 1 for WSRs). The regression lines in (b) were calculated separately for each rainfall type.

6.3.2 Rainfall profiles and translation characteristics

The accumulated rainfall amount as a function of the duration is presented in Figure 6.4b, where a regression line is added for each rainfall type. Except in the case of weak intensity, the regression line for LRs exhibit a smaller slope than for SRs, which indicates that the mean intensity weakens

beyond 80 minutes. Recalling the structure of a typical matured MCS in Figure 3.6, it is likely related to the passage of the intense convective part, followed by the weaker but usually larger stratiform portion of the precipitating cloud. Further inspection is performed by creating composites of 5-min rainfall rates over the event time for all rainfall types (Figure 6.5). Note that different scalings are used for the rainfall rate on the ordinates. Common among all types is a more or less sharp increase of the rainfall rate shortly after the onset of the rainfall event. The profile reaches its maximum typically within 15 minutes before it strongly decreases again. Unlike SRs, the profiles of LRs gradually transition into a regime of largely constant rainfall rates, which indicates the stratiform part of the convective system. Therefore, the classification of rainfall events (Figure 6.4a) with respect to the mean intensity is strongly linked with the intensity of their convective parts, whereas the partitioning regarding the event duration (SRs vs. LRs) separates more organised systems from less organised ones. The profiles of the LR types show similarities to those presented in Fink et al. (2006) showing MCSs with different levels of organisation. It should be noted that the profile of ILRs exhibits a broader peak than any other type. It is assumed that ILR comprises convective clusters with a large spatial extent. In general, the profiles of all rainfall types are highly variable, given the fact that the colour-shaded areas denote the rainfall rates only within plus/minus one half standard deviation.

Only around 5.7% of all events (273 cases) were large enough to be registered by four stations or more, emphasising the dominance of small-sized convective systems in the sampling. Their respective direction of arrival as well as the velocity are presented as a windrose in Figure 6.6a. Evidently, convective systems generally come from easterly directions, but predominantly from the northeast. Here, the three northeasterly sectors contain almost 40% of all cases. Furthermore, the few systems exhibiting a translation velocity of 20 ms^{-1} or more enter the region from the northeast. The systems from the southeast may partly originate from land-sea-breeze interactions at the coast, which are ultimately advected inland. The coastal pattern of the diurnal harmonics in Figure 4.2 already indicated some tendency of inland movement of convective clouds. Regarding typical translation velocities, around 65% of all events propagate with a speed between 5 and 15 ms^{-1}, which is generally in accordance with Figure 4.11. The median is 9.4 ms^{-1} and is slightly higher than the satellite-based average velocity over southern West Africa in chapter 4 (8.2 ms^{-1}). The windrose in Figure 6.6b in turn shows the fractions of rainfall types. The types with weak intensity (WSR, WLR) are barely represented. Given the four-station threshold, it indicates generally low spatial coherence during such events. All other rainfall types originate from almost any of the indicated directions. Some tendency towards the northeastern directions are visible for SRs (SSR, ISR). However, no such conclusion can be made for LRs, which also arrive from the southeast. Again, it remains to be answered whether advected land-sea breeze convection are represented in the southeastern systems.

6.3.3 Diurnal and seasonal cycles

Based on the satellite composites in chapter 4, the diurnal cycle of rainfall in the Inland region of southern West Africa is dominated by convection occurring in the late afternoon and early evening.
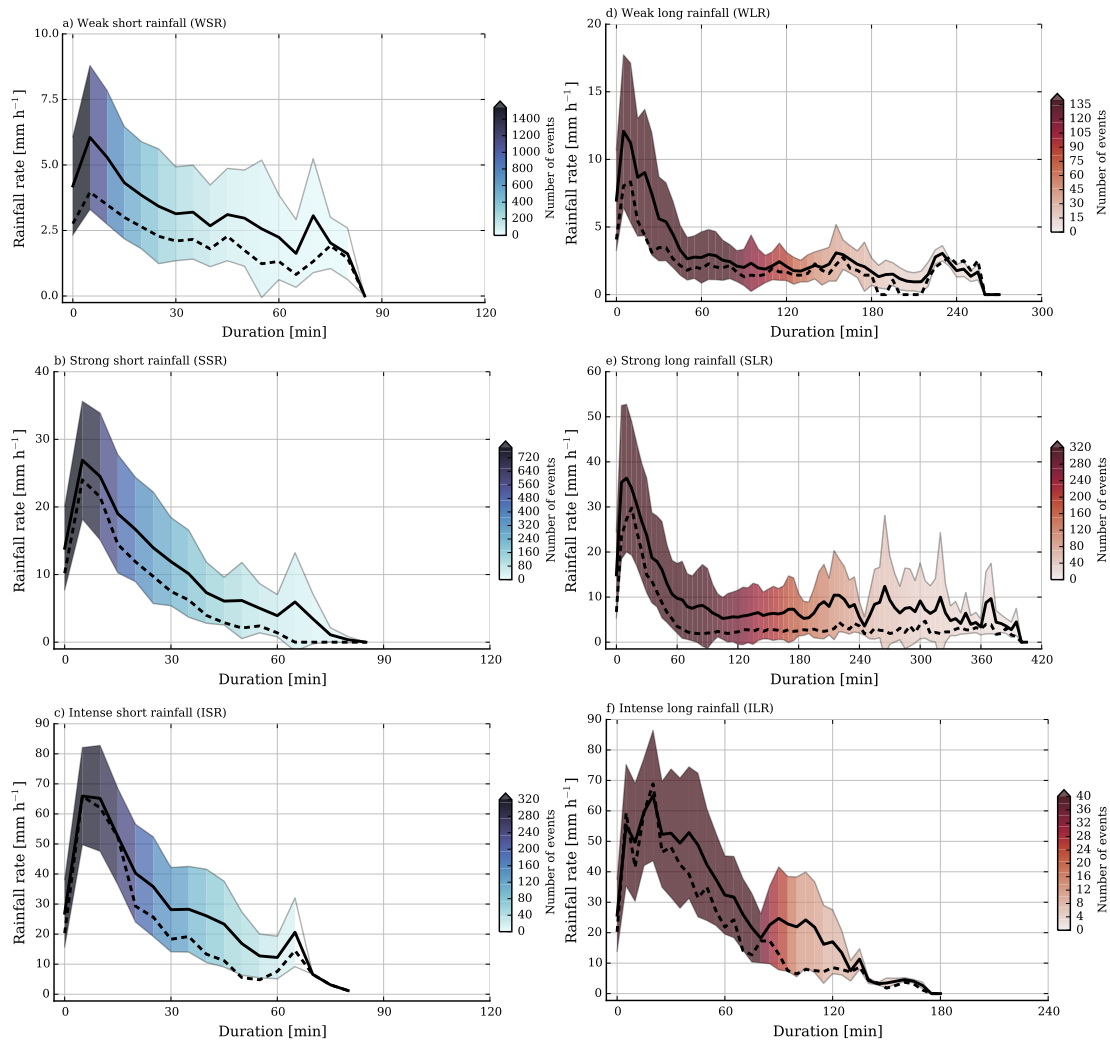
Figure 6.5: Profiles of the mean (solid black line) and median (dashed black line) 5-min rainfall rates against the elapsed time of (a) WSRs, (b) SSRs, (c) ISRs, (d) WLRs, (e) SLRs and (f) ILRs. The coloured area enclose plus/minus one half of the standard deviation. The colours denote the number of convective systems in each 5-min interval used to determine the mean, median and standard deviation profiles. Note the different scalings for some rainfall types. The zero-minute mark is the interval from 0–5 minutes.

Furthermore, intense and highly organised rainfall systems were identified to develop over the course of the night (Figure 4.6). A general perspective of diurnal rainfall in the RG domain is presented in Figure 6.7 as one- and two-dimensional histograms regarding the time of occurrence and peak rainfall amount, binned every hour and 5 mm, respectively. In accordance with the satellite-based analysis, the highest frequencies of rainfall events are found in the afternoon to early evening between 1500 and 1800 UTC (top panel). The occurrence frequency generally fades towards the night and is lowest in the period from 0300 to 1200 UTC. Considering the peak rainfall amount, the distribution of the occurrence frequency is strongly influenced by rainfall events with less than 5 mm, overall accounting for almost 60% of all events (right panel, lowest row). However, the bulk of stronger rainfall with more than 5 mm are still found in the late afternoon.
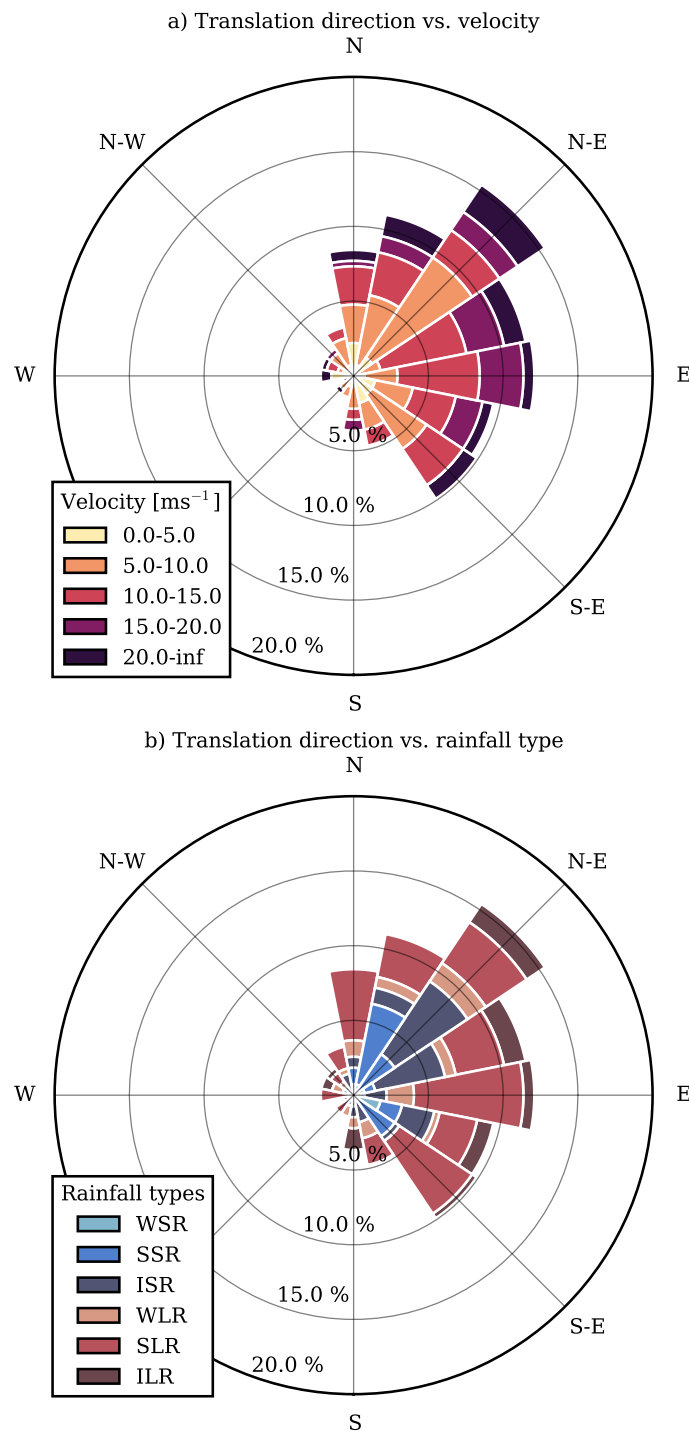
Figure 6.6: Windroses showing the percentage of convective systems arriving from one of 16 direction sectors in combination with (a) the translation velocity of the storms, and (b) the rainfall type.

Interestingly, events with a peak rainfall amount of more than 50 mm also occurred after midnight and in the morning, which may originate from the aforementioned nocturnal organised convection.

In Figure 6.8, diurnal rainfall is shown on a seasonal perspective with respect to both daily
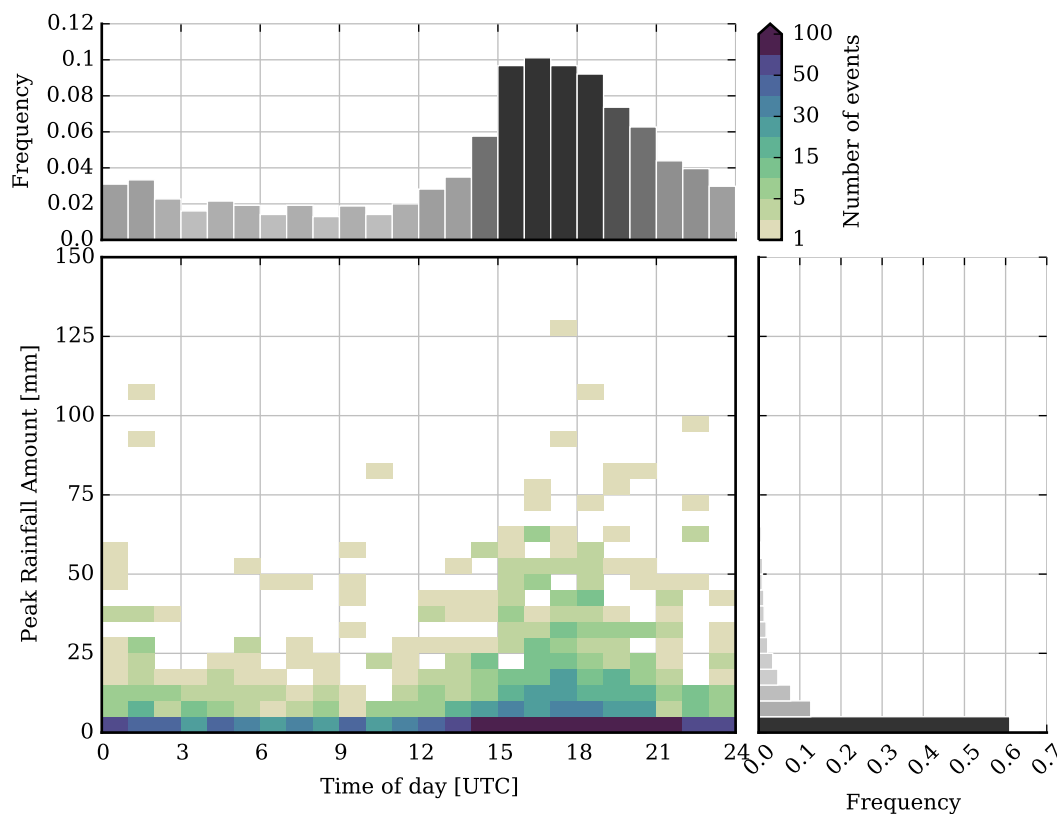
Figure 6.7: One- and two-dimensional histograms of the number of events with respect to the on-set time of rainfall (abscissa and upper panel) and the peak accumulated rainfall amount (ordinate and right panel).

rainfall rate (Figure 6.8a) and the contribution of the rainfall types (Figure 6.8b). As expected, the annual mean of diurnal rainfall (top left panel) shows a distinct diurnal peak around 1900 UTC, which coincides with the diurnal harmonic (red dashed line). In fact, rainfall maximises in the late afternoon/early evening in all months, most pronounced during the two rainy seasons in the year from March–June (primary rainy season) and September–October (secondary rainy season). However, particularly in March and April, a secondary peak is evident after midnight, leading to a shift of the diurnal harmonic away from the primary maximum around 1600 UTC to later hours. Nocturnal rainfall is also visible during September and October. In general, the diurnal harmonic varies little over the course of the year, except for the drier months August and November (1600–1700 UTC). The plot at the top of Figure 6.8b illustrates the diurnal contribution of the rainfall types averaged over the year. The increase of rainfall in the afternoon coincides with an increase of the fractional contribution of SR types (all blue bars), which is highest in the 1500–1800 UTC interval with around 52%. It confirms the satellite-based results of Figure 4.6, which also suggests the highest frequency of diurnal, short-lived convection around this time. Rainfall from WSRs is almost non-existent in the afternoon and remains also small during the night. Of all LR types (red bars), SLRs occur at any time during the day and also dominate the relative contribution of a single type. The contribution of ILRs begins to increase at 1200 UTC and maximises in the 2100–2400 UTC interval. Interestingly, WLRs exhibit a relative maximum during the night. Recalling

the much weaker convective part of its rainfall profile (Figure 6.5d), some WLRs may be related to dissipating nocturnal MCSs. Over the course of the year, LRs are most active from March to October, which comprises both rainy seasons. One distinct feature of the rainy season is that the afternoon rainfall peaks largely stem from LRs. Afternoon rainfall in March and October is increasingly influenced by SRs and marks the transition from and into the main dry season from November to February. With few exceptions, the dry season is largely influenced by SRs. Note that no rainfall was registered where intervals are blank.

These findings are projected onto a seasonal cycle in Figure 6.9, separated for the years 2016 and 2017. Note that monthly rainfall means (solid white lines) were determined from RG stations where at least 90% of monthly data were available. They were then rescaled to their theoretical values mimicking 100% of data availability. Furthermore, the coloured boxes refer to the scale on the right side, denoting the relative contributions of the rainfall types to the mean monthly rainfall. First of all, 2016 and 2017 exhibit distinctively different seasonal cycles. In 2016, the primary rainy season from March to June was weaker than the secondary rainy season in September and October. Here, 2017 resembles the climatological seasonal cycle much closer (see Figure 4.3). Averaged over both years, the mean annual precipitation amount is 1138 mm and is a typical value for the inland region of SWA (Fink et al.; 2017). Across the RG network, the seasonal cycles are highly variable, particularly during the peak of the two rainy seasons. For instance, the spread of $\pm 1\sigma$, indicated by thin white dotted lines, reaches almost 150 mm in September 2016 and again around 130 mm in 2017. These months were strongly influenced by the combination of LRs and the intense types (ISRs, ILRs), where a large spatial inhomogeneity of rainfall intensities may have occurred during their passages. As already indicated above, LRs are most active during the rainy seasons, contributing up to 80% to monthly rainfall, while SRs dominate the main dry season. Interestingly, the fractional contribution of WSRs is increased during the little dry season in July and August (see 4.4). Comparing this to the satellite-based analysis in Figure 4.5, WSRs may partly be represented by isolated shallow echoes (ISEs) or moderate convection (MODs), whose occurrence frequencies maximise in the little dry season in the Inland region. Inversely, the findings suggest that ISEs and MODs are short-lived phenomena.

6.4   Performance evaluation of IMERG

The high temporal resolution of IMERG with 30 minutes allows an evaluation down to the timescale of a rainfall event. To ensure comparability in the following analysis, the RG data were aggregated to half-hourly rainfall as well. The assignment of half-hourly rainfall to the rainfall types is trivial as long as only one type was present in the 30-minute period. If two types occurred in this timespan, all rainfall is attributed to the type with the higher rainfall amount or, if equal, with the longer duration. This happens very rarely (not shown) and is therefore not further discussed. Furthermore, a threshold of 0.1 mm is applied to half-hourly IMERG rainfall to match the lowest possible RG output.
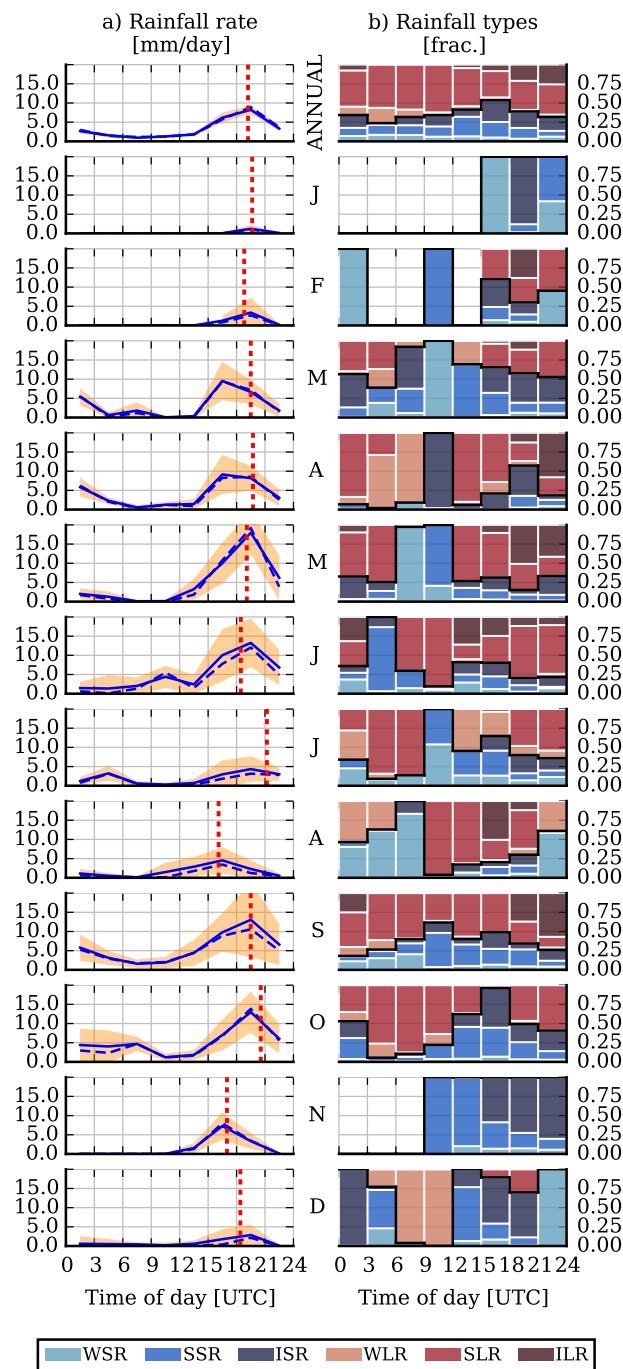
Figure 6.8: Annual perspective of the diurnal cycle of rainfall with regard to (a) the 3-hourly rainfall rate [mm d^{-1}], and (b) the fractional contribution of the rainfall types within each 3-hour interval. The upper two panels show the annual mean.

6.4.1   Regional data quality

Before IMERG is compared to the RG network, a brief overview about its regional data quality is given. As mentioned in section 6.1, RG datasets are used to minimise regional biases and are of particular importance over the usually data-sparse region of southern West Africa (e.g. Panthou et al.; 2014). One available measure in the IMERG dataset that quantifies the "calibration inten-
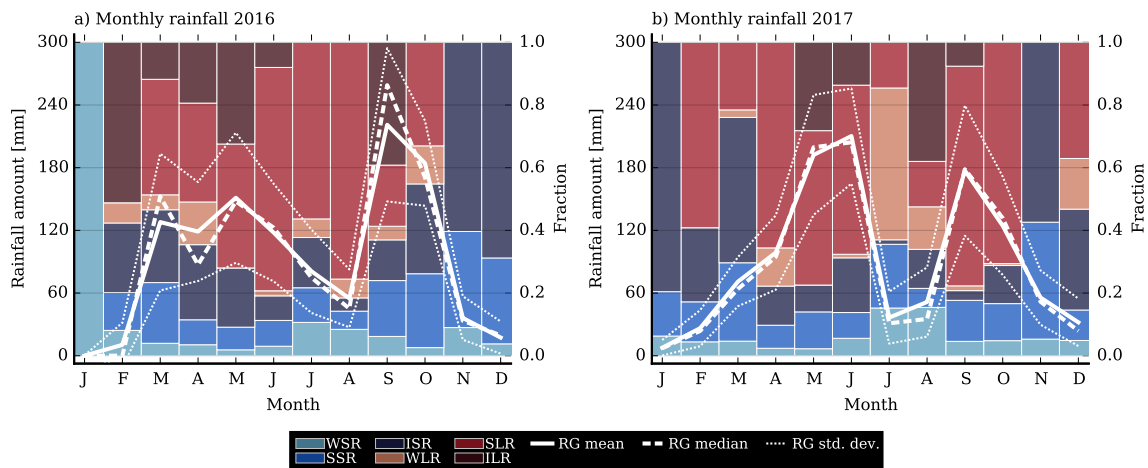
Figure 6.9: Seasonal cycle of monthly rainfall amounts for (a) 2016 and (b) 2017 based on RG data. The coloured bars refer to the fractional contribution of the rainfall types to monthly rainfall (right scale). Note that only months with a temporal coverage of at least 90% at the respective stations were considered for the calculation of the mean (solid white line), median (dashed) and standard deviation (dotted). They were then rescaled to a theoretical 100%-value.

sity" towards RG data is the so-called "gauge relative weight" (GRW hereafter), which ranges from 0 to 100%. The GRW is determined through an inverse-error-variance analysis, where the weight of the RG data is proportional to the reciprocal of its variance estimate (Huffman; 1997). Practically, the variance (GRW) decreases (increases) with more available stations for the calibration of an IMERG gridcell. The regional distribution of the monthly averaged GRW over southern West Africa in the 2016–2017 period is shown in Figure 6.10a. Evidently, the GRW is quite inhomogeneously distributed with "hotspots" located in the western part of Senegal and Togo. The latter also extends into the coastal area of Ghana and thus the RG domain. A GRW of less than 10% is visible in the western part of southern West Africa and large parts of Nigeria. A large number of RGs does exist for Nigeria, as illustrated in Figure 5.3. However, apparently only a fraction of the data entered the Global Telecommunication System (GTS) in 2016 and 2017.

From the Karlsruhe African Surface-Station Database (Vogel et al.; 2018, KASS-D,), six coastal stations in different GRW regimes were selected to evaluate the influence of the calibration in IMERG. Their locations are indicated in Figure 6.10a. It should be noted that RG data were only available for 2016, for which, however, the GRW distribution is similar to that presented here (not shown). Figure 6.10b–g each show the seasonal cycles of 2016 for the RG station (red curve) indicated in the title, the two IMERG products "uncalibrated" (dashed blue line) and "gauge-calibrated" (solid blue line) (see section 6.2), and the monthly GRW indicated as black crosses. Furthermore, Kumasi (Figure 6.10b) refers to the RG station from GMET (WMO number 65442), close to RG13_Airport in Figure 6.2. Some evidence of an improved seasonal cycle is seen for Accra (Figure 6.10d) and Lagos (Figure 6.10e), which exhibit GRW values around 75% and 55%, respectively. However, improvements at the stations Abidjan (Figure 6.10a) and Kumasi, similarly located in a high GRW regime, are marginal and hard to discern. At Warri (Figure 6.10f) and Port Harcourt (Figure 6.10g) in Nigeria with largely less than 25% GRW, differences between the
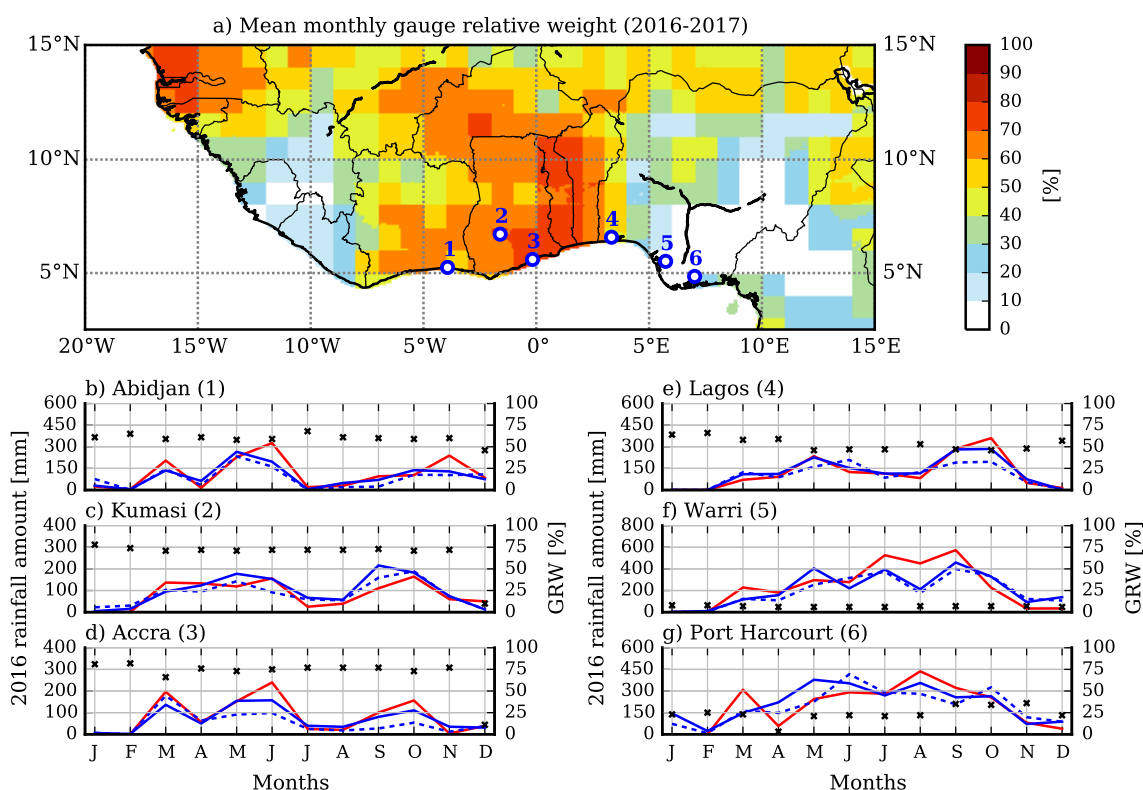
Figure 6.10: (a) Spatial distribution of the mean monthly gauge-relative weight (GRW) within IMERG for the period 2016–2017. The location of six coastal stations indicated in (b)–(g) are marked in the map. (b)–(g) Monthly rainfall amount in 2016 for the six stations based on daily rain gauge data (red curve), the uncalibrated (dashed blue curve) and calibrated (solid blue curve) half-hourly rainfall estimate of IMERG at the nearest gridpoint. The black markers indicate the monthly GRW value. Note the different scales for the monthly rainfall amount.

RG and the uncalibrated IMERG of up to 200 mm are already visible for some months and were barely corrected in the final run. Initially well captured monthly estimates are even pulled away in some instances.

Overall, although the GRW can be considered as a confidence measure for the rainfall estimate in IMERG, a high GRW does not necessarily imply improvements on a pixel-to-pixel basis for specific stations. It may be related to the fact that "large-scale" areal averages of RG data are created within GPCC, leading to a blurring of small-scale details. As seen in Figure 6.9, monthly rainfall can vary a lot even over a relatively small area such as the RG domain. With this premise of strongly gauge-calibrated IMERG gridpoints in the RG domain, the following sections evaluate the performance of IMERG on several timescales.

6.4.2   Seasonal and daily timescales

In analogy to Figure 6.9, the seasonal cycles of IMERG for the years 2016 and 2017 are presented in Figure 6.11, together with the mean monthly rainfall of the RG network (red curve). IMERG is able to capture the basic characteristics of the two rainfall years measured by the RGs by showing a weaker primary than secondary rainy season in 2016 and the opposite situation in 2017. This

leads to high correlation coefficients of r =0.97 and r =0.94, respectively. The mean annual rainfall amount estimated by IMERG is 1194 mm, which slightly overestimates the annual rainfall measured by the RGs (1138 mm). The annually averaged root-mean-square errors (RMSE) of 17 mm and 24 mm, respectively, largely result from deviations during the peaks of the two rainy seasons. Particularly the rainfall in September is underestimated by IMERG in both years, but also the beginning of the little dry season in July 2017 with almost 60 mm less rainfall on average. Perhaps the most striking difference is the far lower annually averaged standard deviation of monthly rainfall within the IMERG pixels (std_IMERG) compared to the RG network (std_RG). While the spread of $\pm 1\sigma$ in the RG data (red-shaded area) strongly increases during the rainy seasons, the $\pm 1\sigma$ spread in IMERG (grey-shaded area) does not vary much throughout both years. This indicates that IMERG has difficulties to resolve the large spatial variability of monthly rainfall in the RG domain on a pixel-to-pixel basis.
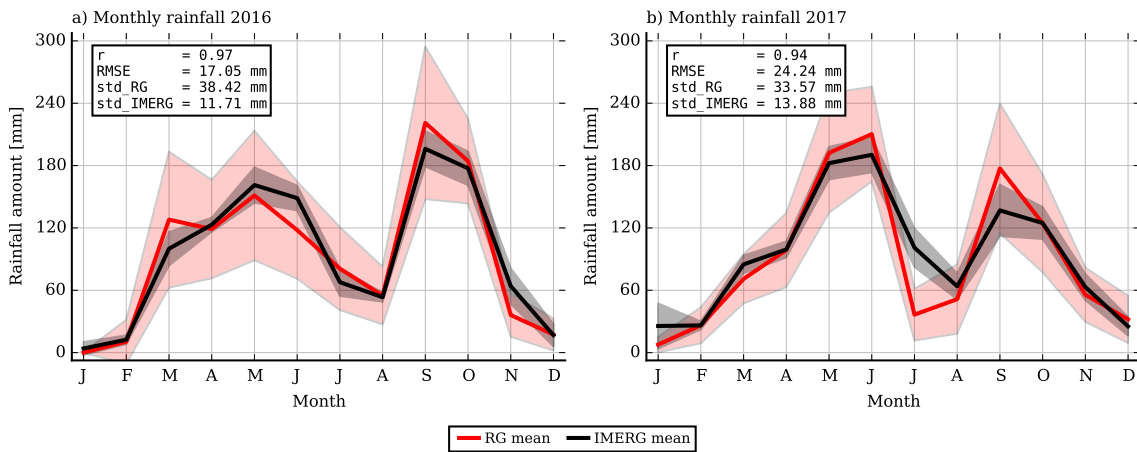
Figure 6.11: Seasonal cycle of monthly rainfall amounts for (a) 2016 and (b) 2017 based on IMERG (black curve) in comparison with the RG data (red curve). The grey and red-shaded area denote the standard deviation derived from IMERG pixels and RG stations, respectively. In accordance with Figure 6.9, only the respective IMERG pixels of stations with at least 90% of monthly data were considered.

To evaluate the daily timescale, the 2×2 contingency table as well as the skill metrics from section 6.2 are used. Here, any non-zero daily rainfall amount in both the IMERG pixels and the RGs are considered as a rainy day. The evaluation of daily rainfall in Figure 6.12 is arranged twofold. First, the box-and-whisker plots are discussed. The boxes comprise the interquartile range of the daily rainfall difference between IMERG and the RGs in cases of hits (green bars), false alarms (yellow) and missed events (purple) sorted by RG station (Figure 6.12a) and by month (Figure 6.12b). The whiskers reach out to the 10th and 90th percentiles, respectively. Here, both 2016 and 2017 are included. In principle, it becomes evident that the largest differences occur during hits and roughly ranges from -12 mm to +8 mm (Figure 6.12a). Although the boxes are not entirely symmetric around the zero-line, the respective median values of the rainfall differences (black lines within the boxes) are close to it. This indicates that IMERG is weakly biased. By definition, false alarms and missed events produce a positive and negative rainfall difference, re-

spectively. Across the RG network, such events are largely linked to low-intense rainfall systems, where the medians are located within ±3 mm. Due to the relatively small RG domain (see Figure 6.2), variations in the box sizes are rather small. Perhaps one exception is RG15_Nsuta. Recalling Figure 6.3, this station exhibits one of the lowest availability of daily rainfall. Thus, the larger interquartile range for false alarms and missed events compared to the other RGs are mainly due to the low sample size. The large daily rainfall differences in the case of hits are conveyed to the seasonal cycle (Figure 6.12b). Again, the medians are close to zero, but overall with a slight tendency towards negative values over the course of the year. Increased interquartile ranges of up to 10 mm for false alarms and missed events are pronounced during the primary rainy season from March to June, but interestingly not during the secondary rainy season in September and October.

The second part of the analysis refers to the curves in the bottom sections of the panels, which represent *POD* (green curve), *FAR* (yellow), *HSS* (black) and *BIAS* (blue). Note that the scalings are found on the right side. Across the RG stations, *POD* exhibit values generally around 0.85, which is equal to one miss per more than five hits (Figure 6.12a). Again, RG15_Nsuta is an exception. *FAR* is largely around 0.5 but increases to values up to 0.75. Thus, false alarms are at least as frequent as hits on a daily basis. However, as indicated by the boxplots, they mostly comprise low daily rainfall amounts. Because of the higher frequency of false alarms than missed events, *BIAS* is larger than zero and generally attains values of around 2. It indicates that IMERG tends to over-observe the frequency of rainfall. The dominance of false alarms is a major factor for the *HSS*, which decreases with higher *FAR*. Overall, *HSS* is larger than zero with values ranging from 0.25 to 0.6. Therefore, IMERG still performs better than random chance on a daily basis. Considering the seasonal cycle (Figure 6.12b), *POD* is high with values over 0.9 during the rainy seasons. However, it is distinctly reduced during the little dry season in July and August, which indicates an increase in missed events. Interestingly, *FAR* increases in that period as well, which consequently causes a reduction of *HSS* from 0.5 down to 0.25. In general, the skill of IMERG as indicated by *HSS* is compromised more during the dry seasons due to the frequent occurrence of false alarms, which even reaches 0.95 in January. Throughout the year, IMERG overestimates the number of rainy days as indicated by the positive *BIAS*, particularly during the main dry season. The higher number of false alarms are partly balanced by the higher number of missed events during the little dry season. Therefore, *BIAS* exhibits comparable values to those during the rainy season ($BIAS \approx 2$).

6.4.3   Subdaily timescale

For subdaily timescales, the same approach as for the daily timescale is applied, however with respect to rainfall events. A rainfall event is defined as period of continuous 30-minute intervals with non-zero rainfall values in the RG data. As soon as one or more corresponding 30-minute intervals in IMERG is non-zero as well, a hit is assigned (green boxes in Figure 6.13). Here, the duration of an IMERG event is allowed to differ from an event in the RG. The corresponding integrated difference in the rainfall amount is accounted for in the boxplots.

Comparing the event-based rainfall differences in Figure 6.14a with the daily counterpart
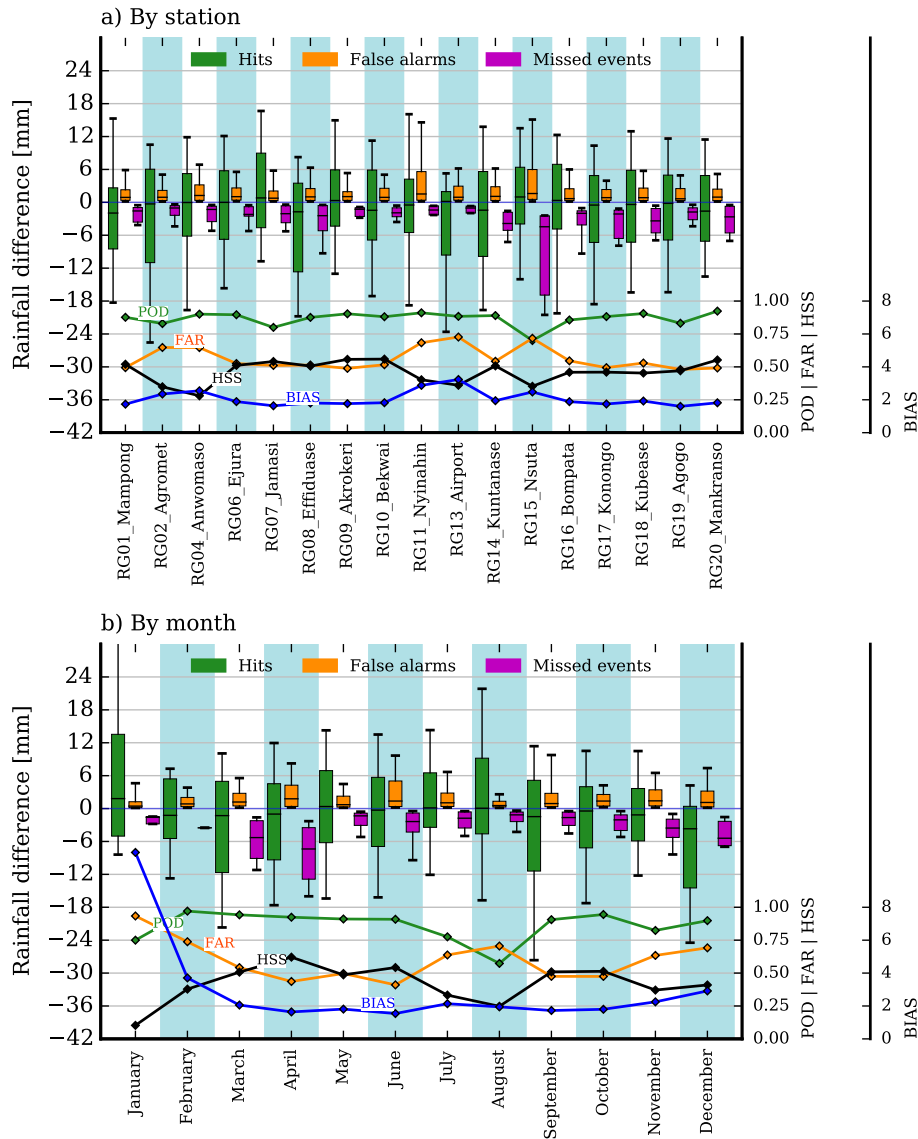
Figure 6.12: Composite of the accumulated daily rainfall difference between IMERG and RG (box-whisker plot) and skill measures (coloured curves, see section 6.2) based on (a) each RG station and (b) each month. Both include the years 2016 and 2017 together. The boxes comprise the interquartile range of rainfall differences and whiskers extend to the 10th and 90th percentiles, respectively, for hits (green), false alarms (orange) and missed events (purple). Note that every skill measure refer to the first right-hand axis except for *BIAS*, which is indicated at the second right-hand axis.

across the RG stations, the distributions in the case of hits are very similar. It suggests that daily rainfall in the RGs are largely constituted by a single event. However, the differences for false alarms are slightly decreased on an event timescale. This, in turn, suggests that IMERG tends to observe several false alarm events throughout the day, which may add up to the daily rainfall difference for false alarms indicated in Figure 6.12a. The interquartile range for missed events are slightly increased at some stations, but tend to be confined to stations with an overall low data availability (e.g RG11_Nyinahin and RG13_Airport). Strong similarities between the daily- and

Figure 6.13: Schematic showing the assignment of hits (green), missed events (purple) and false alarms (orange) on an event timescale. Each box represents a 30-minute interval, where a coloured filling denotes non-zero rainfall values, i.e. at least 0.1 mm.

event-based perspective are seen for the seasonal cycle as well (Figure 6.14b).

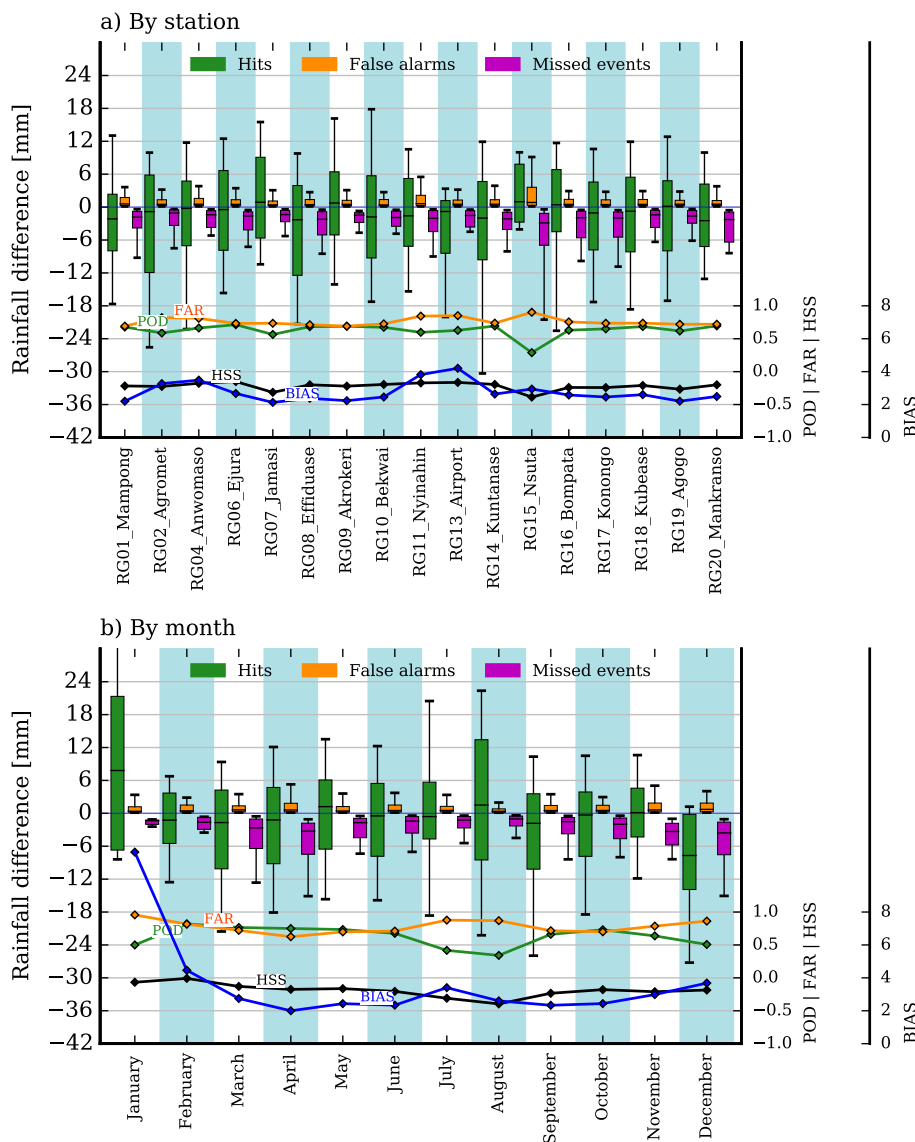Figure 6.14: As Figure 6.12, but based on individual rainfall events. Note the different scale for the skill metrics on the right axes compared to Figure 6.12.

The assumption of IMERG to produce several false alarms throughout the day is supported by a station-wide *FAR* of at least 0.7 (Figure 6.14a), which translates to more than two false

alarm events per one hit. Compared to *FAR*, the *POD* values are slightly lower (0.65 on average) and correspond to roughly 0.5 missed events per one hit. Therefore, it can be concluded that the probability of false alarms in IMERG on a subdaily timescale is more than five times higher than a missed event on average. Accordingly, the *BIAS* metric remains larger than 1 across all RGs. The combination of an increased *FAR* and decreased *POD* compared to the daily timescale is reflected in a reduction of *HSS*, which becomes negative at around -0.2 for all stations. Qualitatively, the accuracy of IMERG is worse than that of a purely random guess, mainly by virtue of the excessive number of false alarms. Over the course of the year, *HSS* is lowest during the little dry season in August, where *HSS* falls to -0.45 (Figure 6.14b). Again, this is where *FAR* and *POD* are highest and lowest, respectively.

More insight into the typical characteristics of RG and IMERG events is given in Table 6.3, where median duration and intensity are summarised for every month and subdivided between hits, false alarms and missed events. In the case of hits, rainfall events in IMERG generally last longer than those in the RGs. Their median ranges from 3–5 hours compared to 1–2 hours from the RGs. However, rainfall events observed by the RGs are stronger than in IMERG. They typically exceed 10 mm hr^{-1}, while that of IMERG systems remain largely under 5 mm hr^{-1}. Overall, despite the weaker intensity, IMERG events reach comparable rainfall amounts with those observed by the RGs due to their longer duration. Season-dependent variations of duration and intensity in IMERG are not obvious. The findings rather reflect a distinct characteristic of IMERG. Both the duration and intensity of false alarms and missed events are lower than for hits, which suggest that short-lived systems as well as weakly convective situations are misinterpreted by IMERG. Moreover, the median intensity of missed events during July and August is reduced compared to the other months. This may indicate a more frequent occurrence of non-convective rainfall, such as drizzle or light rain.

The performance of IMERG is further evaluated with respect to the rainfall types (Figure 6.15). Since the types were identified within the "RG space", false alarms do not exist. Therefore, only *POD* is calculated. Regarding the difference in rainfall amount, there is an apparent dependency with the rainfall intensity. The weak types WSR and WLR are overestimated by IMERG as indicated by mostly positive medians (Figure 6.15a,d). The large interquartile range of up to 20 mm indicates inherent problems with the treatment of these low-intense rainfall systems. The *POD* of WSRs shows a strong seasonality and decreases towards August down to only 0.1, i.e. nine misses per one hit. WLRs in turn are detected more frequently, which may be related to the longer duration. A similar behaviour is visible for the strong types SSR and SLR (Figure 6.15b,e). With the exception of December, the *POD* of SLRs is greater than 0.9 throughout the year. The tendency of overestimation has largely vanished for SSRs and SLRs. However, as indicated by the interquartile range, the variability of the rainfall estimation has increased particularly for SLRs. Finally, the rainfall amounts for the intense types ISR and ILR are mostly underestimated by IMERG, with large variability in both cases. However, ISRs are less prone to be missed than the weaker SR types, exhibiting *POD* values of at least 0.75 in all months except in December. Overall, it can be concluded that IMERG struggles with the rainfall estimation on both ends of the intensity spectrum. Furthermore, rainfall systems are less likely to be missed the more intense

Table 6.3: Seasonal-based comparison of median event duration ("Dur.", in hours) and the median of the mean intensity ("Int.", in mm h^{-1}) as seen by the RGs and IMERG during hits, missed events and false alarms. Note that missed events refer to the RG data, whereas the values for false alarms are taken from IMERG.

	Hits (RGs)		Hits (IMERG)		Missed events (RGs)		False alarms (IMERG)	
	Dur.	Int.	Dur.	Int.	Dur.	Int.	Dur.	Int.
January	1.5	14.4	4.0	5.4	0.5	5.4	0.5	1.0
February	1.5	10.4	4.0	3.2	0.5	6.6	1.0	0.8
March	1.0	12.2	4.5	2.8	1.0	7.2	1.0	1.0
April	1.5	11.8	4.5	4.4	1.0	9.2	1.0	1.2
May	1.5	15.2	4.5	6.4	0.5	5.2	0.5	1.0
June	1.5	8.8	3.5	4.0	0.5	3.8	1.0	1.2
July	1.5	10.8	3.5	4.8	0.5	3.2	0.5	1.4
August	2.0	10.6	5.0	5.6	1.0	2.6	0.5	1.0
September	1.5	10.2	3.5	4.0	0.5	4.4	1.0	1.2
October	1.0	10.4	4.0	3.6	0.5	5.8	1.0	1.0
November	1.0	10.2	3.5	3.4	0.5	9.0	1.0	1.2
December	1.0	15.8	3.0	1.4	0.5	8.2	1.0	1.2

they are and the longer it rains.

A brief comparison of the average duration and intensity of the rainfall types between IMERG and the RGs is given in Table 6.4. Note that the duration is indicated in half-hour steps for the RGs as well due to the aggregation to 30-minute rainfall. In accordance with the findings in Table 6.3, the duration in IMERG is generally longer compared to the RG estimates, with 1.5–2 hours of longer rainfall during the passage of SR types and 2.5–4 hours during LR types. Here, with a comparable intensity in the RGs and IMERG with 1.5 and 1.6 mm h^{-1}, respectively, the overestimation of the rainfall amount for WSRs can be accounted for by the more persistent rainfall in IMERG. The underestimation of rainfall for both the intense types ISR and ILR, in turn, stems from a much lower estimation of the rainfall intensity, suggesting difficulties in IMERG to resolve the intense convective part of the clouds. Overall, the increase of rainfall intensity in IMERG from the weak to intense rainfall types does not scale in the same manner as that in the RGs. Consequently, both the overestimation of the duration and the general underestimation of the intensity lead to an error compensation on the event timescale.

6.4.4   Rainfall-type-based seasonal cycle in IMERG

The findings in the previous section are projected back onto the seasonal cycle to determine how monthly rainfall in IMERG is constituted. First, the station-averaged integrated monthly rainfall difference between IMERG and the RGs are presented in Figure 6.16 for both 2016 and 2017. The bars denote the net difference for each rainfall type and the green curve the net difference of all types combined. Note that only hits are considered here. Despite the low intensity of WSR events in IMERG, they are exclusively overestimated. Again, this is due to the overestimation
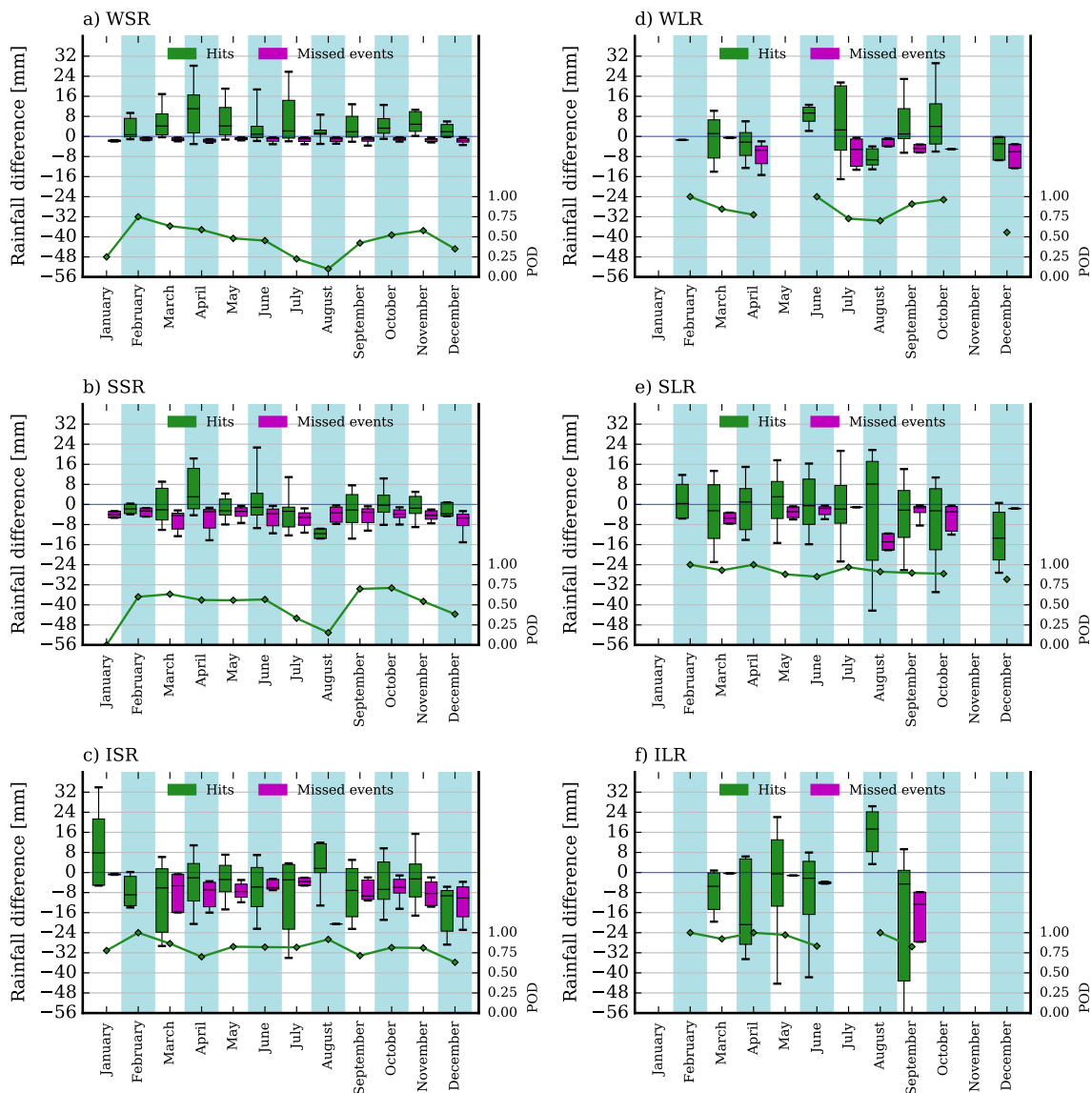
Figure 6.15: Similar to Figures 6.12 and 6.14, but for each rainfall type event. Since the rainfall types are RG-based, only RG perspective is applied here. Therefore, no false alarms are considered. Furthermore, only *POD* is calculated.

of the duration, but also simply because WSRs are numerous. WSRs are hardly represented in August of both years despite their high occurrence frequency in this month, which is explained by the lack of their detection (see Figure 6.15a). With few exceptions, the integrated monthly rainfall amount of ISRs and ILRs are underestimated by IMERG. The relatively large differences for ILR events are exceptional considering the fact that they are rare, accounting only for 1.2% of all events (Figure 6.4a). Although the analysis is based on only two years, some tendencies towards a strong underestimation of SLRs and ILRs during the secondary rainy season in September and October are evident. This is in contrast to the primary rainy season, which experiences both over- and underestimations from SLRs.

The seasonal cycle of missed precipitation (dashed purple line) as well as the monthly relative

Table 6.4: Similar to Table 6.3, but for the rainfall types. Since they are based on RG data, false alarms are not considered.

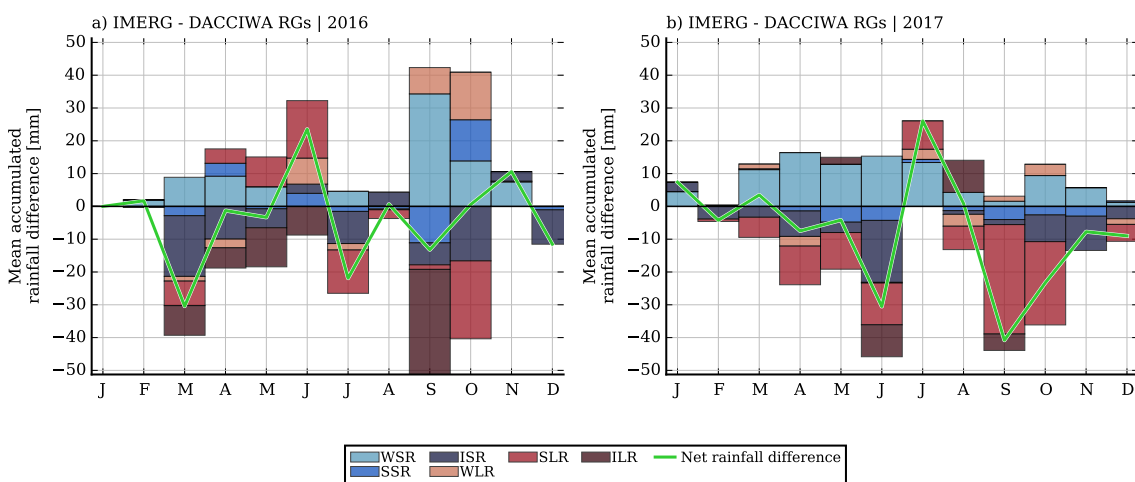|	Hits (RGs)		Hits (IMERG)		Missed events	
	Duration	Intensity	Duration	Intensity	Duration	Intensity
WSR	1.0	3.0	3.0	3.2	0.5	3.0
SSR	1.0	12.4	2.5	3.2	0.5	10.8
ISR	1.0	23.4	3.0	4.0	0.5	19.8
WLR	1.5	9.2	4.0	3.2	1.0	8.8
SLR	2.0	12.8	5.5	5.6	0.5	5.6
ILR	2.0	15.6	6.0	5.0	1.0	16.6

Figure 6.16: Mean monthly rainfall difference between IMERG and the RGs (green curve), broken down further into the contribution of rainfall types (coloured bars) for (a) 2016 and (b) 2017. Note that these differences only comprise hits.

contribution from the rainfall types (coloured bars) are illustrated in Figure 6.17, together with the mean monthly RG (white line) and IMERG rainfall (green line) as a reference. With the exception of September 2016, monthly negative rainfall deficit due to missed events never exceed 21 mm. However, due to the overall low fluctuation in absolute values, their fraction relative to monthly IMERG rainfall is highest during the main dry season from November and February and the little dry season in July and August. During these periods, more than 60% of integrated rainfall emerge from the occurrence of SR types. A distinct increase of the contribution from WSRs is evident during the little dry season, which is in correspondence with the decrease of *POD* in Figure 6.15. Despite the generally high *POD* values for the intense and long-lasting (LR) types, they are strongly represented during both rainy seasons. It indicates that not every IMERG pixel observed rainfall during these episodes. Again, due to the independent treatment of IMERG pixels as stated before in section 6.4.3, the suggested rainfall amounts are an upper estimate.

Following Figure 6.9, the relative contribution of the rainfall types to the monthly rainfall in IMERG (green curve) is presented in Figure 6.18. Furthermore, the yellow bars and yellow dashed
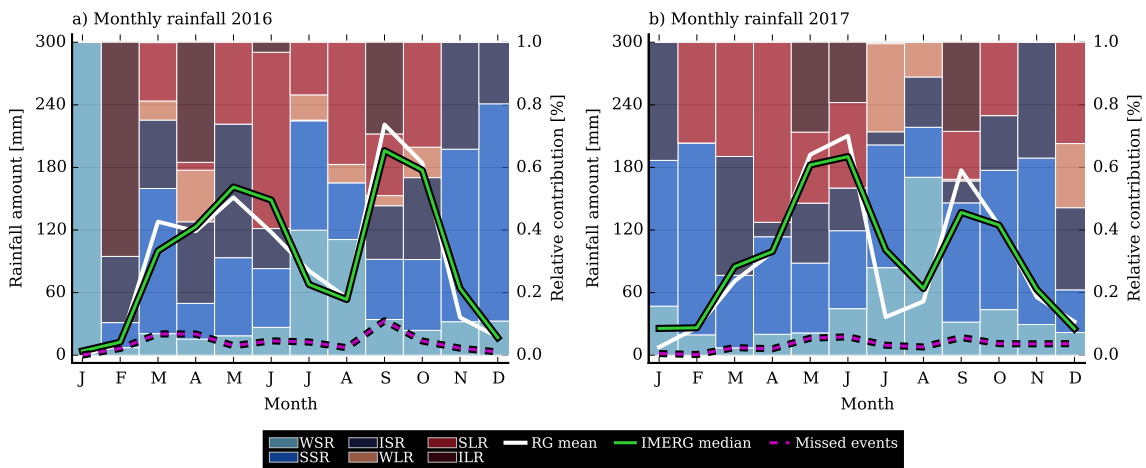
Figure 6.17: Mean seasonal cycle of IMERG (green curve), the RGs (white) and the accumulated rainfall of missed events (dashed purple curve). The coloured bars show the mean fractional contribution to the total monthly missed-event rainfall.

line indicate the fractional and absolute contribution, respectively, by false alarms. Here, an upper estimate of 28.5% of total IMERG rainfall originate from false alarms. It peaks in September 2016 (58 mm) and, similar to the missed events, exhibit the highest relative magnitude during the dry seasons. Given the well represented seasonal cycle of IMERG compared to that of the RGs, false alarms are a crucial contributor, which overcompensates missed events at all times. As seen previously, WSRs account for a larger rainfall amount compared to the RGs, which is 10% overall and reaches up to a monthly fraction of 20%. Furthermore, unlike for the RG data (Figure 6.9), no peak in the little dry season is visible due to the aforementioned tendency of IMERG to miss WSRs during this period. The integrated rainfall for intense types ISRs and ILRs estimated by IMERG only reach 52% of that as measured by the RGs, which is reminiscent of the inability of IMERG to resolve the high rainfall intensity of both types (see Figure 6.4).
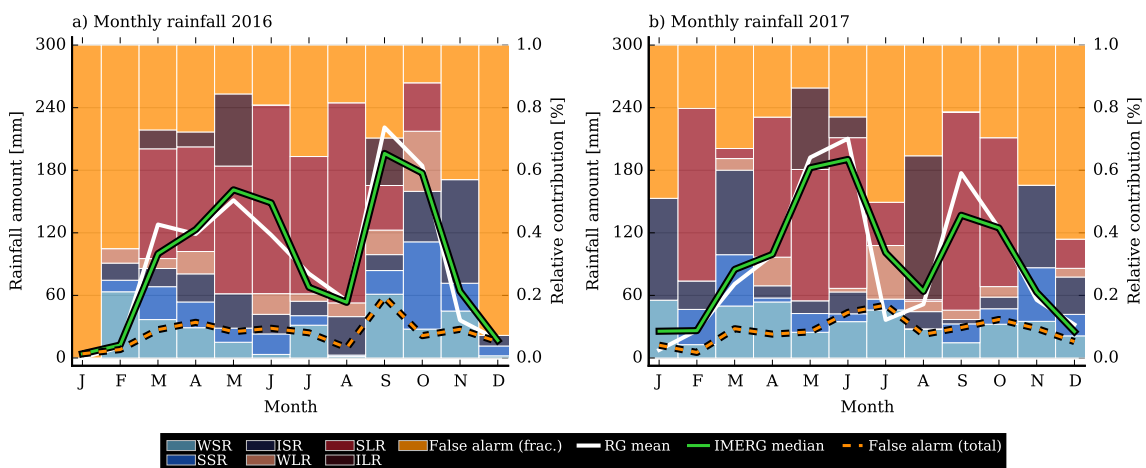

Figure 6.18: Similar to Figure 6.9, but from the perspective of IMERG. The orange bars denote the mean fractional contribution of false alarms to the mean monthly IMERG rainfall.

Generally speaking, the skill of IMERG decreases towards shorter timescales, which is a

known characteristic of TRMM over SWA (Akinsanola et al.; 2017) and which is not surprising given the point-to-pixel comparison performed in this section. However, it is important to note that the well estimated seasonal cycle in IMERG is largely based on error compensation on the event timescale. The overall longer duration, the overestimation of weak rainfall and the frequent occurrence of false alarms are balanced by deficiencies in capturing both high rainfall intensities and short-lasting rainfall episodes. In the following section, properties of precipitating clouds are analysed to gain further insight into both the characteristics of rainfall over SWA and the behaviour of IMERG.

6.5   Link of RG and IMERG rainfall to cloud-top properties

Having identified the strengths and shortcomings of the rainfall retrieval of IMERG, the logical question is what the reasons for the characteristic behaviour of IMERG are, both from a general and seasonal perspective. The latter refers particularly to the distinct deficiency of IMERG to capture weak rainfall during the little dry season. This deficiency is not apparent to the same extent during the rest of the year (see Figure 6.15a). To this end, the CLAAS-2 dataset introduced in section 6.2 is taken to evaluate the cloud properties during rainy episodes. Despite the fact that CLAAS-2 is composed of passive measurements, which largely allows only an analysis of cloud-top features, the main benefit is the high spatiotemporal resolution. Here, each of the 30-minute interval within the RGs and IMERG can be assigned the respective cloud-top properties.

To gain a basic understanding of the clouds involved in rainy periods, the following analyses also make use of a cloud property classification introduced in the framework of the International Satellite Cloud Climatology Project (ISCCP, see Rossow and Schiffer; 1999) based on the cloud-top pressure (CTP) and cloud optical thickness (COT) (Figure 6.19). Three intervals for both CTP and COT were defined, resulting in nine classes overall. While clouds can be distinguished between low, midlevel and high clouds with respect to CTP, the COT separates typical regimes of the different cloud genera in each layer, which are indicated in the boxes. Note that although the high-COT midlevel cloud category is termed "Nimbostratus", it may also comprise growing convective systems that are not deep enough yet to fall into the high-cloud bin. If necessary, the abbreviations of the cloud types from Figure 6.19 are used in the following. As mentioned in section 6.2, the determination of COT requires the availability of sunlight. Therefore, the following analyses using COT refer to daytime only. Because of the 15-minute resolution, two CLAAS-2 snapshots can be assigned to each 30-minute RG/IMERG interval. Here, the means from the two snapshots were calculated for COT and CTP. In addition to COT and CTP information, the cloud phase product of CLAAS-2 (CPH) will be used to identify warm rain events, i.e. rain falling from purely liquid clouds.

6.5.1   Dependency of rainfall intensities on cloud types

Similar to the approach presented by Jin et al. (2018), an overview of the variability of rainfall intensities within the RGs and IMERG is given, as well as their link to the observed clouds.
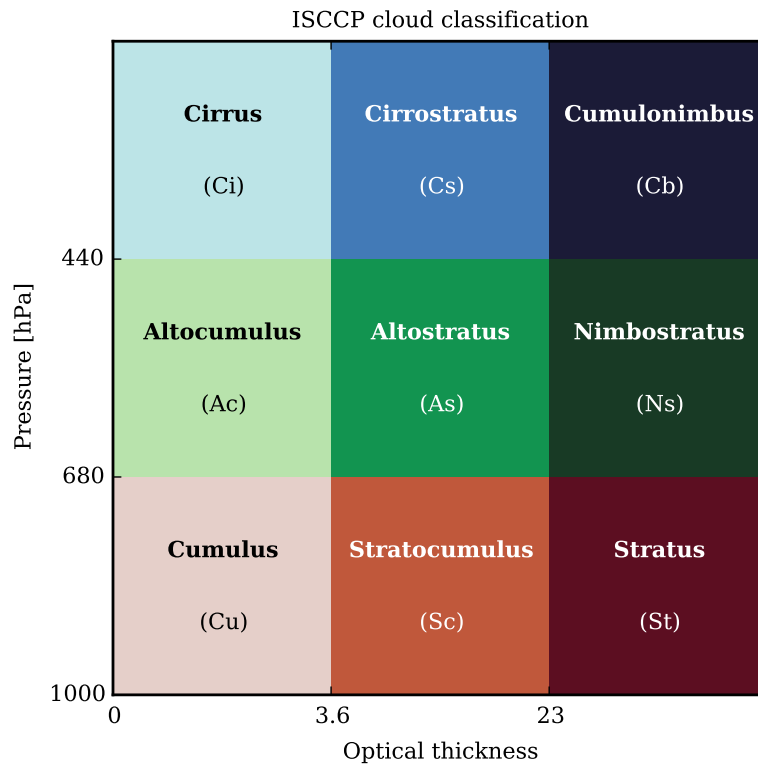
Figure 6.19: ISCCP-based cloud classification (see Rossow and Schiffer; 1999) with regard to the cloud top pressure (CTP) and cloud optical thickness (COT). Each parameter is divided into three regimes, yielding nine categories. Considering CTP, they comprise low- (red shades), midlevel (green shades) and high clouds (blue shades). Concerning COT, typical values of the different cloud genera were regarded.

Based on all non-zero 30-minute values in the RG and IMERG dataset, the 20th, 40th, 60th and 80th percentiles of rainfall intensity are listed in Table 6.5. Here, the half-hourly rainfall was multiplied by two to obtain an hourly rainfall rate. Clearly, the distribution of rainfall intensities within IMERG is shifted towards smaller rainfall rates. Between the 20th and 80th percentile, a difference of 2.5 mm is found for IMERG, whereas the value for the RGs increases by around 9.7 mm for the same interval. The 20th percentile of IMERG itself is already smaller by around 0.5 mm compared to the RGs. Overall, this is consistent with the previous findings, where high intensities were found to be generally underestimated by IMERG. Furthermore, many false alarms produced by IMERG were weak, which increases the IMERG sample on the low-intensity end. The RG percentiles are used to separate five groups P1–P5, with P1 comprising all rainfall rates up to the RG-based 20th percentile, P2 all rainfall rates between the 20th and 40th percentile, etc., in order to obtain groups with the same sample size. However, the ratio of the number of P5 cases in IMERG and RGs is still 78% with a total of non-zero rainfall values of 6733 in the RG dataset.

The probability of rainfall occurrence within the nine ISCCP cloud categories (see Fig. 6.19) are examined for the RGs (Figure 6.20a) and IMERG pixels (Figure 6.21a) under the condition of the presence of a given cloud type. Based on the RGs, the general rain probability is rather low and, not surprisingly, exhibit a maximum of 0.23 for the upper-right bin, i.e. typically *Cb* clouds.

Table 6.5: 20th, 40th, 60th and 80th rainfall percentiles based on all half-hourly rainy periods within the RG and IMERG dataset. Note that half-hourly rainfall amounts lower than 0.1 mm were removed in the RG and IMERG data.

	Rainfall percentiles [mm hr^{-1}]			
	20th	40th	60th	80th
RGs	0.94	2.16	4.34	10.60
IMERG	0.40	0.75	1.44	2.95

In other words, if a pixel is identified with the *Cb* cloud type, rainfall is detected by the RGs in 23% of the cases. The conditional probability quickly decreases towards lower COT values and lower-altitude clouds, which suggests the importance of the ice phase for rain production within convective clouds. In contrast to the RGs, the rain probability in IMERG within the *Cb* bin is significantly higher. More than half of the instances are associated with rainfall in IMERG (0.53). Thus, the probability of rainfall in the presence of the *Cb*-type are higher in IMERG by 0.3 compared to ground observation. Furthermore, IMERG also observes rainfall slightly more frequently for optically thinner clouds. The upper-left bin (cirrus, *Ci*) indicates a probability of 0.05. Therefore, the number of rainy episodes in IMERG are overestimated for high clouds, which comprise mostly ice clouds. However, in both the RGs and IMERG, a small fraction of precipitating high clouds are still liquid based on the CPH product, as indicated by the numbers in parentheses. Here, whenever it rains, up to 3% originate from liquid (supercooled) clouds, which counts as warm rain.

The occurrence of rainfall from midlevel clouds (middle bins) are slightly overestimated by IMERG as well. Interestingly, the fraction of warm rain increases with higher COT, which is observed by both RGs and IMERG (from 0.27 to 0.79 for RGs, Figure 6.20a). One explanation is that these high-COT midlevel clouds largely represent growing convective systems, where the development of the ice phase is suppressed due to large vertical velocities. Since the COT increases with the depth of a convective cloud, the optically thinner midlevel clouds likely contain convective clouds at lower heights within the present altitude interval. They may not be strong enough yet to produce rainfall, which could explain the decreasing occurrence frequency of warm rain. This characteristic is also visible for all P-groups within the RG and IMERG datasets (bottom row of Figs. 6.20 and 6.21). The probability of rainfall from low clouds (bottom bins) remain around 0.01 or less in both RGs and IMERG, where all rainfall periods are associated with clouds purely in the liquid phase.

The bottom panels of Figures 6.20 and 6.21 show how the P-groups are distributed across the nine cloud categories. Note that the sum of the fractions within every P-group is one. Based on ground observations, rainfall of all intensities is largely a function of both CTP and COT, that is, the distribution increases towards the *Cb*-bin in the upper right corners with respect to both parameters (Figure 6.20b–f). The main difference between the P-groups is that the distribution becomes gradually "steeper" from P1 to P5. While 46% of all P1 cases fall into the *Cb*-bin, it
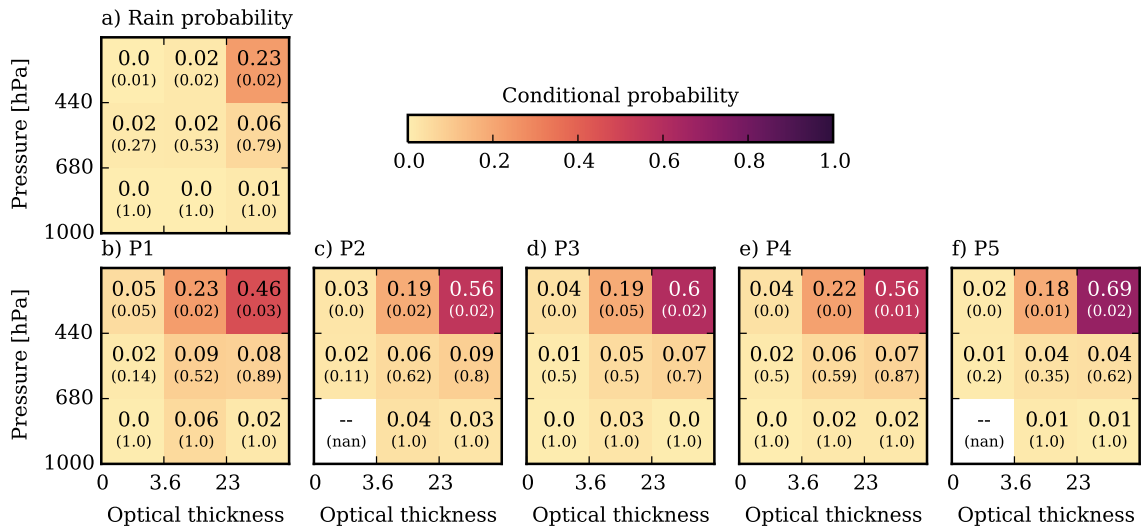
Figure 6.20: Conditional probabilities of rainfall for the nine ISCCP cloud types based on RG measurements. (a) Probability of rainfall under the condition that the respective cloud type is detected at a pixel, i.e. $P(\text{RR} > 0 \,|\, \text{cloud type})$. (b)–(f) Fractional distribution of each P-group within the nine ISCCP cloud types, i.e. $P(\text{cloud type} \,|\, Px)$ with $x = 1...5$. The P-groups are separated from each other by the RG rainfall percentiles in Table 6.5. The values in parentheses indicate the probability of warm rain under the condition of detected rainfall.
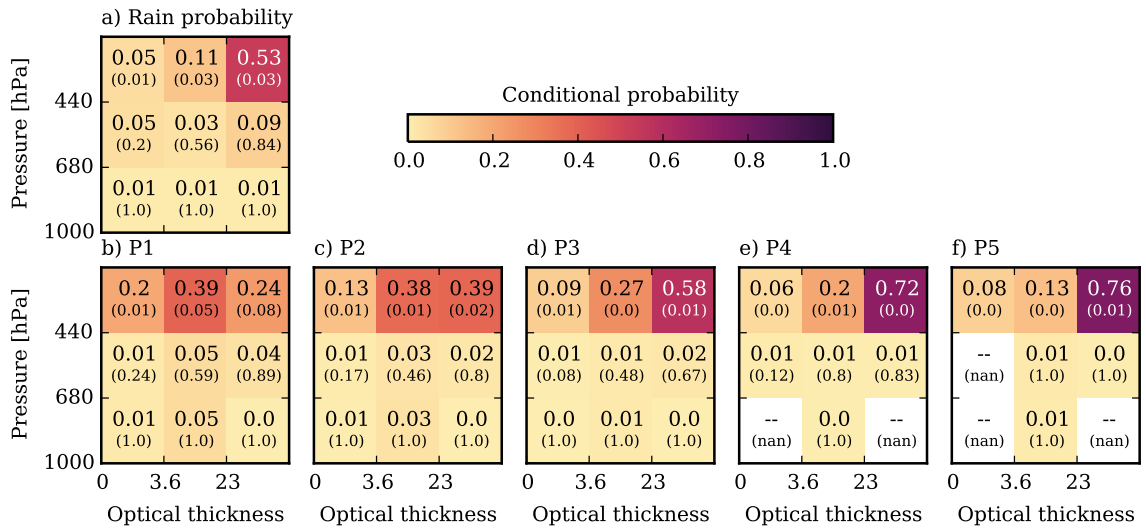
Figure 6.21: As in Figure 6.20, but for IMERG.

increases to 69% in P5. Thus, the presence of deep convective clouds becomes more likely with more intense rainfall. P1 intensities in turn can occur with clouds exhibiting a wider range of CTPs and COTs. However, the fact that the maximum of the distribution is in the *Cb*-bin for all P-groups indicates that the combination of CTP and COT is an unsuitable predictor for rainfall rates and may rather be used for estimating the probability of rainfall in general, which has also been found for TRMM (Jin et al.; 2018). With regard to IMERG, the aforementioned characteristic vanishes for groups lower than P3 (Figure 6.21b,c), i.e. for rainfall rates lower than approximately 2 mm hr^{-1}. Below this threshold, rainfall mainly occurs from high clouds (>84%) with low dependency

on COT. Considering the shift of rainfall rates towards smaller values compared to the RGs, IMERG is prone to over-observe rainfall from optically thin clouds such as cirrus. This deficiency is not unknown and is a common source of error whenever IR-based rainfall estimates are involved (e.g. Kidd and Levizzani; 2011). Looking across all P-groups, the relationship between rainfall intensity and the presence of *Cb* clouds is stronger in IMERG, where the conditional probability from P1 to P5 increases from 0.24 to 0.76. Contrary to this, the probability of rainfall outside of the high-cloud categories decrease from 0.16 in P1 to less than 0.02 in P5 and is generally lower compared to the RGs.
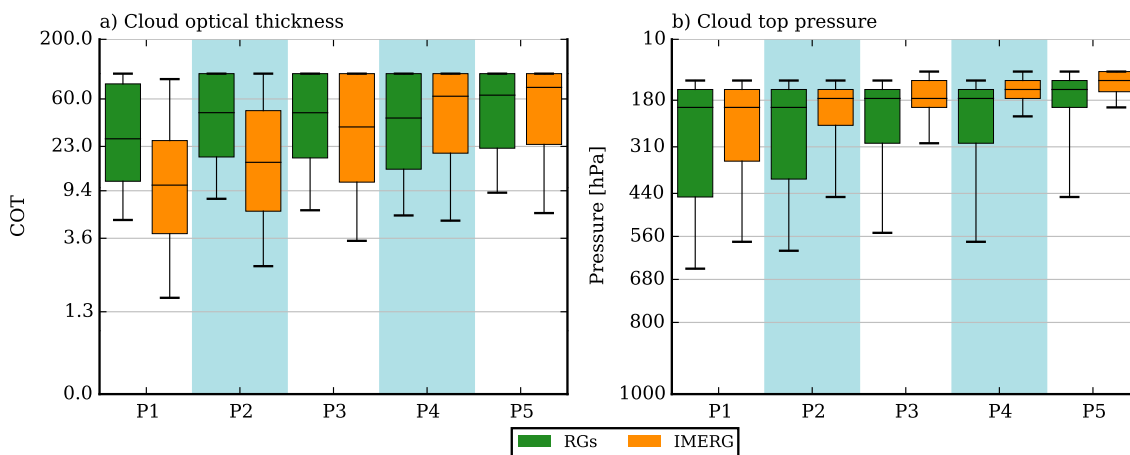

Figure 6.22: Box-whisker plots showing the variability of each P-group with respect to (a) COT, and (b) CTP based on the RGs (green) and IMERG (orange). The boxes comprise the interquartile range, while the whiskers extend to the 10th and 90th percentiles, respectively.

The dependency of rainfall rates on CTP and COT is summarised in Figure 6.22. The variability of each RG (green) and IMERG P-group (orange) is shown as boxes, comprising the interquartile range. The whiskers extend to the 10th and 90th percentiles, respectively. With regard to COT, the medians (black line inside the boxes) increase monotonically with increasing P-group for IMERG, which is absent for the RGs (Figure 6.22a). Thus, IMERG generally uses COT as a predictor for the rainfall intensity, which reflects the strong relationship of IMERG rainfall to the amount of ice particles in the clouds. However, the lack of a clear indication for monotony revealed by the RG data illustrates how low the predictability of the rainfall rate with COT over SWA is. Furthermore, the lower median values specifically of P1 and P2 of IMERG compared to the RGs show that the retrieval is too sensitive to the amount of ice, leading to an overestimation of (weak) rainfall episodes when optically thin clouds are present. In contrast, the lower variability of CTP in all P-groups indicates systematic difficulties of IMERG to relate clouds at lower altitudes to rainfall (Figure 6.22b), where the high-intensity groups P4 and P5 are almost exclusively confined to clouds reaching 200 hPa or less. It should again be emphasised that the findings reflect the situation during daytime only since information of COT is retrieved using sunlight.

6.5.2   Dependency of RG-based rainfall types on cloud types

Following Figures 6.20 and 6.21, the occurrence frequency of the six RG-based rainfall types within the nine ISCCP categories are evaluated (Figure 6.23). Similar to the previous findings, the *Cb*-bin contains the largest fraction of occurrences. In general, the maximum of the *Cb*-bin becomes more pronounced with long rainfall duration (i.e. towards LR types) and higher intensity. WSRs are associated with a wide range of cloud types. While the high-cloud categories still cause the majority of WSR episodes, the fraction from midlevel and low-level clouds together is 43% (Figure 6.23a). For the midlevel categories, a similar shift towards a higher fraction of warm rain with higher COT (from 0.2 to 0.92) is visible like in the previous section. This may also reflect the signals from growing convective systems. This feature is visible for almost every category. The occurrence frequency from the mid- and low-level cloud categories decreases with higher intensity and is only 12% for ILRs (Figure 6.23f). It should be noted that rainy periods associated with MCSs like ILRs, for instance, also contain rather low-intensity rainfall typically towards the end of the overpass from the stratiform part (see Figure 6.5). They explain the contribution also from categories with low COT like the *Ci*-bin in the upper left corner (0.01 for ILRs).
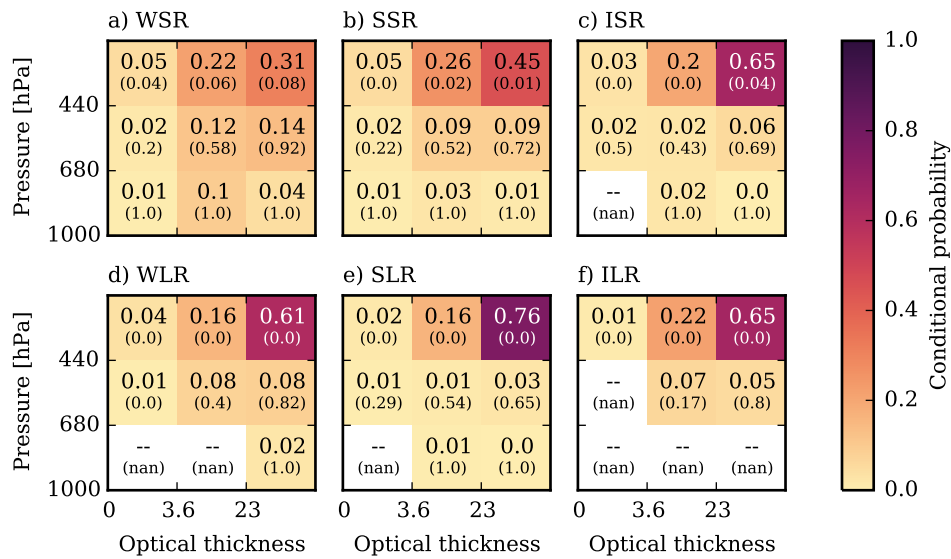
Figure 6.23: As in Figure 6.20b–f, but for the RG-based rainfall types.

As seen in section 6.3, the rainfall types exhibit a seasonality due to changing environmental conditions throughout the WAM season. A seasonal perspective is given in Figure 6.24, which shows the occurrence frequency of CTT on an annual (leftmost column) and a successive bi-monthly basis under the condition of the presence of RG-based rainfall types. Each of them are covered in individual rows (Fig. 6.24a–f). The CTT is binned every 5°C. The different bar colours refer to the COT intervals defined by the ISCCP in Figure 6.19 as well as the fraction of precipitating clouds that occur during the night (grey). The thin dashed red lines separate the three ISCCP layers, where the 680 hPa and 440 hPa surfaces are approximately at 1°C and -22°C, respectively. Note again that the COT is retrieved only during daytime.

Across the rainfall types, both a uni- and bimodal frequency distribution are found on an annual
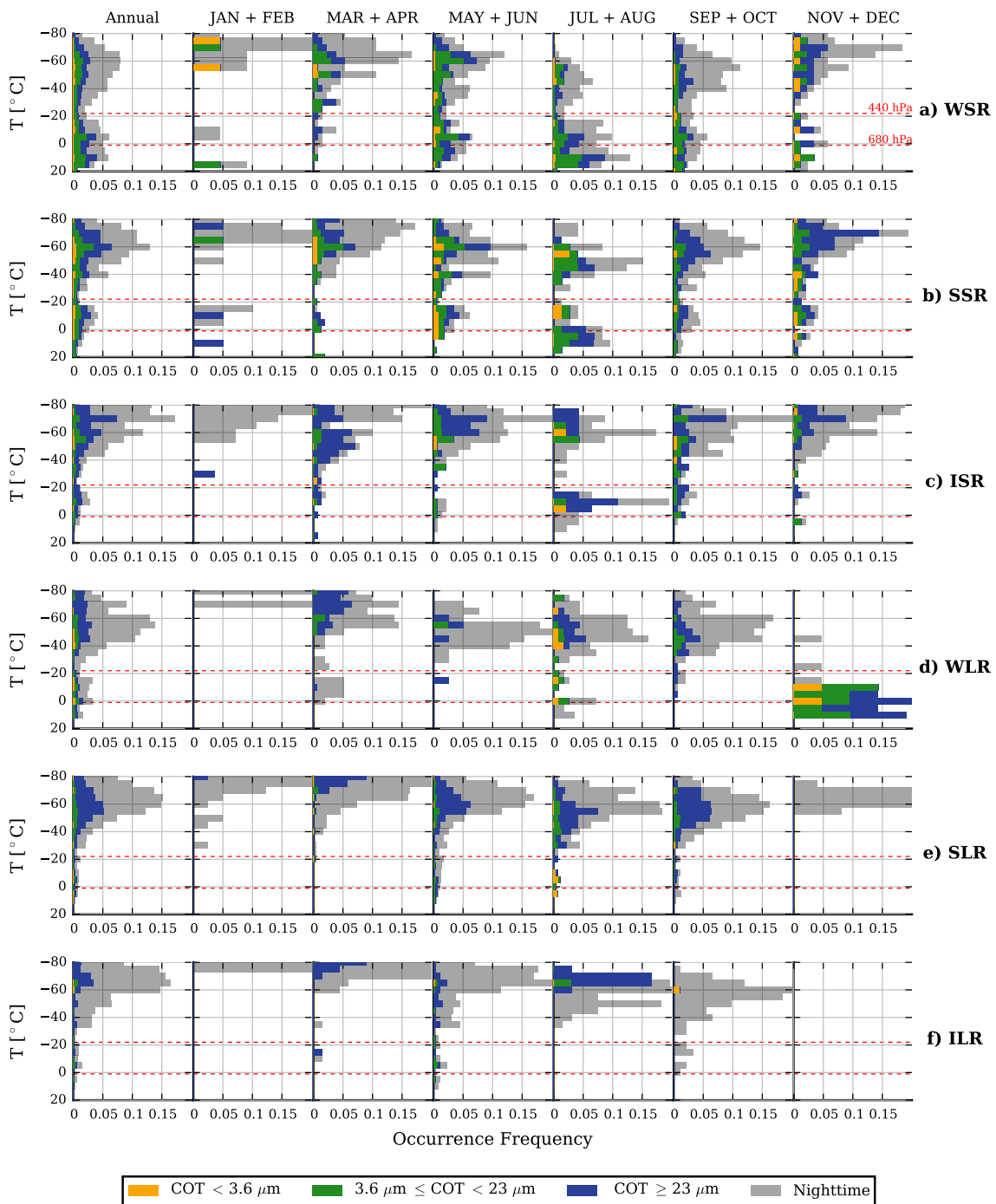
Figure 6.24: Composites of the occurrence frequency of cloud tops with respect to CTT for all RG-based rainfall types (rows) from an annual (leftmost column) and bi-monthly (successive columns) perspective. The different colours of the stacked bars refer to the occurrence frequency of the three ISCCP-based COT intervals (see Figure 6.19) as well as the fraction of nighttime observations (grey). The thin dashed red lines denote the mean layer temperature of the 680 and 440 hPa surface, which separate the ISCCP cloud layers.

basis. The bimodal structure for WSRs exhibit broad peaks (Figure 6.24a, leftmost panel), where the peak at lower levels is too noisy to allow a clear determination of the CTT. Nonetheless, WSR

rainfall originates from clouds with CTTs typically lower than -40°C or higher than -10°C, where the latter has been found to be largely liquid (see Figure 6.23a). This mid- to low-level peak becomes gradually less pronounced towards the MCS-type systems SLR and ILR and turn into the aforementioned unimodal distribution (Figure 6.24e,f). Considering COT, their upper-level peaks are largely compiled of clouds falling into the high-COT categories, i.e. COT ≥ 23 μm (blue shading). Furthermore, different COT distributions within the upper-level peaks are more apparent when SR and LR types are compared. For instance, the fact that a larger fraction of the smaller COT categories (green and yellow shading) is found in the case of WSRs compared to WLRs (Figure 6.24a,c) suggest a decreased potential for more persistent rainfall. Thus, decaying deep convective systems may reflect one potential source for WSR events. Overall, the bimodality suggests the presence of two main precipitating cloud types: First, shallow clouds at lower levels that do not grow anymore, but are capable of producing precipitation-sized drops, e.g. through coalescence; and second, deep convective clouds with cloud tops beyond the -40°C layer, in which strong particle growth typically occur in a deep mixed-phase layer (e.g. Rosenfeld and Lensky; 1998).

On a seasonal scale, the frequency distribution varies substantially for rainfall types with an annual bimodal structure, i.e. all types except for SLR and ILR. Early in the year and throughout the beginning of the primary rainy season in March and April (third column), rainfall originates mostly from the high-top clouds with a large fraction occurring after sunset (see gray shadings). The onset of the occurrence of shallower precipitating clouds starts in May and June (fourth column), however, mostly confined to WSRs and SSRs (Figure 6.24a,b). The little dry season in July and August (fifth column) marks the period where rainfall clouds from the upper- and lower-tropospheric CTT peaks become comparably more frequent. For WSRs, shallower clouds are even the primary source. Furthermore, as indicated by the peak for ISR (Figure 6.24c) they can also become intense. Note, however, that intense types are relatively rare during the little dry season (see Figure 6.9). Progressing into the secondary rainy season in September and October, rainfall from mid- and low-level clouds become less frequent again, but do not completely cease even entering the main dry season in November (rightmost column). The frequency distribution of both SLR and ILR show little variation throughout the year and are largely nocturnal phenomena, which is in accordance with Figure 6.8. However, one notable evolution is found for the maximum frequency, which moves to successively decreased altitudes (i.e. increased CTTs) from beyond -70°C in March and April to -60°C in September and October. This characteristic is reminiscent of the occurrence maximum of the TRMM-PR-based rainfall types *deep (and wide) convective core* (DCC, DWC) in chapter 4 early in the primary rainy season, which were suggested to be favoured around that time of the year due to generally higher instability in the tropospheric column.

6.5.3 Contribution of cloud types to rainfall

Having analysed the occurrence frequency of the precipitating cloud types, their contribution to total (daytime) rainfall is examined in the following. First, a brief overview of the general seasonal cycle of the cloud type frequency is given in Figure 6.25a. It is again expressed as a conditional

probability during cloudy episodes only. The reddish, greenish and bluish colours refer to the three ISCCP height layers with darker colours indicating higher COT (see also the legend below). The first half of the year is dominated by the high-cloud categories, which together account for around 60% in this period. Over half of that fraction is constituted by the low-COT *Ci* category. The occurrence of deep convection, including MCSs, largely starts in March, indicated by the subtle rise of *Cb*. They are relatively rare and account for less than 5% of all cloudy pixels. As mentioned earlier, the stratiform part of MCSs, usually much larger in spatial extent (see. Figure 3.6), also comprises *Cs* and *Ci*. The onset of the little dry season in July is marked by a pronounced increase of the occurrence of both low- and midlevel clouds at the expense of *Ci*. It includes optically thick *Sc* and *Ns* clouds. Accordingly, the fraction of purely liquid clouds increases as well (see yellow markers). On most occasions, it exceeds the fraction of the mid- and low-level clouds combined and indicates a larger amount of supercooled clouds that are high enough to contribute to the high-cloud categories. The supercooled phase at cloud tops is a known characteristic of growing convective systems, which has been observed in environments colder than -30°C (e.g. Rosenfeld and Woodley; 2000). Note, in turn, that not all of the midlevel clouds are liquid as they are composed of clouds with CTTs ranging from 1°C to -20°C (see Figure 6.24). Throughout the rest of the year, the frequency of midlevel clouds gradually decreases, while that of low clouds remains relatively stable. Thus, the secondary rainy season in September and October differs from the primary rainy season in the large presence of low- and midlevel clouds.

The evaluation of the monthly rainfall contribution of the cloud types reveals differences between the RGs (Figure 6.25b) and IMERG (Figure 6.25c), which supports the findings in previous sections. IMERG tends to underestimate the *Cb* fraction during the two rainy seasons and generally overestimates rainfall from *Ci*. The former is associated with high rainfall intensities given the fact that the *Cb* category accounts for roughly 75% of total rainfall during the rainy seasons despite a relatively low occurrence frequency. The higher contribution of rainfall from *Ci* again reflects the over-sensitivity to ice clouds with low COT, which became apparent in Figure 6.22a. The fractional rainfall contribution of low- and midlevel clouds is only notably underestimated by IMERG in July. Here, rainfall originating from these clouds account for around 30% of July rainfall within the RGs, also partly from the high-COT categories *St* and *Ns*. The latter as well as the midlevel medium-COT cloud type *As* are distinctly lower in IMERG (Figure 6.25c). An overall 22% of July precipitation in the RG data is warm rain (yellow markers). Although the percentage is only 10.4% in IMERG, it should be noted that July rainfall was overestimated by a monthly average of 30 mm. Thus, the absolute difference is smaller and rather emphasises the overestimation of rainfall from high-top clouds. To obtain an estimation of the total amount of warm rain, the mean monthly (daytime plus nighttime) values are quantified using solely the cloud phase product of CLAAS-2 and are briefly compared between the RGs and IMERG in Table 6.6. From the standpoint of the RG data, the amount is highest in September with 13.6 mm, followed by June (8.5 mm). Again, the higher value in September is most likely a consequence of the higher occurrence frequency of low- and midlevel clouds compared to June. Overall, warm rain is almost exclusively underestimated by IMERG. However, the difference during the little dry season is rather small with around 1 mm for July and August combined. Nonetheless, with an
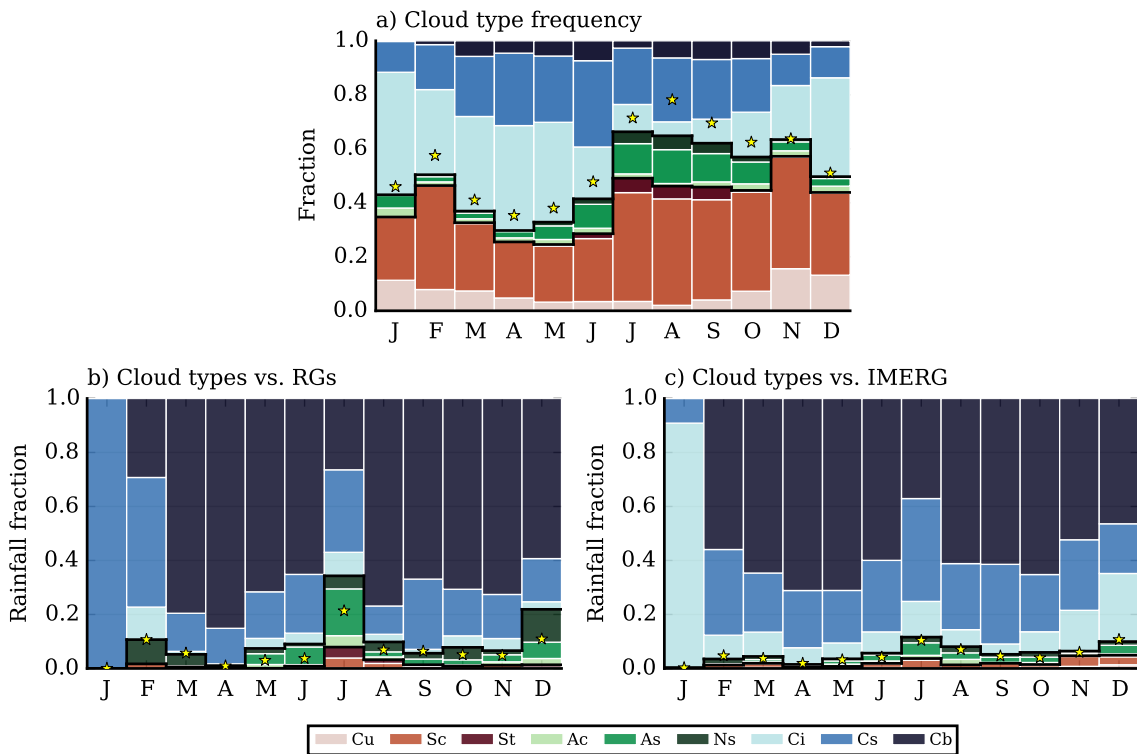
Figure 6.25: (a) Monthly occurrence freuqency of the nine ISCCP cloud types under the condition of a cloudy pixel. The yellow star markers denote the fractional occurrence purely liquid cloud tops. 2016 and 2017 are aggregated. (b)+(c) Fractional contribution of the cloud types to monthly RG and IMERG rainfall, respectively. The yellow star markers denote the fractional contribution of warm rain.

annual total of 33.7 mm, IMERG only reaches 54% of the warm rain detected by the RGs (62.3 mm). In comparison to the annual rainfall (section 6.3.3), warm rain accounts for around 5.5% and 2.8% based on the RGs and IMERG, respectively.

Following the comparison of the integrated rainfall amount between the RGs and IMERG in Fig. 6.16, the origin of the differences is broken down considering the cloud types illustrated in Figure 6.26. Bear in mind that only cases of hits are considered, i.e. rainy periods correctly detected by IMERG. Further note that the ordinate is logarithmically scaled and the stacked bars may not be directly comparable in size. In general, it is evident that the high-top cloud categories indicated by the blue-shaded bars account for the largest deviations in the integrated rainfall estimates from the RGs. Once again, it reflects the importance of the ice phase for the identification of precipitating clouds within IMERG. The systematic overestimation of WSR events is almost exclusively a consequence of the erroneous treatment of high clouds during these weak rainfall events (Figure 6.26a). As suggested in Figure 6.22a, the detection of low-intensity rainfall starts at much lower COT values in IMERG, leading to an overestimation of rainfall by the *Ci* and *Cs* categories. The fact that actual rainfall intensities are not strongly correlated with COT makes them difficult to predict for IMERG. The identification of WSR events throughout the year hardly includes warm rain cases, which is indicated by the general low fluctuation of the rainfall differ-

Table 6.6: Mean monthly amount of warm rain [mm], i.e. rainfall from purely liquid clouds.

	RGs	IMERG
January	0.7	0.2
February	0.3	0.4
March	4.8	1.4
April	4.2	1.4
May	6.0	3.3
June	8.5	4.2
July	6.0	5.8
August	5.1	4.2
September	13.6	6.9
October	6.8	2.8
November	4.4	1.9
December	2.0	1.4
Total	62.3	33.7

ence caused by purely liquid clouds (yellow markers). The underestimation of the more intense rainfall types, e.g. ISRs and SLRs (Figure 6.22b,e), is mostly related to high clouds as well and reaches a monthly difference down to -10 mm. This in turn reflects the inability of IMERG to resolve high rainfall intensities (see Table 6.4), which largely originate from the high-COT bins *Cb* and *Ns*. In some months, warm rain cases are detected by IMERG but mostly underestimated in their rainfall amount, for instance during the primary rainy season for ISRs (Figure 6.26c) and during the secondary rainy season for SSRs (Figure 6.26b).

The relationship between false alarms/missed events and cloud characteristics based on the seasonal cycle is evaluated in Figure 6.27, which follows the approach of Figure 6.24. From a general annual perspective (leftmost column), the major number of false alarms and missed rainfall is related to the occurrence of low and medium COT cloud categories (yellow and green shadings) and stands in contrast to correctly detected rainfall events, particularly of MCSs (e.g. Figure 6.24e). The probability of false alarms is increased during episodes of high cloud cover (Figure 6.27a), less than 14% overall originate the from mid- and low-level cloud categories, i.e. from below the 440 hPa line. Furthermore, a substantial fraction of false alarms occurs after sunset (gray shading) and may be related particularly to the weak but relatively frequent evening convection (see Figure 6.7). Throughout the year, little deviation from the annual profile is experienced, which strongly supports the notion of systematic misjugdement of low- to medium COT ice clouds as rainy clouds by IMERG, irrespective of the season. However, false alarms at mid- and low levels do occur as well and are most frequent during the little dry season in July and August with a total frequency of 26%. One notable feature is the decreased altitude of the maximum occurrence frequency around the -50° level in July and August, which is located higher outside of the little dry season. This seasonal behaviour resembles the long-term ERA-Interim upper-level divergence field in Fig. 4.7, which likely reflects the divergence emerging from convective outflow. The decrease in altitude (i.e. increase in CTT) may be rooted in the reduction of
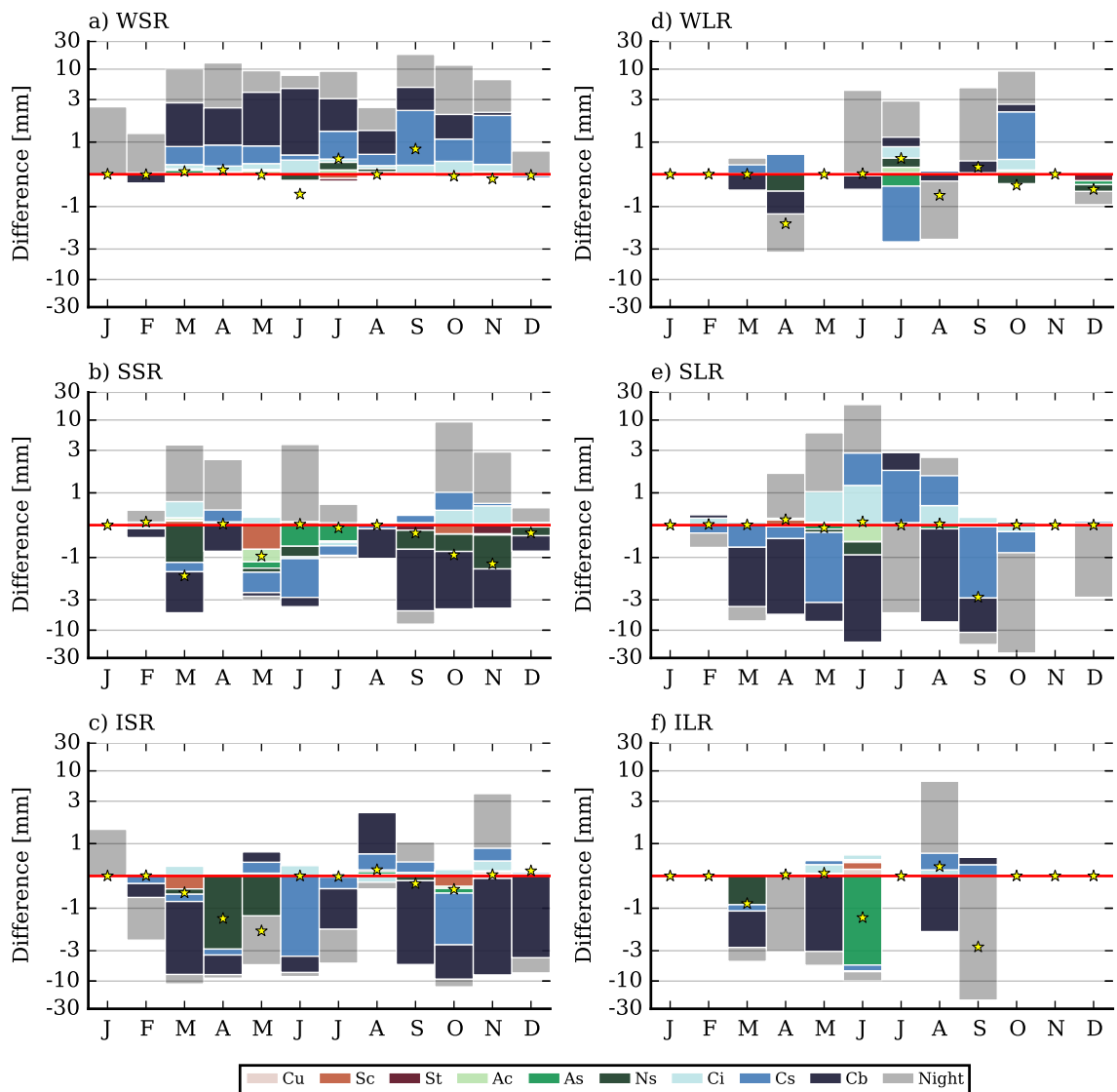
Figure 6.26: Mean monthly difference between IMERG and RG rainfall broken down into the nine ISCCP cloud types based on all RG rainfall types (cf. Figure 6.16). The grey bars denote the net rainfall difference due to clouds occurring during the night. The yellow star markers indicate the rainfall difference caused by warm rain. Note that only hits are considered for this statistic. Furthermore, note that the ordinate is logarithmic. Thus, the stacked bars at the upper (bottom) ends may be scaled differently than the bars below (above).

conditional instability in the little dry season due to an overall moister troposphere. As for missed events, roughly 43% overall are related to mid- to low-level clouds on an annual basis (Figure 6.27b). While still mainly related to high clouds during the main dry season between November and February, potentially from occasional weak deep convection, missed rainfall during the little dry season is clearly linked to warm rain events. Here, almost 65% of all missed events stem from clouds representing the low-cloud categories. The frequency of missed events from the low-levels decreases to both sides of the little dry season, resulting in a unimodal seasonal cycle in accordance with the seasonal cycle of the *POD* in Figure 6.12b.

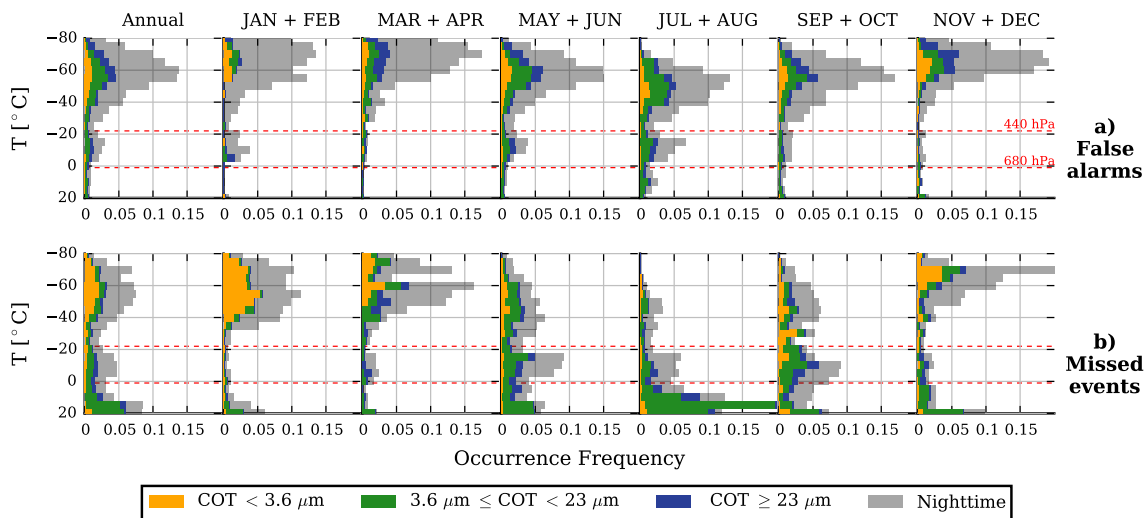Figure 6.27: Monthly occurrence freuqency of the nine ISCCP cloud types under the condition of (a) false alarms and (b) missed events. False alarm rainfall refers to IMERG whereas missed events are associated with rainfall detected by the RGs only. The yellow star markers denote the fractional occurrence purely liquid cloud tops. 2016 and 2017 are aggregated.

The fractional contribution of the cloud types to the falsely detected and missed rainfall basically mirrors the findings mentioned above (Figure 6.28, daytime only). The absolute rainfall amounts (including nighttime) were already presented in Figures 6.17 and 6.18. Again, false alarms are mostly subject to the presence of high clouds with rather low variation over the course of the year (Figure 6.28a). Outside of the dry month of January, the low-COT category Ci reaches a fraction up to 0.16 in May. Assuming an unchanged distribution and equal rainfall amounts during the night, this would correspond to approximately 5 mm. A clear unimodal cycle of the fractional rainfall contribution for mid- and low-level clouds is present for missed events, which peaks in the little dry season (Figure 6.28b). The highest fraction of missed warm rain (yellow markers) occurs in July and September with over 0.61 and 0.53, respectively. Overall, the oversensitivity to optically thin ice-phased clouds is partly compensated by the insufficient ability of IMERG to detect warm rain processes, the latter of which have been found to result largely in WSR events during the little dry season (see Figure 6.17).

6.6   Summary and discussion

A two-year rainfall dataset (2016 and 2017) from up to 17 stations within the Kumasi RG network in southern Ghana was used to (a) monitor the relative occurrence and rainfall distribution among defined rainfall types, and to (b) evaluate the performance and identify potential deficiencies of the satellite-based rainfall product IMERG. For (b), RG data were combined with cloud information from the CLAAS-2 dataset to investigate the link to ISCCP-defined cloud types based on the cloud top pressure (CTP) and cloud optical thickness (COT).

Considering (a), short rainfall events (SRs), i.e. events shorter than 80 min, dominate in number, accounting for almost 90% of all events. However, long rainfall events (LRs), which are
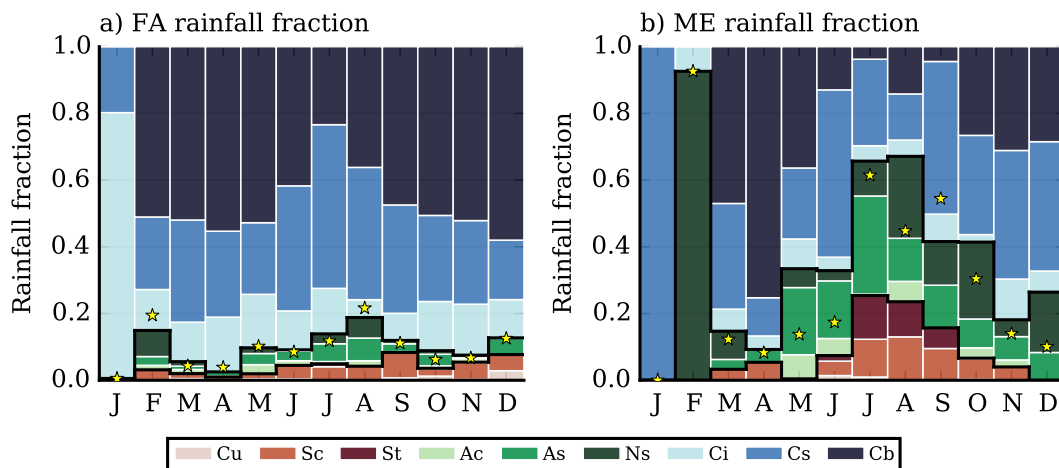
Figure 6.28: Similar to Figure 6.25b+c, but for (a) false alarms and (b) missed events.

typically but not exclusively MCSs entering the RG domain from easterly directions, contribute to around 60% to total rainfall despite being strongly outnumbered. Composites of the diurnal contribution of rainfall show that particularly intense LRs are most active in the evening and early nighttime, whereas SRs contribute most during noon and afternoon. However, the diurnal contribution of the rainfall types is subject to a seasonal cycle, where the general diurnal afternoon/early evening rainfall maximum largely consists of rainfall from LR types during the wet period of the WAM from April to September, while the maximum is constituted of SR rainfall during the main dry season from November to February. Here, March and October represent the transition between these two periods. On a seasonal scale, the rainfall contribution from LR types are generally highest during the primary (March–June) and secondary rainy season (September–October). While SR types dominate the main dry season, the little dry season (July–August) exhibit a distinct peak of the least intense type of SRs (WSR), reminiscent of the occurrence maximum of shallow, warm rain events based on the TRMM-PR analysis in chapter 4.

IMERG was evaluated on a seasonal, daily and sub-daily timescale, which revealed new perspectives of its performance. While the seasonal cycles of 2016 and 2017 are captured well, the skill of IMERG decreases towards shorter timescales. This is not too surprising given the fact that SWA is mostly influenced by convective rainfall, which varies a lot in space and time. However, monthly rainfall in IMERG is partly subject to error compensations with respect to both the different rainfall and cloud types. The rainfall amount during WSR events are almost exclusively overestimated, while that of intense types are underestimated. For the latter, compensatory tendencies occur due to a general overestimation of the event duration and the inability of IMERG to resolve high intensities. Furthermore, IMERG is prone of producing false alarms, which occur throughout the year and overall account for a fourth of total rainfall. Missed events, in turn, are less frequent, but occur predominantly during SR events. A distinct decrease in skill of IMERG is evident for the little dry season, which is rooted in the high frequency of both false alarms and missed events during that period.

Using the CLAAS-2 cloud dataset, some of the aforementioned patterns in the behaviour of

IMERG are clearly correlated to difficulties in the treatment of ice clouds. On average, COT of high clouds is used as a predictor for the rainfall intensity in IMERG. However, the comparison with the RG data reveal three things. First, the rainfall intensity is weakly correlated with COT, which makes it very difficult to predict for IMERG. Second, IMERG is too sensitive to low- and medium-COT ice clouds, leading to many instances of (weak) rainfall and thus false alarms. There is no obvious seasonality of this bias and it is consistent throughout the year. A large part of the overestimation of WSR events emerge from such clouds, which may also include dissipating convective systems and thus prolonged cirrus contamination. Finally, IMERG is too insensitive to rainfall from mid- and low-level clouds, leading to misses particularly of warm rain events. The latter are a pronounced phenomenon during the little dry season, which explains the poor performance of IMERG during this time of the year on the daily and event timescale. However, the absolute error is rather small since warm rain events account for just 5% of total rainfall.

The aforementioned sensitivity towards ice clouds reflects the fundamental principle of IR-based as well as land-based PMW rainfall retrievals. PMW algorithms over land rely on the attenuation of upwelling radiation, which, at MW frequencies, is obtained through scattering of MW signals by precipitation-sized hydrometeors and in particular ice particles (Petty; 1995). Thus, deeper clouds, e.g. deep convection with more ice particles, are related to higher rainfall rates, which became apparent for IMERG. With respect to IR retrievals, rainfall is mainly related to cold CTTs, which, however, includes thin, non-precipitating cirrus clouds and which complicates the detection of warm rain. As Kidd and Levizzani (2011) pointed out, the relationship between rainfall and CTT is simple, yet indirect and varies between, among other things, cloud types and even climatological region. Thus, PMW measurements are physically more direct than IR estimates (Kidd; 2001). It can be assumed that some of the deficiencies, that is, overestimating weak rainfall and missing warm rain events, are due to instances of missing PMW estimates, thus leaving only IR information. However, in the case of warm rain, the detection algorithm of Young et al. (2018) using extended cloud-top information such as COT from CLAAS-2 has revealed a promising way to overcome this issue, which can become important for the moist SWA.

For SWA, IMERG performs well on a monthly scale and is able to detect spatially extended and the majority of intense rainfall systems on a daily and sub-daily scale. However, if the contingency table is taken as a reference, the skill of IMERG is lowered significantly lowered by frequent false alarms and, to a lesser degree, missed events, which prevail particularly during the little dry season of SWA.

7. Synthesis

The present work has explored the nature of convection and their implication to rainfall over the humid and densely populated SWA. The necessity for such an extensive rainfall analysis over the understudied SWA is underpinned by the fact that the skill of quantitative rainfall predictions on short and long time scales is still poor in climate projections and operational forecasting (Christensen et al.; 2013; Vogel et al.; 2018) in this region. Furthermore, in the light of the pronounced interannual to interdecadal rainfall variability (e.g. Nicholson; 2005; Diatta and Fink; 2014), its monitoring through the current and following generations of spaceborne precipitation retrievals becomes progressively more important for SWA, where ground-based observational facilities experience a gradual degradation (Flamant et al.; 2018). Thus, the evaluation of strengths and deficiencies of satellite rainfall estimates was addressed in this work and was realised with a high-resolution rain gauge network around the city of Kumasi in southern Ghana. Overall, the work was centred around three specific questions, for which the results are summarised in the following.

Which rainfall types constitute the total rainfall over SWA, what are their lifetime characteristics and under which conditions do they typically develop from a climatological standpoint?

While the semi-arid Sahelian region were found to depend almost exclusively on MCSs in earlier studies (Mathon and Laurent; 2001; Laing et al.; 2008, e.g.), non-organised convection gets progressively more important towards the coastline. However, MCSs still account for over a half of total rainfall (56% at the coastline, 71% in the Soudan region) despite being strongly outnumbered by non-organised, mostly diurnal convection. The evaluation of the Kumasi RG network data supports this finding, where long rainfall events, most likely MCSs by nature, contribute around 60% to total rainfall. Nonetheless, the moister regime over SWA lowers the dependency of the local population on MCS rainfall.

   The occurrence of any rainfall type is generally linked to two things. The first are midlevel maxima in the vorticity field. They are most pronounced in the case of a passing wave disturbance, which most likely, but not exclusively, represent AEWs. The importance of these midlevel disturbances for the weather prediction over SWA lies in the modification of the midlevel wind field and thus vertical wind shear. The latter has been shown to be useful as a predictor for the level of organisation of convective systems. As explained in chapter 3, stronger vertical wind

shear enhances the probability for higher organised convective systems such as squall lines. Indeed, these systems, which belong to a group called *broad stratiform region* (BSR) in the analysis in chapter 4, typically occur on the downshear (western) flank of the wave disturbance, where vertical wind shear is strongest owing to the superposition of midlevel northeasterlies and the undercutting southwesterly monsoon flow. In contrast, the reduction of vertical wind shear as well as a reduction of conditional instability on the upshear (eastern) side of the wave gives rise to the occurrence of non-organised shallow warm rain convection. Both exhibit a strong seasonality, where MCSs are confined to the rainy seasons, whereas the shallow warm rain type is typically found during the little dry season in July and August. The second factor is low-level moisture convergence. Recalling the description in chapter 3, it deepens the boundary layer to create local PW maxima. Every rainfall type is preceded by low-level moisture convergence, which may be used as an additional predictor in forecasting rainfall over SWA (cf. Dezfuli et al.; 2017).

While the present work mainly focused on rainfall processes on synoptic time scales, it is widely known that so-called *convectively coupled equatorial waves* have an impact on rainfall on intraseasonal and seasonal time scales (e.g. Roundy and Frank; 2004; Kiladis et al.; 2009; Schlueter et al.; 2018). In this regard, it is not known yet how they influence the composition of rainfall types over SWA. This, however, may represent an important aspect for future subseasonal and seasonal rainfall forecasting.

What environmental factors control the development of MCSs over SWA?

With the premise of the dominance of MCSs for rainfall over SWA, the development of an MCS from 10–13 June 2016 during the period of the DACCIWA field campaign was evaluated. This case was exceptional regarding two things. First, the MCS crossed both the dry Savannah and the moister Guinea Coast region while being maintained in both regimes. And second, it caused one of the highest ever recorded daily rainfall amount with 223.5 mm at the southern Nigerian station Abakaliki.

The MCS formed due to diurnal heating, then moved southwestward along a lower-tropospheric wave disturbance and developed into a classical West African squall line in a highly sheared environment with pronounced midlevel dryness. Strong moisture flux convergence over Nigeria prior to the MCS passage led to extreme values in precipitable water (PW) and was caused by the formation of a local, short-lived heat low. According to the pressure tendency equation, the latter resulted from tropospheric warming due to MCS-forced subsidence as well as surface insolation in the resulting almost cloud-free atmosphere. In an extremely moist environment, the MCS strongly intensified and initiated the formation of a moist mid- to low-tropospheric vortex, which resulted in a deceleration of the MCS and high rainfall accumulation at Abakaliki. As shown by the vorticity equation, strong low-level vortex stretching and upper-level vertical vorticity advection led to a deep cyclonic flow. The latter was facilitated by the decrease of moist static stability and increase of background relative vorticity, which made the MCS "dynamically large" relative to the Rossby radius of deformation. MCS maintenance and the development of new convective cells during the subsequent westward movement along the Guinea Coast is suggested to occur

through constant moisture supply and lifting associated with the vortex, eventually causing high rainfall amounts at coastal stations in Ghana and Ivory Coast farther west as well.

This case study again supports vertical wind shear and moisture convergence as general predictors for convective organisation. A novel aspect for MCS dynamics over SWA, however, is the influence of lower-tropospheric vortices on their maintenance. Following the DACCIWA overview paper by Knippertz et al. (2017), similar vortices appear relatively frequent over SWA, but there is a lack of understanding about their origin. The vortex in the case study was MCS-induced and required both the significant spatial extent of the MCS as well as the generation of a moist environment (PW) by far exceeding the 99th percentile. This implies that such extreme rainfall cases exhibit rather low recurrence frequencies, similar to that of the Ougadougou event in 2009 (+100 years). However, in the light of climate change, an increase in extreme rainfall amounts have been found to scale with the moisture content according to the Clausius-Clapeyron equation (around 7% per K) (Westra et al.; 2013; Lehmann et al.; 2015) and are assumed to manifest themselves particularly in the large convergence zones in the tropics (e.g. Trenberth et al.; 2003; Trenberth; 2011) and thus SWA. Future scientific studies may address the question how susceptible a gradually moister environment over the Guinea Coast region becomes to such extreme rainfall events.

How do state-of-the-art spaceborne rainfall measurements perform over SWA un-der the presence of differently characterised clouds and rainfall systems?

As mentioned, the identification of interannual to interdecadal variabilities over West Africa in general is likely to shift to the usage of spaceborne precipitation retrievals due to the degradation of ground-based observational networks. Thus, the widely used half-hourly, gridded and gauge-calibrated precipitation dataset of GPM, IMERG (V5), was compared to data from the minutely-recording rain gauge (RG) network established around Kumasi (Ghana) on several time scales. The high temporal resolution of both datasets allowed the assignment of rainfall episodes to certain types of rainfall, which were defined by thresholding the individual rainfall events in the rain gauge datasets with respect to intensity and duration.

Rainfall on a monthly and seasonal timescale in IMERG agrees well with the RG data, which is likely to be in part due to the regional calibration of IMERG with station data ingested in the Global Telecommunication System (GTS). On finer time scales, the skill of IMERG decreases and is subject to error compensations. Overestimation tendencies emerge from both a high frequency of false alarms as well as a too long-lasting rainy period during actual weak and short rainfall events. False alarms contribute to around a fourth of total rainfall detected by IMERG. On the other hand, this is largely balanced by missed events and a strong underestimation of intense rainfall events. Here, IMERG fails to resolve the high intensity, while the rainfall duration is still overestimated. The inclusion of the CLAAS-2 cloud dataset in the analysis revealed that IMERG is too sensitive for thin ice clouds. This may be of particular importance for dissipating convective systems, which can feature long-lasting anvil debris falsely detected as rain-bearing clouds. It is likely that this causes the overestimation of the duration of rainfall events in many

cases. However, rainfall from shallow, purely liquid clouds, i.e. warm rain, is a major source for (low-intense) missed events, which frequently occurs during the little dry season. This is the reason why IMERG, based on some skill metrics, performs worst during this period on a seasonal basis. However, given the fact that warm rain accounts for only 5% of total rainfall, according to the RG data, the absolute difference in warm rain between IMERG and the RGs is rather small.

These deficiencies of IMERG are not entirely unknown and are based on the principle that the detection of rainfall over land relies primarily on the scattering of microwave signals in ice clouds. This, in turn, strongly depends on the composition of cloud systems, which is different in various regions on earth. For instance, Petković and Kummerow (2017) found opposing estimation tendencies regarding convection between the Amazon region (underestimation) and central Africa (overestimation) and linked them to differences in the cloud depth and thus the amount of ice within the clouds. Thus, convective systems over SWA are shallower than in central Africa, which is plausible given the more pronounced maritime character of SWA. With respect to the latter, a typical maritime phenomenon is warm rain (e.g. Schumacher and Houze; 2003), which is clearly a weakness of IMERG over land. Here, a moister environment in a future climate state (e.g. Trenberth et al.; 2003) may also lead to higher cloudiness in low- and midlevels with a potentially higher frequency of warm rain events. Young et al. (2018) already showed the potential of using spaceborne cloud datasets to delineate regions of higher warm rain probability, which may be of value for improving rainfall estimations in combination with IMERG and future generations of spaceborne rainfall retrievals.

Overall, the benefit of IMERG for a relatively data-sparse region such as SWA has to be emphasised, not least because of the spatiotemporally continuous monitoring of rainfall. Thus, it will play a crucial role in identifying and detecting rainfall variabilities on multiple timescales in this region, whose economies are highly dependent on the availability of rain water. It is and will also be important for the purpose of model validation. Because of the data paucity over SWA, a substantial part of the current understanding of the complex WAM circulation stem from modelling and continues to be so in the future. Furthermore, this work has also stressed the importance of rainfall validation that was made possible with a network of high-resolution rain gauges. In the first instance, the identified behaviour of IMERG may be representative for the humid SWA alone. It remains to be evaluated how IMERG performs for instance in the semi-arid Sahel to better understand IMERG in a different climatic regime in West Africa.

A. Appendix
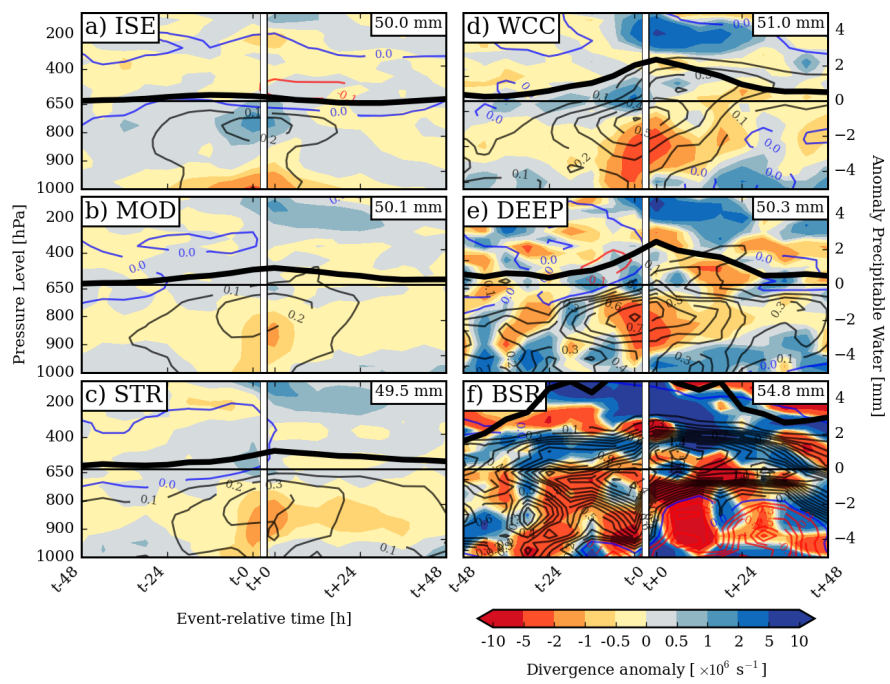
Figure A.1: Same as Figure 4.8, but for the Coast region only.
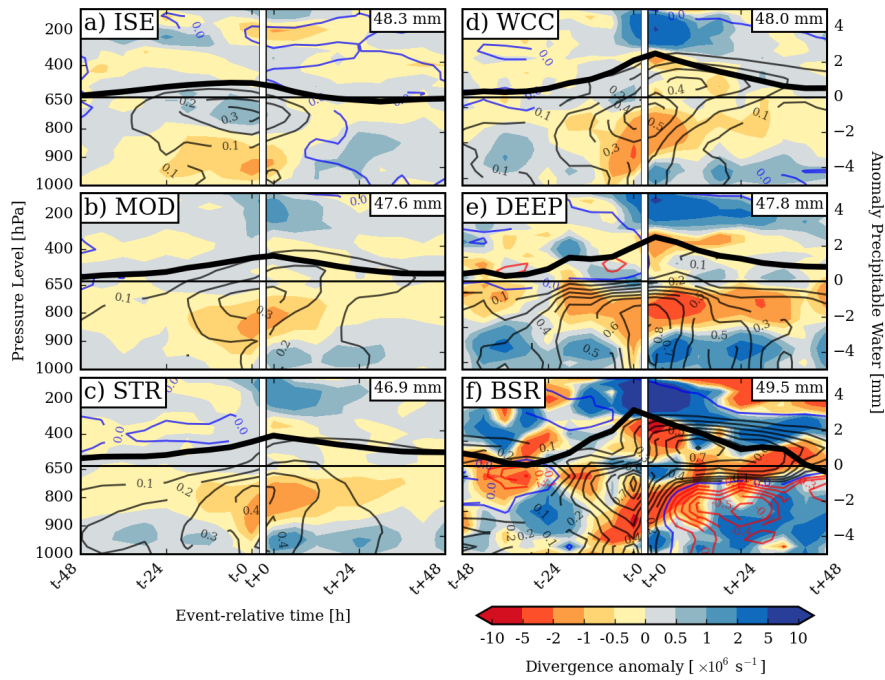
Figure A.2: Same as Figure 4.8, but for the Inland region only.
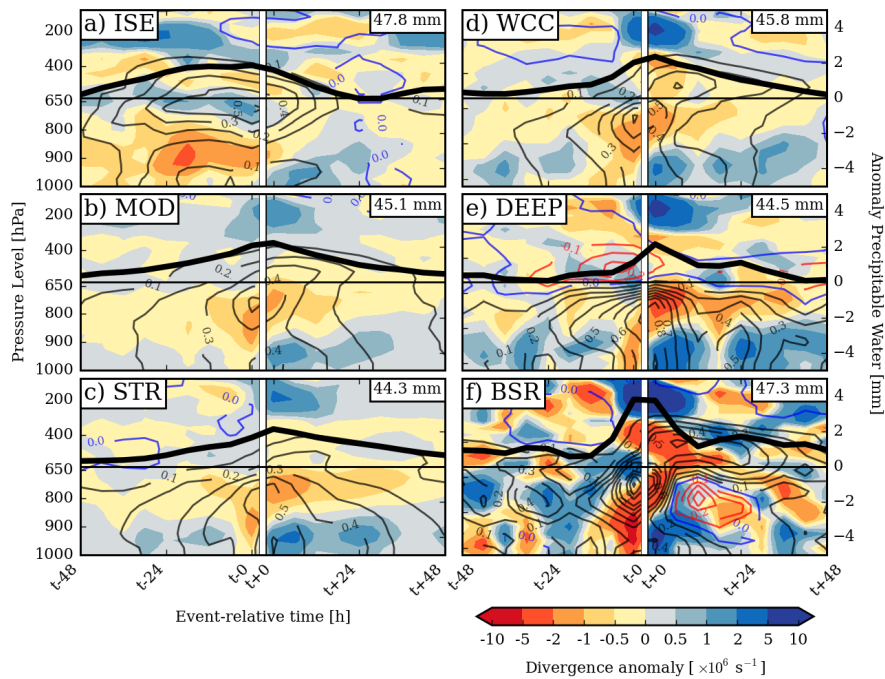
Figure A.3: Same as Figure 4.8, but for the Soudan region only.
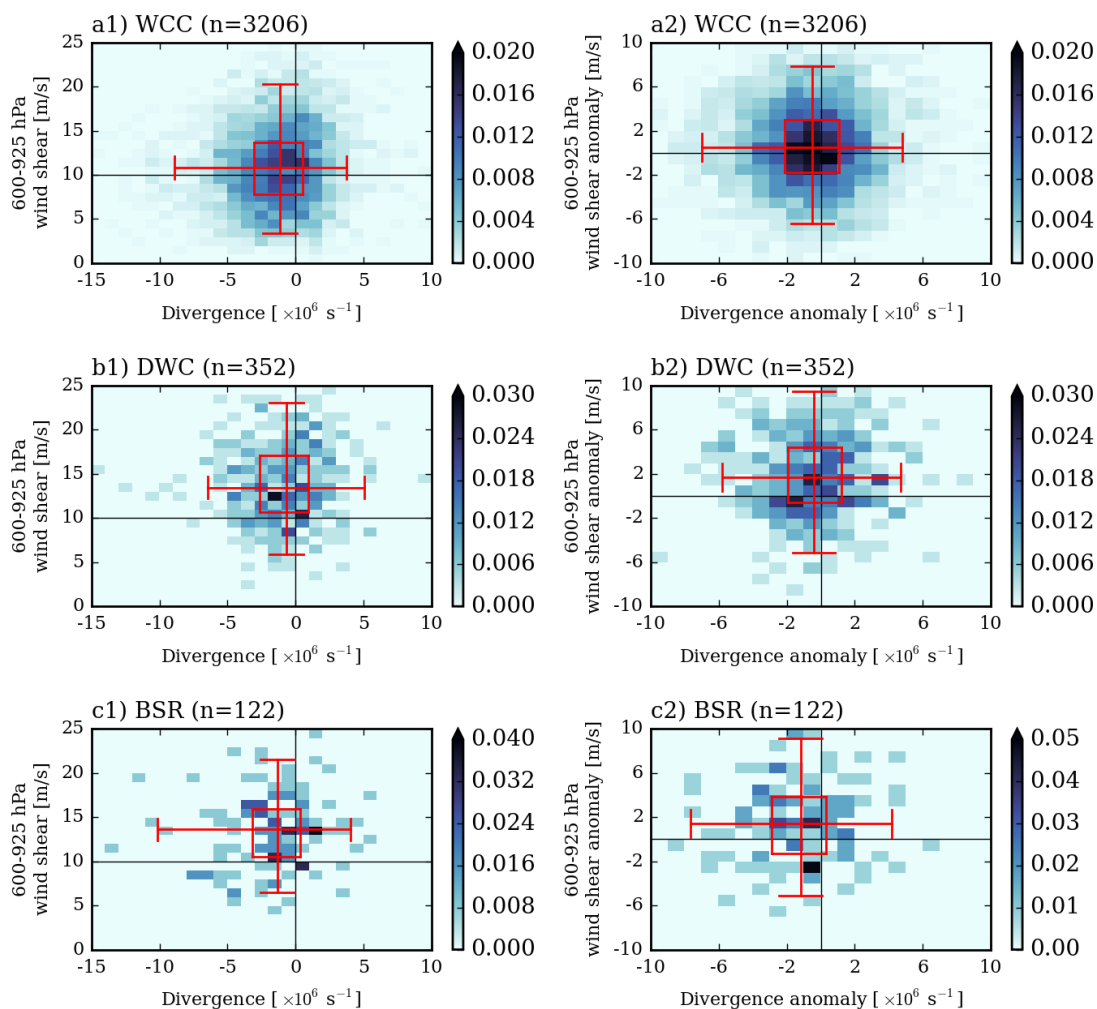
Figure A.4: Two-dimensional occurrence frequency [in %] of the 12-hour pre-storm 600-925 hPa vertical windshear (y-axis) against divergence in the lowest 100 hPa (x-axis) for WCC (top row), DWC (middle) and BSR (bottom) with respect to absolute value (left column) and the anomaly value (right column) from a long-term mean. The anomaly values are used to compile Figures 4.8 and 4.9 in chapter 4. The 2D box-whisker plot display the lower and upper quartile, the median (inside the box) and the 2.5 and 97.5 percentile respectively, thus encompassing 95% of the datapoints.
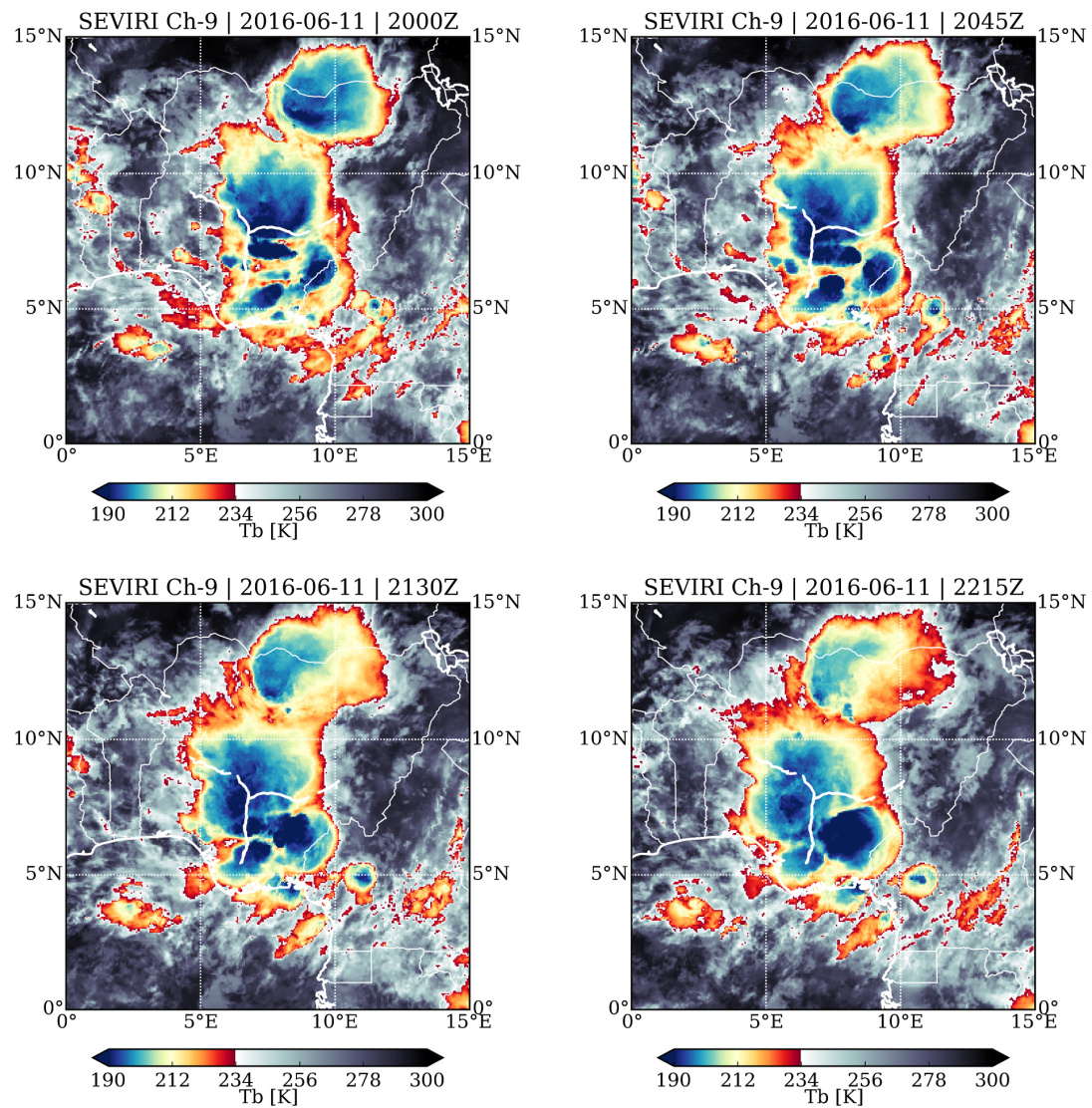
Figure A.5: 45-minutely sequence of IR cloud images from SEVIRI (11 June 2016, 2000–2215 UTC) showing the development of the MCS over Nigeria. The coloured area denote cloud-top temperatures of 233 K or less.
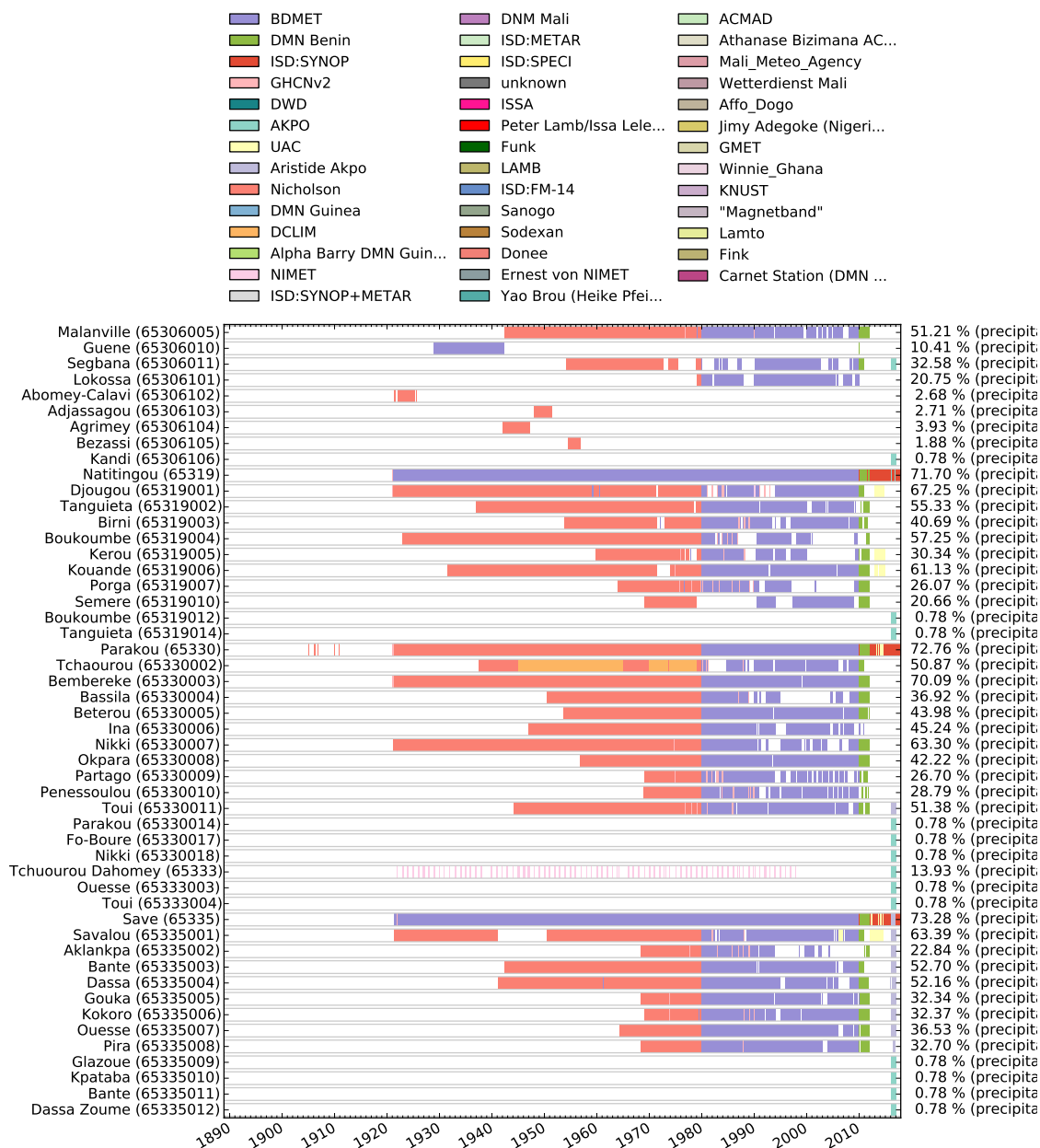
Figure A.6: Availability chart for an exemplary set of rain gauge stations used for the analysis in chapter 5. The coloured bars denote the period with available data as well as the source indicated at the top. On the left axis, the station name and station ID are indicated, on the right axis the availability percentage from 1888–2017. The rain gauge data are stored in the Karlsruhe African Surface-Station Database (KASS-D).
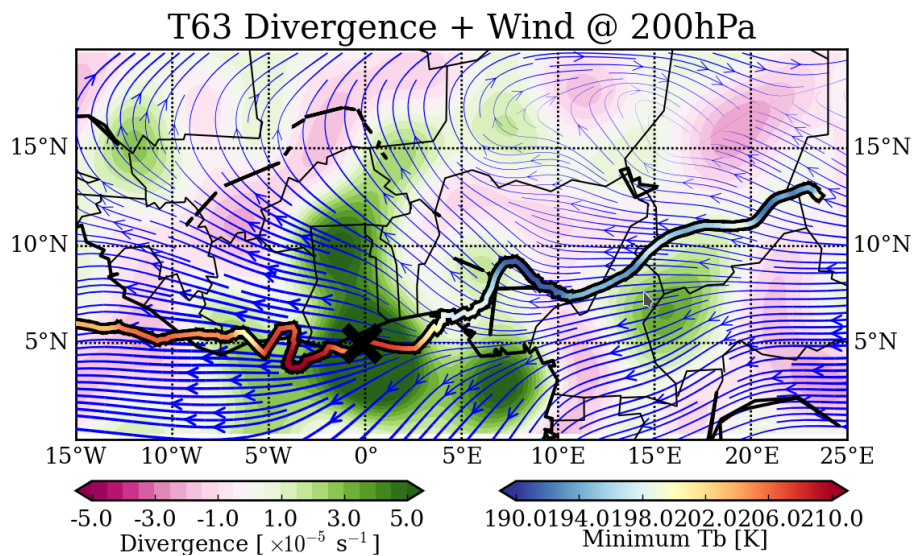
Figure A.7: ERA5 upper-level truncated (T63) divergence (shaded) and wind field (blue stream-lines) at 200 hPa on 12 June, 1400 UTC, as well as the MCS track with indications of its minimum IR-based cloud-top temperature along the path (coloured line). The black x-mark denotes the position of the MCS.
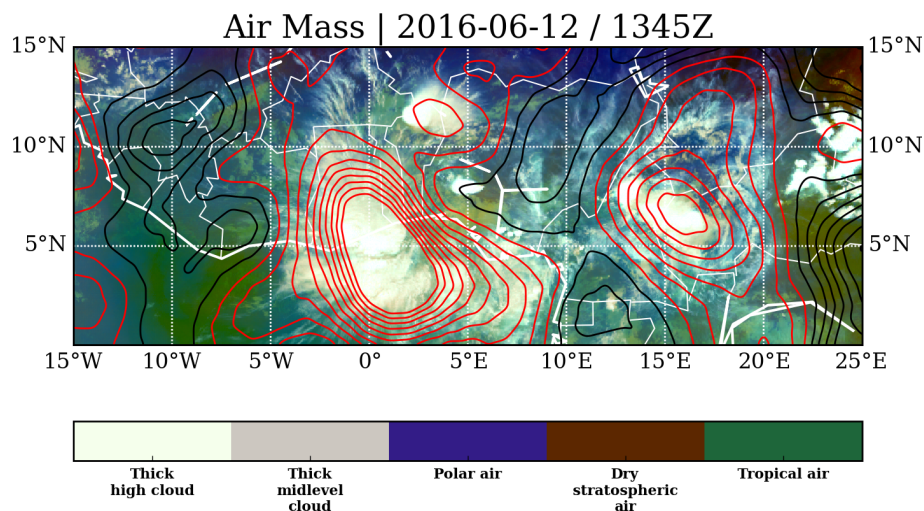
Figure A.8: Divergence field derived from atmospheric motion vectors of EUMETSAT for 12 June, 1345 UTC. Divergence is denoted by red contours with an interval step of 0.25 s^{-1}, and convergence accordingly (black contours). Colour-shaded is the "Airmass" product (see colourbar) derived from the method of Lensky and Rosenfeld (2008). High clouds such as deep convection are white.

B. List of abbreviations

ACT   Atlantic cold tongue

AEJ   African easterly jet

AEW   African easterly wave

AMMA   African Monsoon Multidisciplinary Analysis

AMS   American Meteorological Society

BSR   Broad stratiform region

CAPE   Convective available potential energy

CDF   Cumulative distribution function

CIN   Convective inhibition

CLAAS   Cloud property dataset using SEVIRI

CM SAF   Satellite Application Facility on Climate Monitoring

COPT81   Convection Profonde Tropicale 1981

COT   Cloud optical thickness

CP   Coastal phase

CPH   Cloud phase

CTP   Cloud-top pressure

CTT   Cloud-top temperature

DACCIWA   Dynamics-Aerosol-Chemistry-Cloud-Interactions in West Africa

DCAPE   Downdraft CAPE

DCC   Deep convective core

DIAB   Diabatic heating term in the ITT

DIV   Divergence term in the VTE

DWC   Deep and wide convective core

ECMWF   European Centre for Medium-range Weather Forecasts

EL	Equilibrium level
EP	Evaporation/precipitation term in the PTE
ERA	ECMWF Reanalysis
EUMETSAT	European Organisation for the Exploitation of Meteorological Satellites
FAR	False alarm ratio
GATE	Global Atmospheric research Program Atlantic Tropical Experiment
GC	Guinea Coast
GCM	General circulation model
GMET	Ghana Meteorological Agency
GPCC	Global Precipitation Climatology Centre
GPM	Global Precipitation Measurement
GRW	Gauge relative weight
HADV	Horizontal advection term in the VTE
HSS	Heidke skill score
ILR	Intense long rainfall
IMERG	Integrated Multi-Satellite Retrievals for GPM
IR	Infrared
ISE	Isolated shallow echo
ISCCP	International Satellite Cloud Climatology Project
ISR	Intense short rainfall
ITCZ	Intertropical convergence zone
ITF/ITD	Intertropical front / discontinuity
ITT	Integrated temperature tendency
LCL	Lifting condensation level
LFC	Level of free convection
LLWS	Low-level wind shear
LR	Long rainfall
MCS	Mesoscale convective system
METAR	Meteorological Aviation Routine Weather Report
MetOP	Meteorological Operational Satellite

MFC	Moisture flux convergence
MHS	Microwave Humidity Sounder
MOD	Moderate convection
MSLP	Mean sea level pressure
MW	Microwave
NOAA	National Oceanic and Atmospheric Administration
NLLJ	Nocturnal low-level jet
NWP	Numerical weather prediction
NP	Nigerian phase
OCS	Organised convective system
PMW	Passive microwave
POD	Probability of detection
PTE	Pressure tendency equation
PV	Potential vorticity
PW	Precipitable water
RES	Residual term in the PTE, ITT, VTE
RG	Rain gauge
SAL	Saharan air layer
SAPHIR	Sounder for Probing Vertical Profiles of Humidity
SEVIRI	Spinning Enhanced Visible and Infrared Imager
SHL	Saharan heat low
SLR	Strong long rainfall
SP	Sahelian phase
SR	Short rainfall
SSR	Strong short rainfall
SST	Sea surface temperature
STR	Strong convection
SWA	Southern West Africa
SYNOP	Surface synoptic observations
TADV	Temperature advection term in the ITT

TEJ	Tropical easterly jet
TILT	Tilting term in the VTE
TRMM	Tropical Rainfall Measuring Mission
TRMM-PR	TRMM precipitation radar
UTC	Coordinated Universal Time
VADV	Vertical advection term in the VTE
VMT	Vertical motion term in the ITT
VTE	Vorticity equation
WAM	West African monsoon
WCC	Wide convective core
WLR	Weak long rainfall
WMO	World Meteorological Organization
WSR	Weak short rainfall

C. List of symbols

B	Buoyancy force
c_p	Specific heat capacity for isobaric processes
C	Moisture sink due to condensation
ζ	Relative vorticity
E	Moisture/mass source due to evaporation
η	Absolute vorticity
f	Planetary vorticity
g	Gravitational acceleration
$\boldsymbol{k}$	Vertical unit vector
l	Time lag
λ_R	Rossby radius of deformation
N	Brunt-Väisälä frequency
p	Air pressure
P	Mass sink due to precipitation
ϕ	Geopotential
φ	Direction of storm movement
ω	Vertical velocity in isobaric coordinates
q	Specific humidity
$\dot{Q}$	Diabatic heat rate
r	Mixing ratio or correlation coefficient
R_d	Gas constant of dry air
ρ	Air density
t	Time
T	Air temperature

T_b	Brightness temperature
T_v	Virtual temperature
θ	Potential temperature
u	Zonal wind speed
v	Meridional wind speed
V	Tangential wind speed
$\boldsymbol{v_h}$	Horizontal wind vector
w	Vertical velocity in cartesian coordinates

Bibliography

Acheampong, P. K. (1982). Rainfall anomaly along the coast of Ghana. its nature and causes, *Geografiska Annaler. Series A. Physical Geography* pp. 199–211.

Akinsanola, A., Ogunjobi, K., Ajayi, V., Adefisan, E., Omotosho, J. and Sanogo, S. (2017). Comparison of five gridded precipitation products at climatological scales over West Africa, *Meteorology and Atmospheric Physics* **129**(6): 669–689.

Alexander, L., Zhang, X., Peterson, T., Caesar, J., Gleason, B., Tank, A. K., Haylock, M., Collins, D., Trewin, B., Rahimzadeh, F. et al. (2006). Global observed changes in daily climate extremes of temperature and precipitation, *Journal of Geophysical Research: Atmospheres* **111**(D5).

Andronache, C. (2018). *Remote Sensing of Clouds and Precipitation*, Springer.

Arkin, P. A. (1979). The relationship between fractional coverage of high cloud and rainfall accumulations during GATE over the b-scale array, *Monthly Weather Review* **107**(10): 1382–1387.

Arriaga, A. (2000). Microwave humidity sounder (MHS).

Aspliden, C. I., Tourre, Y. and Sabine, J. B. (1976). Some climatological aspects of West African disturbance lines during GATE, *Monthly Weather Review* **104**(8): 1029–1035.

Awaka, J., Iguchi, T., Kumagai, H. and Okamoto, K. (1997). Rain type classification algorithm for TRMM precipitation radar, *Geoscience and Remote Sensing, 1997. IGARSS'97. Remote Sensing-A Scientific Vision for Sustainable Development., 1997 IEEE International*, Vol. 4, IEEE, pp. 1633–1635.

Awumbila, M. (2017). Drivers of migration and urbanization in Africa: Key trends and issues, *International Migration* **7**: 8.

Banacos, P. C. and Schultz, D. M. (2005). The use of moisture flux convergence in forecasting convective initiation: Historical and operational perspectives, *Weather and Forecasting* **20**(3): 351–366.

Benas, N., Finkensieper, S., Stengel, M., van Zadelhoff, G.-J., Hanschmann, T., Hollmann, R. and Meirink, J. F. (2017). The msg-SEVIRI-based cloud property data record CLAAS-2, *Earth System Science Data* **9**(2): 415.

Berrisford, P., Kållberg, P., Kobayashi, S., Dee, D., Uppala, S., Simmons, A., Poli, P. and Sato, H. (2011). Atmospheric conservation properties in era-interim, *Quarterly Journal of the Royal Meteorological Society* **137**(659): 1381–1399.

Berry, G. J. and Thorncroft, C. (2005). Case study of an intense African easterly wave, *Monthly Weather Review* **133**(4): 752–766.

Birch, C. E., Marsham, J. H., Parker, D. J. and Taylor, C. M. (2014). The scale dependence and structure of convergence fields preceding the initiation of deep convection, *Geophysical Research Letters* **41**(13): 4769–4776.

Bonsignori, R. (2007). The microwave humidity sounder (MHS): in-orbit performance assessment, *Sensors, Systems, and Next-Generation Satellites XI*, Vol. 6744, International Society for Optics and Photonics, p. 67440A.

Buckle, C. (1996). *Weather and climate in Africa*, Longman.

Burpee, R. W. (1972). The origin and structure of easterly waves in the lower troposphere of north Africa, *Journal of the Atmospheric Sciences* **29**(1): 77–90.

Burpee, R. W. (1974). Characteristics of north African easterly waves during the summers of 1968 and 1969, *Journal of the Atmospheric Sciences* **31**(6): 1556–1570.

Charney, J. G. and Stern, M. (1962). On the stability of internal baroclinic jets in a rotating atmosphere, *Journal of the Atmospheric Sciences* **19**(2): 159–172.

Chen, T.-C. (2006). Characteristics of African easterly waves depicted by ECMWF reanalyses for 1991–2000, *Monthly weather review* **134**(12): 3539–3566.

Christensen, J. H., Kanikicharla, K. K., Marshall, G. and Turner, J. (2013). Climate phenomena and their relevance for future regional climate change.

Cornforth, R., Mumba, Z., Parker, D. J., Berry, G., Chapelon, N., Diakaria, K., Diop-Kane, M., Ermert, V., Fink, A. H., Knippertz, P. et al. (2017). Synoptic systems, *Meteorology of Tropical West Africa: The Forecasters Handbook* pp. 40–89.

Cotton, W. R., Lin, M.-S., McAnelly, R. L. and Tremback, C. J. (1989). A composite model of mesoscale convective complexes, *Monthly Weather Review* **117**(4): 765–783.

Dai, A. and Wang, J. (1999). Diurnal and semidiurnal tides in global surface pressure fields, *Journal of the atmospheric sciences* **56**(22): 3874–3891.

Davis, C. A. and Galarneau Jr, T. J. (2009). The vertical structure of mesoscale convective vortices, *Journal of the Atmospheric Sciences* **66**(3): 686–704.

Dee, D. P., Uppala, S., Simmons, A., Berrisford, P., Poli, P., Kobayashi, S., Andrae, U., Balmaseda, M., Balsamo, G., Bauer, P. et al. (2011). The era-interim reanalysis: Configuration

and performance of the data assimilation system, *Quarterly Journal of the royal meteorological society* **137**(656): 553–597.

Derrien, M. and Le Gléau, H. (2005). Msg/SEVIRI cloud mask and type from safnwc, *International Journal of Remote Sensing* **26**(21): 4707–4732.

Desbois, M., Capderou, M., Eymard, L., Roca, R., Viltard, N., Viollier, M. and Karouche, N. (2007). Megha-tropiques: un satellite hydrométéorologique franco-indien.

Desbois, M., Kayiranga, T., Gnamien, B., Guessous, S. and Picon, L. (1988). Characterization of some elements of the Sahelian climate and their interannual variations for July 1983, 1984 and 1985 from the analysis of METEOSAT ISCCP data, *Journal of Climate* **1**(9): 867–904.

Dezfuli, A. K., Ichoku, C. M., Mohr, K. and Huffman, G. J. (2017). Precipitation characteristics in west and east Africa, from satellite and in-situ observations, *Journal of Hydrometeorology* .

Diatta, S. and Fink, A. H. (2014). Statistical relationship between remote climate indices and West African monsoon variability, *International Journal of Climatology* **34**(12): 3348–3367.

Donat, M., Alexander, L., Yang, H., Durre, I., Vose, R., Dunn, R., Willett, K., Aguilar, E., Brunet, M., Caesar, J. et al. (2013). Updated analyses of temperature and precipitation extreme indices since the beginning of the twentieth century: The hadex2 dataset, *Journal of Geophysical Research: Atmospheres* **118**(5): 2098–2118.

Doswell III, C. A., Davies-Jones, R. and Keller, D. L. (1990). On summary measures of skill in rare event forecasting based on contingency tables, *Weather and Forecasting* **5**(4): 576–585.

Doswell III, C. A. and Rasmussen, E. N. (1994). The effect of neglecting the virtual temperature correction on CAPE calculations, *Weather and forecasting* **9**(4): 625–629.

Draper, D. W., Newell, D. A., Wentz, F. J., Krimchansky, S. and Skofronick-Jackson, G. M. (2015). The global precipitation measurement (GPM) microwave imager (GMI): Instrument overview and early on-orbit performance, *IEEE Journal of Selected Topics in Applied Earth Observations and Remote Sensing* **8**(7): 3452–3462.

Durran, D. R. and Klemp, J. B. (1982). On the effects of moisture on the brunt-väisälä frequency, *Journal of the Atmospheric Sciences* **39**(10): 2152–2158.

Duvel, J. P. (1990). Convection over tropical Africa and the Atlantic ocean during northern summer. Part II: Modulation by easterly waves, *Monthly Weather Review* **118**(9): 1855–1868.

Easterling, D. R., Evans, J., Groisman, P. Y., Karl, T. R., Kunkel, K. E. and Ambenje, P. (2000). Observed variability and trends in extreme climate events: a brief review, *Bulletin of the American Meteorological Society* **81**(3): 417–426.

Elagib, N. A. and Elhag, M. M. (2011). Major climate indicators of ongoing drought in Sudan, *Journal of Hydrology* **409**(3-4): 612–625.

Eldridge, R. (1957). A synoptic study of West African disturbance lines, *Quarterly Journal of the Royal Meteorological Society* **83**(357): 303–314.

Engel, T., Fink, A. and Knippertz, P. (2017). Extreme flooding in the West African cities of dakar and Ouagadougou-atmospheric dynamics and implications for flood risk assessments, *EGU General Assembly Conference Abstracts*, Vol. 19, p. 11983.

EUMETSAT (2015).   Divergence product: Product guide, *Technical Report EUM/TSS/MAN/15/795706 v1C*.

Fink, A. H., Engel, T., Ermert, V., van der Linden, R., Schneidewind, M., Redl, R., Afiesimama, E., Thiaw, W. M., Yorke, C., Evans, M. et al. (2017). Mean climate and seasonal cycle, *Meteorology of Tropical West Africa: The Forecasters' Handbook* pp. 1–39.

Fink, A. H. and Njeri, J. (2018). rainfall_westafrica_june_july_2016, *Sedoo/Baobab database, doi:10.6096/BAOBAB-DACCIWA.1750* .

Fink, A. H., Pohle, S., Pinto, J. G. and Knippertz, P. (2012). Diagnosing the influence of diabatic processes on the explosive deepening of extratropical cyclones, *Geophysical Research Letters* **39**(7).

Fink, A. H. and Reiner, A. (2003). Spatiotemporal variability of the relation between African easterly waves and West African squall lines in 1998 and 1999, *Journal of Geophysical Research: Atmospheres* **108**(D11).

Fink, A., Pohle, S. and Hoffmann, R. (2008). Spatial and temporal rainfall climatologies of Benin, *2008) IMPETUS Atlas Benin: Research Results* **2007**: 21–22.

Fink, A., Vincent, D. and Ermert, V. (2006). Rainfall types in the West African Sudanian zone during the summer monsoon 2002, *Monthly weather review* **134**(8): 2143–2164.

Fitzpatrick, R. G., Bain, C. L., Knippertz, P., Marsham, J. H. and Parker, D. J. (2015). The West African monsoon onset: A concise comparison of definitions, *Journal of Climate* **28**(22): 8673–8694.

Flamant, C., Chaboureau, J.-P., Parker, D., Taylor, C., Cammas, J.-P., Bock, O., Timouk, F. and Pelon, J. (2007). Airborne observations of the impact of a convective system on the planetary boundary layer thermodynamics and aerosol distribution in the inter-tropical discontinuity region of the West African monsoon, *Quarterly Journal of the Royal Meteorological Society* **133**(626): 1175–1189.

Flamant, C., Knippertz, P., Fink, A. H., Akpo, A., Brooks, B., Chiu, C. J., Coe, H., Danuor, S., Evans, M., Jegede, O. et al. (2018). The Dynamics–Aerosol–Chemistry–Cloud Interactions in West Africa field campaign: Overview and research highlights, *Bulletin of the American Meteorological Society* **99**(1): 83–104.

Fortune, M. (1980). Properties of African squall lines inferred from time-lapse satellite imagery, *Monthly Weather Review* **108**(2): 153–168.

Galarneau Jr, T. J., Bosart, L. F., Davis, C. A. and McTaggart-Cowan, R. (2009). Baroclinic transition of a long-lived mesoscale convective vortex, *Monthly weather review* **137**(2): 562–584.

Galvin, J. (2010). Two easterly waves in West Africa in summer 2009, *Weather* **65**(8): 219–227.

Gilmore, M. S. and Wicker, L. J. (1998). The influence of midtropospheric dryness on supercell morphology and evolution, *Monthly Weather Review* **126**(4): 943–958.

Glickman, T. S. and Zenk, W. (2000). *Glossary of meteorology*, American Meteorological Society.

Grecu, M., Olson, W. S., Munchak, S. J., Ringerud, S., Liao, L., Haddad, Z., Kelley, B. L. and McLaughlin, S. F. (2016). The GPM combined algorithm, *Journal of Atmospheric and Oceanic Technology* **33**(10): 2225–2245.

Grist, J. P. and Nicholson, S. E. (2001). A study of the dynamic factors influencing the rainfall variability in the West African Sahel, *Journal of climate* **14**(7): 1337–1359.

Gu, G. and Adler, R. F. (2004). Seasonal evolution and variability associated with the West African monsoon system, *Journal of climate* **17**(17): 3364–3377.

Gu, G., Adler, R. F., Huffman, G. J. and Curtis, S. (2004). African easterly waves and their association with precipitation, *Journal of Geophysical Research: Atmospheres* **109**(D4).

Hagos, S. M. and Cook, K. H. (2007). Dynamics of the West African monsoon jump, *Journal of Climate* **20**(21): 5264–5284.

Hall, N. M., Kiladis, G. N. and Thorncroft, C. D. (2006). Three-dimensional structure and dynamics of African easterly waves. Part II: Dynamical modes, *Journal of the Atmospheric Sciences* **63**(9): 2231–2245.

Hamilton, R., Archbold, J. and Douglas, C. (1945). Meteorology of Nigeria and adjacent territory, *Quarterly Journal of the Royal Meteorological Society* **71**(309-310): 231–264.

Hannak, L., Knippertz, P., Fink, A. H., Kniffka, A. and Pante, G. (2017). Why do global climate models struggle to represent low-level clouds in the West African summer monsoon?, *Journal of Climate* **30**(5): 1665–1687.

Hastings, D. A., Dunbar, P. K., Elphingstone, G. M., Bootz, M., Murakami, H., Maruyama, H., Masaharu, H., Holland, P., Payne, J., Bryant, N. A. et al. (1999). The global land one-kilometer base elevation (globe) digital elevation model, version 1.0, *National Oceanic and Atmospheric Administration, National Geophysical Data Center* **325**: 80305–3328.

He, X., Kim, H., Kirstetter, P.-E., Yoshimura, K., Chang, E.-C., Ferguson, C. R., Erlingis, J. M., Hong, Y. and Oki, T. (2015). The diurnal cycle of precipitation in regional spectral model simulations over West Africa: Sensitivities to resolution and cumulus schemes, *Weather and Forecasting* **30**(2): 424–445.

Heidke, P. (1926). Berechnung des erfolges und der güte der windstärkevorhersagen im sturmwarnungsdienst, *Geografiska Annaler* **8**(4): 301–349.

Hersbach, H. and Dee, D. (2016). ERA5 reanalysis is in production, *ECMWF Newsletter 147* .

Heymsfield, G., Geerts, B. and Tian, L. (2000). TRMM precipitation radar reflectivity profiles as compared with high-resolution airborne and ground-based radar measurements, *Journal of Applied Meteorology* **39**(12): 2080–2102.

Holton, J. R. and Hakim, G. J. (2012). *An introduction to dynamic meteorology*, Vol. 88, Academic press.

Hou, A. Y., Kakar, R. K., Neeck, S., Azarbarzin, A. A., Kummerow, C. D., Kojima, M., Oki, R., Nakamura, K. and Iguchi, T. (2014). The global precipitation measurement mission, *Bulletin of the American Meteorological Society* **95**(5): 701–722.

Houze Jr, R. A., Rutledge, S. A., Biggerstaff, M. and Smull, B. (1989). Interpretation of doppler weather radar displays of midlatitude mesoscale convective systems, *Bulletin of the American Meteorological Society* **70**(6): 608–619.

Houze, R. A. (2004). Mesoscale convective systems, *Reviews of Geophysics* **42**(4).

Houze, R. A. and Betts, A. K. (1981). Convection in GATE, *Reviews of Geophysics* **19**(4): 541–576.

Houze, R. A., Rasmussen, K. L., Zuluaga, M. D. and Brodzik, S. R. (2015). The variable nature of convection in the tropics and subtropics: A legacy of 16 years of the tropical rainfall measuring mission satellite, *Reviews of Geophysics* **53**(3): 994–1021.

Houze, R. A., Wilton, D. C. and Smull, B. F. (2007). Monsoon convection in the himalayan region as seen by the TRMM precipitation radar, *Quarterly Journal of the Royal Meteorological Society* **133**(627): 1389–1411.

Huffman, G. J. (1997). Estimates of root-mean-square random error for finite samples of estimated precipitation, *Journal of Applied Meteorology* **36**(9): 1191–1201.

Huffman, G. J., Bolvin, D. T., Braithwaite, D., Hsu, K., Joyce, R., Xie, P. and Yoo, S.-H. (2015). Nasa global precipitation measurement (GPM) integrated multi-satellite retrievals for GPM (IMERG), *Algorithm theoretical basis document, version* **4**: 30.

Huffman, G. J. and Norman Jr, G. A. (1988). The supercooled warm rain process and the specification of freezing precipitation, *Monthly weather review* **116**(11): 2172–2182.

Iguchi, T., Kozu, T., Meneghini, R., Awaka, J. and Okamoto, K. (2000). Rain-profiling algorithm for the TRMM precipitation radar, *Journal of Applied Meteorology* **39**(12): 2038–2052.

Janiga, M. A. and Thorncroft, C. D. (2014). Convection over tropical Africa and the east Atlantic during the West African monsoon: Regional and diurnal variability, *Journal of Climate* **27**(11): 4159–4188.

Janiga, M. A. and Thorncroft, C. D. (2016). The influence of African easterly waves on convection over tropical Africa and the east Atlantic, *Monthly Weather Review* **144**(1): 171–192.

Jin, D., Oreopoulos, L., Lee, D., Cho, N. and Tan, J. (2018). Contrasting the co-variability of daytime cloud and precipitation over tropical land and ocean, *Atmospheric Chemistry and Physics* **18**(4): 3065–3082.

Judex, M. and Thamm, H. (2008). IMPETUS atlas Benin: Research results 2000–2007.

Kamara, S. I. (1986). The origins and types of rainfall in West Africa, *Weather* **41**(2): 48–56.

Kawanishi, T., Kuroiwa, H., Kojima, M., Oikawa, K., Kozu, T., Kumagai, H., Okamoto, K., Okumura, M., Nakatsuka, H. and Nishikawa, K. (2000). TRMM precipitation radar, *Advances in Space Research* **25**(5): 969–972.

Kidd, C. (2001). Satellite rainfall climatology: a review, *International Journal of Climatology* **21**(9): 1041–1066.

Kidd, C. and Levizzani, V. (2011). Status of satellite precipitation retrievals, *Hydrology and Earth System Sciences* **15**(4): 1109–1116.

Kiladis, G. N., Thorncroft, C. D. and Hall, N. M. (2006). Three-dimensional structure and dynamics of African easterly waves. Part I: Observations, *Journal of the Atmospheric Sciences* **63**(9): 2212–2230.

Kiladis, G. N., Wheeler, M. C., Haertel, P. T., Straub, K. H. and Roundy, P. E. (2009). Convectively coupled equatorial waves, *Reviews of Geophysics* **47**(2).

Knievel, J. C. and Johnson, R. H. (2003). A scale-discriminating vorticity budget for a mesoscale vortex in a midlatitude, continental mesoscale convective system, *Journal of the atmospheric sciences* **60**(6): 781–794.

Knippertz, P., Coe, H., Chiu, J. C., Evans, M. J., Fink, A. H., Kalthoff, N., Liousse, C., Mari, C., Allan, R. P., Brooks, B. et al. (2015). The DACCIWA project: Dynamics–aerosol–chemistry–cloud interactions in West Africa, *Bulletin of the American Meteorological Society* **96**(9): 1451–1460.

Knippertz, P. and Fink, A. H. (2008). Dry-season precipitation in tropical West Africa and its relation to forcing from the extratropics, *Monthly Weather Review* **136**(9): 3579–3596.

Knippertz, P., Fink, A. H., Deroubaix, A., Morris, E., Tocquer, F., Evans, M. J., Flamant, C., Gaetani, M., Lavaysse, C., Mari, C. et al. (2017). A meteorological and chemical overview of the DACCIWA field campaign in West Africa in June–July 2016, *Atmospheric Chemistry and Physics Discussions* pp. 1–45.

Knippertz, P., Fink, A. H., Schuster, R., Trentmann, J., Schrage, J. M. and Yorke, C. (2011). Ultra-low clouds over the southern West African monsoon region, *Geophysical research letters* **38**(21).

Kojima, M., Miura, T., Furukawa, K., Hyakusoku, Y., Ishikiri, T., Kai, H., Iguchi, T., Hanado, H. and Nakagawa, K. (2012). Dual-frequency precipitation radar (DPR) development on the global precipitation measurement (GPM) core observatory, *Earth Observing Missions and Sensors: Development, Implementation, and Characterization II*, Vol. 8528, International Society for Optics and Photonics, p. 85281A.

Kong, K.-y. (2006). 9b. 4 understanding the genesis of hurricane vince through the surface pressure tendency equation.

Kuettner, J. P. and Parker, D. E. (1976). GATE: Report on the field phase, *sciences* **57**(1).

Kummerow, C., Barnes, W., Kozu, T., Shiue, J. and Simpson, J. (1998). The tropical rainfall measuring mission (TRMM) sensor package, *Journal of atmospheric and oceanic technology* **15**(3): 809–817.

Kummerow, C., Simpson, J., Thiele, O., Barnes, W., Chang, A., Stocker, E., Adler, R., Hou, A., Kakar, R., Wentz, F. et al. (2000). The status of the tropical rainfall measuring mission (TRMM) after two years in orbit, *Journal of Applied meteorology* **39**(12): 1965–1982.

Lafore, J.-P., Beucher, F., Peyrillé, P., Diongue-Niang, A., Chapelon, N., Bouniol, D., Caniaux, G., Favot, F., Ferry, F. and Guichard, F. (2017a). A multi-scale analysis of the extreme rain event of Ouagadougou in 2009, *Quarterly Journal of the Royal Meteorological Society* **143**(709): 3094–3109.

Lafore, J. P., Chapelon, N., Beucher, F., Kane, M. D., Gaymard, A., Kasimou, A., Lepape, S., Mumbae, Z., Orji, B., Osika, D. et al. (2017b). West African synthetic analysis and forecast, *Meteorology of Tropical West Africa: The Forecasters Handbook* pp. 423–451.

Lafore, J. P., Chapelon, N., Diop, M., Gueye, B., Largeron, Y., Lepape, S., Ndiaye, O., Parker, D. J., Poan, E., Roca, R. et al. (2017c). Deep convection, *Meteorology of Tropical West Africa: The Forecasters Handbook* pp. 90–129.

Laing, A. G., Carbone, R., Levizzani, V. and Tuttle, J. (2008). The propagation and diurnal cycles of deep convection in northern tropical Africa, *Quarterly Journal of the Royal Meteorological Society* **134**(630): 93–109.

Lamb, P. J. and Peppler, R. A. (1992). Further case studies of tropical Atlantic surface atmospheric and oceanic patterns associated with sub-saharan drought, *Journal of climate* **5**(5): 476–488.

Lavaysse, C., Flamant, C., Janicot, S., Parker, D., Lafore, J.-P., Sultan, B. and Pelon, J. (2009). Seasonal evolution of the West African heat low: a climatological perspective, *Climate Dynamics* **33**(2-3): 313–330.

Le Barbé, L., Lebel, T. and Tapsoba, D. (2002). Rainfall variability in West Africa during the years 1950–90, *Journal of climate* **15**(2): 187–202.

Le Blancq, F. (2011). Diurnal pressure variation: the atmospheric tide, *Weather* **66**(11): 306–307.

Lebel, T. and Ali, A. (2009). Recent trends in the central and western Sahel rainfall regime (1990–2007), *Journal of Hydrology* **375**(1): 52–64.

Lebel, T., Parker, D. J., Flamant, C., Bourlès, B., Marticoréna, B., Mougin, E., Peugeot, C., Diedhiou, A., Haywood, J., Ngamini, J.-B. et al. (2010). The AMMA field campaigns: multiscale and multidisciplinary observations in the West African region, *Quarterly Journal of the Royal Meteorological Society* **136**(S1): 8–33.

Lehmann, J., Coumou, D. and Frieler, K. (2015). Increased record-breaking precipitation events under global warming, *Climatic Change* **132**(4): 501–515.

Lensky, I. and Rosenfeld, D. (2008). Clouds-aerosols-precipitation satellite analysis tool (CAPSAT), *Atmospheric Chemistry and Physics* **8**(22): 6739–6753.

Leroux, S. and Hall, N. M. (2009). On the relationship between African easterly waves and the African easterly jet, *Journal of the Atmospheric Sciences* **66**(8): 2303–2316.

L'hote, Y., Mahé, G., Somé, B. and Triboulet, J. P. (2002). Analysis of a Sahelian annual rainfall index from 1896 to 2000; the drought continues, *Hydrological Sciences Journal* **47**(4): 563–572.

Liu, C. and Zipser, E. J. (2009). "warm rain" in the tropics: Seasonal and regional distributions based on 9 yr of TRMM data, *Journal of Climate* **22**(3): 767–779.

Lothon, M., Saïd, F., Lohou, F. and Campistron, B. (2008). Observation of the diurnal cycle in the low troposphere of West Africa, *Monthly Weather Review* **136**(9): 3477–3500.

Maranan, M. and Fink, A. H. (2016). Radiosonde - all sites, *Sedoo/Baobab database, doi:10.6096/BAOBAB-DACCIWA.1656* .

Maranan, M., Fink, A. H., Knippertz, P., Francis, S. D., Akpo, A. B., Jegede, G. and Yorke, C. (2019). Interactions between convection and a moist vortex associated with an extreme rainfall event over southern West Africa, *Monthly Weather Review* **147**(7): 2309–2328.

Maranan, M., Fink, A. and Knippertz, P. (2018). Rainfall types over southern West Africa: Objective identification, climatology and synoptic environment, *Quarterly Journal of the Royal Meteorological Society* .

Markowski, P. and Richardson, Y. (2011). *Mesoscale meteorology in midlatitudes*, Vol. 2, John Wiley & Sons.

Mathon, V. and Laurent, H. (2001). Life cycle of Sahelian mesoscale convective cloud systems, *Quarterly Journal of the Royal Meteorological Society* **127**(572): 377–406.

Mathon, V., Laurent, H. and Lebel, T. (2002). Mesoscale convective system rainfall in the Sahel, *Journal of applied meteorology* **41**(11): 1081–1092.

Mekonnen, A., Thorncroft, C. D. and Aiyyer, A. R. (2006). Analysis of convection and its association with African easterly waves, *Journal of Climate* **19**(20): 5405–5421.

Mohr, K. I. and Thorncroft, C. D. (2006). Intense convective systems in West Africa and their relationship to the African easterly jet, *Quarterly Journal of the Royal Meteorological Society* **132**(614): 163–176.

Molini, L., Parodi, A., Rebora, N. and Craig, G. (2011). Classifying severe rainfall events over Italy by hydrometeorological and dynamical criteria, *Quarterly Journal of the Royal Meteorological Society* **137**(654): 148–154.

Negri, A. J., Adler, R. F., Nelkin, E. J. and Huffman, G. J. (1994). Regional rainfall climatologies derived from Special Sensor Microwave Imager (SSM/I) data, *Bulletin of the American Meteorological Society* **75**(7): 1165–1182.

Nicholls, S. D. and Mohr, K. I. (2010). An analysis of the environments of intense convective systems in West Africa in 2003, *Monthly Weather Review* **138**(10): 3721–3739.

Nicholson, S. (2005). On the question of the "recovery" of the rains in the West African Sahel, *Journal of arid environments* **63**(3): 615–641.

Nicholson, S. E. (1981). Rainfall and atmospheric circulation during drought periods and wetter years in West Africa, *Monthly Weather Review* **109**(10): 2191–2208.

Nicholson, S. E. (2009a). On the factors modulating the intensity of the tropical rainbelt over West Africa, *International Journal of Climatology: A Journal of the Royal Meteorological Society* **29**(5): 673–689.

Nicholson, S. E. (2009b). A revised picture of the structure of the monsoon and land ITCZ over West Africa, *Climate Dynamics* **32**(7-8): 1155–1171.

Nicholson, S. E. (2013). The West African Sahel: A review of recent studies on the rainfall regime and its interannual variability, *ISRN Meteorology* **2013**.

Nicholson, S. E. and Grist, J. P. (2003). The seasonal evolution of the atmospheric circulation over West Africa and equatorial Africa, *Journal of Climate* **16**(7): 1013–1030.

Nicholson, S. E., Klotter, D. and Dezfuli, A. K. (2012). Spatial reconstruction of semi-quantitative precipitation fields over Africa during the nineteenth century from documentary evidence and gauge data, *Quaternary Research* **78**(1): 13–23.

Nicholson, S. E., Some, B., McCollum, J., Nelkin, E., Klotter, D., Berte, Y., Diallo, B., Gaye, I., Kpabeba, G., Ndiaye, O. et al. (2003). Validation of TRMM and other rainfall estimates with a high-density gauge dataset for West Africa. Part I: Validation of gpcc rainfall product and pre-TRMM satellite and blended products, *Journal of Applied Meteorology* **42**(10): 1337–1354.

Nicholson, S. E., Tucker, C. J. and Ba, M. (1998). Desertification, drought, and surface vegetation: An example from the West African Sahel, *Bulletin of the American Meteorological Society* **79**(5): 815–830.

Nolan, D. S., Zhang, C. and Chen, S.-h. (2007). Dynamics of the shallow meridional circulation around intertropical convergence zones, *Journal of the atmospheric sciences* **64**(7): 2262–2285.

Omotosho, J. (1985). The separate contributions of line squalls, thunderstorms and the monsoon to the total rainfall in Nigeria, *International Journal of Climatology* **5**(5): 543–552.

Ooyama, K. V. (1982). Conceptual evolution of the theory and modeling of the tropical cyclone, *Journal of the Meteorological Society of Japan. Ser. II* **60**(1): 369–380.

Paeth, H., Fink, A. H., Pohle, S., Keis, F., Mächel, H. and Samimi, C. (2011). Meteorological characteristics and potential causes of the 2007 flood in sub-saharan Africa, *International Journal of Climatology* **31**(13): 1908–1926.

Panthou, G., Vischel, T. and Lebel, T. (2014). Recent trends in the regime of extreme rainfall in the central Sahel, *International Journal of Climatology* **34**(15): 3998–4006.

Parker, D., Burton, R., Diongue-Niang, A., Ellis, R., Felton, M., Taylor, C., Thorncroft, C., Bessemoulin, P. and Tompkins, A. (2005a). The diurnal cycle of the West African monsoon circulation, *Quarterly Journal of the Royal Meteorological Society* **131**(611): 2839–2860.

Parker, D. J. (2017a). *Meteorology of tropical West Africa: The Forecasters handbook*, John Wiley & Sons.

Parker, D. J., Kassimou, A., Orji, B. N., Osika, D. P., Hamza, I., Diop-Kane, M., Fink, A., Galvin, J., Guichard, F., Lamptey, B. L. et al. (2017b). Local weather, *Meteorology of Tropical West Africa: The Forecasters Handbook* pp. 130–174.

Parker, D. J., Thorncroft, C. D., Burton, R. R. and Diongue-Niang, A. (2005b). Analysis of the African easterly jet, using aircraft observations from the JET2000 experiment, *Quarterly Journal of the Royal Meteorological Society* **131**(608): 1461–1482.

Payne, S. W. and McGarry, M. M. (1977). The relationship of satellite inferred convective activity to easterly waves over West Africa and the adjacent ocean during phase iii of GATE, *Monthly Weather Review* **105**(4): 413–420.

Petković, V. and Kummerow, C. D. (2017). Understanding the sources of satellite passive microwave rainfall retrieval systematic errors over land, *Journal of Applied Meteorology and Climatology* **56**(3): 597–614.

Petty, G. W. (1995). The status of satellite-based rainfall estimation over land, *Remote Sensing of Environment* **51**(1): 125–137.

Polavarapu, R. and Austin, G. (1979). A review of the garp Atlantic tropical experiment (GATE), *Atmosphere-Ocean* **17**(1): 1–13.

Ramel, R., Gallée, H. and Messager, C. (2006). On the northward shift of the west african monsoon, *Climate Dynamics* **26**(4): 429–440.

Raymond, D. and Jiang, H. (1990). A theory for long-lived mesoscale convective systems, *Journal of the atmospheric sciences* **47**(24): 3067–3077.

Redelsperger, J.-L., Thorncroft, C. D., Diedhiou, A., Lebel, T., Parker, D. J. and Polcher, J. (2006). African Monsoon Multidisciplinary Analysis: An international research project and field campaign, *Bulletin of the American Meteorological Society* **87**(12): 1739–1746.

Redl, R., Fink, A. H. and Knippertz, P. (2015). An objective detection method for convective cold pool events and its application to northern Africa, *Monthly Weather Review* **143**(12): 5055–5072.

Reed, R. J., Norquist, D. C. and Recker, E. E. (1977). The structure and properties of African wave disturbances as observed during phase iii of GATE, *Monthly Weather Review* **105**(3): 317–333.

Riemann-Campe, K., Fraedrich, K. and Lunkeit, F. (2009). Global climatology of convective available potential energy (CAPE) and convective inhibition (CIN) in era-40 reanalysis, *Atmospheric Research* **93**(1): 534–545.

Roebeling, R., Deneke, H. and Feijt, A. (2008). Validation of cloud liquid water path retrievals from SEVIRI using one year of CloudNET observations, *Journal of applied Meteorology and Climatology* **47**(1): 206–222.

Romatschke, U. and Houze, R. A. (2010). Extreme summer convection in south america, *Journal of Climate* **23**(14): 3761–3791.

Romatschke, U., Medina, S. and Houze, R. A. (2010). Regional, seasonal, and diurnal variations of extreme convection in the south asian region, *Journal of climate* **23**(2): 419–439.

Rosenfeld, D. and Lensky, I. M. (1998). Satellite-based insights into precipitation formation processes in continental and maritime convective clouds, *Bulletin of the American Meteorological Society* **79**(11): 2457–2476.

Rosenfeld, D. and Woodley, W. L. (2000). Deep convective clouds with sustained supercooled liquid water down to -37.5 c, *Nature* **405**(6785): 440.

Rossow, W. B. and Schiffer, R. A. (1999). Advances in understanding clouds from ISCCP, *Bulletin of the American Meteorological Society* **80**(11): 2261–2288.

Rotunno, R., Klemp, J. B. and Weisman, M. L. (1988). A theory for strong, long-lived squall lines, *Journal of the Atmospheric Sciences* **45**(3): 463–485.

Roundy, P. E. and Frank, W. M. (2004). A climatology of waves in the equatorial region, *Journal of the atmospheric sciences* **61**(17): 2105–2132.

Rowell, D. P. and Milford, J. R. (1993). On the generation of African squall lines, *Journal of Climate* **6**(6): 1181–1193.

Salonen, K. and Borman, N. (2016). *Atmospheric motion vector observations in the ECMWF system: Fifth year report*, European Centre for Medium-Range Weather Forecasts.

Sanogo, S., Fink, A. H., Omotosho, J. A., Ba, A., Redl, R. and Ermert, V. (2015). Spatio-temporal characteristics of the recent rainfall recovery in West Africa, *International Journal of Climatology* **35**(15): 4589–4605.

Schlueter, A., Fink, A. H., Knippertz, P. and Vogel, P. (2018). A systematic comparison of tropical waves over northern Africa. Part I: Influence on rainfall, *Journal of Climate, under revision* .

Schrage, J. M. and Fink, A. H. (2012). Nocturnal continental low-level stratus over tropical West Africa: Observations and possible mechanisms controlling its onset, *Monthly Weather Review* **140**(6): 1794–1809.

Schrage, J. M., Fink, A. H., Ermert, V. and Ahlonsou, E. D. (2006). Three MCS cases occurring in different synoptic environments in the sub-Sahelian wet zone during the 2002 West African monsoon, *Journal of the atmospheric sciences* **63**(9): 2369–2382.

Schröder, M., König, M. and Schmetz, J. (2009). Deep convection observed by the spinning enhanced visible and infrared imager on board meteosat 8: Spatial distribution and temporal evolution over Africa in summer and winter 2006, *Journal of Geophysical Research: Atmospheres* **114**(D5).

Schumacher, C. and Houze, R. A. (2003). The TRMM precipitation radar's view of shallow, isolated rain, *Journal of Applied Meteorology* **42**(10): 1519–1524.

Schuster, R., Fink, A. H. and Knippertz, P. (2013). Formation and maintenance of nocturnal low-level stratus over the southern West African monsoon region during AMMA 2006, *Journal of the Atmospheric Sciences* **70**(8): 2337–2355.

Schwendike, J. and Jones, S. C. (2010). Convection in an African easterly wave over West Africa and the eastern Atlantic: A model case study of helene (2006), *Quarterly Journal of the Royal Meteorological Society* **136**(S1): 364–396.

Simpson, J., Kummerow, C., Tao, W.-K. and Adler, R. F. (1996). On the tropical rainfall measuring mission (TRMM), *Meteorology and Atmospheric physics* **60**(1-3): 19–36.

Smull, B. F. and Houze Jr, R. A. (1987). Rear inflow in squall lines with trailing stratiform precipitation, *Monthly weather review* **115**(12): 2869–2889.

Sommeria, G. and Testud, J. (1984). COPT 81: A field experiment designed for the study of dynamics and electrical activity of deep convection in continental tropical regions, *Bulletin of the American Meteorological Society* **65**(1): 4–10.

Stein, T. H., Parker, D., Delanoë, J., Dixon, N., Hogan, R. J., Knippertz, P., Maidment, R. I. and Marsham, J. (2011). The vertical cloud structure of the West African monsoon: A 4 year climatology using Cloudsat and CALIPSO, *Journal of Geophysical Research: Atmospheres* **116**(D22).

Stengel, M., Kniffka, A., Meirink, J., Lockhoff, M., Tan, J. and Hollmann, R. (2014). CLAAS: the CM SAF cloud property data set using SEVIRI, *Atmospheric Chemistry and Physics* **14**(8): 4297–4311.

Subrahmanyam, K. and Kumar, K. (2013). Megha-tropiques/saphir measurements of humidity profiles: validation with airs and global radiosonde network, *Atmospheric Measurement Techniques Discussions* **6**(6): 11405–11437.

Sui, C.-H. and Yanai, M. (1986). Cumulus ensemble effects on the large-scale vorticity and momentum fields of GATE. Part I: Observational evidence, *Journal of the atmospheric sciences* **43**(15): 1618–1642.

Sultan, B. and Janicot, S. (2003). The West African monsoon dynamics. Part II: The "preonset" and "onset" of the summer monsoon, *Journal of climate* **16**(21): 3407–3427.

Taylor, C. M., Belušić, D., Guichard, F., Parker, D. J., Vischel, T., Bock, O., Harris, P. P., Janicot, S., Klein, C. and Panthou, G. (2017). Frequency of extreme Sahelian storms tripled since 1982 in satellite observations, *Nature* **544**(7651): 475–478.

Tetzlaff, G. and Peters, M. (1988). A composite study of early summer squall lines and their environment over West Africa, *Meteorology and Atmospheric Physics* **38**(3): 153–163.

Thiaw, W. M. and Kumar, V. B. (2015). NOAA African desk: Twenty years of developing capacity in weather and climate forecasting in Africa, *Bulletin of the American Meteorological Society* **96**(5): 737–753.

Thorncroft, C. and Blackburn, M. (1999). Maintenance of the African easterly jet, *Quarterly Journal of the Royal Meteorological Society* **125**(555): 763–786.

Thorncroft, C. D., Nguyen, H., Zhang, C. and Peyrille, P. (2011). Annual cycle of the West African monsoon: regional circulations and associated water vapour transport, *Quarterly Journal of the Royal Meteorological Society* **137**(654): 129–147.

Thorncroft, C., Parker, D., Burton, R., Diop, M., Ayers, J., Barjat, H., Devereau, S., Diongue, A., Dumelow, R., Kindred, D. et al. (2003). The JET2000 project: Aircraft observations of the African easterly jet and African easterly waves: Aircraft observations of the African easterly jet and African easterly waves, *Bulletin of the American Meteorological Society* **84**(3): 337–352.

Tjemkes, S. A. (2005). On the conversion from radiances to equivalent brightness temperatures, *URL: http://www. eumetsat. int/groups/ops/documents/document/pdf_msg_ seviri_rad2bright. pdf* .

Tompkins, A. M. and Adebiyi, A. A. (2012). Using Cloudsat cloud retrievals to differentiate satellite-derived rainfall products over West Africa, *Journal of Hydrometeorology* **13**(6): 1810–1816.

Trenberth, K. E. (2011). Changes in precipitation with climate change, *Climate Research* **47**(1-2): 123–138.

Trenberth, K. E., Dai, A., Rasmussen, R. M. and Parsons, D. B. (2003). The changing character of precipitation, *Bulletin of the American Meteorological Society* **84**(9): 1205–1218.

Trenberth, K., Jones, P., Ambenje, P., Bojariu, R., Easterling, D., Klein Tank, A., Parker, D., Rahimzadeh, F., Renwick, J., Rusticucci, M. et al. (2007). Observations: surface and atmospheric climate change. chapter 3, *Climate change* pp. 235–336.

UN (2014). *World Urbanization Prospects: The 2014 Revision-Highlights*, UN.

UN (2015). World population prospects: The 2015 revision, *United Nations Econ Soc Aff* **33**(2): 1–66.

Upton, G. J. (2002). A correlation–regression method for tracking rainstorms using rain-gauge data, *Journal of Hydrology* **261**(1-4): 60–73.

van der Linden, R., Fink, A. H. and Redl, R. (2015). Satellite-based climatology of low-level continental clouds in southern West Africa during the summer monsoon season, *Journal of Geophysical Research: Atmospheres* **120**(3): 1186–1201.

Vizy, E. K. and Cook, K. H. (2018). Mesoscale convective systems and nocturnal rainfall over the West African Sahel: role of the inter-tropical front, *Climate Dynamics* **50**(1-2): 587–614.

Vogel, P., Knippertz, P., Fink, A. H., Schlueter, A. and Gneiting, T. (2018). Skill of global raw and postprocessed ensemble predictions of rainfall over northern tropical Africa, *Weather and Forecasting* **33**(2): 369–388.

Vollmert, P., Fink, A. H. and Besler, H. (2003). Ghana dry zone" und "Dahomey Gap": Ursachen für eine Niederschlagsanomalie im tropischen Westafrika, *Erde* **134**(4): 375–393.

Weisman, M. L. and Klemp, J. B. (1982). The dependence of numerically simulated convective storms on vertical wind shear and buoyancy, *Monthly Weather Review* **110**(6): 504–520.

Westra, S., Alexander, L. V. and Zwiers, F. W. (2013). Global increasing trends in annual maximum daily precipitation, *Journal of Climate* **26**(11): 3904–3918.

Whiteman, C. D. (2000). *Mountain meteorology: fundamentals and applications*, Oxford University Press.

WHO (2007). Wfp, 2007, *Communitybased management of severe acute malnutrition: A Joint Statement by the World Health Organization, the World Food Programme, the United Nations System Standing Committee on Nutrition and the United Nations Children's Fund. Geneva, New York, Rome* .

Williams, M. and Houze Jr, R. A. (1987). Satellite-observed characteristics of winter monsoon cloud clusters, *Monthly Weather Review* **115**(2): 505–519.

WMO (2009). Manual on codes: International codes volume i. 1, part a—alphanumeric codes.

Yang, G.-Y. and Slingo, J. (2001). The diurnal cycle in the tropics, *Monthly Weather Review* **129**(4): 784–801.

Young, M. P., Chiu, J. C., Williams, C. J., Stein, T. H., Stengel, M., Fielding, M. D. and Black, E. (2018). Spatio-temporal variability of warm rain events over southern west africa from geostationary satellite observations for climate monitoring and model evaluation, *Quarterly Journal of the Royal Meteorological Society* **144**(716): 2311–2330.

Zawislak, J. and Zipser, E. J. (2010). Observations of seven African easterly waves in the east Atlantic during 2006, *Journal of the Atmospheric Sciences* **67**(1): 26–43.

Zhang, C., Nolan, D. S., Thorncroft, C. D. and Nguyen, H. (2008). Shallow meridional circulations in the tropical atmosphere, *Journal of Climate* **21**(14): 3453–3470.

Zuluaga, M. D. and Houze, R. A. (2013). Evolution of the population of precipitating convective systems over the equatorial indian ocean in active phases of the madden–julian oscillation, *Journal of the Atmospheric Sciences* **70**(9): 2713–2725.

Zuluaga, M. D. and Houze, R. A. (2015). Extreme convection of the near-equatorial americas, Africa, and adjoining oceans as seen by TRMM, *Monthly Weather Review* **143**(1): 298–316.

Danksagung / Acknowledgment

Zuallererst möchte ich mich bei meinem Betreuer Prof. Dr. Andreas Heinrich Fink bedanken, denn du hast mir erst die Möglichkeit gegeben, diese Doktorandenstelle anzutreten und damit Teil der Arbeitsgruppe und der DACCIWA-Familie zu werden. Stets hast du dich darum bemüht, meinen Weg als Wissenschaftler zu fördern. Neben den vielen wertvollen fachlichen Diskussionen habe ich nicht zuletzt gelernt was es heißt, eine "data rat" zu sein. Ich hoffe, dass ich dem zumindest halbwegs Ehre machen konnte. Es war und ist ein Privileg, mit dir zu arbeiten. Mittlerweile akzeptiere ich sogar Kölsch als Getränk!

Im gleichen Atemzug danke ich Prof. Dr. Peter Knippertz, zunächst formell für die Übernahme des Korreferats, aber vor allem persönlich für die vielen wissenschaftlichen Hilfestellungen, Paperdiskussionen und, ganz wichtig, die Sommer-BBQs. Was für Andreas gilt, gilt auch für dich: In all den Gesprächen, die wir geführt hatten, habe ich immer eure Kompetenz und insbesondere eure Ehrlichkeit geschätzt. Bei letzterem auch eure offenkundige Abneigung gegen den FC Bayern. Nochmal, ich durfte mich glücklich schätzen, euch als Betreuer und Ansprechpartner zu haben.

I would like to thank the people in the working group "Atmospheric dynamics", many who I can happily call friends now. You guys were not less important work-wise, but I specifically enjoyed the familiarity within the group. I remember, when I started here, we were a group of six or seven. It has grown a lot since, and I can safely say for the better. Thanks again for everything! Likewise, I thank the people and buddies outside the working group, also those who have now left KIT. Always a pleasure to have some pints of fermented hops tea with you while hiking, watching football and Formula 1 and Super Bowl, or simply for having a good time. Particularly, the Oststadt group rocks!

Ich danke auch der gesamten Donnerstag-Fußball-Gruppe für die qualitativ hochklassigen Spiele, auch wenn mir mittlerweile ein Zeh fehlt (danke Florian E.).

To the entire DACCIWA community and particularly to the colleagues and friends at KNUST, many thanks! It was a pleasure to work with you and I enjoyed the cordiality whenever I was in Ghana. Thanks for your understanding whenever the food was too spicy. I am really not good in eating spicy meals. And hats off to the drivers for avoiding potholes as well as they could. My

back would not be there today!

Ein spezieller Dank geht an meine ehemaligen Studienkollegen weathermandk1, DasPeterle, Phil, LAQ, KU, sjae und Phälicks, von denen ich sagen kann, Freunde fürs Leben zu sein. Ich weiß nicht, wie das Studium ohne euch verlaufen wäre. Und ich möchte es eigentlich auch gar nicht wissen, denn die Zeit von damals bis jetzt war einfach cool. Und das bleibt auch so!

An Joyce-Anne Vogler, meine beste Freundin, die ich von Tag null an kenne: "Hurrrrz"!

Ich widme diese Arbeit meinen Eltern, Merlita und Chanito Maranan, und meinen Paten, Gloria und Franz Glökler. Für alles, was ihr für mich getan habt. Für die Tatsache, dass ihr immer für mich da seid. Für die Liebe, die ihr mir entgegenbringt. Mama, Papa, Ninang, Ninong, ich hoffe, ich habe euch stolz gemacht.